

# Steady-State and Dynamic Analysis of the LCC-Type Parallel Resonant Converter

by

Vivek Agarwal

B.Sc., University of Delhi, Delhi, 1985

M.E., Indian Institute of Science, Bangalore 1990

A Dissertation Submitted in Partial Fulfillment of the  
Requirements for the Degree of  
**DOCTOR OF PHILOSOPHY**

in the  
Department of Electrical and Computer Engineering

We accept this dissertation as conforming  
to the required standard

---

Dr. A. K. S. Bhat, Supervisor (Dept. of Electrical and Computer Engineering)

---

Dr. J. M. S. Kim, Department Member (Dept. of Electrical and Computer Engineering)

---

Dr. H. H. L. Kwok, Department Member (Dept. of Electrical and Computer Engineering)

---

Dr. S. Dost, Outside Member, (Dept. of Mechanical Engineering)

---

Dr. W. G. Dunford, External Examiner, (Univ. of British Columbia)

© VIVEK AGARWAL, 1994

University of Victoria

All rights reserved. This dissertation may not be reproduced in whole or in part, by photocopy or other means, without the permission of the author.

Supervisor: Dr. A. K. S. Bhat

## Abstract

This thesis presents the steady-state and dynamic analysis of the series-parallel resonant converter (SPRC), which is a popular configuration of the resonant power converters. The dynamic analysis includes both large and small-signal analysis. This converter is operated in variable frequency as well as fixed frequency control modes.

For the variable frequency operation, various operating modes, including the multiple conduction modes, of the converter have been identified. A generalized steady-state solution for these modes is obtained using the state-space approach. Design curves for converter gain and peak component stresses, versus the normalized load current, have been obtained. The boundaries between the various modes of operations (continuous capacitor voltage mode and discontinuous capacitor voltage mode as well as leading and lagging power factor modes) have been obtained. Experimental results obtained from a 100 W converter are presented to verify the theory.

Discrete time domain large-signal models have been derived for the converter operating in variable frequency mode for continuous and discontinuous current modes. These models have been used to study the large-signal behavior of the converter for step change in input supply voltage, step change in load, etc. The models are also used to determine the peak component stresses and discrete state response of the converter for large-signal transients. Theoretical results have been verified using SPICE simulation and experiments. It is shown by an experimental converter that most of the drawbacks of the open loop system can be overcome by operating the converter with a closed loop.

The large-signal equations for the converter operating in variable frequency and continuous current mode have been linearized about the steady-state operating point

to obtain a linearized small-signal state-space model in discrete time domain. Multiple loops have been used to control the dynamics of the converter. An outer voltage feedback loop takes care of the output voltage regulation. An inner state variable feedback loop is also incorporated to improve the dynamics of the converter. The small-signal models obtained are used to study the small-signal behavior of the converter for parameters like control to output transfer function and audio-susceptibility. Experimental results are presented to verify the key theoretical results.

A small-signal equivalent circuit model has also been obtained to study the small-signal behavior of the converter. This model represents the converter dynamics in a more accessible and flexible format. It gives more physical insight into the converter dynamics and can be solved for the various transfer functions conveniently. Both exact (discrete time domain) and approximate (continuous time domain) models are obtained. When the exact model is used, the results are found to be accurate up to the switching frequency. Analytical results are verified using an experimental converter.

The different operating modes of the fixed frequency pulse-width modulated SPRC have been identified. The steady-state analysis and a discrete time domain model for the large-signal analysis are presented for the predominant mode for a capacitor ratio of 1. The large-signal model has been linearized to perform the small-signal analysis much on the same lines as for the variable frequency operation. These models have been used to study the large and small-signal dynamics of the SPRC.

## Examiners:

---

Dr. A. K. S. Bhat, ~~Supervisor~~ (Dept. of Electrical and Computer Engineering)

---

Dr. J. M. S. Kim, ~~Department~~ Member (Dept. of Electrical and Computer Engineering)

---

Dr. H. H. L. Kwok, Department Member (Dept. of Electrical and Computer Engineering)

---

Dr. S. Dost, ~~Outside Member~~ (Dept. of Mechanical Engineering)

---

Dr. W. G. Dunford, External Examiner, (Univ. of British Columbia)

# Table of Contents

<b>Abstract</b>	<b>ii</b>
<b>Table of Contents</b>	<b>v</b>
<b>List of Tables</b>	<b>ix</b>
<b>List of Figures</b>	<b>x</b>
<b>Acknowledgements</b>	<b>xvii</b>
<b>Dedication</b>	<b>xviii</b>
<b>1 Introduction</b>	<b>1</b>
1.1 DC to DC Converters . . . . .	2
1.2 Resonant Converters . . . . .	2
1.3 Operation of the SPRC . . . . .	4
1.3.1 Operation in Leading p.f. (Below Resonance) Mode . . . . .	6
1.3.2 Operation in Lagging p.f. (Above Resonance) Mode [12] . . . . .	7
1.4 Literature Survey . . . . .	11
1.5 Thesis Outline . . . . .	16
1.5.1 The DC Analysis of the Series-Parallel Resonant Converter (Chapter 2) . . . . .	17
1.5.2 Large-Signal Analysis of SPRC using Discrete Time Domain Modeling (Chapter 3) . . . . .	18
1.5.3 Small-Signal Analysis using Discrete Time Domain Modeling (Chapter 4) . . . . .	19
1.5.4 Small-Signal Equivalent Circuit Modeling of the SPRC (Chap- ter 5) . . . . .	19
1.5.5 Constant Frequency, Pulse-Width Modulated Operation of the SPRC (Chapter 6) . . . . .	20

<b>2</b>	<b>DC Analysis of the LCC-Type Parallel Resonant Converter</b>	<b>21</b>
2.1	Introduction . . . . .	22
2.2	SPICE Simulation and the Operating Modes . . . . .	23
2.2.1	Continuous Capacitor Voltage Mode (CCVM) . . . . .	24
2.2.2	The Discontinuous Capacitor Voltage Mode (DCVM) . . . . .	29
2.3	Analysis . . . . .	30
2.3.1	General Solutions . . . . .	31
2.3.2	Determination of the Initial State Vector $[x_0]$ . . . . .	34
2.3.3	Determination of the Interval Durations . . . . .	35
2.3.4	Particular Cases . . . . .	37
2.4	Converter Gain and Component Stresses . . . . .	39
2.5	Boundaries Between the Various Modes of Operation . . . . .	48
2.5.1	Boundary Between Leading and Lagging Power Factor Mode of Operation . . . . .	48
2.5.2	Boundaries Between DCVM and CCVM Operation . . . . .	50
2.6	Design of the Converter . . . . .	50
2.7	Experimental Verification . . . . .	57
2.8	Conclusions . . . . .	63
<b>3</b>	<b>Large-Signal Analysis Using Discrete Time Domain Modeling</b>	<b>65</b>
3.1	Introduction . . . . .	65
3.2	Converter Operation . . . . .	68
3.3	The Discrete Time Domain Model of the SPRC . . . . .	70
3.3.1	$k^{th}$ Event . . . . .	70
3.3.2	$(k + 1)^{th}$ Event . . . . .	73
3.3.3	Evaluation of $\alpha_k$ and $\beta_k$ . . . . .	74
3.3.4	The Output Equations . . . . .	75
3.3.5	Peak Component Stresses . . . . .	75
3.4	The Discrete State-Space Model . . . . .	77
3.4.1	Selection of Discrete State Variables . . . . .	77
3.4.2	Formulation of the Model . . . . .	78
3.4.3	The Steady State . . . . .	78
3.5	Design of the Converter . . . . .	79
3.6	Results of the Analysis . . . . .	80
3.6.1	Sudden Switching ON of the Supply Voltage . . . . .	80
3.6.2	Step Change in Input Supply Voltage . . . . .	88
3.6.3	Step Change in Operating Frequency . . . . .	88
3.6.4	Step Change in Load . . . . .	96
3.6.5	Effect of the Output Filter . . . . .	102
3.7	Experimental Results . . . . .	106

3.8	Discontinuous Current Mode (DCM) . . . . .	109
3.8.1	Converter Operation in DCM . . . . .	113
3.8.2	Discrete Time Domain Model for DCM . . . . .	116
3.8.3	Analytical Results for DCM . . . . .	119
3.9	Observations and Conclusions . . . . .	135
<b>4</b>	<b>Small-Signal Analysis using Discrete Time Domain Modeling</b>	<b>141</b>
4.1	Introduction . . . . .	142
4.2	The Discrete State-Space Model of the SPRC . . . . .	144
4.3	Linearization of SPRC about the Equilibrium Point . . . . .	145
4.4	State Feedback Control . . . . .	151
4.4.1	State Variable Feedback . . . . .	151
4.4.2	Control Law . . . . .	152
4.4.3	Integration with SPRC Model . . . . .	153
4.4.4	The Complete Control Scheme . . . . .	154
4.5	Dynamic Performance Parameters . . . . .	154
4.5.1	Stability Aspects and Closed Loop Operation . . . . .	158
4.6	Experimental Results . . . . .	164
4.7	Conclusions . . . . .	166
<b>5</b>	<b>Small-Signal Equivalent Circuit Model</b>	<b>173</b>
5.1	Introduction . . . . .	173
5.2	Converter Operation and Terminology . . . . .	176
5.3	Small-Signal Equivalent Circuit Modeling . . . . .	179
5.3.1	Large-Signal State Equations for Resonant Tank (Step 1) . . . . .	181
5.3.2	Input and Output Equations (Step 2) . . . . .	182
5.3.3	Perturbation and Linearization (Step 3) . . . . .	183
5.3.4	Elimination of $\hat{\alpha}$ (Step 4) . . . . .	185
5.3.5	Final Small-Signal Equations (Step 5) . . . . .	185
5.3.6	Elimination of Intermediate Variables (Step 6) . . . . .	186
5.3.7	Interfacing with the Input and Output Sections of the Converter (Step 7) . . . . .	190
5.4	Dynamic Performance Parameters . . . . .	190
5.5	Experimental Results . . . . .	198
5.6	Conclusions . . . . .	201
<b>6</b>	<b>Steady-State and Dynamic Analysis for Fixed Frequency Operation</b>	<b>202</b>
6.1	Introduction . . . . .	203
6.2	Operating Modes of a FF PWM SPRC . . . . .	206
6.2.1	Design of the Converter . . . . .	208

TABLE OF CONTENTS

viii

6.3	Steady-State Analysis using State-Space Approach . . . . .	214
6.3.1	General Solutions . . . . .	214
6.3.2	Steady-State Solutions . . . . .	215
6.3.3	Design Curves . . . . .	219
6.4	Large-Signal Analysis . . . . .	219
6.4.1	Terminology . . . . .	221
6.4.2	Discrete Time Domain Model for the FF PWM SPRC . . . . .	222
6.4.3	The Discrete State-Space Model . . . . .	224
6.4.4	Results of the Analysis . . . . .	225
6.4.5	Closed Loop Example: . . . . .	227
6.5	Small-Signal Analysis of FF PWM SPRC . . . . .	227
6.5.1	Linearization of SPRC About the Equilibrium Point . . . . .	228
6.5.2	Dynamic Performance Parameters . . . . .	232
6.6	Observations and Conclusions . . . . .	233
<b>7</b>	<b>Conclusions</b>	<b>249</b>
7.1	Major Contributions . . . . .	249
7.2	Summary of the Thesis Work . . . . .	251
7.3	Suggestions for Future Work . . . . .	257
	<b>Bibliography</b>	<b>259</b>
	<b>Appendices</b>	<b>270</b>
<b>A</b>	<b>General Solutions for <math>k^{th}</math> Event</b>	<b>270</b>
<b>B</b>	<b>Large-Signal State Equations for CCM</b>	<b>272</b>
<b>C</b>	<b>A, B, C Constants for DCM</b>	<b>273</b>
<b>D</b>	<b>A, B, C Constants for Fixed Frequency Operation, Predominant Mode</b>	<b>274</b>

## List of Tables

2.1	Variation of key parameters for $f_n = 0.8$ and variable load (from near load short circuit to near load open circuit) . . . . .	54
2.2	Variation of key parameters for fixed $Q = 4.17$ and variable $f_n$ , below resonance . . . . .	54
2.3	Variation of key parameters for fixed $Q = 4.17$ and variable $f_n$ , above resonance . . . . .	55
2.4	Voltage Regulation, for $f_n$ less than 0.8 . . . . .	56
2.5	Voltage Regulation, for $f_n$ greater than 0.8 . . . . .	56
2.6	Voltage Regulation during the multiple modes . . . . .	57
2.7	Comparison of simulation and experimental results for output voltage variation with change in operating frequency . . . . .	58
2.8	Comparison of interval durations obtained by Experiments, Simulation and Analysis, for $f_n = 0.35$ , four interval mode . . . . .	59
2.9	Comparison of component stresses and gain obtained using Experiments, Simulation and Analysis, for $f_n = 0.35$ , four interval mode . . . . .	59
2.10	Comparison of interval durations obtained by Experiments, Simulation and Analysis, for $f_n = 0.6$ , two interval mode . . . . .	59
2.11	Comparison of component stresses and gain obtained using Experiments, Simulation and Analysis for $f_n = 0.6$ , two interval mode . . . . .	60
4.1	Comparison with [73] . . . . .	158
5.1	Notation . . . . .	177
5.2	Steady-State Expressions . . . . .	178
5.3	Partial Derivatives . . . . .	186
5.4	Small-Signal Coefficients for the Resonant Tank Equations . . . . .	187
5.5	Small-Signal Coefficients for the Input and Output Equations . . . . .	188
5.6	Coefficients $\nu_{ijs}$ . . . . .	190
5.7	Coefficients $C_{ijs}$ . . . . .	191

# List of Figures

1.1	Complete circuit diagram of the LCC-type parallel resonant converter. Details of the snubbers are not shown in the diagram . . . . .	5
1.2	Typical waveforms of the SPRC operating in leading p.f. (below resonance) and continuous current mode. . . . .	8
1.3	Typical waveforms of the SPRC operating in discontinuous current mode. . . . .	8
1.4	Typical waveforms of the SPRC operating in lagging p.f. (above resonance) mode. . . . .	9
1.5	Typical Waveforms of the SPRC operating in above resonance, discontinuous capacitor voltage mode. . . . .	12
2.1	Equivalent Circuits for the three different intervals: (a) Interval A, (b) interval B, and (c) Interval C. ( $L = L_s + L_l$ , where $L_l$ is the leakage inductance of the hi transformer.) . . . . .	25
2.2	Typical operating waveforms of the LCC-type PRC (Fig. 2.1) for various modes of operation, obtained using SPICE. The current waveforms are magnified by a factor of 20 for the sake of clarity. . . . .	26
2.3	Comparison of MATLAB (state-space analysis) and SPICE simulation results. Plots of gain versus $J$ for two values of $f_n$ are given. . . . .	40
2.4	Plot of gain versus $f_n$ with $Q$ as a parameter (for $\frac{C_s}{C_t} = 1$ ) obtained using SPICE simulation. 3-dimensional plot is also included. . . . .	41
2.5	Normalized design curves for the peak stresses, obtained using SPICE simulation. . . . .	42
2.6	The boundaries between the various modes of operation. . . . .	49
2.7	(a) The boundaries between the CCV and DCV modes of operation. (b) Comparison between the actual boundary and the approximate one using curve fitting. . . . .	51
2.8	Typical waveforms obtained from the experimental set up ( $v_{ab}$ , $v_{ct}$ and $i$ ): (a),(b) Continuous Capacitor Voltage Mode. (c),(d): Discontinuous Capacitor Voltage Mode . . . . .	61

2.9	Plots of gain versus $f_n$ obtained using the experimental converter (marked "exp") along with those obtained using SPICE-3. . . . .	32
2.10	Plot of efficiency of the converter as a function of $f_n$ , with $Q$ as a parameter. . . . .	62
3.1	Basic circuit diagram of LCC type PRC (half-bridge version) in discrete time domain. Details of snubber circuits are not shown. . . . .	69
3.2	Typical waveforms of the SPRC circuit starting from the $k^{th}$ instant for lagging power factor mode of operation. The various intervals are marked. . . . .	69
3.3	Equivalent circuits for the two different intervals: (a) Interval B (b) Interval A. $L = L_s + L_l$ , where $L_l$ is the leakage inductance of the hf transformer. . . . .	71
3.4	The output section of the SPRC referred to the primary side . . . . .	71
3.5	Transients caused by Switching ON the input supply . . . . .	82
3.6	Switching ON transients continued . . . . .	84
3.7	Switch OFF transients: (a) The resonating inductor current. (b) Output variables. (c) Peak anti-parallel diode current. . . . .	86
3.8	Results for step change in input supply voltage from 25V to 50V: (a) Resonant inductor current during the transient phase. (b) Parallel capacitor voltage during the transient phase. (c),(d) SPICE plots corresponding to (a) and (b) respectively. . . . .	89
3.9	Peak component stresses for step change in the input voltage. . . . .	91
3.10	Variation in state variables for step change in the input voltage. (a) Tank state variables. (b) Output state variables. In (b), the SPICE results are also included for the sake of comparison. . . . .	92
3.11	Results obtained for a sudden change in the operating frequency from 200 kHz to 210 kHz. (a) Resonant inductor current. (b) Parallel capacitor voltage. (c), (d) SPICE plots corresponding to (a) and (b). . . . .	93
3.12	Peak component stresses as obtained from the model due to variation in frequency. . . . .	95
3.13	Discrete state variables for step change in the operating frequency. (a) Tank state variables. (b) Output state variables. In (b), SPICE results are also included for comparison. . . . .	97
3.14	Results obtained for a step change in load resistance to twice the rated value. (a) Resonant inductor current. (b) Parallel capacitor voltage during the transient phase. (c),(d) SPICE plots corresponding to (a) and (b) respectively. . . . .	98

3.15	(a) Peak component stresses as obtained from the model due to step change in load. (b) The discrete state (tank) variables. (c) Output state variables. In (c), SPICE results are also included for comparison.	100
3.16	Transient waveforms during the step change in load from full load to open circuit condition. (a) Resonating inductor current. (b) Parallel capacitor voltage. (c), (d) Discrete state variables. . . . .	103
3.17	Transient waveforms during the step change in load from full load to short circuit condition. (a) Resonating inductor current. (b) Parallel capacitor voltage. (c) Output Current. . . . .	105
3.18	Effect of the characteristic impedance of the output filter section on the response of the converter during switching ON. (a),(b) The peak resonating inductor current and the parallel capacitor voltage. (c) Discrete state variable $x_1$ corresponding to tank current. (d) Discrete state variable $x_3$ corresponding to parallel capacitor voltage. (e) Discrete state variable $x_5$ corresponding to output voltage. . . . .	107
3.19	Experimental waveforms during the transients caused by switching ON the dc supply of the converter (0 to 25 Volts). The instant where the step change occurs is shown by an arrow. (a) The very initial stage of the resonant inductor current. This Figure corresponds to Fig. 3.5(a). (b) Resonating inductor current during the entire transient phase. (c) Parallel capacitor voltage during the transient phase. (d) Output voltage. Details of the converter: $L_s = 17.74\mu H$ ; $C_s = 0.047\mu F$ ; $C_t = 0.047\mu F$ ; $C_f = 1\mu F$ ; $L_f = 1000\mu H$ ; Input dc voltage, $2E = 50$ Volts; Switches used: IRF 640 MOSFET's . . . . .	110
3.20	Experimental waveforms during the transients caused by a step change in the input supply from 25 Volts to 50 Volts: (a) Resonant inductor current. (b) Parallel capacitor voltage. (c) Output voltage. . . . .	111
3.21	Experimental waveforms during the transients caused by a step change in the operating frequency from 200 kHz to 210 kHz. (a) Resonant inductor current. (b) Parallel capacitor voltage. (c) Output voltage. . . . .	111
3.22	Experimental waveforms for a step change in the load from full load to half full load current (load resistance doubled). (a) Parallel capacitor voltage. (b) Resonant inductor current. (c) Output voltage. (d) Closed loop results for a step change in the load from full load to half load. . . . .	112
3.23	(a) Typical waveforms of the SPRC circuit operating in just DCM and DCVM mode of operation starting from the $k^{th}$ instant. (b) Discontinuous current mode waveforms showing the presence of a fourth interval ( $d_k$ ) during the "fixed ON time, variable frequency" gating control of the output power. The various intervals are marked in both the figures.	114

3.24	The equivalent circuits of the SPRC during the various intervals of DCVM and just DCM mode, using the constant current model. (a) During interval $a_k$ . (b) During interval $c_k$ . (c) Interval $d_k$ . During this interval all the switches are OFF and no supply is connected across points "a" and "b" . . . . .	115
3.25	Waveforms during the transients caused by switching ON the input supply to the converter from 0 to 75 V . . . . .	121
3.26	SPICE plots during the transients caused by switching ON the input supply from 0 to 75 V. . . . .	122
3.27	The discrete state variables ( $x_{1(k)}$ , and $x_{2(k)}$ ) and output state variables during the switching ON of the converter. In (a), $x_{3(k)}$ has not been plotted explicitly as it remains zero through out the transient phase. In (b), SPICE results are also included for comparison. . . . .	124
3.28	Effect of a smaller filter capacitor ( $C_f = 0.5\mu F$ ) value. (a) Resonating Inductor Current. (b) Discrete state variables. (c) Output Variables. . . . .	125
3.29	Waveforms during the transients caused by sudden load variation (full load to half load). . . . .	126
3.30	The discrete state (tank) variables during sudden variation of load (full load to half load). The variables $x_{1(k)}$ and $x_{3(k)}$ are not plotted explicitly, as they remain zero through out the transient phase. . . . .	128
3.31	Output variables during the transients caused by sudden load variation from full load to half the rated load, as obtained with the model and SPICE. . . . .	129
3.32	Transient waveforms during the step change in load from full load to short circuit condition. (a) Resonating inductor current. (b) Parallel capacitor voltage. (c),(d) SPICE plots corresponding to (a) and (b), respectively. . . . .	131
3.33	Discrete state (tank) variables during the step change from full load to short circuit conditions. . . . .	133
3.34	Output variables, current and voltage during a step change from full load to short circuit conditions. SPICE results are also included for the sake of comparison. . . . .	134
3.35	Experimental waveforms during the transients caused by switching ON the supply to the converter. . . . .	136
3.36	Experimental waveforms during the transients caused by a sudden load variation (from full load to half load). (a) Resonant inductor current. (b) Parallel capacitor voltage. . . . .	137
4.1	Complete control scheme of the SPRC. Note that the terms $x_{1(k+1)}$ , $x_{2(k+1)}$ etc. represent the sampled values. . . . .	156

4.2	Control to output bode plots for frequency controlled, open loop, without state feedback case. Details of the converter: Half bridge configuration with the details given in section 4.5. The plots obtained with the model of [73] are also included for comparison. . . . .	156
4.3	(a) Open loop audio-susceptibility bode plot obtained with the proposed model. (b) Output impedance transfer function. . . . .	157
4.4	Open loop control to output transfer function at half the rated load condition. Load resistance = $13.4 \Omega$ , $f_{switching} = 245 kHz$ . . . . .	159
4.5	(a) Open loop audio-susceptibility bode plot obtained with the proposed model for half the rated load condition. (b) Output impedance transfer function. . . . .	160
4.6	Trajectory of the open loop poles of the state feedback controlled SPRC. $S_3 = 1.0$ , while the ratio $\frac{S_1}{S_2}$ is varied. . . . .	163
4.7	Trajectory of the open loop poles of the state feedback controlled SPRC. $S_3 = 1.0$ , while the ratio $\frac{S_1}{S_2}$ is made negative. As the magnitude of this ratio becomes smaller, the roots (except $\lambda_1$ and $\lambda_4$ ) move towards the left of the origin. . . . .	163
4.8	MATLAB realization of the controlled SPRC. The commands used are standard and can be found in MATLAB manual. Note that disturbances $\delta E$ and $\delta i_{out}$ are treated as inputs to the system. . . . .	165
4.9	Comparison of the state feedback controlled SPRC's audio-susceptibility gain with a frequency controlled SPRC. . . . .	165
4.10	Comparison of the state feedback controlled SPRC's output impedance gain with an ordinary frequency controlled SPRC. . . . .	168
4.11	Experimental bode plots, obtained with the help of Hewlett Packard's 3577A network analyzer, for the control to output transfer function of the SPRC. These plots are for the open loop case. (a),(b): Gain and phase plots for the full load case. (c),(d) Gain and phase plots for the half full load case . . . . .	169
4.12	Experimental bode plot for the control to output transfer function for the closed loop operation of the frequency controlled SPRC, without state feedback . . . . .	171
4.13	Experimental bode plot for the control to output transfer function corresponding to Fig. 4.12, with the inner state feedback loop incorporated. . . . .	172
5.1	Waveforms showing the effect of perturbation on the circuit variables. The notation used is clearly marked and followed through out the chapter. . . . .	180

5.2	Two port hybrid parameter, small-signal equivalent circuit model of the SPRC developed in this chapter. The hybrid parameters have been defined in section 5.3. The output section of the SPRC is shown connected to the linearized small-signal model of the resonant tank.	180
5.3	Small-signal multiple port model of the SPRC . . . . .	191
5.4	Bode plot of control to output transfer function obtained with the approximate small-signal equivalent circuit model. . . . .	194
5.5	(a) Bode plot of output impedance transfer function obtained with the approximate small-signal equivalent circuit model. (b) Audio-susceptibility transfer function. . . . .	195
5.6	(a) The bode plot of the audio-susceptibility parameter. (b) Input admittance parameter. . . . .	196
5.7	Control to output transfer function obtained with <i>exact</i> small-signal equivalent circuit model. The plot of Fig. 5.4 is included for the sake of comparison. . . . .	199
5.8	Output impedance transfer function obtained with the exact model. The plot of Fig. 5.5(a) is also included for the sake of comparison. . . . .	199
5.9	Audio-susceptibility transfer function obtained with the exact model. The plot of Fig. 5.5(b) is also included for the sake of comparison. . . . .	200
5.10	Experimental waveforms corresponding to Fig. 5.7 These plots were obtained using a network analyzer (HP 3577A). The details of the converter are the same as given in section 5.4 . . . . .	200
6.1	The full bridge version of the SPRC suitable for fixed frequency operation. The timing sequence of the gating signals to the various switches is shown in Fig. 6.3. . . . .	207
6.2	Equivalent circuits of the SPRC for various intervals during different operating modes. . . . .	207
6.3	Time sequence of the gating pulses to the switches of the inverter bridge for fixed frequency PWM operation of the converter. . . . .	209
6.4	The various operating modes of the FF PWM SPRC for the design example with $C_s/C_t = 1$ . . . . .	212
6.5	The various operating modes of the FF PWM SPRC for the design example with $C_s/C_t = 2$ . . . . .	213
6.6	Normalized load current versus the phase shift $T_{sft}$ for regulated output voltage. . . . .	220
6.7	Peak component stresses for regulated output voltage. . . . .	220
6.8	Typical waveforms of the FF PWM SPRC circuit starting from the $k^{th}$ instant for lagging power factor mode of operation. The various intervals are marked. . . . .	235

6.9	(a) Resonating inductor and (b) parallel capacitor voltage, for step change in input voltage supply from 0V to 25V at half the rated load conditions. In all the plots the step change occurs at the origin. (c),(d): SPICE plots corresponding to (a) and (b). . . . .	236
6.10	Peak component stresses (p.u.) for step change in input supply. Note that all these plots have been obtained with discrete set of points obtained one per half cycle, and connected to give an over all continuous picture. . . . .	238
6.11	Discrete state variables: (a) Tank state variables. (b) Output state variables. SPICE results are also plotted for the sake of comparison. .	239
6.12	(a) Resonating inductor and (b) parallel capacitor voltage, for step change in load from half the rated load to quarter the rated load. (c),(d): SPICE plots corresponding to (a) and (b). . . . .	240
6.13	Peak component stresses (p.u.) for step change in load from half the rated load to quarter the rated load. . . . .	242
6.14	Discrete state variables for step change in load from half the rated load to quarter the rated load. . . . .	243
6.15	(a) Resonating inductor and (b) Parallel capacitor voltage for closed loop operation example where the duty cycle changes in response to a step change in load from half the rated load to quarter the rated load. (c),(d): SPICE plots corresponding to (a) and (b). . . . .	244
6.16	Peak component stresses (p.u.) for closed loop operation example where the duty cycle changes in response to a step change in load from half the rated load to quarter the rated load. . . . .	246
6.17	Discrete state variables for closed loop operation example where the duty cycle changes in response to a step change in load from half the rated load to quarter the rated load: (a) Tank state variables. (b) Output state variables. SPICE results are also plotted for the sake of comparison. . . . .	247
6.18	Results of the small-signal analysis: (a) The plot of control to output transfer function. (b) Plot of audio-susceptibility. (c) Plot of output impedance transfer function as obtained with the small-signal model obtained in this chapter. . . . .	248

## Acknowledgements

I would like to thank my supervisor, Professor Ashoka Bhat, for his guidance, encouragement and support during the course of this research work. I am grateful for his help in the preparation of this manuscript and for the financial assistance (through NSERC). I thank the members of my examining committee for their valuable suggestions.

I wish to thank my friends and professors at the Indian Institute of Science, Bangalore for building my basic concepts.

I thank my friends in the faculty of engineering at the University of Victoria, who gave me constant support throughout my research work and made my stay a memorable one.

I am grateful to my parents for their sacrifice, love and support. Finally, I am thankful for the encouragement given by other family members towards the decision to pursue a doctoral degree in Canada. Kamal, deserves a special mention. He has been a constant source of inspiration.

**To my parents and to my country, India**

# Chapter 1

## Introduction

The recent advancement in microelectronics, very large scale integration (VLSI) and fast switching power semiconductor devices have made possible compact, light weight and efficient power electronic systems. The frequency at which the power semiconductor devices can operate affects the size and weight of the converters. The advancement in power semiconductors and control circuits has given rise to high frequency power converters with more reliability. A major research area in power electronics tries to find ways of designing, analyzing and controlling these converters. This thesis is concerned with the steady-state and dynamic analysis of the series-parallel resonant converter (SPRC) operating in both variable and fixed frequency modes.

This chapter begins with a brief introduction to the topics of DC to DC converters and resonant converters, discussed in sections 1.1 and 1.2, respectively. The series-parallel resonant converter (SPRC) is the most popular configuration of the resonant converters. Its operation is described in section 1.3. A literature survey on the topics related to SPRC and resonant converters in general is given in section 1.4. And finally, section 1.5 gives an outline of this thesis.

## 1.1 DC to DC Converters

DC to DC converters are used to convert one level of DC voltage to another. Various configurations of these converters have been proposed so far based on the way the devices are switched and the way they are connected in the circuit. All these converters can be classified into two major categories.

- (1) The pulse-width modulated (PWM) converters.
- (2) The resonant converters.

The PWM converters suffer from the following drawbacks:

- (a) High switching stresses on the switches,
- (b) high power losses during the switching, and
- (c) electromagnetic interference (EMI) produced due to large  $di/dt$  and  $dv/dt$ .

The disadvantages of PWM converters become more pronounced as the switching frequency is increased. However, an increase in the switching frequency facilitates the use of smaller magnetic components like the transformer and the filters. This is desirable because the converter size and weight goes down (and power density goes up).

## 1.2 Resonant Converters

Resonant converters [1-87] offer a novel solution to this problem. In resonant converters, it is possible to have switching at either zero current or zero voltage. This overcomes some of the drawbacks mentioned above. The switching frequency can be high resulting in light, efficient and less costly converters. As mentioned earlier, the development of fast switching devices has spurred interest in the concept of resonant power conversion.

In the past, three main resonant converter configurations have been discussed [1-87]. They are the series resonant converter (SRC) [1, 2, 24, 25, 41, 42, 48], parallel resonant converter (PRC) [3, 29, 32], and the series-parallel resonant converter (SPRC) [5-23]. The SRC has a simple circuit configuration and a good power conversion efficiency. But since the link appears to the load as a high frequency current source, the SRC is more suitable for loads with small and slow impedance variations [8]. The SRC has the following main disadvantages:

- (1) The voltage regulation is difficult when the range of load resistance is too wide or when it changes too rapidly.
- (2) For a small output voltage and a large output current, the output filter capacitor is quite bulky because it has to handle large ripple current.

The PRC overcomes some of these drawbacks, but introduces some of its own. For example, the fast changing loads are more compatible with the load connected across the resonating capacitor, as is indeed the case with PRC which appears as voltage source. The PRC is self protected under load short circuit conditions because the resonating inductor offers considerable impedance at the high switching frequency, thereby limiting the resonating current to a safe value. On the other hand, a PRC needs protection against open load conditions. Another problem with the PRC is that the peak resonating current carried by the switches and resonating elements does not decrease with a reduction in load current. Therefore the efficiency of a PRC falls down under low load conditions. The SPRC configuration was proposed to combine the desirable features of SRC and PRC. Using a proper design, the SPRC has the following main advantages over the first two [7, 8]. They are:

- (1) Full power control range with a small variation in frequency.
- (2) High efficiency from full load to part load.

### 1.3 Operation of the SPRC

Fig. 1.1 shows the basic circuit diagram of SPRC. The SPRC has an extra capacitor in series with the resonating inductor, as compared to the PRC. Hence the SPRC is also called as LCC-type parallel resonant converter [7]. The diagram shows a half bridge configuration, which is sufficient for explaining the concept and can easily be extended to a full bridge configuration. The parallel resonating capacitor can be placed either on the primary side or on the secondary side of the high frequency transformer. In Fig. 1.1, the parallel capacitor has been placed on the secondary side. With this modification, it is possible to use the leakage inductances of the transformer as part of the resonating inductance, thereby taking into account the effect of high frequency transformer [14, 30]. The high frequency inverter stage of Fig. 1.1 consists of a resonant circuit switched by means of power semiconductor switches. This hf inverter in the resonant converter of Fig. 1.1, can be operated at a frequency which is either below or above the resonant frequency of the resonating elements mentioned above. Depending upon value of  $f_n$ , the ratio of switching frequency to the resonant frequency, various modes of operation are possible. These modes can be identified on the basis of the parallel capacitor voltage wave shape and the phase relation of resonant current with respect to the square voltage  $v_{ab}$ . When the current leads  $v_{ab}$ , it is called leading power factor (below resonance) mode operation. When the current lags  $v_{ab}$ , it is called lagging power factor (above resonance) mode operation. Depending on the value of load current, the converter may also enter the discontinuous capacitor voltage mode (DCVM) in which the parallel capacitor is shorted for certain intervals of operation. The following section describes the operating modes of the SPRC reported in the literature [7, 8, 12].

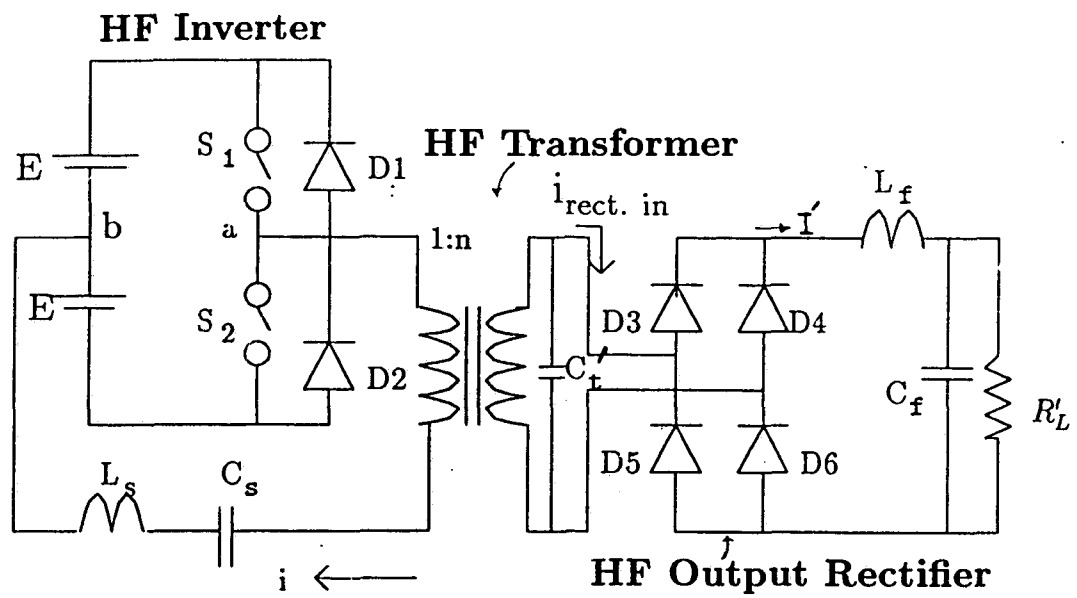


Figure 1.1: Complete circuit diagram of the LCC-type parallel resonant converter. Details of the snubbers are not shown in the diagram

### 1.3.1 Operation in Leading p.f. (Below Resonance) Mode

Depending on the switching frequency, the operation of the converter in leading p.f. (below resonance) mode can either be continuous current mode (CCM) or the discontinuous current mode (DCM). Operation of the resonant converter operating in leading p.f. mode in the CCM is briefly explained below.

Fig. 1.2(a) shows typical waveforms for the converter operating in leading p.f. mode in the CCM. The resonating current leads the square-wave voltage  $v_{ab}$ . During the positive half cycle, when switch S1 is switched ON, the current is transferred from D2 to S1. This current through S1 goes to zero sinusoidally and as it tries to reverse itself, diode D1 takes over conduction. The same sequence is repeated in the other half cycle with S2, D2 pair. The switching losses in the inverter devices and rectifiers are low in the circuits of the type explained above due to the sine waves that occur from the use of resonant circuits as opposed to square wave in the conventional converter. This results in easier EMI filtering. These converter circuits offer improvements over PWM converters due to higher efficiency, higher switching frequency, smaller high-frequency (HF) transformer and lower switching stresses.

The leading p.f. mode operation results in natural commutation of switches, allowing the use of fast thyristors including Asymmetric SCR's. The main problems associated with the operation in leading p.f. mode are the need for lossy RC snubbers, fast recovery feedback diodes and di/dt limiting inductors [11]. Power control is obtained by varying the frequency of operation below the frequency corresponding to full load, demanding the design of reactive elements and associated output filters for the lowest frequency of operation.

When SCR's (or transistors with proper gating signals) are used as switches and the switching frequency is decreased to control the output power, the inverter output

current can become discontinuous [11, 13]. Typical waveforms are shown in Fig. 1.3 for resonant inductor current ( $i$ ), the parallel capacitor voltage ( $v_{ct}$ ) and the rectifier input current. Same problems as discussed above for the leading p.f. mode operation, namely the need for lossy RC snubbers and fast recovery diodes, etc. occur in this case also. As the switching frequency is decreased the ripple level goes up. In order to meet the low ripple requirements, larger output filters are required for such operating conditions. The main advantage of operating the converter in this mode is that the switch current is zero both at the time of turn-on and turn-off, resulting in negligible switching losses. Also the ratings of lossy RC snubbers are much less in this case. Thus, the converter may be operated at higher frequencies. But the switch peak currents are higher for the same output power compared to the CCM.

The aforementioned disadvantages can be overcome by operating the converter in above resonance mode when gate or base turn off switches are used. In this case, the switches are forced to turn off before the current in the resonating components reverses. The operation of resonant inverters in lagging p.f. (above resonance) mode is described in section 1.3.2.

### 1.3.2 Operation in Lagging p.f. (Above Resonance) Mode [12]

Fig. 1.4 shows waveforms for lagging p.f. (above resonance) mode of operation. The resonating current is lagging the square-wave voltage  $v_{ab}$ . Assume that D1 is conducting initially. When the current goes to zero sinusoidally and as it tries to reverse its direction, switch S1 takes over since the gating signal for S1 is already present. S1 is turned-off at the end of half-period ( $T_s$ ). This causes D2 to turn-on. When the current through D2 goes to zero, S2 is turned-on. S2 is turned-off at  $2T_s$ , completing the cycle. It is clear from the operation that the commutating

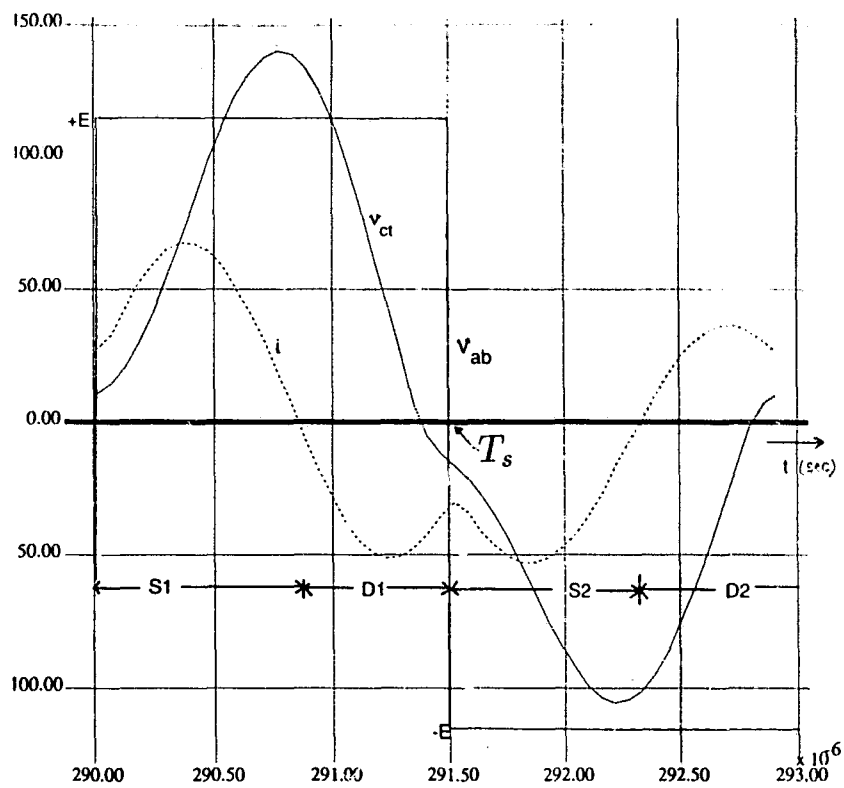


Figure 1.2: Typical waveforms of the SPRC operating in leading p.f. (below resonance) and continuous current mode.

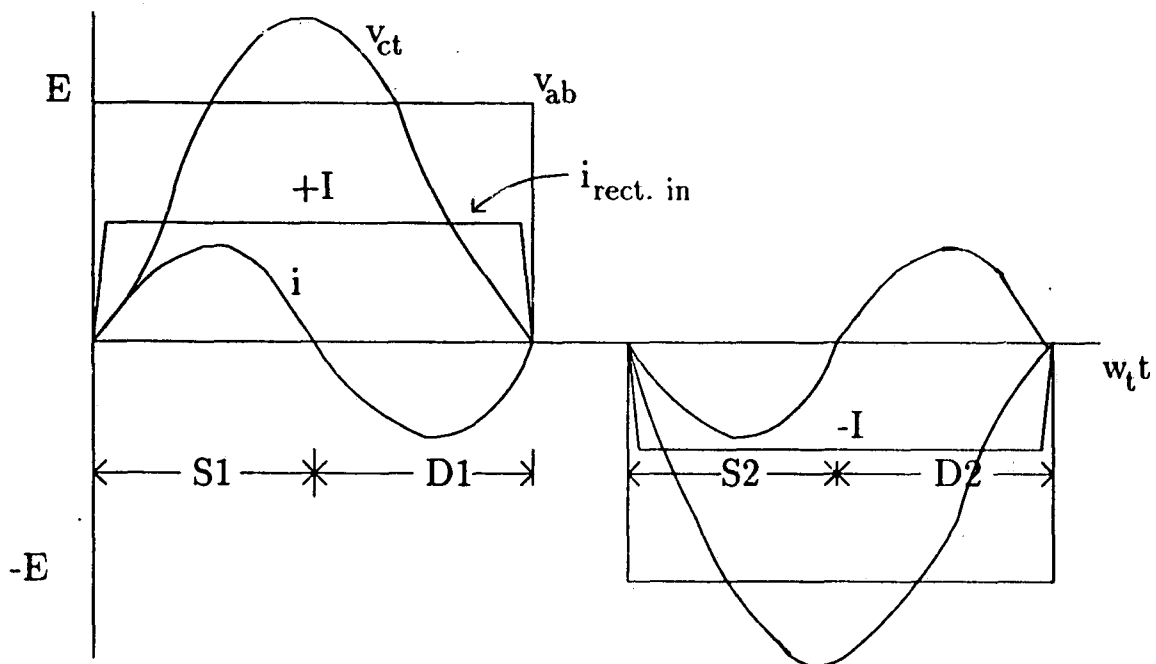


Figure 1.3: Typical waveforms of the SPRC operating in discontinuous current mode.

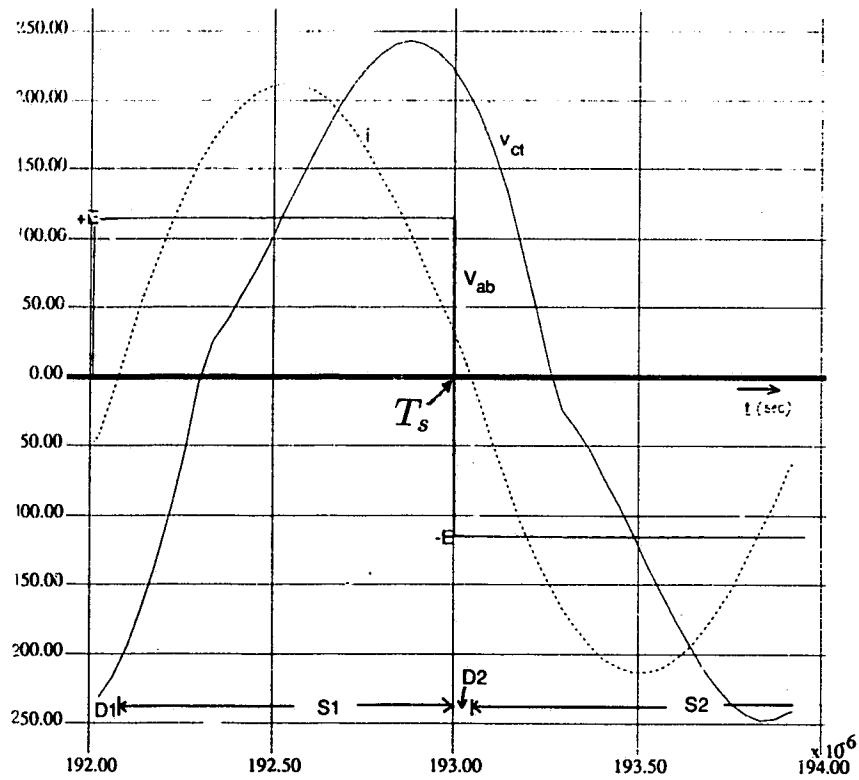


Figure 1.4: Typical waveforms of the SPRC operating in lagging p.f. (above resonance) mode.

components here have the function of merely wave-shaping the voltage and current in the converter circuit. Further, the switches turn on with zero voltage when the adjacent diodes are conducting. Hence, there are no turn-on losses associated with such operation. The input dc supply is not subjected to short circuits during current commutation from one pair of switches to the other pair. Hence, there is no need of current limiting inductances. Since the switches in this type of operation take over conduction from their anti-parallel diodes, there is no snubber discharge into the switch. This results in lossless snubber operation as the snubbers need not have current limiting resistances. Further, the voltage across the diodes remain negative for the duration of the conduction of the switches. Hence the diodes have considerable time to turn-off. However, the diodes should turn off before the next cycle starts. Thus the diodes need not be of fast recovery type. Nevertheless, in order to increase the frequency of operation, medium speed diodes are still required. Generally, the internal parasitic diode of power semiconductor switches (eg: MOSFETs) can be used for this purpose. It must be noted that the converter operates only in the CCM for lagging p.f. mode of operation. Power control for load (or line) variations in this case is achieved by increasing the switching frequency above the value corresponding to the full load case.

The operation of the resonant converter in lagging p.f. mode of operation reduces many disadvantages of leading p.f. mode of operation. But it also has some drawbacks. It should be noted that very high frequency switching has limitations from the converter operation point of view. At high switching frequencies, the effect of stray wiring inductance becomes significant. The turn-off and the transformer core losses go up. Design of control circuit becomes more difficult.

Whether the converter operates in leading or lagging p.f. mode, the parallel capacitor voltage can be continuous or discontinuous. Based on this, the operation

of converter can also be classified as continuous capacitor voltage mode (CCVM) or discontinuous capacitor voltage mode (DCVM) [12]. Although CCVM is the predominant mode, DCVM occurs when the load current goes above a critical value [12, 33]. Fig. 1.5 shows the DCV, lagging p.f. mode case. In this mode the parallel capacitor voltage becomes zero for certain intervals of operation.

## 1.4 Literature Survey

Resonant converters were known as early as 1960's [1-3]. N. Mapham [3] was the first one to report the use of parallel resonant converters. The basic circuit configuration and the operation of the circuit was well documented in this paper. But due to the non availability of fast switches at that time, the frequency of operation was quite low. Also, an extensive analysis was not possible due to lack of computing facilities required to solve the complex mathematical equations.

Analysis and Design of resonant converters gained momentum in the early 1980's. Myers and Peck [4] used the PRC configuration in lagging p.f. mode in 1981. Later, in 1982, Frank and Der [68] also used the PRC in lagging p.f. mode. Ranganathan *et al* [29] used a constant current model to analyze a PRC for operation below resonance and identified the different modes of operation. Steigerwald [32] operated the parallel resonant converter above resonance and showed its advantages.

References [67] and [5] are the first ones to report the use of the SPRC configuration. Later, Steigerwald compared the relative merits and demerits of the three different resonant converter topologies in [8]. He clearly showed the advantages of SPRC over the other two configurations. An analysis using state-space approach and design of SPRC was reported in [7, 12] for operation in the leading power factor mode. This converter has been analyzed for operation in the lagging power factor

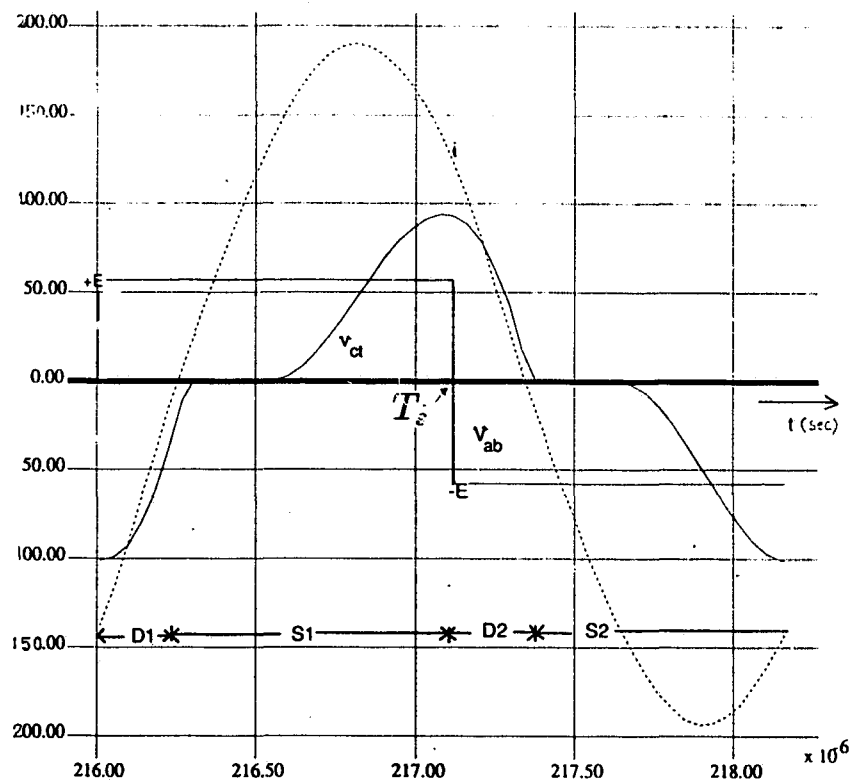


Figure 1.5: Typical Waveforms of the SPRC operating in above resonance, discontinuous capacitor voltage mode.

mode in [12], including the discontinuous capacitor voltage mode. In both the cases, constant current model was used. An approximate analysis and design using complex AC circuit analysis approach using fundamental components of the waveforms has been reported in [8]. Recently, a lot of work has been reported on the analysis and design aspects of SPRC [10-23].

The DC analysis (or the steady-state analysis) is very important to get a complete understanding of the steady-state working of a resonant converter. A complete DC analysis for the SRC and the PRC are available in the literature [24, 51]. However a complete DC analysis for the SPRC is not available in the literature. The different modes of operation of the SPRC, including the multiple conduction modes, are not known.

The specifications of any converter includes the criteria for load regulation, fluctuations in supply voltage, stability, response time, variations in frequency and duty ratio and input harmonic generation, etc. How the converter will respond to a perturbation in any (or all) of these quantities, is very crucial for performance evaluation and design considerations. Also important is the transient response of the system. Thus there was a need for developing large-signal and small-signal models for the different resonant converter configurations, which could be used for studying the effects of transients and perturbations. Over the years many authors have reported many such models [41-57], each different from each other in one or the other aspect and each having its own drawbacks and advantages as compared to the others. These are discussed next.

A large-signal model, such as the one reported in [48] is useful for determining the dynamic and transient response of the converters. This model stresses more on transient conditions as against the steady-state conditions. This model is simple and useful for determining component ratings, which are mostly determined by the

transient conditions, for example, a sudden short circuit. The small-signal analysis on the other hand is concerned with the effect of small perturbations (and hence the name "small-signal") on the steady-state operating conditions.

Reference [51] has described a sample-data modeling approach leading to a discrete time model for small-signal analysis. But it is not easy to use this model for compensator design. The model described in [56] has limited accuracy and hence its use is limited. A small-signal continuous time model for SPRC, with diode conduction angle control, derived from the large-signal model of [48] is given in [42]. This model was actually obtained by linearizing the non linear discrete time equations about the steady-state values. The non linear equations prevent the derivation of a general input-output transfer function. This small-signal model is based on low ripple approximations of the supply and the output voltages which actually amounts to a low frequency approximation. Thus the model of [42] is valid only for frequencies lower than the sampling frequency, which is usually the case. Another model was proposed in [49]. In this model, which is discrete in nature, the converter is modeled by a lumped parameter equivalent circuit. Just like the model of [42] this model also assumes low frequency approximations. Reference [43] describes yet another model based on the extended describing function concept. In the small-signal modeling of converters presented in [50], the inherently non-linear blocks of the control system, namely the control block and the rectifier are modeled as delay elements. This model is easy to use for compensator design.

All the models described above are for SRC or PRC. Thus there is a need to formulate such models for the SPRC. During the course of this work, an approximate small-signal analysis for the SPRC was performed in [73], where in all the resonant tank waveforms were approximated by their fundamental components.

Most of the dc power conditioning applications involve a regulated voltage output.

For this purpose, a feed back loop is included as part of the control strategy, to regulate the voltage [42]. In some other suggested control strategies, some more feedback loops (called inner feedback loops [54]) are also incorporated to limit the output current or the resonant tank current or voltage. In one feedback loop system, the output voltage is regulated by comparing it with a reference voltage and using the error signal as a control signal. This error signal is used for modulating the conduction angle of the transistor [42]. In the multi feed-back loop systems the inner feedback loops provide a pulse by pulse control of the inductor current or capacitor voltage while the outer loop as usual takes care of the output voltage regulation [54]. Such multi-loop systems have been found to show excellent stability and dynamic performances. Reference [54] describes a discrete time model involving an inner feedback loop. This model is simple and is based on more commonly used frequency control (or  $\gamma$  control). In fact this model follows the same approach as in [42].

The output power of a resonant converter can be controlled by varying the switching frequency. However, controlling the output power by varying the frequency either in lagging p.f. mode or leading p.f. mode, has some disadvantages. Some of these drawbacks have already been described in section 1.3. In addition to these, the design of filter components is more difficult for operation in variable frequency mode.

This was the motivation to look for an alternate power control strategy. This gave rise to “fixed frequency control” of resonant converters. Reference [15] summarizes the various methods of fixed frequency control. All these methods offer some or the other advantage. But at the same time they all suffer from one or the other drawback.

Some authors [15, 16, 18] have reported the fixed frequency operation and its analysis for the SPRC. Reference [15] has described the method based on fixed-frequency PWM control (using the phase-shifting technique) of the SPRC. This scheme offers advantages such as high efficiency for large load variations with a narrow range of

duty-cycle ratio control and protection against load short circuit conditions. An analysis and design procedure based on complex ac circuit theory has been presented with an approximate model. This approach uses only the fundamental components of the waveforms.

Reference [18] on the other hand gives the steady-state analysis of one of the modes (leading p.f. continuous current mode) based on the state-plane technique. However the different operating modes for the fixed frequency operation are not known. Apart from that, there is a limited treatment of the dynamic analysis of the SPRC for the fixed frequency operation. An approximate small-signal analysis was presented in [73], using the extended describing function method. Small-signal analysis was also reported in [84] using a combination of extended describing function method and the state-space approach. These two papers appeared during the course of this thesis work. In this thesis, however, the small-signal analysis has been performed independently using only the state-space technique.

## 1.5 Thesis Outline

All that explained in the last few paragraphs was the motivation for the work included in this thesis. The various objectives set forth, based on the literature survey presented in section 1.4, were realized and included here in the various chapters of this thesis, whose outline is given next.

A complete DC analysis of the series-parallel resonant converter is presented in chapter 2. Chapter 3 is devoted to the large-signal analysis using a discrete time domain model. This model is very convenient to predict the large-signal behavior of the converter because of the simplification it offers in the calculations. Chapter 4 is based on the small-signal modeling of the converter for variable frequency op-

eration. For this purpose the large-signal state equations derived in chapter 3, to perform the large-signal analysis, have been linearized about a steady-state operating point to obtain a linearized small-signal model. This model has been used to study the small-signal behavior of the converter. A more convenient way of predicting the small-signal behavior of the converter is to use a small-signal equivalent circuit model. Such a model is more practical to handle because the various transfer functions can be obtained using the laws of linear circuit theory. Details of the small-signal equivalent circuit modeling of the SPRC are presented in chapter 5. As explained earlier, the variable frequency operation has some disadvantages, which can be overcome by operating the converter in fixed frequency mode. The steady-state analysis of the converter operating in fixed frequency mode is presented in chapter 6. The predominant modes are identified and their dynamic (both large and small signal) analysis is also presented in the same chapter. Finally, chapter 7 summarizes the important contributions of this thesis work and ends with suggestions for future work on this topic. The following sections briefly describe the contents of the various chapters.

### **1.5.1 The DC Analysis of the Series-Parallel Resonant Converter (Chapter 2)**

The SPRC can operate in various modes over a wide switching frequency range. Although the DC analysis and the different operating modes of the SRC and PRC are available in [24, 51], such an analysis and the operating modes for the SPRC, including the multiple conduction modes, were not available in the literature. Therefore this part of the thesis work was devoted to the following:

- (1) To identify the different operating modes (including the multiple conduction modes) of the transistorized SPRC over a wide range of switching frequency using SPICE-3 simulation.

- (2) To present the DC analysis of transistorized SPRC.
- (3) To obtain the various design curves, gain (ratio of the converter output voltage referred to primary side to the input supply voltage) versus normalized load current, and component stresses versus normalized load current.
- (4) To analyze the simulation results theoretically, using the state-space approach.
- (5) To verify the results experimentally.

### **1.5.2 Large-Signal Analysis of SPRC using Discrete Time Domain Modeling (Chapter 3)**

Large-signal analysis determines the response of a system to large variations in its steady-state operating condition. The dynamic response of the converter during the transients is quite significant because it determines the choice of appropriate component ratings. The operation of the resonant converter being inherently discrete, it is only natural to go for discrete time domain modeling. Such a modeling, as is shown in this chapter, reduces the computer simulation time drastically and the key design parameters like the peak component stresses and the state response can be determined fairly easily. The main objectives of this chapter are:

- (1) To develop discrete time domain large-signal models of the SPRC operating in the CCM and DCM.
- (2) To obtain the large-signal discrete state-space models from the large-signal equations of (1).
- (3) To determine the expressions for the peak component stresses.
- (4) To use the developed models to study the different types of transients.
- (5) To verify the theoretical results using SPICE and experiments.

### **1.5.3 Small-Signal Analysis using Discrete Time Domain Modeling (Chapter 4)**

Small-signal analysis is concerned with the response of the converter to small perturbations in its steady-state operating conditions. The goals of this chapter are:

- (1) To linearize the non-linear discrete time domain, large-signal model of chapter 3 about a steady-state operating point to obtain a linearized small-signal model.
- (2) To use the small-signal model so developed to study the small-signal dynamics of the converter.
- (3) To realize a multiple feedback loop system [54] to control the SPRC. An outer loop is used to regulate the output voltage. Whereas, an inner loop, based on state variable feedback is also used to improve the dynamics.
- (4) To obtain experimental verification of the key theoretical results.

### **1.5.4 Small-Signal Equivalent Circuit Modeling of the SPRC (Chapter 5)**

While performing the small-signal analysis of the resonant converters, mainly two approaches have been followed.

- (1) Obtaining a purely theoretical model, based on the state-space method or the transfer function approach.
- (2) Obtaining a somewhat more practical equivalent circuit model.

In this context the small-signal equivalent circuit models are more convenient to handle as they can be solved for the various transfer functions fairly easily. Therefore, this chapter is devoted to obtaining a two port hybrid parameter model for studying the small-signal behavior of the SPRC. Again the small-signal modeling is done in discrete time domain. However, an approximate continuous time domain model is

also derived. Experimental verification is presented for the key theoretical results.

### **1.5.5 Constant Frequency, Pulse-Width Modulated Operation of the SPRC (Chapter 6)**

The advantages of a fixed frequency operation over a variable frequency one have been discussed earlier in this chapter. Constant frequency operation of the SPRC using PWM control is presented in this chapter. The objectives of this chapter are:

- (1) To identify the different operating modes of the SPRC operating in fixed frequency mode and to present the steady-state analysis.
- (2) To present the large-signal analysis.
- (3) To present the small-signal analysis by linearizing the large-signal state equations developed for the large-signal analysis.
- (4) To verify the theoretical results using SPICE.

## Chapter 2

# DC Analysis of the LCC-Type Parallel Resonant Converter

In this chapter, the various operating modes of a transistorized series-parallel resonant converter (SPRC), (including multiple conduction modes) are identified. A generalized steady-state solution for these modes is obtained using the state-space approach. As an example two of the predominant modes are treated as particular cases. The equations are numerically solved using the PRO-MATLAB software. Design curves for converter gain versus the normalized load current have been obtained. Peak component stresses have also been plotted against the normalized load current. The boundaries between the various modes of operations (CCVM and DCVM as well as leading and lagging power factor mode) have been obtained. Experimental results are included to verify the theoretical results.

## 2.1 Introduction

The LCC type parallel resonant converter (also called as series-parallel resonant converter (SPRC)) [7,8,10,12] has become quite popular because of its relative advantages over other configurations, namely, the series resonant converter (SRC) and the parallel resonant converter (PRC) [8]. Some of these advantages are reproduced again:

- (1) Full power control range with a small variation in frequency.
- (2) High efficiency from full load to part load.

The various operating modes and the DC analysis are very important to get a complete understanding of the steady-state working of a resonant converter. The complete DC analysis for the SRC and the PRC is available in the literature [24,25,70]. However, a complete DC analysis for the transistorized SPRC is not available in the literature. The transistorized SPRC is capable of operating in various other modes, other than the ones reported in [7,12]. These modes include the "multiple conduction modes" also. In the multiple conduction modes, the voltage and current waveforms repeat themselves a number of times because the resonant frequency is much higher than the switching frequency. This results in a number of submodes which must be analyzed. For classification purposes, it has been found more appropriate to classify on the basis of parallel capacitor voltage waveforms, because it is this waveform which is rectified, filtered and applied across the load. This is in direct contrast to the case of SRC, presented in [24], where the resonating capacitor current is rectified and filtered to get the load voltage.

Multiple conduction modes (MCM) were first reported in [24] (for SRC) and [70] (for PRC). It is shown in this chapter, that the MCM are capable of both the leading and lagging power factor mode of operation, as the normalized switching frequency

is reduced below 0.5.

While the ideal SRC and the PRC are second order systems, the SPRC is a third order system. This makes the DC analysis of SPRC with multiple conduction modes quite complex. Therefore, there is a need to represent the system model compactly. Use of matrix notation greatly simplifies the handling of the equations.

The remaining chapter is divided into the following sections. Section 2.2 deals with the identification of the various modes (including multiple conduction modes) and also explains the operation of the converter. Section 2.3 presents a general method of analysis for any mode of operation. As an example, analysis of two of the modes, with 2 and 4 intervals respectively is presented. The state-space system model equations are represented in matrix notation to simplify the presentation. PRO-MATLAB was used for solving the transcendental equations. In section 2.4, plot of converter gain versus normalized load current has been obtained both analytically and by SPICE simulation. The component stresses are also plotted against normalized load current. The plot of gain versus  $f_n$  (normalized switching frequency) has been obtained for different values of  $Q$ . Section 2.5 is devoted to determination of the boundaries between the different modes of operation. Section 2.6 gives the complete design of the converter for steady-state operation. All the results have been verified experimentally in section 2.7. All the experimental plots are presented along with the other plots for the sake of comparison. Finally section 2.8 states the conclusions.

## **2.2 SPICE Simulation and the Operating Modes**

In this section, the different operating modes (including the multiple conduction modes) are identified using SPICE-3 simulation program. In the simulation it is assumed that bipolar transistors or MOSFET's are used as the switches. Therefore,

the resonating current does not become discontinuous at any time [11]. The operating modes and the analysis presented in the earlier papers[7,12] were mainly concentrated for values of  $f_n > 0.5$ , where,

$$f_n = \omega_t / \omega_0 ;$$

$\omega_t$  = angular switching frequency and  $\omega_0 = 1/(LC_e)^{1/2}$  is the angular resonance frequency and  $C_e = C_s C_t / (C_s + C_t)$ .

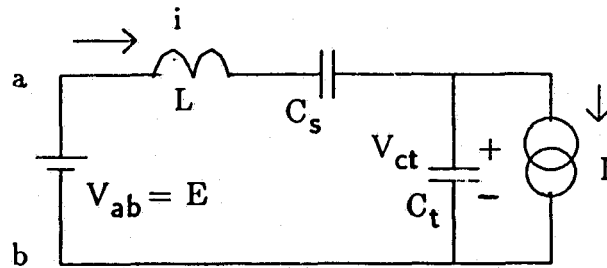
Multiple conduction modes, however, occur in the range  $f_n < 0.5$ . The present chapter is concerned with a complete range of  $f_n$  and accordingly different operating modes will be presented in this section. The switch and diode capacitances were included in the SPICE model to make it as close to the practical converter as possible.

As the parallel capacitor voltage  $v_{ct}$  switches polarity, the rectifier input current does it too. Based on this there are two major intervals of operation, A and B, [Fig. 2.1(a), 2.1(b)] respectively. A third interval, C, is also present in the discontinuous capacitor voltage mode in which the parallel capacitor is shorted [Fig. 2.1(c)]. Some of the typical waveforms obtained from SPICE simulation are shown in Fig. 2.2. The values of the components used in the SPICE simulation are also given in Fig. 2.2. In the figures shown, the sequence in which different intervals occur are also marked. The following two modes were identified [Figs. 2.2(a)-2.2(g)] using the parallel capacitor voltage.

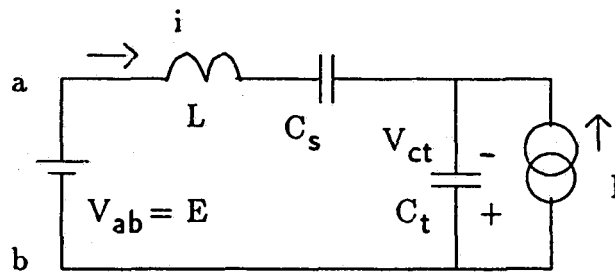
### 2.2.1 Continuous Capacitor Voltage Mode (CCVM)

In this mode the parallel capacitor voltage is always continuous [Figs. 2.2(a) - 2.2(d)]. Only intervals A and B occur either once or repeatedly.

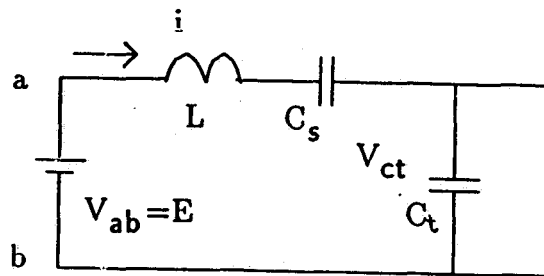
In Fig 2.2(a), the current  $i$  is lagging the voltage  $v_{ab}$  and the converter is operating in lagging power factor (above resonance) mode. During this mode the switches



(a)

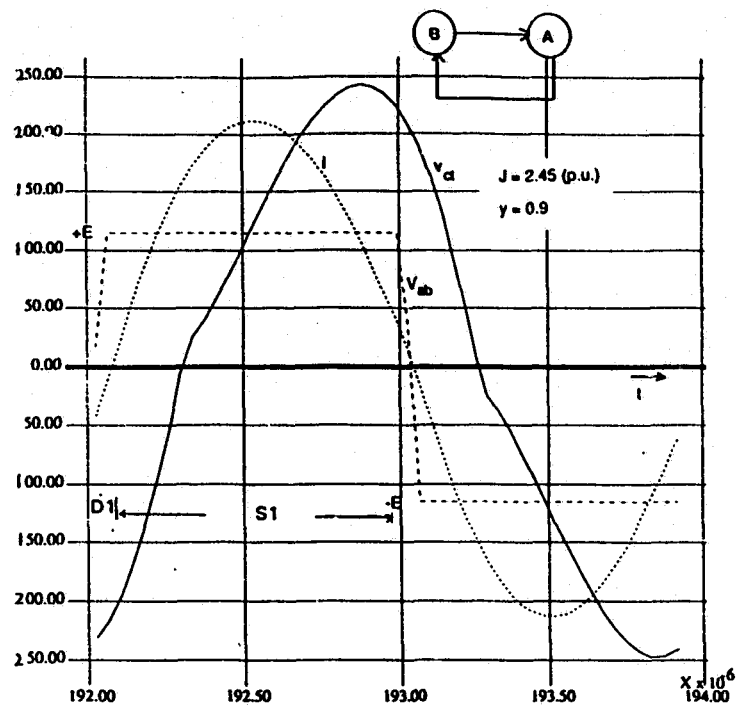


(b)

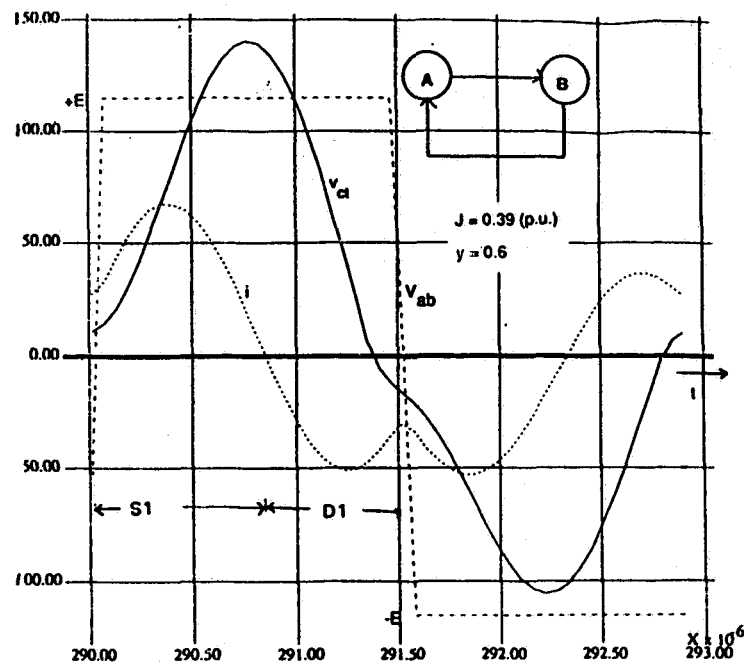


(c)

Figure 2.1: Equivalent Circuits for the three different intervals: (a) Interval A, (b) Interval B, and (c) Interval C. ( $L = L_s + L_l$ , where  $L_l$  is the leakage inductance of the hf transformer.)

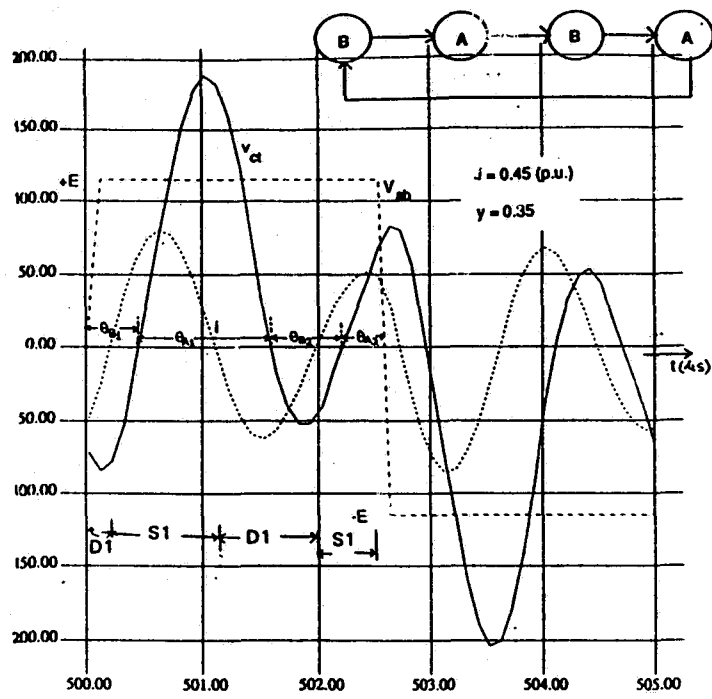


(a)

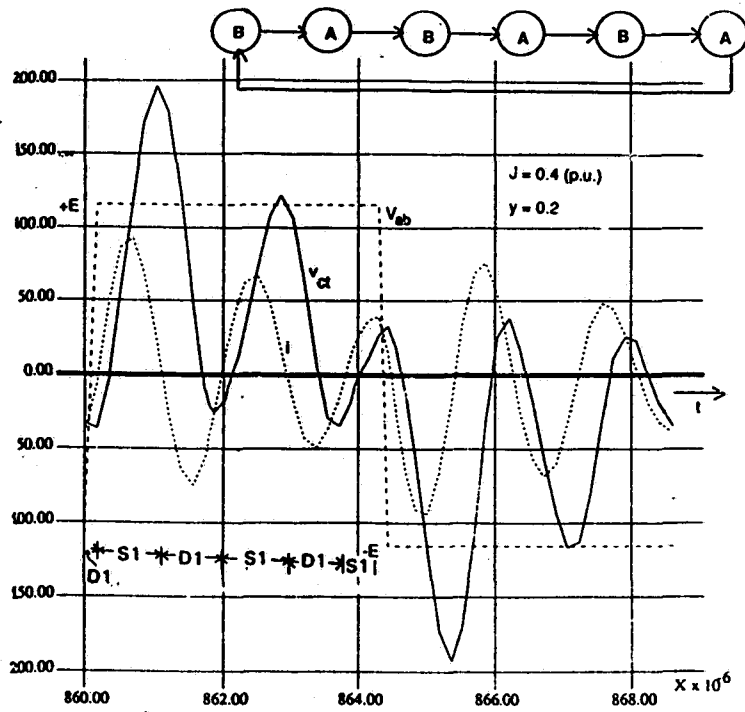


(b)

Figure 2.2: Typical operating waveforms of the LCC-type PRC (Fig. 2.1) for various modes of operation, obtained using SPICE. The current waveforms are magnified by a factor of 20 for the sake of clarity.



(c)



(d)

Fig. 2.2 (continued)

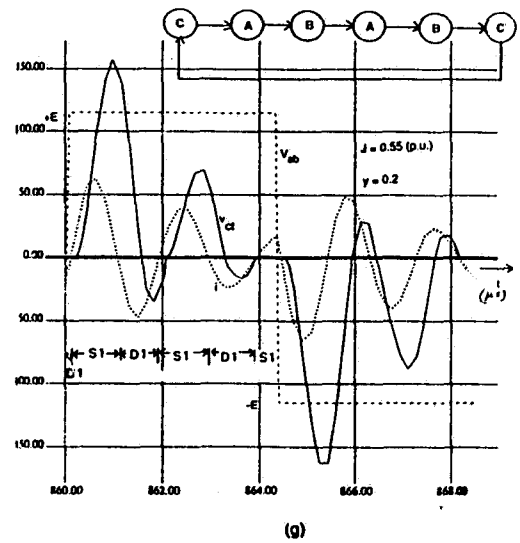
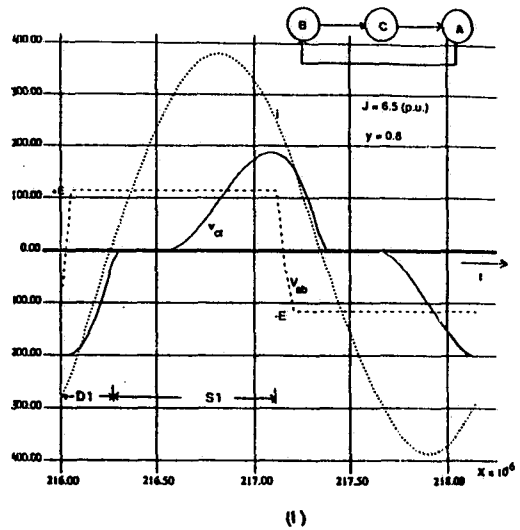
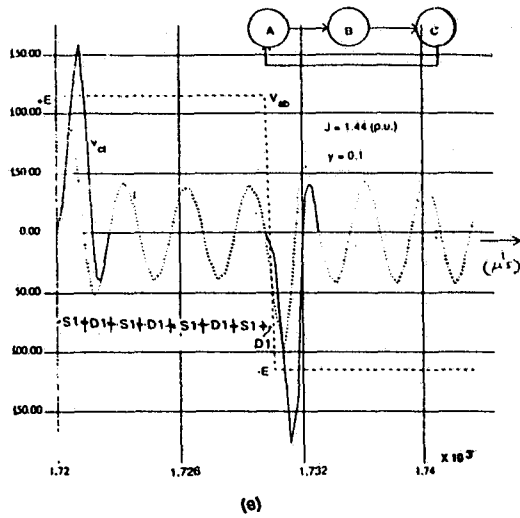


Fig. 2.2 (continued)

undergo zero voltage switching (ZVS) because the tank current is transferred to them from their anti-parallel diodes. Fig. 2.2(b) waveforms correspond to leading power factor (below resonance) mode of operation since the resonating current  $i$  is leading the voltage  $v_{ab}$ . This corresponds to the zero current switching (ZCS). The intervals and the devices conducting in each of them have been marked in all the Figures, which explains the converter operation.

As the switching frequency is decreased as compared to that in Fig. 2.2(a) or 2.2(b), the converter enters the multiple conduction modes. Figs. 2.2(c) and 2.2(d) show two such waveforms. It must be noted that both the switch and the diode conduct more than once in every half cycle.

The CCVM can have only an even number of intervals, if the symmetry condition has to be satisfied. For example [Fig. 2.2(b)], if the first interval of the half cycle is "A" then the last interval in that half cycle must be B, or else the symmetry condition will be violated since if A occurs at the end, then the next half cycle starts with B. Therefore, this condition ensures that the number of "A" intervals is same as the number of "B" intervals, irrespective of which one of them is the first to occur in a half cycle.

### 2.2.2 The Discontinuous Capacitor Voltage Mode (DCVM)

The mode in which the parallel capacitor voltage is discontinuous, i.e. the capacitor voltage  $v_{ct}$  is zero for certain intervals of operation. [Figs. 2.2(e) - 2.2(g)]. However, the resonating current is still continuous.

Fig. 2.2(e) shows an example of leading power factor mode operation, where as, Fig. 2.2(f) shows lagging power factor mode operation. In Fig. 2.2(e), the parallel capacitor voltage becomes discontinuous towards the end of each half cycle while in

Fig. 2.2(f) the discontinuity in parallel capacitor voltage occurs in between intervals B and A. However, the current still remains continuous.

Just like in CCVM, in DCVM also we get multiple conduction modes as the switching frequency is decreased. Where as the CCVM multiple conduction modes appear for low values of load current, the DCVM multiple conduction modes occur for high values of load current. Fig. 2.2(g) shows one such example. It corresponds to lagging power factor mode operation.

The DCVM can have both even and odd number of intervals. For example, in Fig. 2.2(e) and 2.2(f) each of the interval occurs only once, where as, in Fig. 2.2(g), each interval occurs twice causing an even number of intervals. It should be noted that interval "C" can appear either at the beginning of the half cycle or at the end. If it occurs at the end only, then interval "A" or "B" in the successive half cycle must have a zero initial parallel capacitor voltage condition.

## 2.3 Analysis

The SPRC converter is analyzed using the state-space approach for different modes identified in section 2.2. Steady-state solutions are derived. In order to obtain the initial state vector, lengths of the different intervals are to be calculated. They have been obtained numerically, using the PRO-MATLAB software. The complexity of the solution increases as the number of intervals in a mode increases. The CCVM with two intervals [Fig 2.2(a)] and the DCVM with three intervals [Fig. 2.2(f)] have been analyzed in [7,12] respectively.

First we present a general method of analysis. The general formulae so obtained, are subsequently used to analyze two of the predominant modes. They contain 4 intervals [Fig. 2.2(c)] and 2 intervals [Fig. 2.2(b)], respectively. Note that the modes

shown in Fig. 2.2(c) and Fig. 2.2(b) occur only within some specified range of load current  $J$  and for selected values of  $f_n$  only.

### 2.3.1 General Solutions

As given in [7], starting with the basic differential equations, one can get the general solutions. Then the steady-state solutions can be obtained by matching the boundary conditions. The three state variables namely the resonating current( $i$ ), the series capacitor voltage( $v_{cs}$ ) and the parallel capacitor voltage ( $v_{ct}$ ) are represented by column matrix  $[x(\theta)]$ . Similarly,  $[x_{\theta i}]$  is the column matrix containing the values of all the three state variables at the beginning of an interval. Further,  $\theta = \omega_0 t$ , where  $t = 0$  implies the beginning of the interval considered.

For the A and B intervals, the general solution is given by [7]:

$$[x(\theta)] = [F(\theta)][x_{\theta i}] + [G(\theta)][u_M] \quad (2.1)$$

While for the C interval, it is given by [12]

$$[x(\theta)] = [F_1(\theta)][x_{\theta i}] + [G_1(\theta)][u_C] \quad (2.2)$$

$$\text{where, } [x(\theta)]^T = [i(\theta) \ v_{cs}(\theta) \ v_{ct}(\theta)] \quad (2.3)$$

$$[x_{\theta i}]^T = [i_i \ v_{csi} \ v_{cti}] \quad (2.4)$$

$$[F(\theta)] = \begin{pmatrix} b_1 & -b_2/Z & -b_2/Z \\ Z(C_e/C_s)b_2 & 1 - (C_e/C_s)b_3 & -(C_e/C_s)b_3 \\ Z(C_e/C_t)b_2 & -(C_e/C_t)b_3 & 1 - (C_e/C_t)b_3 \end{pmatrix} \quad (2.5)$$

$$[G(\theta)] = \begin{pmatrix} b_2/Z & (C_e/C_t)b_3 \\ (C_e/C_s)b_3 & (C_e/C_s)((1/C_t)t - Z(C_e/C_t)b_2) \\ (C_e/C_t)b_3 & -(C_e/C_s)(1/C_t)t - Z(C_e/C_t)^2b_2 \end{pmatrix} \quad (2.6)$$

$$[F_1(\theta)] = \begin{pmatrix} \cos(\omega_s t) & -\frac{1}{Z}(\frac{C_s}{C_e})^{1/2} \sin(\omega_s t) & 0 \\ Z(\frac{C_s}{C_e})^{1/2} \sin(\omega_s t) & \cos(\omega_s t) & 0 \\ 0 & 0 & 0 \end{pmatrix} \quad (2.7)$$

$$[G_1(\theta)] = \begin{pmatrix} \frac{1}{Z}(\frac{C_s}{C_e})^{1/2} \sin(\omega_s t) & 0 \\ 1 - \cos(\omega_s t) & 0 \\ 0 & 0 \end{pmatrix} \quad (2.8)$$

$$[u_M]^T = [u_A]^T = [E \quad I] \quad \text{for interval A}$$

$$[u_M]^T = [u_B]^T = [E \quad -I] \quad \text{for interval B}$$

$$[u_C]^T = [E \quad 0] \quad \text{for interval C}$$

$$b_1 = \cos \omega_0 t; \quad b_2 = \sin \omega_0 t; \quad b_3 = 1 - \cos \omega_0 t \quad (2.9)$$

$$Z = (L/C_e)^{1/2}; \quad C_e = C_s C_t / (C_s + C_t); \quad \omega_s = \frac{1}{\sqrt{LC_s}} \quad (2.10)$$

The general solutions given by (2.1) and (2.2) are normalized using the base quantities given below:

$$V_B = E_{min} = \frac{V_{smin}}{2} V; \quad Z_B = Z \Omega; \quad I_B = V_B/Z; \quad T_B = 1/f_0 \quad (2.11)$$

The value of the state-variables at the end of any interval can be obtained by evaluating the corresponding state equations at that instant. Also note that the notation  $[F(\theta_k)]$  or  $[G(\theta_k)]$ ,  $k = 1, 2, \dots$  means the value of matrices  $[F(\theta)]$  and  $[G(\theta)]$  evaluated at  $\theta = \theta_k$  where  $\theta_k$  denotes the length of  $k^{th}$  interval.  $[x_0]$  is used to define the initial state vector evaluated at  $\theta_i = 0$ .

For the CCVM case with A as the first interval, using the general solution (2.1), we can obtain the following:

At the end of the first interval (interval A), the state variable matrix is given by the following:

$$[x_1] = [F(\theta_1)][x_0] + [G(\theta_1)][u_A] \quad (2.12)$$

At the end of the second interval (B interval), the state variable matrix is given by:

$$[x_2] = [F(\theta_2)][x_1] + [G(\theta_2)][u_B] \quad (2.13)$$

The value of  $x_1$  can be substituted to obtain:

$$[x_2] = [F(\theta_2)]([F(\theta_1)][x_0] + [G(\theta_1)][u_A]) + [G(\theta_2)][u_B] \quad (2.14)$$

This yields:

$$\begin{aligned} [x_2] = & [F(\theta_2)][F(\theta_1)][x_0] + [F(\theta_2)][G(\theta_1)][u_A] \\ & + [G(\theta_2)][u_B] \end{aligned} \quad (2.15)$$

Proceeding in a similar way, one can get:

$$\begin{aligned} [x_3] = & [F(\theta_3)][F(\theta_2)][F(\theta_1)][x_0] + [F(\theta_3)][F(\theta_2)][G(\theta_1)][u_A] \\ & + [F(\theta_3)][G(\theta_2)][u_B] + [G(\theta_3)][u_A] \end{aligned} \quad (2.16)$$

$$\begin{aligned} [x_4] = & [F(\theta_4)][F(\theta_3)][F(\theta_2)][F(\theta_1)][x_0] + [F(\theta_4)][F(\theta_3)][F(\theta_2)][G(\theta_1)][u_A] \\ & + [F(\theta_4)][F(\theta_3)][G(\theta_2)][u_B] + [F(\theta_4)][G(\theta_3)][u_A] + [G(\theta_4)][u_B] \end{aligned} \quad (2.17)$$

⋮

$$\begin{aligned} [x_n] = & [F(\theta_n)][F(\theta_{n-1})][F(\theta_{n-2})] \dots [F(\theta_1)][x_0] \\ & + [F(\theta_n)][F(\theta_{n-1})] \dots [F(\theta_2)][G(\theta_1)][u_A] \\ & + [F(\theta_n)][F(\theta_{n-1})] \dots [F(\theta_3)][G(\theta_2)][u_B] \\ & \vdots \\ & + [F(\theta_n)][G(\theta_{n-1})][u_{(-1)^n}] + [G(\theta_n)][u_m] \end{aligned} \quad (2.18)$$

$$u_m = u_B; \text{ if } n \text{ is even}$$

$$= u_A; \text{ if } n \text{ is odd}$$

Equation (2.18) leads to the following general form for the value of state vector at the end of  $n^{th}$  interval.

$$[x_n] = \prod_{i=0}^{n-1} [F(\theta_{n-i})][x_0] + \sum_{j=1}^n \left( \prod_{k=0}^{n-j-1} [F(\theta_{n-k})] \right) [G(\theta_j)][u_m] \quad (2.19)$$

### 2.3.2 Determination of the Initial State Vector $[x_0]$

**Case(I): Continuous  $v_{ct}$ , with interval A first ( $n$  is even)**

Applying the symmetry condition  $[x_n] = -[x_0]$  to (2.19), we get:

$$\begin{aligned} -[x_0] &= \prod_{i=0}^{n-1} [F(\theta_{n-i})][x_0] + \sum_{j=1}^n \left( \prod_{k=0}^{n-j-1} [F(\theta_{n-k})] \right) [G(\theta_j)][u_m] \\ -[x_0] - \prod_{i=0}^{n-1} [F(\theta_{n-i})][x_0] &= \sum_{j=1}^n \left( \prod_{k=0}^{n-j-1} [F(\theta_{n-k})] \right) [G(\theta_j)][u_m] \\ [x_0] &= -\left( [I_3] + \prod_{i=0}^{n-1} [F(\theta_{n-i})] \right)^{-1} \left[ \sum_{j=1}^n \left( \prod_{k=0}^{n-j-1} [F(\theta_{n-k})] \right) [G(\theta_j)][u_m] \right] \end{aligned} \quad (2.20)$$

where  $[I_3]$  denotes a  $3 \times 3$  identity matrix.

**Case(II): Continuous  $v_{ct}$ , with interval B first ( $n$  is even)**

The expression for  $[x_0]$  can be obtained from (2.19) if  $u_m$  is replaced by  $u_A$  if  $n$  is even and by  $u_B$  if  $n$  is odd. Apart from that  $u_A$  and  $u_B$  are interchanged.

**Case(III): Discontinuous  $v_{ct}$**

Depending on whether  $n$  is even or odd,  $n^{th}$  interval is B or A respectively.

For the Discontinuous parallel capacitor voltage mode (DCVM) [e.g. Fig. 2.2(g)], the discontinuous portion of  $v_{ct}$  is represented by the general solution given by (2.2), which yields the state vector at the end of interval C,

$$[x_{n+1}] = [F_1(\theta_{n+1})][x_n] + [G_1(\theta_{n+1})][u_C] \quad (2.21)$$

Substituting the value of  $[x_n]$  from (2.18), we get:

$$[x_{n+1}] = [F_1(\theta_{n+1})] \left[ \prod_{i=0}^{n-1} [F(\theta_{n-i})] \right] [x_0] + \sum_{j=1}^n \left( \prod_{k=0}^{n-j-1} [F(\theta_{n-k})] \right) [G(\theta_j)] [u_m] + [G_1(\theta_{n+1})][u_C] \quad (2.22)$$

Using the symmetry condition  $[x_{n+1}] = -[x_0]$ ;

$$[x_0] = - \left[ [I_3] + [F_1(\theta_{n+1})] \left[ \prod_{i=0}^{n-1} [F(\theta_{n-i})] \right]^{-1} \right] \left[ [F(\theta_{n+1})] \left[ \sum_{j=1}^n \left( \prod_{k=0}^{n-j-1} [F(\theta_{n-k})] \right) [G(\theta_j)] \right] [u_m] + [G_1(\theta_{n+1})][u_C] \right] \quad (2.23)$$

### 2.3.3 Determination of the Interval Durations

For operating modes involving more than two intervals, no closed form solutions are possible for the interval durations (denoted by  $\theta$ 's) [12]. They must be obtained using the numerical techniques. Since the multiple conduction modes involve more than two intervals, the lengths of the various intervals must be obtained numerically. What follows is a general method of determining the durations of these intervals.

#### (a) Continuous Capacitor Voltage Case

Let there be  $n$  intervals ( $n$  is always even for CCVM) denoted by  $\theta_1 \dots \theta_n$ , a total of  $n$  unknowns. Let  $\theta_s$  be the length of one half cycle of the driving frequency and is known. Then;

$$\theta_s = \theta_1 + \dots + \theta_n \quad (2.24)$$

All we need to determine is  $(n - 1)$  unknowns. The  $n^{\text{th}}$  one can be determined using (2.24). However, to determine the first  $(n - 1)$  unknowns, we need as many equations. These equations can be derived from the fact that parallel capacitor voltage is zero at the end of each of these intervals (except the  $n^{\text{th}}$ ). Equation (2.19) leads to the following  $(n - 1)$  transcendental equations.

$$\begin{aligned}\xi(1) &= 0 = \psi_1(\theta_1) \\ \xi(2) &= 0 = \psi_2(\theta_1, \theta_2) \\ &\vdots \\ \xi(n - 1) &= 0 = \psi_{n-1}(\theta_1 \dots \theta_{n-1})\end{aligned}\tag{2.25}$$

where  $\xi$  denotes the third element of the state variable matrix corresponding to  $v_{ct}$  and  $\psi$  is a non linear transcendental function evaluated at  $\theta = (\theta_1, \theta_2 \dots \theta_{n-1})$ , using the RHS of (2.19).

### (b) Discontinuous Capacitor Voltage Case

The same set of equations hold except that now the expression for  $[x_0]$  is given by (2.23) and  $n$  is replaced by  $(n + 1)$ .

### The Numerical Solution

Set of equations (2.25) need to be solved numerically. Newton Raphson method can be used as below:

**Step 1.**  $\theta_{1(g)} \dots \theta_{n-1(g)}$  are assigned as initial guess values to first  $(n - 1)$  intervals yielding the vector  $[\theta_g]$

**Step 2.** Determine  $[x_0]$  using (2.20) or (2.23).

**Step 3.** Determine  $[\xi] = [\xi(1) \ \xi(2) \ \dots \ \xi(n-1)]$ . Check if they are all zero. If yes, go to step (7). Else proceed.

**Step 4.** Evaluate the following  $(n-1) \times (n-1)$  matrix at the guessed value  $[\theta_g]$ .

$$[J] = \begin{bmatrix} \frac{\partial \psi_1}{\partial \theta_1} & \dots & \frac{\partial \psi_1}{\partial \theta_{n-1}} \\ \dots & \dots & \dots \\ \frac{\partial \psi_{n-1}}{\partial \theta_1} & \dots & \frac{\partial \psi_{n-1}}{\partial \theta_{n-1}} \end{bmatrix}$$

**Step 5.** Determine the increment in the value of  $[\theta_g]$  as below:

$$[\delta\theta_g] = -[J]^{-1}[\xi]^T \quad (2.26)$$

**Step 6.** Determine  $[\theta_{g(new)}] = [\theta_g] + [\delta\theta_g]$

Go to Step (2).

**Step 7.**  $\theta_g$  is the actual value of the lengths of the intervals. Use them to determine the gain of the converter.

### 2.3.4 Particular Cases

The general and steady-state solutions derived in section 2.3 can be used directly to obtain solutions of particular cases. Two particular cases are presented below to illustrate the procedure.

**(a) (CCVM) - Four Interval Mode [Fig. 2.2(c)]**

Using (2.20), the initial state vector  $[x_0]$  for the four interval mode (Fig. 2.2(c)) can be obtained directly as below:

$$[x_0] = -[P_1]^{-1}[Q_1] \quad (2.27)$$

$$\text{where } [P_1] = [I + [F(\theta_{A_2})][F(\theta_{B_2})][F(\theta_{A_1})][F(\theta_{B_1})]] \quad (2.28)$$

$$\begin{aligned} [Q_1] = & [F(\theta_{A_2})][F(\theta_{B_2})][F(\theta_{A_1})][G(\theta_{B_1})][u_B] \\ & + [F(\theta_{A_2})][F(\theta_{B_2})][G(\theta_{A_1})][u_A] + [F(\theta_{A_2})][G(\theta_{B_2})][u_B] + [G(\theta_{A_2})][u_A] \end{aligned} \quad (2.29)$$

where  $\theta$ 's are marked in Fig. 2.2(c) for the 4 interval mode. They can be evaluated using the method of section 2.3.

As another example, the two interval mode of Fig. 2.2(b) has been analyzed in the following section following the same technique.

**(b) (CCVM) - Two Interval Mode [Fig. 2.2(b)]**

The initial state vector for the two interval mode (Fig. 2.2(b)) can be obtained using (2.20) as

$$[x_0] = [P_2]^{-1}[Q_2] \quad (2.30)$$

$$\text{where } [P_2] = [I + [F(\theta_{B_1})][F(\theta_{A_1})]] \quad (2.31)$$

$$[Q_2] = -[F(\theta_{B_1})][G(\theta_{A_1})][u_A] - [G(\theta_{B_1})][u_B] \quad (2.32)$$

PRO-MATLAB was used to evaluate the durations of different intervals for the two cases of section 2.3.4.

## 2.4 Converter Gain and Component Stresses

Once the initial state vector and the various intervals are known, the gain can be obtained by integrating the expression for the parallel capacitor voltage  $v_{ct}$ , in the different intervals. For example, the expression for gain for the two interval mode discussed in the previous section is as given below.

$$M = \frac{1}{T_s} \left[ \int_0^{t_{A1}} v_{ctA} d(\omega t_1) + \int_0^{t_{B1}} v_{ctB} d(\omega t_2) \right] \quad (2.33)$$

where the expressions for  $v_{ctA}$  ( $v_{ct}$  corresponding to interval A,  $0 < t < t_{A1}$ ) and  $v_{ctB}$  ( $v_{ct}$  corresponding to interval B,  $0 < t' < t_{B1}$ ,  $t' = t - t_{A1}$ ) can be obtained from (2.1).

The analysis presented above was used to obtain the converter gains, plotted in Fig. 2.3 for two values of  $f_n$  for which the particular cases analyzed in section 2.3.4 occur. In the same figure, the converter gain plots obtained with SPICE are also given for comparison. It is observed that the results for the two interval mode ( $f_n = 0.6$ ) are closer to SPICE as compared to the four interval mode ( $f_n = 0.35$ ). This is due to the problems associated with the convergence of numerical solutions in MATLAB, as the number of variables (lengths of the various intervals) increases. The SPICE results on the other hand are affected by the simulation time step. Also, conduction losses of the switches and the passive elements are taken into account in SPICE simulation. The plot of gain versus  $f_n$  with  $Q = \frac{\omega_0 L}{R'_L}$  as the parameter, and the peak component stresses, obtained using SPICE are plotted in Figs. 2.4 and 2.5, respectively. Fig. 2.4 also shows a second resonant peak at  $f_n \approx 0.3$ . There are infinite resonant peaks such as this one as we reduce the switching frequency further (eg.  $f_n = 1/5, 1/7$  etc.). This type of phenomenon was also observed and explained in [24] for the SRC.

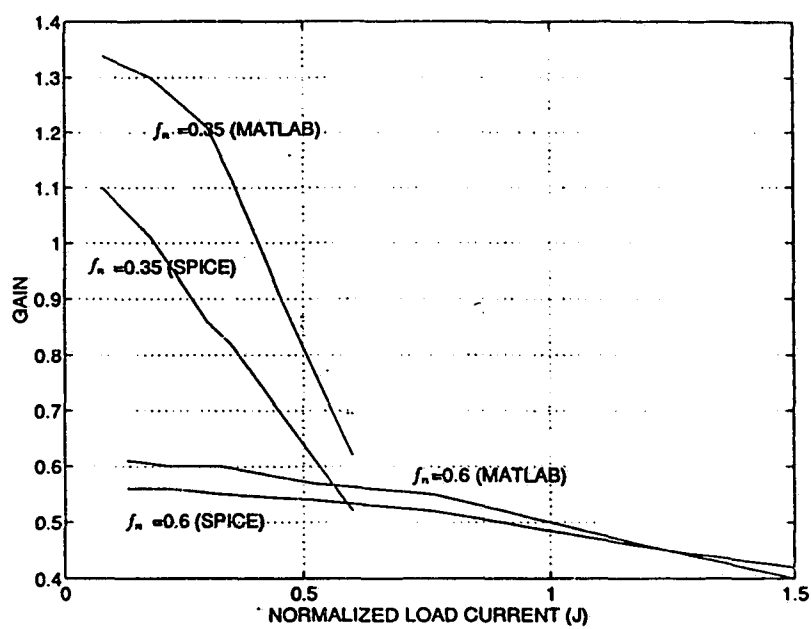


Figure 2.3: Comparison of MATLAB (state-space analysis) and SPICE simulation results. Plots of gain versus  $J$  for two values of  $f_n$  are given.

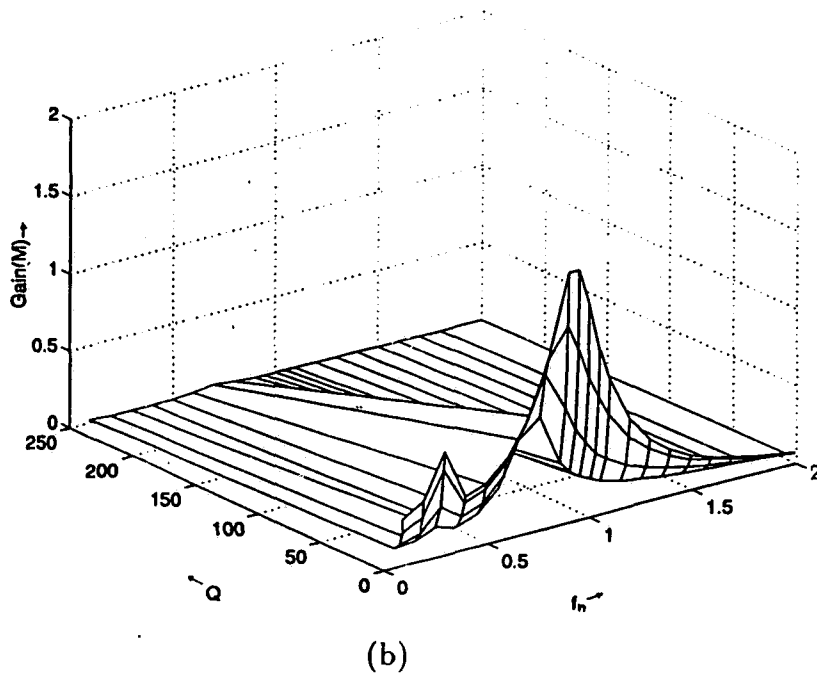
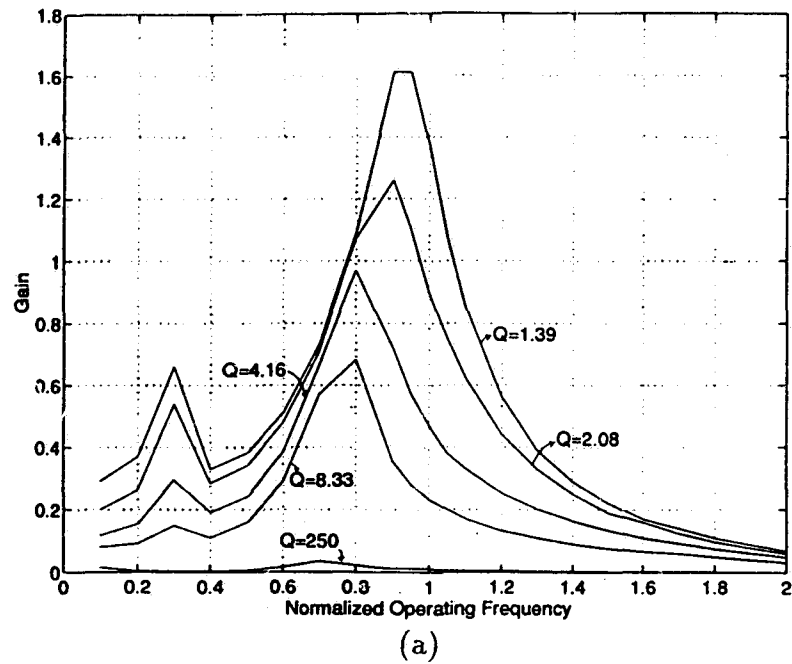


Figure 2.4: Plot of gain versus  $f_n$  with  $Q$  as a parameter (for  $\frac{C_s}{C_t} = 1$ ) obtained using SPICE simulation. 3-dimensional plot is also included.

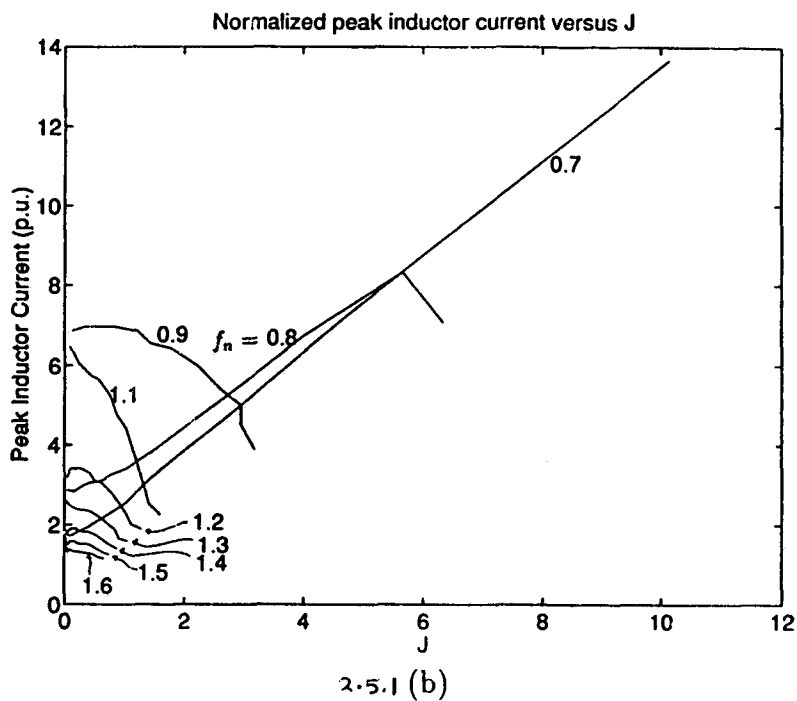
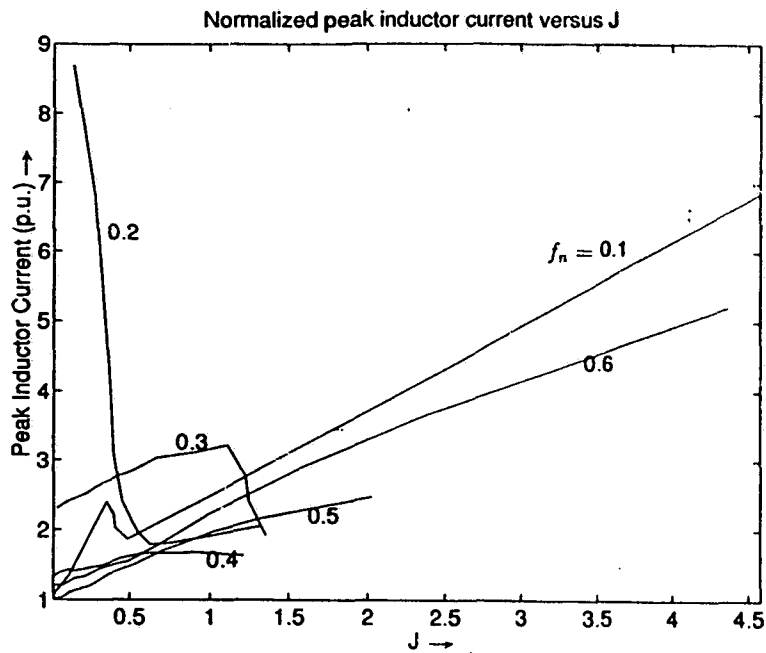


Fig. 2.5 Normalized design curves (obtained using SPICE simulation).  
 2.5.1(a),(b) Normalized peak inductor current ( $J_{Lp}$ ) Vs J, with  $f_n$  as a parameter.  
 2.5.1(c) 3-Dimensional view of the plots of 2.5.1(a) and (b).

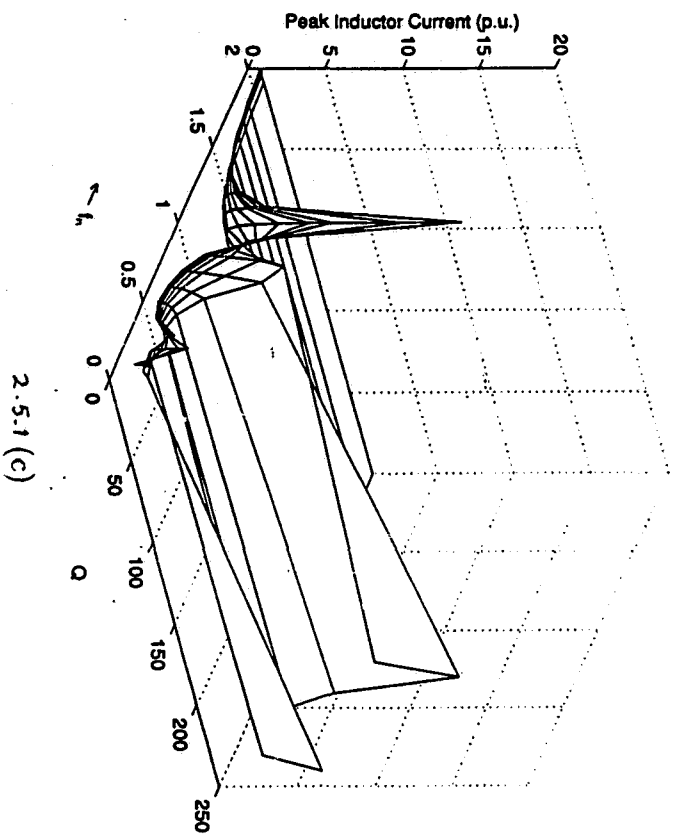


Fig. 2.5 (continued)

2.5.1 (c)

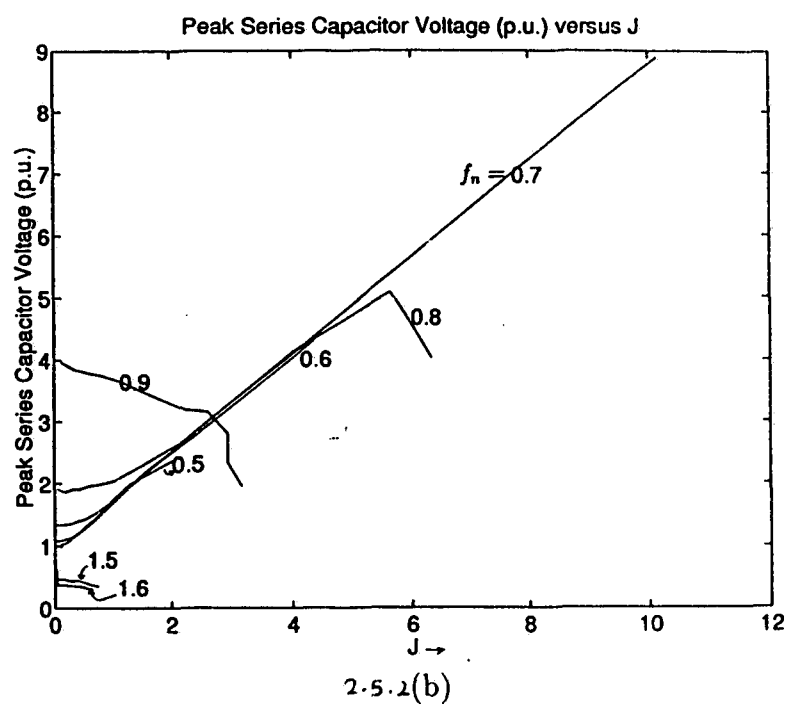
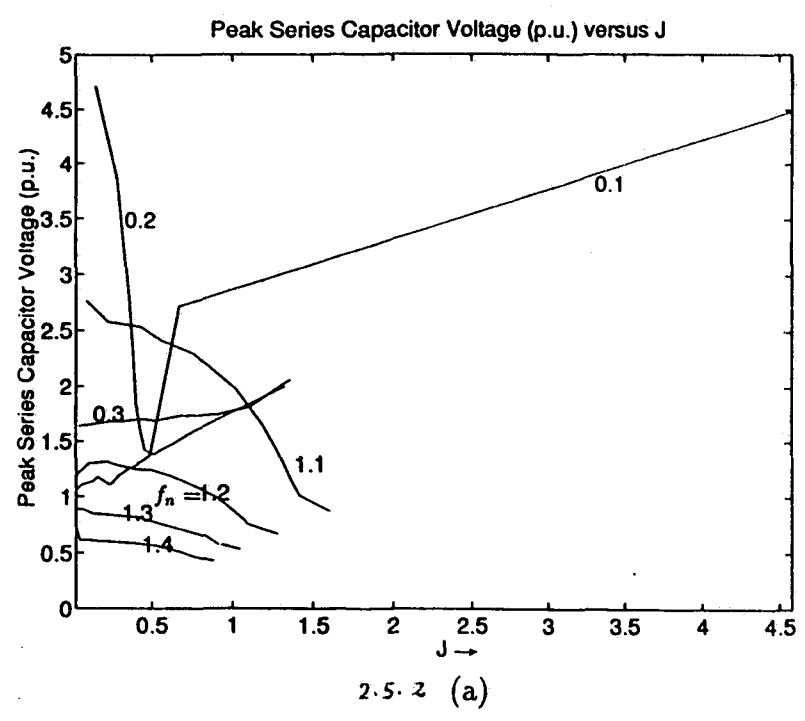
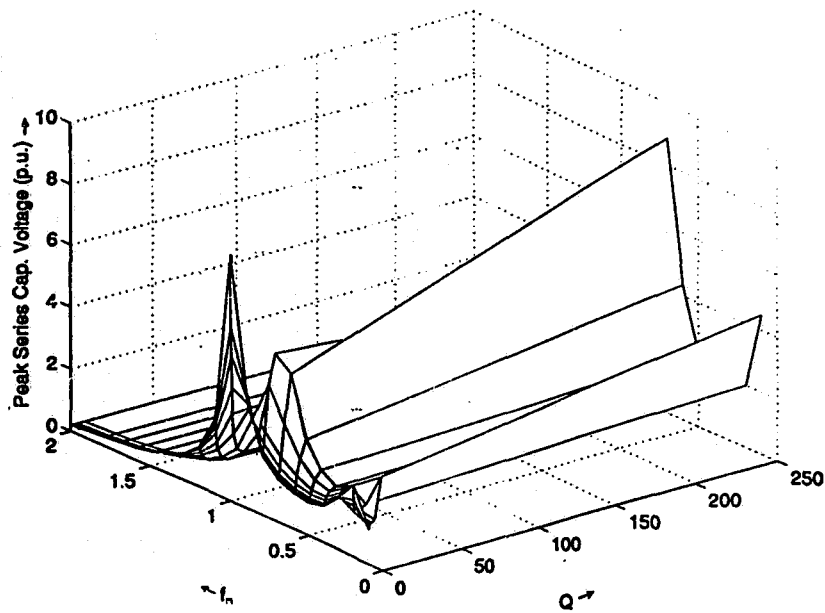


Fig. 2.5 (continued)  
 2.5.2(a),(b) Normalized peak series capacitor voltage ( $m_{csp}$ ) Vs J, with  $f_n$  as a parameter.  
 2.5.2(c) 3-Dimensional view of the plots of 2.5.2(a) and (b).



2.5.2 (c)

Fig. 2.5 (continued)

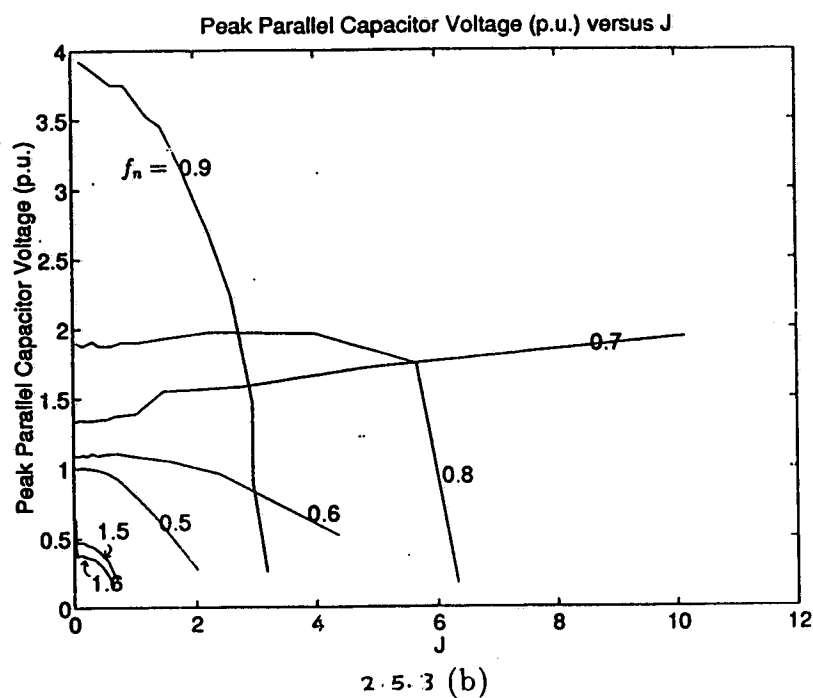
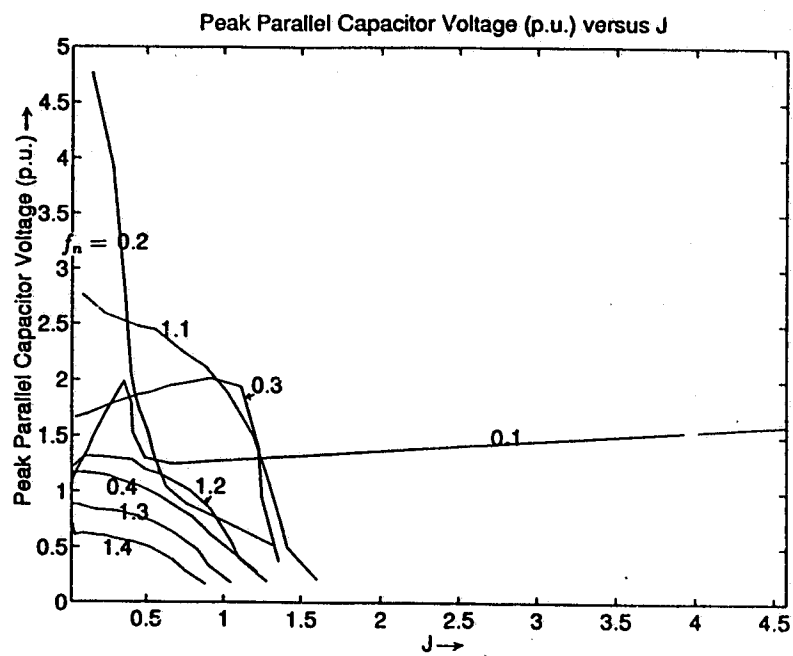
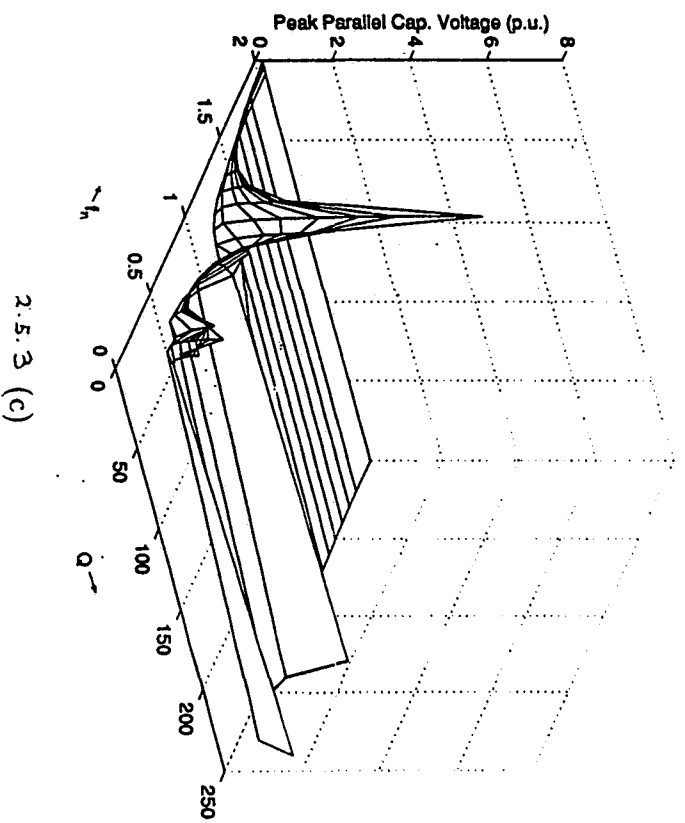


Fig. 2.5 (continued)

2.5.3(a),(b) Normalized peak parallel capacitor voltage ( $m_{ctp}$ ) Vs J, with  $f_n$  as a parameter.

2.5.3(c),(d) 3-Dimensional view of the plots of 2.5.3(a) and (b).



2.5.3 (c)

Fig. 2.5 (continued)

## 2.5 Boundaries Between the Various Modes of Operation

### 2.5.1 Boundary Between Leading and Lagging Power Factor Mode of Operation

. When the load current exceeds a critical value called  $J_{AR}$ , the converter enters the above resonance mode. Naturally, this value depends on the value of  $f_n$ . Fig. 2.6(a) shows the boundaries between the lagging and leading power factor modes of operations. While the converter operates in lagging p.f. mode for all values of  $f_n > 1.0$  [4], it is found to operate in leading p.f. mode between values  $0.5 < f_n < 0.7$ . The region below  $f_n < 0.5$  does not follow any fixed pattern regarding leading or lagging power factor mode of operation. However, as will be shown subsequently, the multiple conduction modes do enter lagging power factor mode (above resonance). An expression for  $J_{AR}$  in the range  $0.7 < f_n < 1.0$  was determined by fitting a curve in the data obtained by repeated spice simulations. The idea is to fit the most appropriate polynomial expression into this data. Standard techniques, like the least square fitting, are available for this purpose. It can be shown that the boundary between the two modes can be described by the following polynomial.

$$J_{AR} = K_5 f_n^5 + K_4 f_n^4 + K_3 f_n^3 + K_2 f_n^2 + K_1 f_n + K_0 \quad (2.34)$$

where,

$$K_5 = -0.15; \quad K_4 = 0.64; \quad K_3 = -1.13; \quad K_2 = 0.96; \quad K_1 = -0.42 \quad K_0 = 0.07$$

The curve obtained with this polynomial is plotted along with the actual one in Fig. 2.6(b).

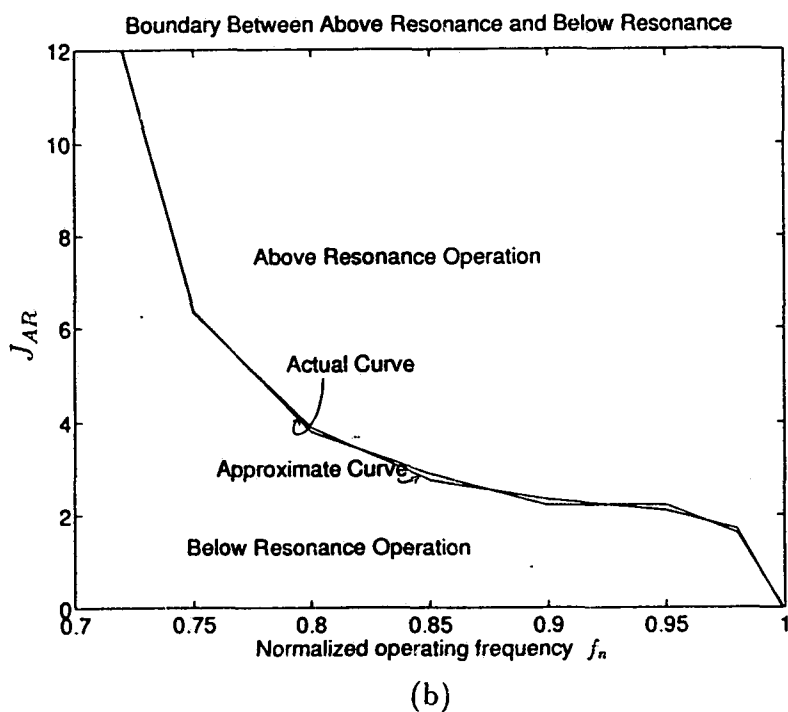
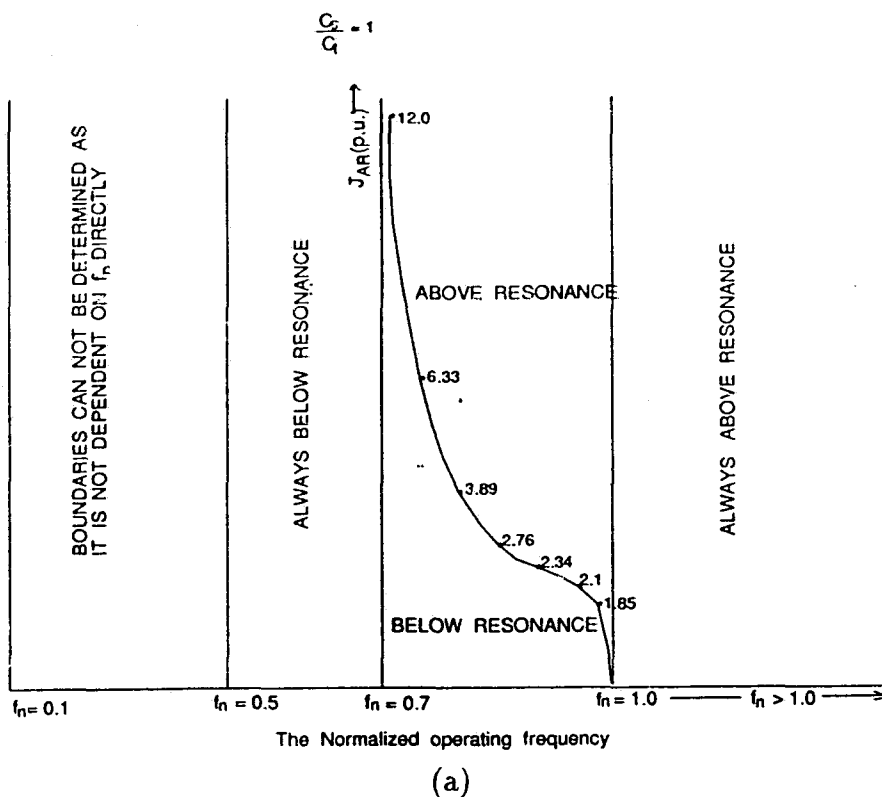


Fig.2.6(a) The boundaries between the various modes of operation. (b) Comparison between the actual boundary and the approximate one using curve fitting. The two are very close.

### 2.5.2 Boundaries Between DCVM and CCVM Operation

Boundary between DCVM and CCVM is determined by a critical value of the load current (called  $J_{crit}$ ), beyond which the DCVM operation occurs. Boundary obtained with repeated spice simulations is shown in Fig. 2.7(a). The zone of multiple conduction modes is separately marked. A polynomial expression was fit into this boundary. It is found that more accurate expressions can be obtained if they are obtained separately for the multiple and non multiple modes. Fig. 2.7(b) shows the boundary for the non multiple modes. It can be approximated by the following polynomial:

$$J_{crit} = k_7 f_n^7 + k_6 f_n^6 + k_5 f_n^5 + k_4 f_n^4 + k_3 f_n^3 + k_2 f_n^2 + k_1 f_n + k_0 \quad (2.35)$$

where,

$$k_7 = 0.33 ; \quad k_6 = -1.10 ; \quad k_5 = 1.81 ; \quad k_4 = -1.24 ; \quad k_3 = -0.30$$

$$k_2 = 1.0 ; \quad k_1 = -0.56 ; \quad k_0 = 0.1$$

The curve obtained with this polynomial is plotted along with the actual one in Fig. 2.7(b). Similarly, the expression for  $J_{crit}$ , for the multiple conduction modes(MCM) is found to be:

$$J_{crit(MCM)} = -196.67 f_n^3 + 128.5 f_n^2 - 22.68 f_n + 1.43 \quad (2.36)$$

The above expressions (2.34), (2.35) and (2.36) can be used as simple design tools to get a preliminary idea about the mode of operation (leading p.f. or lagging p.f. or DCVM or CCVM) once the operating frequency is known.

## 2.6 Design of the Converter

This section presents a design example. Design was done for worst case loading i.e. for maximum load current with minimum input voltage. Corresponding to this the

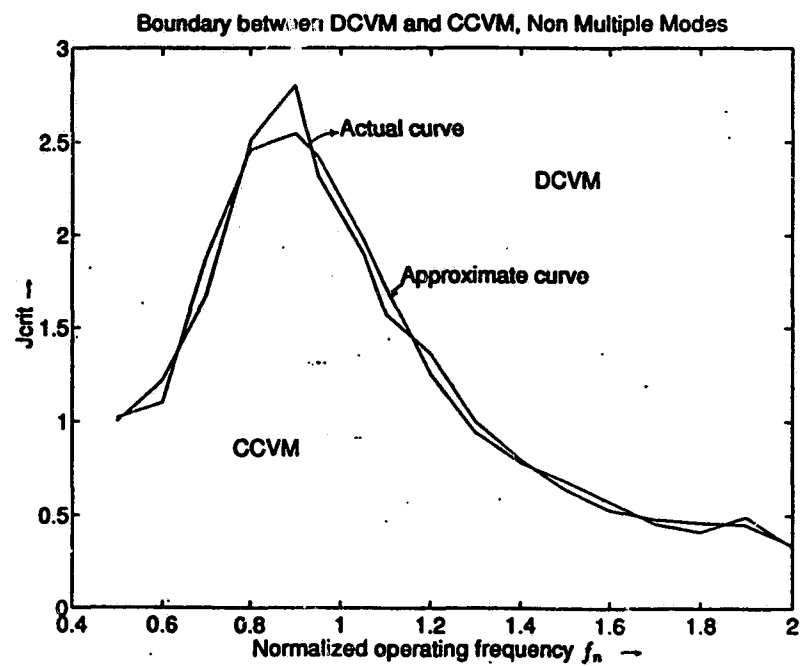
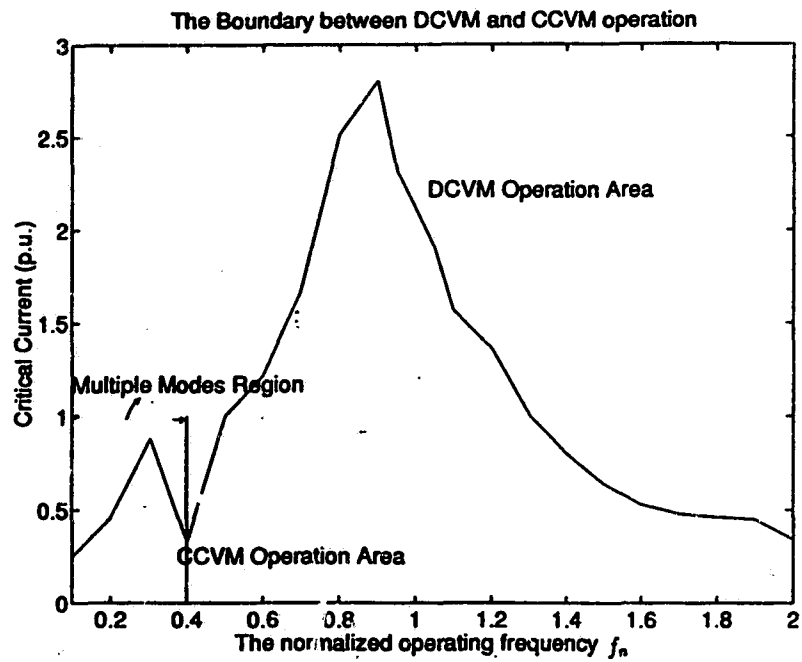


Figure 2.7: (a) The boundaries between the CCV and DCV modes of operation. (b) Comparison between the actual boundary and the approximate one using curve fitting.

converter is kept under operation in DCVM. Using the design method given in [12], an SPRC was designed with the following specifications.

Input supply voltage,  $V_{smin} = 50 \text{ V}$ .

Output voltage of the converter,  $V_0 = 0 \text{ to } 24\text{V}$ , variable.

Maximum output power,  $P_o = 100 \text{ Watts @ } 24 \text{ V}$ .

Switching frequency,  $f_t = 200 \text{ kHz}$ .

All the quantities are normalized using the base quantities given by (2.11).

Using the design procedure discussed in [12], the different values used are:

Normalized load current,  $J = \frac{I}{(E/Z)} = 4.3 \text{ p.u. ;}$

where  $I$  is the primary side reflected load current.

$$I_d = 100/24 = 4.16 \text{ A}$$

Normalized switching frequency (at full load),

$$f_n = \frac{f_t}{f_0} = 0.8 \quad (2.37)$$

where  $f_0 (= \omega_0/2\pi; \omega_0 = 1/(LC_e)^{1/2})$  is the resonant frequency.

Converter Gain,  $M = 1.036$ .

To obtain 24 V output, the required transformer turns ratio,

$$n = 1.036 \times 25/24 = 1.08.$$

$$Z = (L/C_e)^{1/2} = 27.85 \quad (2.38)$$

$$\omega_0 = \frac{2\pi \times f_t}{f_n} = 1/(LC_e)^{1/2} \quad (2.39)$$

Solving equations (2.38) and (2.39) simultaneously, resonating component values obtained are:

$$L = 17.74\mu H ; C_s = 0.047\mu F ; C_t = n^2 C'_t = 0.047\mu F.$$

There are basically three kinds of applications:

A1. The operating frequency is held constant and the load is varied irrespective of the gain: Table 2.1 gives the range of gain for the designed converter for leading and lagging power factor modes of operation.

A2. The load is held constant, and the operating frequency is varied to obtain variable output voltage: Tables 2.2 and 2.3 give the range of gain obtainable for this application. Separate tables are given for the leading and lagging power factor modes of operation. As can be seen from Table 2.3, the multiple conduction modes are capable of operating in lagging power factor mode.

A3. The gain is kept constant with changing load by suitably adjusting the operating frequency (voltage regulation): Tables 2.4, 2.5 and 2.6 show the regulation of the output voltage for below resonance, above resonance, and multiple conduction modes, respectively. The gain is kept constant (equal to the rated value) and the load is varied. The tables show that very little variation in operating frequency is required to maintain a constant rated gain, even when the load current shows a large variation from full load to open circuit condition. It requires slightly higher switching frequency variation for the above resonance case than below resonance case. Another observation is that the peak tank current decreases till the load current reaches about one fourth its rated value. Subsequently, it remains nearly constant irrespective of the load current. Table 2.6 shows that the multiple conduction modes are capable of supplying the rated gain only at lower load currents.

Table 2.1: Variation of key parameters for  $f_n = 0.8$  and variable load (from near load short circuit to near load open circuit)

$Q$	$J$	Gain	$\eta$	$P_o$	$J_{Lp}$	$v_{ct(peak)}$	$J_{switch(rms)}$	$J_{switch(avg)}$	$J_{diode(avg)}$
250	6.33	0.023	14.98	3.24 W	7.05	4.45 V	2.45	1.11	1.57
8.33	5.65	0.68	79.52	86.63	8.32	43.75	4.08	2.57	0.27
4.17	4.01	0.97	85.66	87.75	6.73	49	3.37	2.17	0.01
2.08	2.22	1.07	86.20	53.55	4.7	49.25	2.41	1.61	0.076
1.39	1.52	1.09	86.49	37.35	3.89	48.50	1.91	1.14	0.16
0.93	1.02	1.10	85.68	25.43	3.4	47.50	1.58	0.86	0.24
0.69	0.77	1.10	83.81	19.13	3.27	47.50	1.45	0.77	0.29
0.55	0.61	1.10	80.93	15.08	3.11	47.00	1.44	0.79	0.34
0.37	0.41	1.10	77.58	10.35	3.05	47.00	1.28	0.63	0.38
0.28	0.31	1.11	73.35	7.88	2.97	47.75	1.25	0.62	0.41
0.14	0.16	1.11	60.68	3.83	2.83	47.00	1.18	0.57	0.43
0.06	0.06	1.13	39.09	1.58	2.87	47.50	1.13	0.53	0.50

Table 2.2: Variation of key parameters for fixed  $Q = 4.17$  and variable  $f_n$ , below resonance

$f_n$	$J$	Gain	$\eta$	$P_o$	$J_{Lp}$	$v_{ct(peak)}$	$J_{switch(rms)}$	$J_{switch(avg)}$	$J_{diode(avg)}$	Mode
0.1	0.49	0.12	59.58	1.35 W	1.87	32.5 V	0.40	0.16	0.12	DCVM
0.5	1.01	0.24	72.52	5.63	1.97	20.0	0.76	0.37	0.21	DCVM
0.6	1.59	0.39	78.21	13.77	2.9	26.25	1.21	0.62	0.31	DCVM
0.7	2.75	0.66	82.82	41.175	4.78	39.5	3.37	1.25	0.37	DCVM

Table 2.3: Variation of key parameters for fixed  $Q = 4.17$  and variable  $f_n$ , above resonance

$f_n$	J	Gain	$\eta$	$P_o$	$J_{Lp}$	$v_{et(peak)}$	$J_{switch(rms)}$	$J_{switch(avg)}$	$J_{diode(avg)}$	Mode
0.2	0.63	0.15	66.0	2.25 W	1.79	26 V	0.50	0.21	0.14	DCVM
0.3	1.22	0.30	77.05	8.1	2.78	35	0.92	0.43	0.22	DCVM
0.35	0.84	0.21	70.59	3.83	1.94	22.75	0.62	0.27	0.20	DCVM
0.4	0.79	0.19	69.97	3.38	0.79	19.25	0.59	0.26	0.16	DCVM
0.8	4.01	0.97	85.66	87.75	6.73	49	3.37	2.16	0.01	DCVM
0.9	2.94	0.72	82.59	47.48	5.0	36.75	2.41	1.38	0.30	DCVM
1.0	1.93	0.47	77.98	20.48	3.41	23.75	1.53	0.90	0.34	DCVM
1.1	1.37	0.331	71.57	11.25	2.78	18.5	1.14	0.64	0.32	CCVM
1.2	1.04	0.25	66.76	5.85	2.21	14.0	0.87	0.49	0.29	CCVM
1.3	0.83	0.20	60.83	3.83	1.89	12.0	0.77	0.46	0.24	CCVM
1.4	0.68	0.16	57.09	2.51	1.57	9.64	0.58	0.28	0.22	CCVM
1.5	0.54	0.13	51.26	1.68	1.39	8.64	0.50	0.23	0.20	CCVM
1.6	0.47	0.11	46.56	1.19	1.27	7.37	0.46	0.22	0.18	CCVM
1.7	0.39	0.09	40.75	0.82	1.11	6.72	0.38	0.17	0.18	CCVM
1.8	0.31	0.08	32.58	0.52	0.98	5.67	0.40	0.20	0.17	CCVM
2.0	0.21	0.05	23.26	0.24	0.86	4.68	0.26	0.10	0.14	CCVM
2.4	0.08	0.01	6.47	0.03	0.67	3.09	0.18	0.07	0.10	CCVM

Table 2.4: Voltage Regulation, for  $f_n$  less than 0.8

<i>Simulation</i>			
J	$f_n$	Gain	$J_{Lp}$
0.03	0.78	1.0	3.07
0.13	0.77	1.0	3.08
0.28	0.77	1.0	3.23
0.37	0.77	1.0	3.33
0.56	0.77	1.0	3.38
0.70	0.77	1.0	3.56
0.94	0.77	1.0	3.64
1.47	0.77	1.0	4.2
2.0	0.77	1.0	5.12
4.1	0.8	1.0	7.49

Table 2.5: Voltage Regulation, for  $f_n$  greater than 0.8

<i>Simulation</i>			
J	$f_n$	Gain	$J_{Lp}$
4.1	0.8	1.0	7.48
1.89	1.0	1.0	4.7
1.50	1.05	1.0	5.19
1.02	1.13	1.0	4.93
0.72	1.15	1.0	4.32
0.48	1.17	1.0	3.82
0.36	1.17	1.0	4.31
0.26	1.17	1.0	4.31
0.12	1.17	1.0	4.01
0.04	1.17	1.0	3.96

Table 2.6: Voltage Regulation during the multiple modes

<i>Simulation</i>			
$J$	$f_n$	Gain	$J_{Lp}$
0.36	0.19	1.0	4.44
0.27	0.26	1.0	3.70
0.24	0.16	1.0	3.46
0.14	0.28	1.0	3.02
0.11	0.13	1.0	3.9
0.07	0.14	1.0	4.44
0.06	0.29	1.0	2.78

## 2.7 Experimental Verification

The experimental converter using power MOSFETs was used to verify the results obtained from the analysis and SPICE simulation. The details of this converter are given in Fig. 2.8. No transformer was used in the experimental set up. The Converter was operated in a frequency range of 50 to 500 kHz. Some of the waveforms are shown in Figs. 2.8(a)-2.8(d). The plots of gain versus  $J$  obtained using the experimental set up are included in Fig. 2.9 along with those obtained using the SPICE, for the sake of comparison. All the values are in per unit with respect to the base quantities defined by (2.11).

Fig. 2.10 shows the variation of efficiency for different values of  $Q$  with change in  $f_n$ . It is observed that the efficiency during the multiple conduction modes is comparable to the lower order (non multiple) modes. Thus SPRC is suitable for operation over a wide range of  $f_n$  for applications where a wide range of output is required. Data for the efficiency calculations were taken from the manufacturer's data sheet for the components used in the experimental set up.

Tables 2.4 - 2.6 show the experimental results for the output voltage regulation

Table 2.7: Comparison of simulation and experimental results for output voltage variation with change in operating frequency

Mode	Simulation						Experimental					
	$f_{switch}$	$I_d$	$V_o$	$i_L(peak)$	$v_{cs}(peak)$	$v_{ct}(peak)$	$f_{switch}$	$I_d$	$V_o$	$i_L(peak)$	$v_{cs}(peak)$	$v_{ct}(peak)$
BA	500	0.20	1.5	0.8	4.70	5.0	500	0.18	1.0	0.80	4.54	4.7
BA	460	0.31	2.0	1.0	6.3	5.5	460	0.27	1.6	0.92	5.91	5.27
BA	420	0.40	3.0	1.10	8.5	7.5	420	0.37	2.3	1.07	7.54	6.36
BA	380	0.55	3.6	1.4	11.0	9.0	380	0.5	3.0	1.30	9.91	7.82
BA	340	0.80	5.2	1.6	15.0	12.5	340	0.70	4.09	1.55	13.27	10.18
BA	310	1.10	6.8	1.8	20.5	14.0	310	0.9	5.20	1.85	18.0	12.36
BCA	280	1.43	9.0	2.0	30.0	20.0	280	1.20	7.0	2.30	26.11	16.0
BCA	260	1.75	11.0	2.1	35.5	23	260	1.50	9.1	2.75	33.71	20.0
BCA	240	2.01	12.7	2.3	49.0	25.0	240	2.02	12.10	3.48	50.91	25.83
BCA	225	2.54	16.0	3.45	62.0	30.0	225	2.62	15.76	4.4	68.18	34.81
BCA	210	2.92	18.1	3.75	84.0	34.0	210	3.50	21.19	5.72	95.45	44.5
BCA	200	3.88	23.3	6.18	105.0	49.0	200	3.0	19.0	5.1	88.0	38.0
CAC	180	3.0	18.2	5.09	90.0	42.72	180	2.60	16.2	3.75	78.0	36.0
AC	165	2.17	13.1	3.74	70.0	33.3	165	2.0	12.5	3.25	69.0	31.25
ACB	150	1.55	9.31	2.72	56.37	26.38	150	1.50	9.5	2.5	55.5	28.0
AB	145	1.39	8.36	2.44	53.63	23.61	145	1.40	8.5	2.25	54.0	25.5
AB	115	0.85	5.2	1.63	41.81	18.06	115	1.0	6.0	1.8	45.0	19.0
ABC	105	0.78	4.65	1.58	40.91	18.88	105	0.80	5.0	1.6	43.0	20.0
ABC	95	0.75	4.48	1.55	40.0	17.77	95	0.77	4.8	1.50	43.0	22.0
CABC	85	0.81	4.86	1.72	42.72	21.39	85	0.83	5.2	1.75	43.0	25.0
CABC	75	1.09	6.5	2.47	47.27	31.85	75.0	1.03	6.4	2.35	47.0	32.0
CABC	65	1.57	9.4	3.59	57.27	48.19	65	1.25	8.0	2.78	52.5	43.5
ABC	60	1.11	6.69	2.58	47.27	34.58	60	1.0	6.3	2.40	47.0	34.0
CABAC	50	0.61	3.65	1.66	38.0	25.0	50	0.58	3.5	1.60	38.0	30.0

↑ Leading p.f. Mode → Lagging p.f. Mode ↓

Rated

Switching Frequency in kHz:  
 Voltage Quantities in Volts  
 Current Quantities in Amps

Table 2.8: Comparison of interval durations obtained by Experiments, Simulation and Analysis, for  $f_n = 0.35$ , four interval mode

J	Experimental				Simulation				Analysis			
	$t_{B_1}$	$t_{A_1}$	$t_{B_2}$	$t_{A_2}$	$t_{B_1}$	$t_{A_1}$	$t_{B_2}$	$t_{A_2}$	$t_{B_1}$	$t_{A_1}$	$t_{B_2}$	$t_{A_2}$
0.18	0.25	0.60	0.38	0.19	0.36	0.63	0.38	0.08	0.38	0.58	0.43	0.05
0.30	0.24	0.64	0.30	0.24	0.31	0.63	0.39	0.09	0.35	0.58	0.42	0.08
0.35	0.22	0.66	0.28	0.24	0.30	0.63	0.40	0.09	0.33	0.59	0.41	0.10
0.45	0.20	0.72	0.23	0.27	0.26	0.67	0.37	0.14	0.29	0.61	0.40	0.14
0.60	0.15	0.75	0.25	0.21	0.16	0.76	0.34	0.16	0.22	0.67	0.34	0.20

Table 2.9: Comparison of component stresses and gain obtained using Experiments, Simulation and Analysis, for  $f_n = 0.35$ , four interval mode

J	Experimental				Simulation				Analysis			
	$J_{Lp}$	$m_{csp}$	$m_{ctp}$	Gain	$J_{Lp}$	$m_{csp}$	$m_{ctp}$	Gain	$J_{Lp}$	$m_{csp}$	$m_{ctp}$	Gain
0.18	3.28	2.12	2.52	1.38	2.96	1.93	1.93	1.11	4.42	2.65	2.64	1.32
0.30	2.46	1.72	1.96	0.87	2.85	1.82	1.82	0.86	4.21	2.52	2.51	1.21
0.35	2.19	1.56	1.80	0.72	2.75	1.78	1.80	0.82	3.98	2.38	2.38	1.12
0.45	2.05	1.50	1.60	0.55	2.50	1.60	1.60	0.70	3.36	2.06	2.05	0.91
0.60	1.92	1.48	1.56	0.44	2.00	1.43	1.23	0.52	2.53	1.63	1.61	0.62

Table 2.10: Comparison of interval durations obtained by Experiments, Simulation and Analysis, for  $f_n = 0.6$ , two interval mode

J	Experimental		Simulation		Analysis	
	$t_{A_1}$	$t_{B_1}$	$t_{A_1}$	$t_{B_1}$	$t_{A_1}$	$t_{B_1}$
0.13	0.87	0.02	0.84	0.02	0.79	0.04
0.22	0.84	0.03	0.82	0.04	0.78	0.05
0.33	0.79	0.04	0.79	0.06	0.77	0.07
0.52	0.77	0.06	0.76	0.09	0.74	0.10
0.76	0.74	0.10	0.71	0.13	0.70	0.13
1.24	0.67	0.17	0.65	0.18	0.63	0.20
1.50	0.63	0.18	0.63	0.22	0.59	0.24

Table 2.11: Comparison of component stresses and gain obtained using Experiments, Simulation and Analysis for  $f_n = 0.6$ , two interval mode

J	Experimental				Simulation				Analysis			
	$J_{Lp}$	$m_{csp}$	$m_{ctp}$	Gain	$J_{Lp}$	$m_{csp}$	$m_{ctp}$	Gain	$J_{Lp}$	$m_{csp}$	$m_{ctp}$	Gain
0.13	1.31	1.13	1.11	0.57	1.21	1.10	1.08	0.56	1.28	1.11	1.08	0.61
0.22	1.36	1.14	1.10	0.57	1.31	1.11	1.08	0.56	1.32	1.13	1.08	0.60
0.33	1.56	1.22	1.16	0.58	1.46	1.17	1.12	0.55	1.42	1.18	1.08	0.60
0.52	1.81	1.32	1.09	0.51	1.61	1.26	1.10	0.54	1.62	1.29	1.08	0.57
0.76	2.02	1.52	1.12	0.50	1.88	1.47	1.09	0.52	1.90	1.47	1.08	0.55
1.24	2.59	1.86	1.08	0.40	2.38	1.86	1.02	0.45	2.48	1.89	1.05	0.45
1.50	2.05	2.16	1.05	0.38	2.71	2.07	1.0	0.42	2.69	2.12	1.0	0.40

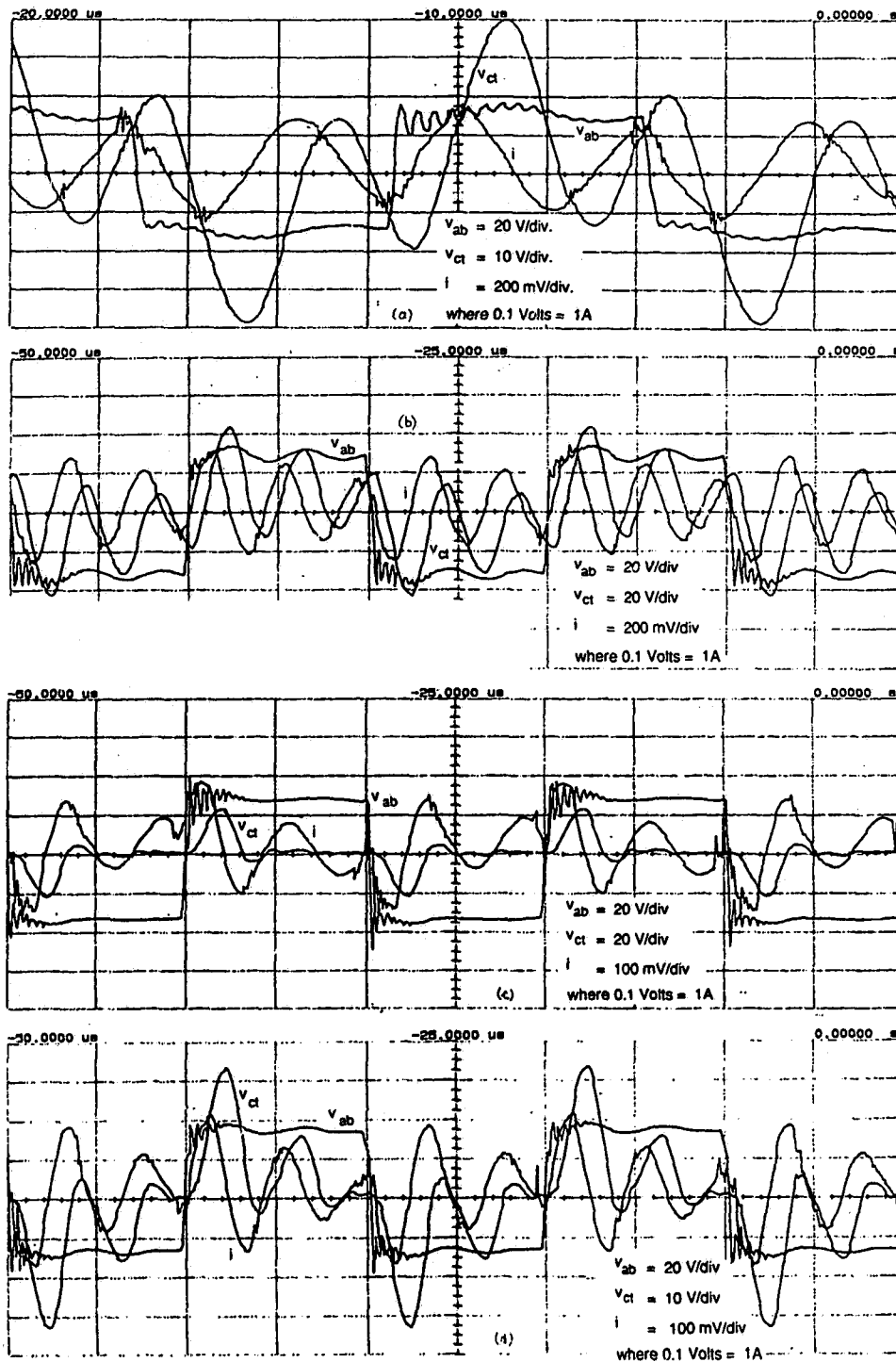


Figure 2.8: Typical waveforms obtained from an experimental set up ( $v_{ab}$ ,  $v_{ct}$  and  $i$ ):  
 (a), (b) Continuous Capacitor Voltage Mode with 4 and 6 intervals respectively  
 (c), (d) Discontinuous Capacitor Voltage Mode.  
 [Details of the converter: Switches used - IRF 130, MOSFETs; Feedback diodes internal to MOSFETs; Input dc voltage,  $2E = 50$  V;  $L = 17.7\mu H$ ;  $C_s = 0.047\mu F$ ;  $C_t = 0.047\mu F$ ]

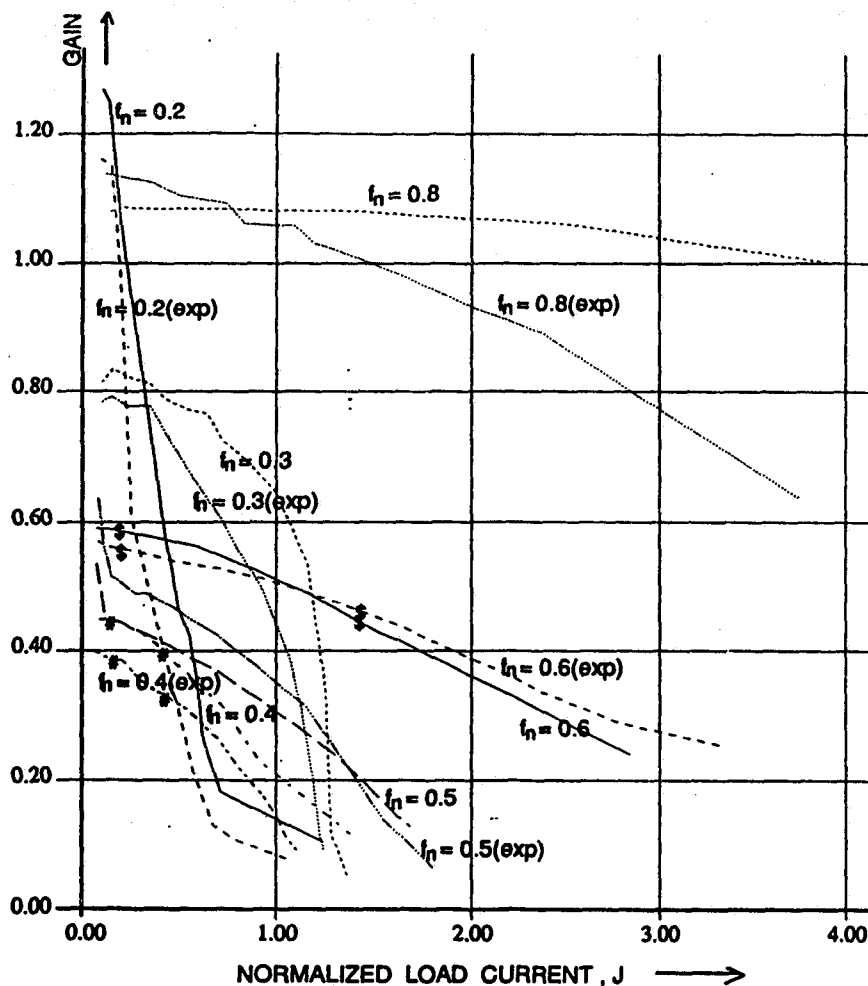


Figure 2.9: Plots of gain versus  $f_n$  obtained using the experimental converter (marked "exp") along with those obtained using SPICE-3.

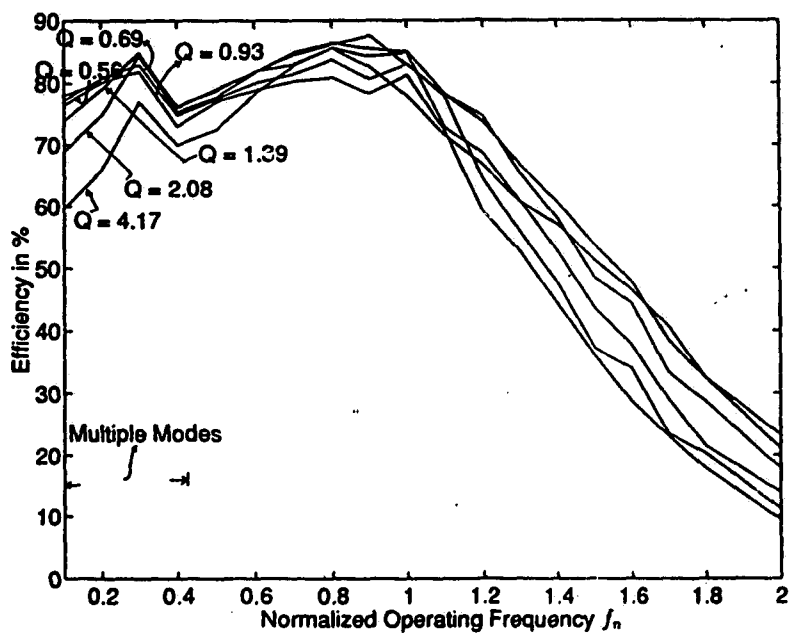


Figure 2.10: Plot of efficiency of the converter as a function of  $f_n$ , with  $Q$  as a parameter.

application. Table 2.7 compares the theoretical and experimental values of the component stresses for the entire range of the converter output voltage. Both above resonance and below resonance cases are considered. The modes with respect to the number of intervals per half cycle of the switching frequency are also given. For example AB denotes occurrence of an "A" interval followed by a "B" interval in a two interval mode.

Tables 2.8 - 2.11 compare the interval durations and the peak component stresses for the four and two interval cases, obtained with theory, SPICE and experiments.

## 2.8 Conclusions

Various operating modes of the SPRC, including the multiple conduction modes, have been identified using computer simulation. General solutions for all the modes of operation have been presented. As an example, two of the predominant modes, with four and two intervals respectively, have been selected as the particular cases and the converter gain for those modes have been analytically obtained. The results obtained with analysis and simulation have been compared. The converter gain and peak component stresses have been plotted against per unit load current. Boundaries between the various modes, CCVM and DCVM as well as between leading and lagging p.f. modes, have been obtained and plotted. Simple expressions, meant for aiding the design engineer, have been obtained using numerical techniques. The theoretical and simulation results have been compared with the experimental results. To control the output voltage, the operating frequency can be varied in two directions. The range of frequency variation is slightly higher (up to  $f_n = 2.0$ ) for above resonance case (as compared to the below resonance operation) for a full range output voltage control. The type of converter control discussed in this chapter (including multiple

conduction modes) can be utilized in power supplies meant to serve a wide range of voltage requirements. Multiple conduction modes are capable of supplying the rated gain for very low output current values.

## **Chapter 3**

# **Large-Signal Analysis Using Discrete Time Domain Modeling**

In this chapter, a discrete time domain model for the LCC-type parallel resonant converter has been derived. This model has been used to predict the large-signal behavior of the converter. The peak component stresses and the dynamic response of the key state variables, as obtained from the large-signal analysis, using PRO-MATLAB software are plotted. SPICE results are included to verify the analytical results. Large-signal analysis of the SPRC operating in discontinuous current mode is also presented in this chapter. Theoretical results are experimentally verified.

### **3.1 Introduction**

The various modes in which the SPRC operates in steady state were identified and analyzed in chapter 2. The steady-state analysis of chapter 2 is useful for better understanding and designing of the converter, but only under steady-state and not

during the transients. The dynamic response of the converter during the transient events is bound to govern proper design procedures and the choice of appropriate component ratings to be used. But the transient analysis is not easy to perform because of the following difficulties in modeling the transient events.

- (a) The exact nature of the transient disturbance is unpredictable.
- (b) The actual dynamic response of the converter during the transients is quite complex.

Thus, there is a need for a model which could give the major design constraints (such as the peak component ratings) without going into the complexities of an exact transient analysis. A discrete time domain model greatly simplifies this problem. Such simplification in predicting the transient behavior assumes greater significance for the SPRC, the mathematical analysis of which is more complex than the other two configurations. Such an approach was for the first time reported in [48] for a series resonant converter. Later on it was used for small-signal analysis of series resonant converter [42] and parallel resonant converter [54].

Small-signal analysis of an SPRC using an approximate method (extended describing function method) has been presented in [73]. However, large-signal modeling and behavior of SPRC is not available in the literature.

The dynamic response of the converter during the transients is quite significant [74, 75] and must be considered while formulating the design procedures for the converter. Especially regarding the choice of appropriate component ratings because it is mostly during the transients (such as switching ON/OFF of the converter or sudden load variation), that the converter components have to bear the maximum stress. Therefore it is useful to perform the large-signal analysis.

In this chapter, the discrete time domain modeling of the series-parallel resonant converter is presented to show the effectiveness of such a model in predicting the

transient behavior of the converter. It is shown that using this model, only the initial conditions at the beginning of every half cycle of the operating frequency are sufficient to predict the peak component stresses and the state behavior. A complete large-signal analysis is presented based on this modeling. Step change from full load to short circuit or open circuit conditions, which are actually the particular cases of transients caused due to a sudden variation in load, are of particular interest from a practical point of view. The behavior of the converter during these conditions is analyzed. Although the analysis and results have been presented for the converter designed to operate in lagging power factor mode under steady-state conditions, it can be modified for leading power factor mode of operation with some minor changes.

This chapter is divided into the following sections. The operation of the converter and the terminology used in this chapter are presented in section 3.2. Section 3.3 gives the details of derivation of the discrete time domain model. Necessary equations are included to clearly show the steps involved in the derivation of the model. Expressions for the peak component stresses are also given in the same section. The choice of state variables and the discrete state-space model is presented in section 3.4. Section 3.5 gives the details of the converter which will be used to illustrate the use of the large-signal model derived in sections 3.3 and 3.4, in predicting the large-signal behavior of the designed converter. Section 3.6 describes the implementation of the discrete time model on the computer and its use in determining the dynamic response of the converter during the transient conditions. Transient conditions caused due to different types of external disturbances are considered. To verify the results of theory, experimental results are included in section 3.7. Section 3.8 describes the large signal modeling and results for the DCM operation. Section 3.9 states the conclusions.

## 3.2 Converter Operation

In Fig. 3.1, the basic circuit diagram of the SPRC has been redrawn with all the circuit quantities shown as discrete quantities. Fig. 3.2 illustrates typical waveforms starting from  $k^{th}$  instant onwards, for the continuous current mode, in which the SPRC operates. The inductor current is lagging the voltage  $v_{ab}$  and is operating in the lagging p.f. (above resonance) mode. The converter operation for this mode is explained next. In Fig. 3.2, the switch S1 is turned ON at time instant  $t_{0(k)}$ . This being a lagging power factor mode of operation, the inductor current has a negative value at that instant. The parallel capacitor voltage  $v_{ct}$  starts rising and becomes positive at instant  $t_{1(k)}$ . As the parallel capacitor voltage switches polarity, the load current does it too. The tank current is being carried by the parallel diode D1 at the beginning of the positive half cycle of  $v_{ab}$ . This continues till a point "P", where the current is transferred to the switch S1. At  $t_{2(k)}$ , S1 is turned-off and the next half cycle begins with the conduction of D2. There is no natural commutation of the switches here. But the turn on losses are almost negligible.

The second half cycle is exactly the same except that all the variables now have an opposite polarity as compared to the first half cycle. The first half cycle is called as the  $k^{th}$  event, the second half cycle as the  $(k + 1)^{th}$  event and so on. Each of these events are split into two sub-events depending upon the polarity of the parallel capacitor voltage ( $v_{ct}$ ) or the load current. There are explicit equations for each of these sub-events (called interval "A" and interval "B" [Fig. 3.3]).

The total conduction angle (switch + diode) is denoted by  $\gamma_k$  [42, 48, 54]. As shown in Fig. 3.2

$$\gamma_k = \alpha_k + \beta_k \quad (3.1)$$

$$\text{where } \alpha_k = \omega_0(t_{1(k)} - t_{0(k)}) \quad (3.2)$$



$$\text{and } \beta_k = \omega_0(t_{0(k+1)} - t_{1(k)}) \quad (3.3)$$

“ $\alpha_k$ ” stands for the length of interval B and “ $\beta_k$ ” stands for the length of interval A referred to the  $k^{\text{th}}$  event.

$$\text{Further } \omega_0 = \frac{1}{\sqrt{LC_e}}; \quad C_e = \frac{C_s C_t}{C_s + C_t} \quad (3.4)$$

The low ripple approximation, wherein the input and output voltages as well as the output current are assumed constant during an event (one half period)[42, 48], is followed. The variations in these quantities during an event are negligible as compared to the step changes they undergo at the beginning or end of an event.

### 3.3 The Discrete Time Domain Model of the SPRC

The following discrete time domain equations have been derived with respect to Fig. 3.2 using the models shown in Fig. 3.3. It should be noted that the subscript “ $0(k)$ ” denotes the value of that variable at the beginning of  $k^{\text{th}}$  interval while “ $0(k+1)$ ” implies at the beginning of  $(k+1)^{\text{th}}$  interval.  $E(t_{0(k)})$  and  $I(t_{0(k)})$  denote the input voltage of the dc bus and the reflected load current at the beginning of the  $k^{\text{th}}$  event and are assumed constant throughout this event in accordance with the “low ripple approximation” described in section 3.2.

#### 3.3.1 $k^{\text{th}}$ Event

Interval  $t_{0(k)} < t < t_{1(k)}$

The  $k^{\text{th}}$  event starts at time instant  $t_{0(k)}$ . The parallel capacitor voltage  $v_{ct}$  remains negative until instant  $t_{1(k)}$ . This interval, which has been called as interval B [12], can be described by the following discrete equations with  $t'$  as the running variable.

$$t' = t - t_{0(k)} \quad (3.5)$$

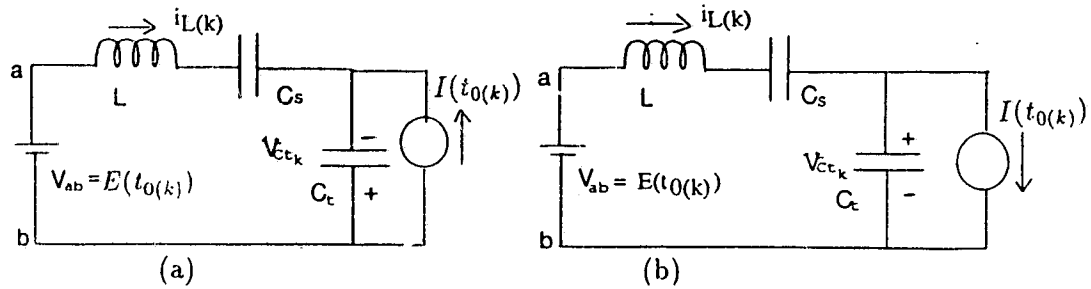


Figure 3.3: Equivalent circuits for the two different intervals: (a) Interval B (b) Interval A.  $L = L_s + L_l$ , where  $L_l$  is the leakage inductance of the hf transformer.

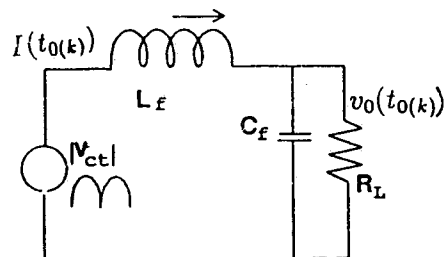


Figure 3.4: The output section of the SPRC referred to the primary side

The resonant inductor current, the series capacitor voltage and the parallel capacitor voltage for this interval are given by:

$$i_L(t') = A_{1B_k} \sin(\omega_0 t') + B_{1B_k} \cos(\omega_0 t') + C_{1B_k} \quad (3.6)$$

$$v_{cs}(t') = A_{2B_k} [1 - \cos(\omega_0 t')] + B_{2B_k} \sin(\omega_0 t') + C_{2B_k}(\omega_0 t') + v_{cs}(t_{0(k)}) \quad (3.7)$$

$$v_{ct}(t') = A_{3B_k} [1 - \cos(\omega_0 t')] + B_{3B_k} \sin(\omega_0 t') + C_{3B_k}(\omega_0 t') + v_{ct}(t_{0(k)}) \quad (3.8)$$

The constants used in the above equation are defined as below:

$$A_{1B_k} = [E(t_{0(k)}) - (v_{cs}(t_{0(k)}) + v_{ct}(t_{0(k)}))]/Z; B_{1B_k} = (i_L(t_{0(k)}) + (C_e/C_t)I(t_{0(k)}))$$

$$C_{1B_k} = -(C_e/C_t)I(t_{0(k)})$$

$$A_{2B_k} = Z(C_e/C_s)A_{1B_k}; B_{2B_k} = Z(C_e/C_s)B_{1B_k}; C_{2B_k} = Z(C_e/C_s)C_{1B_k}$$

$$A_{3B_k} = Z(C_e/C_t)A_{1B_k}; B_{3B_k} = Z(C_e/C_t)B_{1B_k}; C_{3B_k} = -Z(C_e/C_s)C_{1B_k}$$

$$\text{where } Z = \sqrt{\frac{L}{C_e}}$$

Interval  $t_{1(k)} < t < t_{0(k+1)}$ .

During this sub-event, the voltage  $v_{ct}$  (and the reflected load current) remains positive.

This is called interval A. Let  $t''$  be the running variable for this interval.

$$t'' = t - t_{1(k)} \quad (3.9)$$

Equations describing this interval are:

$$i_L(t'') = A_{1A_k} \sin(\omega_0 t'') + B_{1A_k} \cos(\omega_0 t'') + C_{1A_k} \quad (3.10)$$

$$v_{cs}(t'') = A_{2A_k} [1 - \cos(\omega_0 t'')] + B_{2A_k} \sin(\omega_0 t'') + C_{2A_k}(\omega_0 t'') + v_{cs}(t_{1(k)}) \quad (3.11)$$

$$v_{ct}(t'') = A_{3A_k} [1 - \cos(\omega_0 t'')] + B_{3A_k} \sin(\omega_0 t'') + C_{3A_k}(\omega_0 t'') + v_{ct}(t_{1(k)}) \quad (3.12)$$

As before, the constants used in the above equations are defined below:

$$A_{1A_k} = [E(t_{0(k)}) - (v_{cs}(t_{1(k)}) + v_{ct}(t_{1(k)}))]/Z; B_{1A_k} = (i_L(t_{1(k)}) - (C_e/C_t)I(t_{0(k)}))$$

$$\begin{aligned}
C_{1A_k} &= (C_e/C_t)I(t_{0(k)}) \\
A_{2A_k} &= Z(C_e/C_s)A_{1A_k}; B_{2A_k} = Z(C_e/C_s)B_{1A_k}; C_{2A_k} = Z(C_e/C_s)C_{1A_k} \\
A_{3A_k} &= Z(C_e/C_t)A_{1A_k}; B_{3A_k} = Z(C_e/C_t)B_{1A_k}; C_{3A_k} = -Z(C_e/C_s)C_{1A_k}
\end{aligned}$$

$A_{1B_k}$ ,  $A_{2B_k}$  etc. denote the constants involving the initial values of the three variables (resonant current, series capacitor voltage and parallel capacitor voltage) at instant  $t_{0(k)}$ , while  $A_{1A_k}$ ,  $A_{2A_k}$  etc. involve initial conditions at instant  $t_{1(k)}$ . These values can be evaluated in terms of  $A_{1B_k}$ ,  $A_{2B_k}$  etc. using (3.6) - (3.8).

### 3.3.2 $(k + 1)^{th}$ Event

The  $(k + 1)^{th}$  event starts at time instant  $t_{0(k+1)} (= t_{2(k)})$ , which is also the end point of  $k^{th}$  event. Thus the final values of the variables for the  $k^{th}$  event are the initial values for the  $(k + 1)^{th}$  event. The equations representing the two intervals of the  $(k + 1)^{th}$  event can be written in the same way as for the  $k^{th}$  event except that now the A, B, C constants will get redefined. For interval  $t_{0(k+1)} < t < t_{1(k+1)}$ , the A, B, C constants will be defined in terms of the initial conditions at instant  $t_{0(k+1)}$ , while those for interval  $t_{1(k+1)} < t < t_{0(k+2)}$  will be defined in terms of the initial conditions at instant  $t_{1(k+1)}$ .

The equations (3.5) - (3.12), describing the  $k^{th}$  event along with those for the  $(k + 1)^{th}$  event, describe one full cycle of the SPRC operation. The initial values of the  $(k + 1)^{th}$  event are expressed in terms of the initial values of the  $k^{th}$  event as below:

$$\begin{aligned}
i_L(t_{0(k+1)}) &= A_{1B_k} \cdot \sin(\gamma_k) + B_{1B_k} \cdot \cos(\gamma_k) + C_{1B_k}(2\cos(\beta_k) - 1) \quad (3.13) \\
v_{cs}(t_{0(k+1)}) &= A_{2B_k}(1 - \cos(\gamma_k)) + B_{2B_k} \sin(\gamma_k) + C_{2B_k}(\alpha_k - \beta_k + 2\sin(\beta_k))
\end{aligned}$$

$$+v_{cs}(t_{0(k)}) \quad (3.14)$$

$$v_{ct}(t_{0(k+1)}) = A_{3B_k}(1 - \cos(\gamma_k)) + B_{3B_k}\sin(\gamma_k) + C_{3B_k}(\alpha_k - \beta_k) \\ + 2.Z \frac{C_e}{C_t} C_{1B_k}\sin(\beta_k) + v_{ct}(t_{0(k)}) \quad (3.15)$$

### 3.3.3 Evaluation of $\alpha_k$ and $\beta_k$

Equation (3.1) relates the half period of the driving frequency to the sum of  $\alpha_k$  and  $\beta_k$ . Since the switching frequency is known, if  $\alpha_k$  can be determined,  $\beta_k$  can also be determined. For that another equation is required which comes from the fact that the parallel capacitor voltage  $v_{ct}$  is zero at time instant  $t_{1(k)}$ . Making use of (3.8) and substituting the values of  $A, B, C$  constants, we end up with a transcendental equation of the following form.

$$f.\sin(\alpha_k) + g.\cos(\alpha_k) = h \quad (3.16)$$

Solution of this equation yields the following result, which was also derived earlier in continuous time domain [12].

$$\alpha_k = l.\pi - \sin^{-1}\left(\frac{h}{\sqrt{f^2 + g^2}}\right) - \tan^{-1}\left(\frac{g}{f}\right) \quad (3.17)$$

Where  $l = 1$  for  $f_n$  (Normalized operating frequency)  $> 1$  and  $0$  for  $f_n < 1$

$$f = E(t_{0(k)})\sin(\gamma_k) \quad (3.18)$$

$$g = E(t_{0(k)})(1 + \cos(\gamma_k)) \quad (3.19)$$

$$h = g - Z.C_{1B_k}\sin(\gamma_k) + Z.I(t_{0(k)})(C_e/C_s)(\gamma_k/2)(g/E(t_{0(k)})) \quad (3.20)$$

Once determined, the value of  $\alpha_k$  can be substituted in (3.1) to give  $\beta_k$ .

### 3.3.4 The Output Equations

To consider the dynamic response of the SPRC it is necessary that the dynamic equations representing the output section of the SPRC be considered where the output current and voltage can no longer be considered constants (unlike in the steady state analysis).

Fig. 3.4 shows the output section of the SPRC. The non linear equations representing this section are:

$$I(t_{0(k+1)}) = I(t_{0(k)}) + 1/L_f \left[ \int_{t_{0(k)}}^{t_{0(k+1)}} |v_{ct}(\tau)| d\tau \right] - 1/L_f [v_0(t_{0(k)})(t_{0(k+1)} - t_{0(k)})] \quad (3.21)$$

$$v_0(t_{0(k+1)}) = v_0(t_{0(k)}) + \frac{(I(t_{0(k)}) - \frac{v_0(t_{0(k)})}{R_L})(t_{0(k+1)} - t_{0(k)})}{C_f} \quad (3.22)$$

The integration interval in (3.21) can be split into two. One being  $t_{0(k)}$  to  $t_{1(k)}$  and the other being  $t_{1(k)}$  to  $t_{0(k+1)}$ . Value of  $v_{ct}$  can then be substituted using (3.8) and (3.12) with an additional negative sign introduced for the interval B expression to account for the absolute value of  $v_{ct}$ . The following simplified expression is obtained.

$$\begin{aligned} I(t_{0(k+1)}) = & I(t_{0(k)}) + 1/X_{L_f} \cdot A_{3B_k} ((\beta_k - \alpha_k) + 2 \cdot \sin(\alpha_k) \\ & - \sin(\gamma_k)) + 1/X_{L_f} \cdot B_{3B_k} (2 \cdot \cos(\alpha_k) - 1 - \cos(\gamma_k)) \\ & - 1/2 X_{L_f} \cdot C_{3B_k} (\alpha_k - \beta_k)^2 + 2 \cdot Z/X_{L_f} (C_e/C_t) C_{1B_k} (1 - \cos(\beta_k)) \\ & + 1/X_{L_f} \cdot v_{ct}(t_{0(k)}) (\beta_k - \alpha_k) - 1/X_{L_f} \cdot v_0(t_{0(k)}) \gamma_k \end{aligned} \quad (3.23)$$

where  $X_{L_f} = \omega_0 L_f$ .

### 3.3.5 Peak Component Stresses

#### Peak Inductor Current

It can be shown that the peak inductor current is given by:

$$i_{L(\text{peak})} = -i_L(t_{0(k)}), -(v_{cs}(t_{0(k)}) + v_{ct}(t_{0(k)})) < E(t_{0(k)}), i_L(t_{0(k)}) < 0 \quad (3.24)$$

$$= (A_{1A_k}^2 + B_{1A_k}^2)^{1/2} + C_{1A_k},$$

$$-(v_{cs}(t_{0(k)}) + v_{ct}(t_{0(k)})) > E(t_{0(k)}), i_L(t_{0(k)}) > 0 \quad (3.25)$$

### Peak Series Capacitor Voltage

The voltage  $v_{cs}$  will be at its peak when the inductor current is zero. The value of the angle at which this will happen, can be found out by equating (3.6) or (3.10) to zero, depending upon whether it is lagging or leading power factor mode of operation. This yields the following:

$$\theta_{cspk} = -\sin^{-1}[C_{1B_k}/(A_{1B_k}^2 + B_{1B_k}^2)^{1/2}] - \tan^{-1}(B_{1B_k}/A_{1B_k}), i_L(t_{0(k)}) < 0 \quad (3.26)$$

$$= \pi + \sin^{-1}[C_{1A_k}/(A_{1A_k}^2 + B_{1A_k}^2)^{1/2}] - \tan^{-1}(B_{1A_k}/A_{1A_k})$$

$$i_L(t_{0(k)}) > 0 \quad (3.27)$$

This value can then be substituted in (3.7) or (3.11) to obtain the maximum series capacitor voltage.

### Peak Parallel Capacitor voltage

The peak parallel capacitor voltage occurs at the following angle.

$$\theta_{ctp_k} = \pi + \sin^{-1}[C_{3A_k}/(A_{3A_k}^2 + B_{3A_k}^2)^{1/2}] - \tan^{-1}(B_{3A_k}/A_{3A_k})$$

$$i_L(t_{0(k)}) < -I(t_{0(k)}) \quad (3.28)$$

$$= -\sin^{-1}[C_{3B_k}/(A_{3B_k}^2 + B_{3B_k}^2)^{1/2}] - \tan^{-1}(B_{3B_k}/A_{3B_k})$$

$$i_L(t_{0(k)}) > -I(t_{0(k)}) \quad (3.29)$$

These values can then be substituted in (3.8) or (3.12), depending on the mode of operation, to obtain the peak parallel capacitor voltage.

## 3.4 The Discrete State-Space Model

### 3.4.1 Selection of Discrete State Variables

The following discrete state variables were chosen (corresponding to the energy storage elements in the circuit) to arrive at the discrete state-space model with reference to Fig. 3.2.

For  $k^{\text{th}}$  event:

$$x_{1(k)} = -i_L(t_{0(k)}) \quad (3.30)$$

$$x_{2(k)} = -v_{cs}(t_{0(k)}) \quad (3.31)$$

$$x_{3(k)} = -v_{ct}(t_{0(k)}) \quad (3.32)$$

For the  $(k+1)^{\text{th}}$  event, these variables get redefined as:

$$x_{1(k+1)} = i_L(t_{0(k+1)}) \quad (3.33)$$

$$x_{2(k+1)} = v_{cs}(t_{0(k+1)}) \quad (3.34)$$

$$x_{3(k+1)} = v_{ct}(t_{0(k+1)}) \quad (3.35)$$

Apart from the above three, two additional discrete state variables were introduced for the output section of the SPRC.

$$x_{4(k)} = I(t_{0(k)}) \quad (3.36)$$

$$x_{5(k)} = v_o(t_{0(k)}) \quad (3.37)$$

for the  $k^{\text{th}}$  event. It must be pointed out here that the same choice of state variables will hold for the below resonance operation also, except that the signs will have to be reversed in (3.30) and (3.33).

### 3.4.2 Formulation of the Model

Using the state variables just introduced and incorporating them in equations (3.13) to (3.15) and (3.22), (3.23) the following discrete state-space model was obtained.

$$x_{1(k+1)} = A_{1B_k} \cdot \sin(\gamma_k) + B_{1B_k} \cdot \cos(\gamma_k) + C_{1B_k} (2\cos(\beta_k) - 1) \quad (3.38)$$

$$x_{2(k+1)} = A_{2B_k} (1 - \cos(\gamma_k)) + B_{2B_k} \sin(\gamma_k) + C_{2B_k} (\alpha_k - \beta_k + 2\sin(\beta_k)) - x_{2(k)} \quad (3.39)$$

$$x_{3(k+1)} = A_{3B_k} (1 - \cos(\gamma_k)) + B_{3B_k} \sin(\gamma_k) + C_{3B_k} (\alpha_k - \beta_k) + 2Z \frac{C_e}{C_t} C_{1B_k} \sin(\beta_k) - x_{3(k)} \quad (3.40)$$

$$x_{4(k+1)} = x_{4(k)} + 1/X_{Lf} \cdot A_{3B_k} ((\beta_k - \alpha_k) + 2 \cdot \sin(\alpha_k) - \sin(\gamma_k)) + \frac{1}{X_{Lf}} \cdot B_{3B_k} (2 \cdot \cos(\alpha_k) - 1 - \cos(\gamma_k)) - \frac{1}{2X_{Lf}} \cdot C_{3B_k} (\alpha_k - \beta_k)^2 + \frac{2Z}{X_{Lf}} \frac{C_e}{C_t} C_{1B_k} (1 - \cos(\beta_k)) - \frac{1}{X_{Lf}} \cdot x_{3(k)} (\beta_k - \alpha_k) - \frac{1}{X_{Lf}} \cdot x_{5(k)} \gamma_k \quad (3.41)$$

$$x_{5(k+1)} = x_{5(k)} + \gamma_k X_{Cf} (x_{4(k)} - \frac{x_{5(k)}}{R_L}) \quad (3.42)$$

Where  $X_{Cf} = \frac{1}{\omega_0 C_f}$ . This completes the formulation of the discrete state-space model represented by equations (3.38) through (3.42). These are non linear discrete equations and are of the following general form.

$$x_{i(k+1)} = f_i(x_{1(k)}, x_{2(k)}, x_{3(k)}, x_{4(k)}, x_{5(k)}, \gamma_k, E(t_{0(k)})) \quad (3.43)$$

Where “ $f_i$ ” represents some non-linear function and  $i = 1 \dots 5$ .

### 3.4.3 The Steady State

During the steady state.

$$x_{i(k)} = x_{i(k+1)} \quad (3.44)$$

Applying this condition to equations (3.38) to (3.42), and then solving the equations simultaneously, the following steady-state expressions are obtained.

$$\begin{aligned} x_{1(k)} = & -(E(t_{0(k)})/Z).sin(\gamma_k)/(1 + cos(\gamma_k)) - (C_e/C_t).I(t_{0(k)}) \\ & + (C_e/C_t).I(t_{0(k)}).[cos(\alpha_k) + cos(\beta_k)]/(1 + cos(\gamma_k)) \end{aligned} \quad (3.45)$$

$$\begin{aligned} x_{2(k)} = & Z.I(t_{0(k)})(C_e/C_s)(C_e/C_t)[sin(\beta_k) - sin(\alpha_k)]/(1 + cos(\gamma_k)) \\ & - Z.(C_e/C_t)(C_e/C_s).I(t_{0(k)}).(\gamma_k - 2\alpha_k)/2 \end{aligned} \quad (3.46)$$

$$\begin{aligned} x_{3(k)} = & Z.I(t_{0(k)})(C_e/C_t)^2[sin(\beta_k) - sin(\alpha_k)]/(1 + cos(\gamma_k)) \\ & + Z.(C_e/C_t)(C_e/C_s).I(t_{0(k)}).(\gamma_k - 2\alpha_k)/2 \end{aligned} \quad (3.47)$$

And similarly for the output current and voltage.

$$x_{4(k)} = I(t_{0(k)}) \quad (3.48)$$

$$x_{5(k)} = (2/\gamma_k)(C_e/C_t)E(t_{0(k)}).(\frac{-sin(\gamma_k/2 - \alpha_k)}{cos(\gamma_k/2)} + (\gamma_k/2 - \alpha_k)) \quad (3.49)$$

The subscript "k" may be dropped from the above steady-state expressions for obvious reasons. These steady-state solutions are same as those derived in continuous time domain, in [12].

### 3.5 Design of the Converter

An SPRC has been designed using the procedure given in [12], to illustrate the use of discrete time domain model, derived earlier, for predicting the large-signal behavior of the converter. Design is done for the worst case loading conditions i.e. for maximum load current with minimum input voltage. At the rated design conditions given below, the converter operates in lagging power factor mode of operation. The SPRC designed has the following specifications:

Input supply voltage,  $V_{smin}(= 2E) = 50 \text{ V}$ .

Output voltage of the converter,  $V_0 = 24 \text{ V}$ .

Output voltage ripple,  $V_{0(p-p)} = \pm 0.025$  V.

Output current ripple,  $I_{p-p} = \pm 0.010$  A.

Maximum output power,  $P_o = 100$  Watts.

Switching frequency,  $f_t = 200$  kHz.

The design values obtained are:

Normalized load current,  $J = \frac{I}{(E/Z)} = 4.3$  p.u.;  $n = 1$ .

$L = 17.74\mu H$  ;  $C_s = 0.047\mu F$  ;  $C_t = n^2 C'_t = 0.047\mu F$ .

The rated load resistance is,  $R'_L = 6.0$   $\Omega$ .

Using the second harmonic component, values of the filter components for the given ripple specifications are:  $L_f \approx 1000$   $\mu H$ ; and  $C_f \approx 1$   $\mu F$ .

## 3.6 Results of the Analysis

The discrete time domain model described in sections 3.3 and 3.4 was used in predicting the transient behavior of the designed converter operating under open loop conditions. PRO-MATLAB was used to solve the discrete time domain equations on the computer. These results are also verified using SPICE software. Results obtained for four types of step changes in the operating conditions of the converter are presented below. It must be noted that in all the plots, the step change in the operating condition takes place at the origin.

### 3.6.1 Sudden Switching ON of the Supply Voltage

Fig. 3.5(a) shows the initial stage of the transient phase caused by switching ON the input dc supply to the converter. These waveforms show a leading power factor operation during the initial phase although the converter is designed to operate in lagging power factor mode during steady state. Figs. 3.5(b) and (c) show the

inductor current and parallel capacitor voltage during the entire transient phase. As can be noticed from these figures, the resonating inductor doesn't have to undergo additional stress during the transients and hence the steady-state design specifications are sufficient. But the parallel capacitor voltage experiences an overshoot of almost 1 p.u. and hence the rating should be carefully chosen in case of an open loop operation.

Figs. 3.5(d) and (e) show the SPICE plots corresponding to Figs. 3.5(b) and (c). There is a good agreement between the transient behavior predicted by the model and SPICE results. The effect of below resonance operation during the transient phase is shown in Fig. 3.5(f), which shows that the anti-parallel diode peak current is much higher during the transient phase as compared to its steady-state value. Fig. 3.6(a) shows plots of the variation in peak component stresses during the transients. Fig. 3.6(b) shows how the discrete state variables vary during the transient phase. The point marked "CO" (cross over) on Fig. 3.6(b) symbolizes the time instant where the lagging power factor operation of the converter is restored. It can be seen from these plots that the converter takes about five hundred microseconds to reach the steady state. This is a direct consequence of putting a large filter inductor at the output. As is shown later, a smaller value results in a faster response. The output variables (output current and voltage) defined as state variables  $x_4$  and  $x_5$ , are plotted in Fig. 3.6(c) obtained from the discrete model and SPICE. It can be seen once again that the results are quite close.

When the converter supply is switched OFF, the circuit variables behave as shown in Figs. 3.7(a) and (b). The tank current shows a smooth exponential decay without additional stresses. The output variables too show a similar trend. It is observed that just like during the switching ON, in this case also, the anti-parallel diodes have to undergo an additional peak current stress. This fact is illustrated in Fig. 3.7(c). It was observed that the converter alternates between leading and lagging power factor

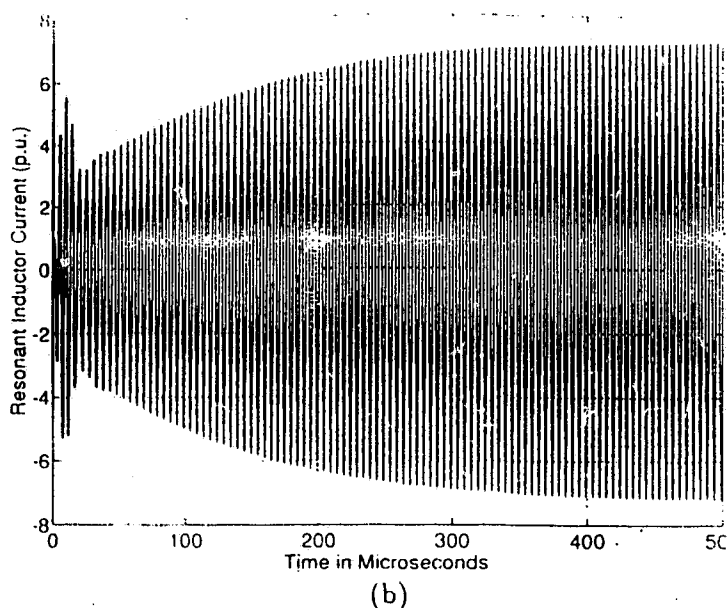
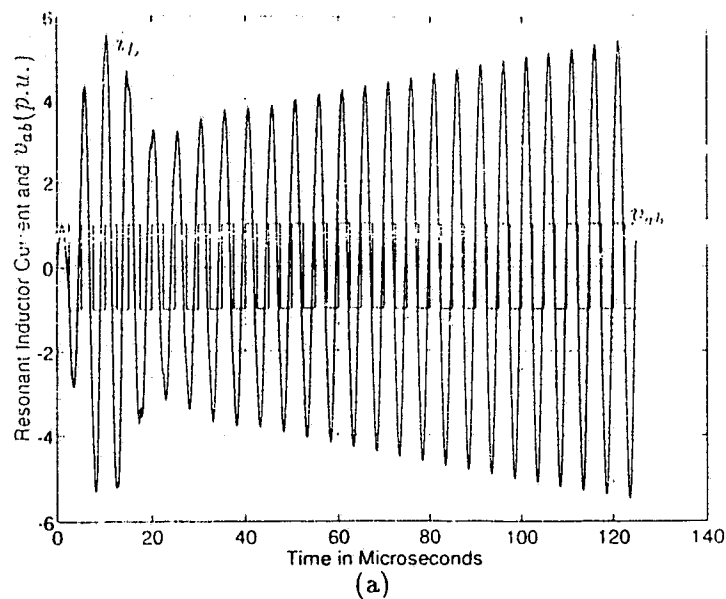


Figure 3.5: Transient waveforms caused by switching ON the input supply to the converter. Resonant inductor current during (a) the very initial transient phase and (b) the entire transient phase. (c) Parallel capacitor voltage during the transient phase. (d), (e) SPICE plots corresponding to (b) and (c). (f) Peak anti-parallel diode current.

Note: Component values used correspond to the design example and  $L_f = 1000 \mu H$

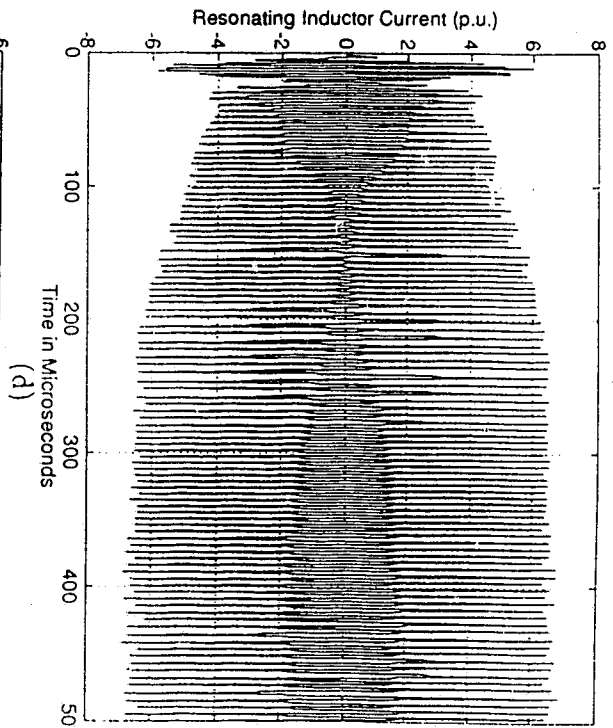
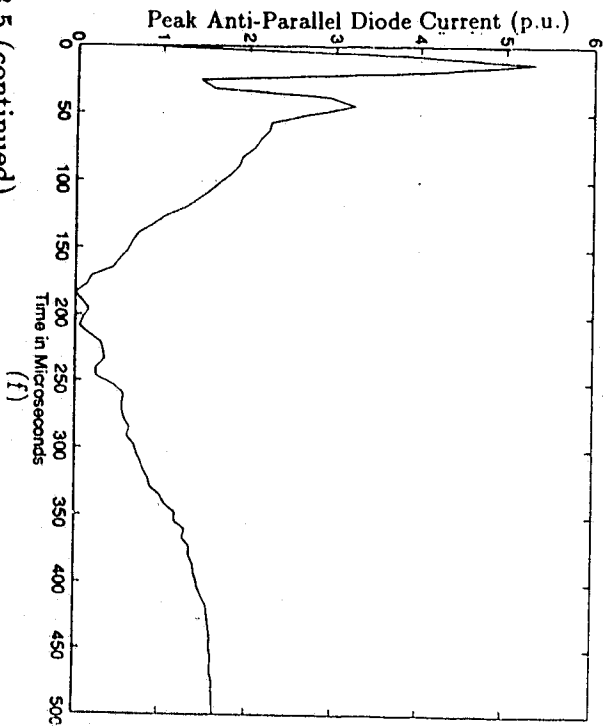
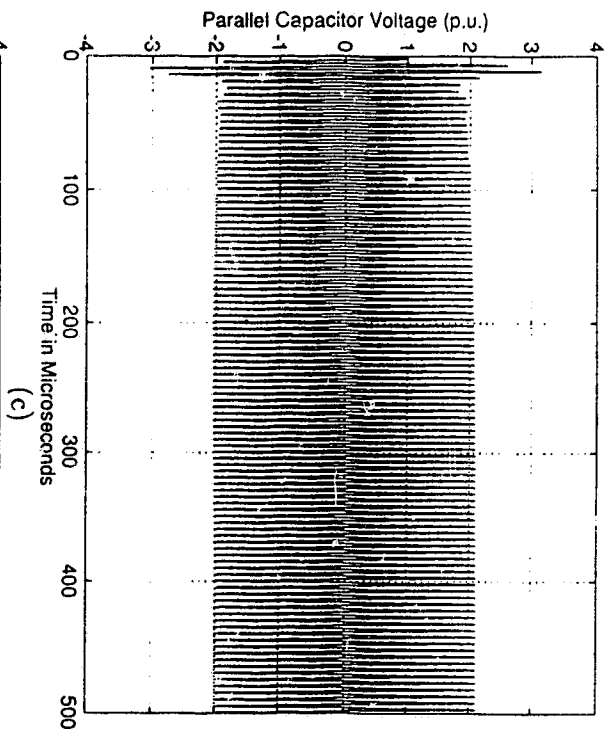
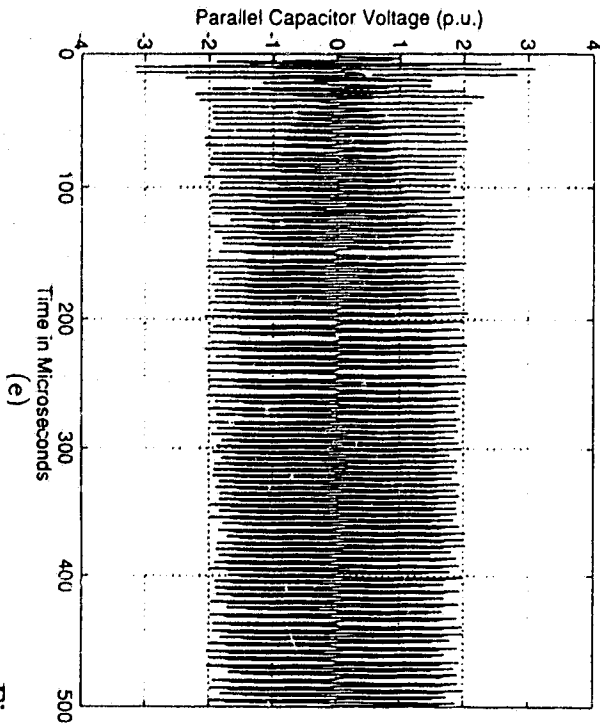


Fig. 3.5 (continued)

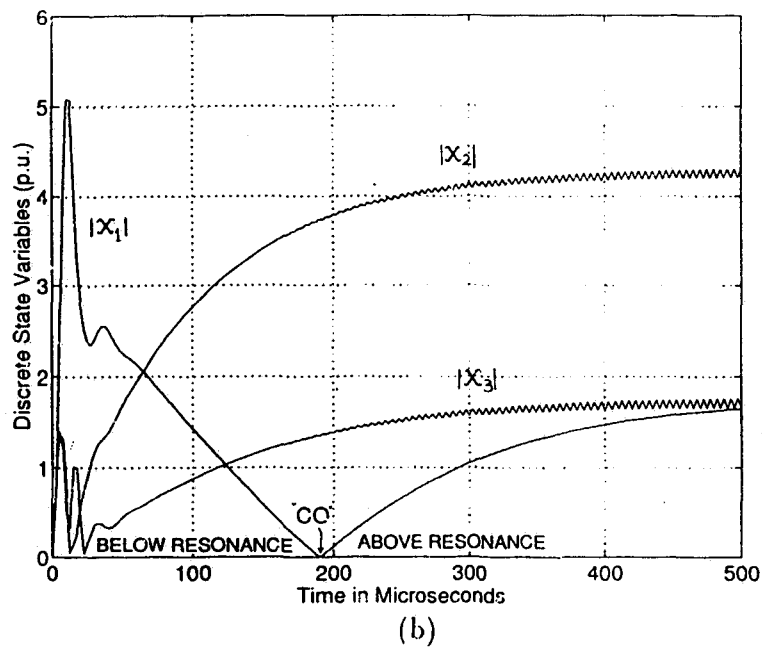
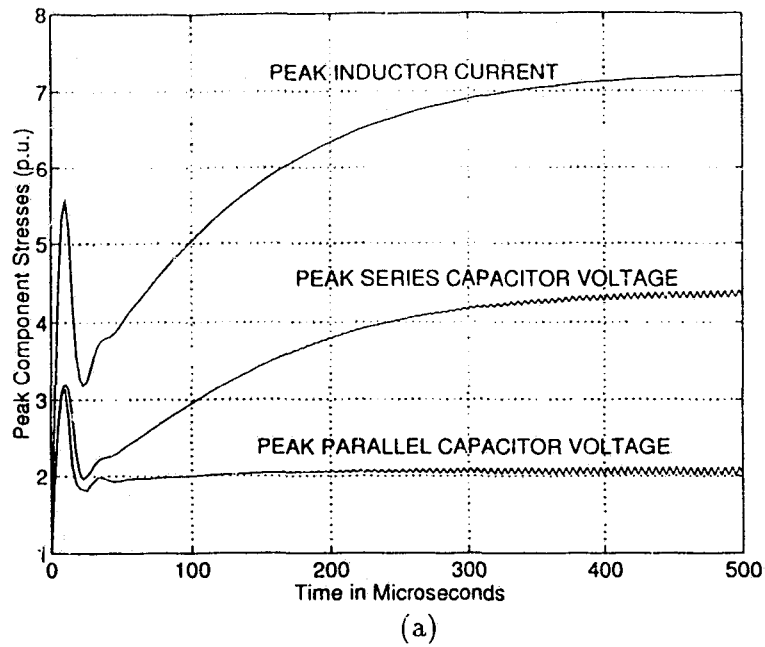


Figure 3.6: Switching ON transients continued.

(a) Peak component stresses as obtained from the model. (b) The discrete state (tank) variables as obtained from the model. (c) Output state variables. In (c), SPICE results are also plotted.

Note: All these plots have been obtained with discrete set of points obtained one per half cycle, and connected to give an over all continuous picture. Further, the step change in the operating condition occurs at origin in all the plots.

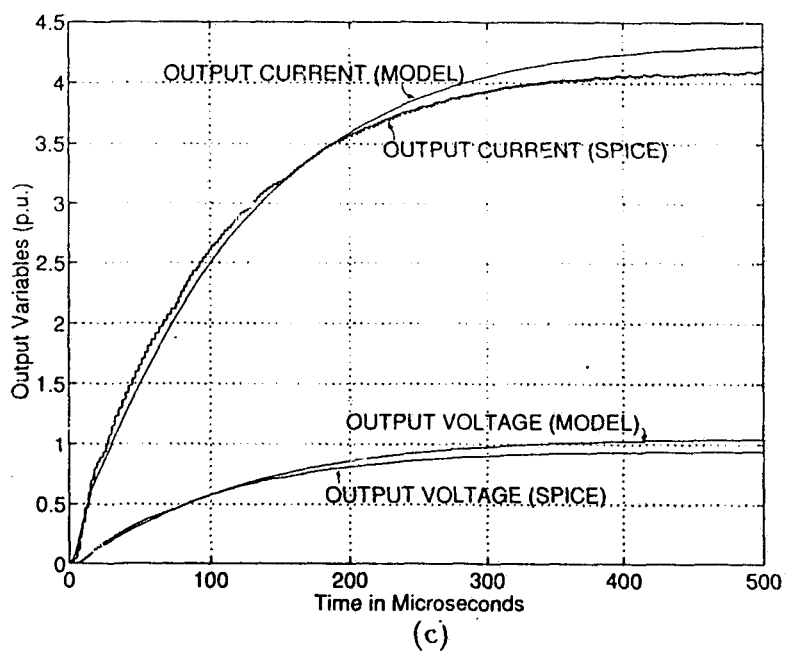
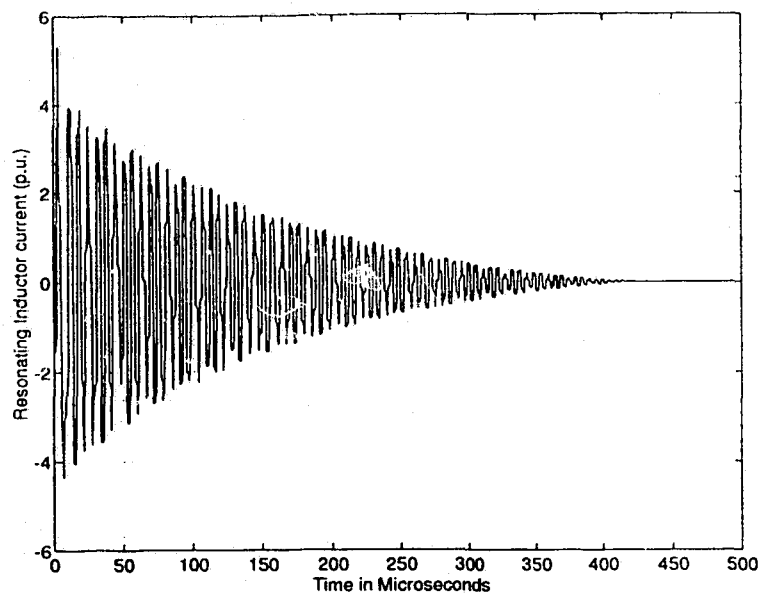
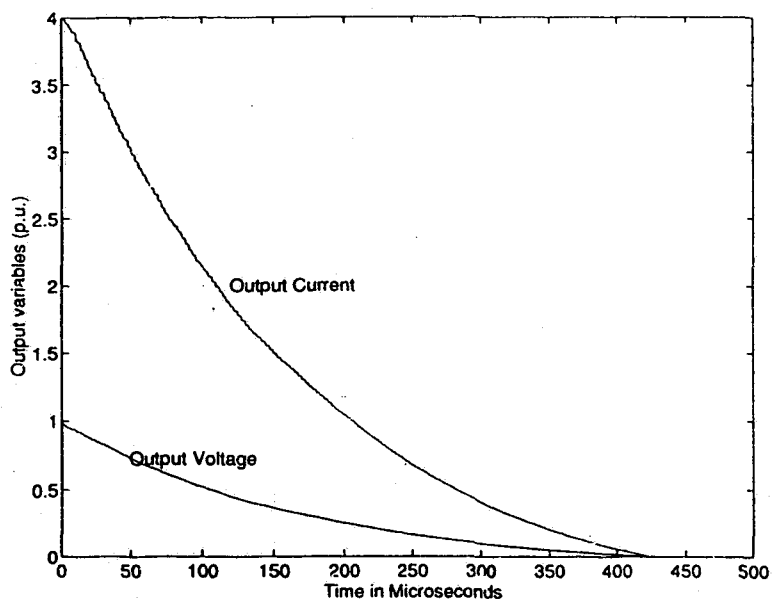


Fig. 3.6 (continued)



(a)



(b)

Figure 3.7: Switch OFF transients: (a) The resonating inductor current. (b) Output variables. (c) Peak anti-parallel diode current.

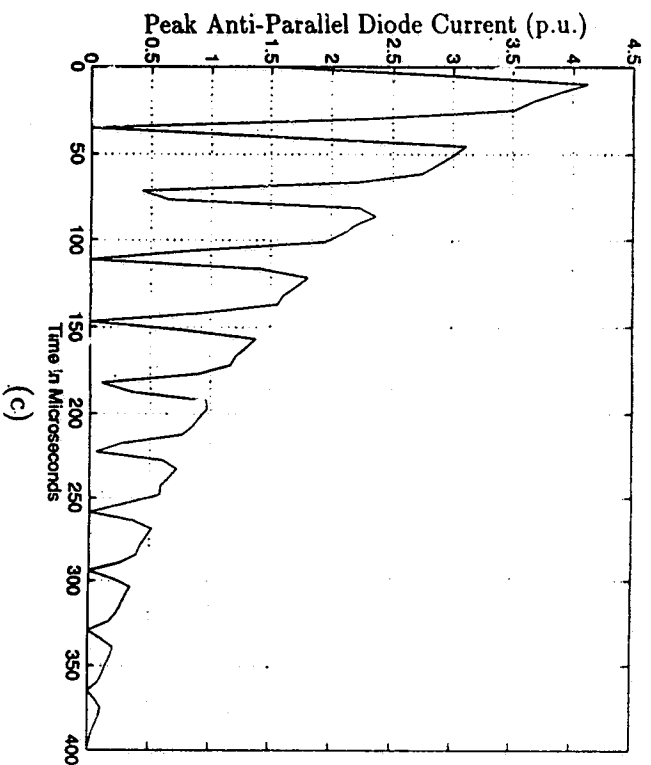


Fig. 3.7 (continued)

(c)

mode of operation till it is completely switched off.

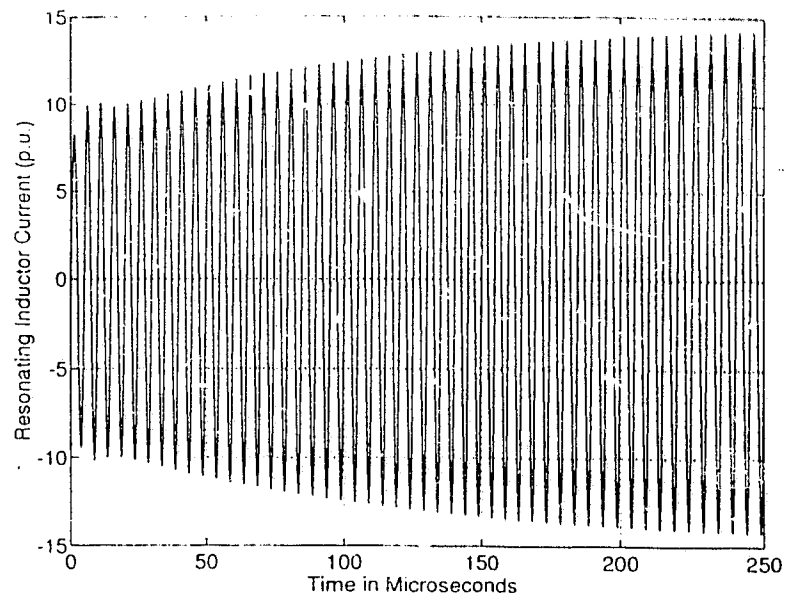
### 3.6.2 Step Change in Input Supply Voltage

Effect of input voltage variation, when input voltage is changed from 1 p.u. to 2 p.u., is shown in this section. Fig. 3.8(a) shows effect of this disturbance on the tank current, which smoothly settles to a new steady-state value in about 250  $\mu$ s.

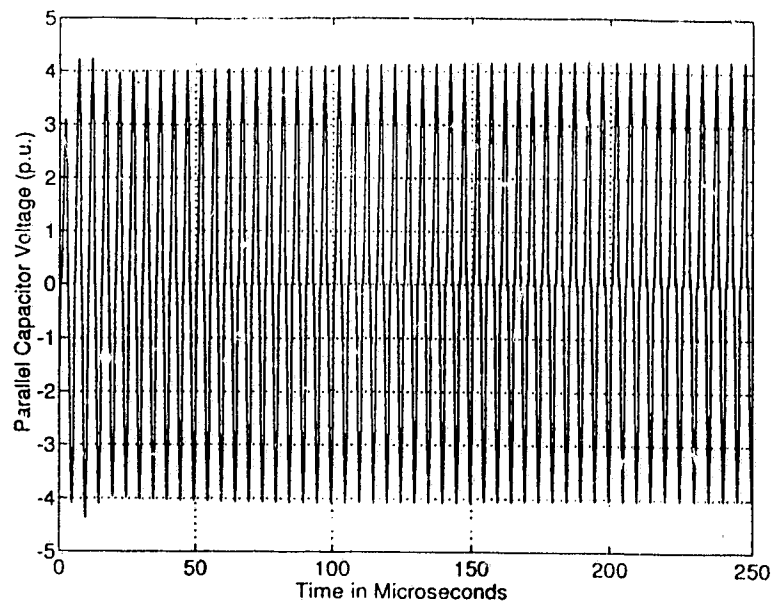
The transient waveform given in Fig. 3.8(b) shows the variation of the parallel capacitor voltage. Figs. 3.8(c) and (d) show the corresponding SPICE plots. The peak component stresses are plotted in Fig. 3.9. The peak parallel capacitor voltage plot shows that the capacitor experiences approximately 5 percent more stress than the new steady-state stress. But since normally some higher margin is given while selecting components, this over stressing can be ignored. The tank state variables are plotted in Fig. 3.10(a). The figure shows that the converter temporarily enters the below resonance mode of operation before recovering back at point "CO". Fig. 3.10(b) compares the plots of the output state variables obtained from the model and SPICE.

### 3.6.3 Step Change in Operating Frequency

An example is considered where the operating frequency is given a step increment of 10 kHz. This variation is sufficient to cause non-linear transients. At the same time, this alteration doesn't alter the basic mode of operation shown in Fig. 3.2. Figs. 3.11(a) to (d) show the inductor current and parallel capacitor voltage variation from model and SPICE. Fig. 3.12 shows the peak stresses as obtained with the model. As can be seen from these plots there are no appreciable additional stresses on the components during this kind of transients. Figs. 3.13(a) and (b) show the variation

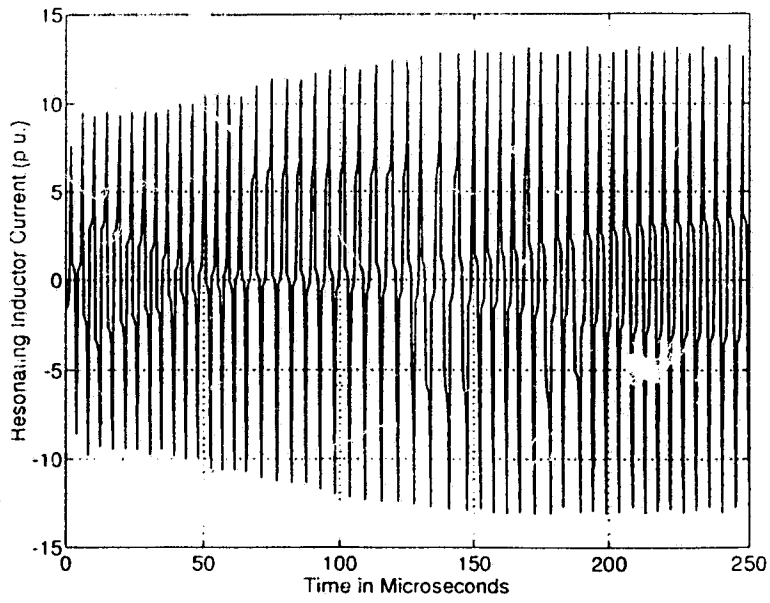


(a)

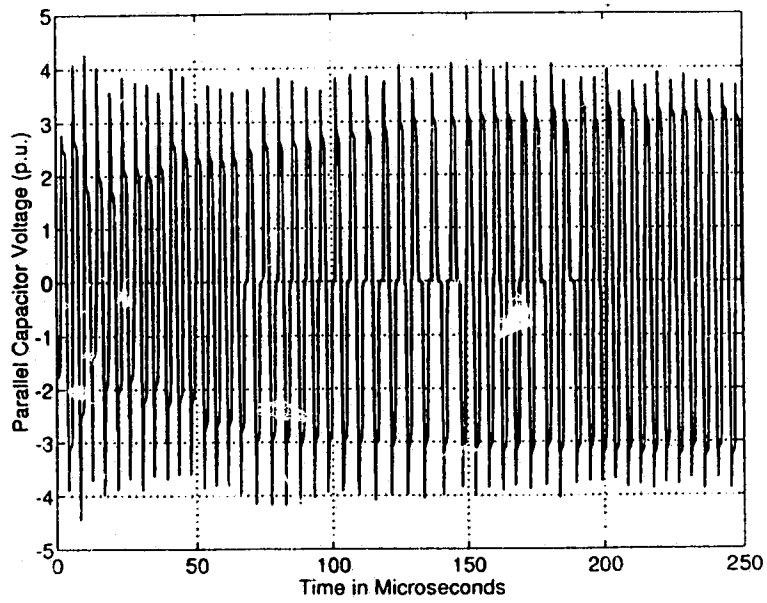


(b)

Figure 3.8: Results for step change in input supply voltage from 25V to 50V: (a) Resonant inductor current during the transient phase. (b) Parallel capacitor voltage during the transient phase. (c),(d) SPICE plots corresponding to (a) and (b) respectively.



(c)



(d)

Fig. 3.8 (continued)

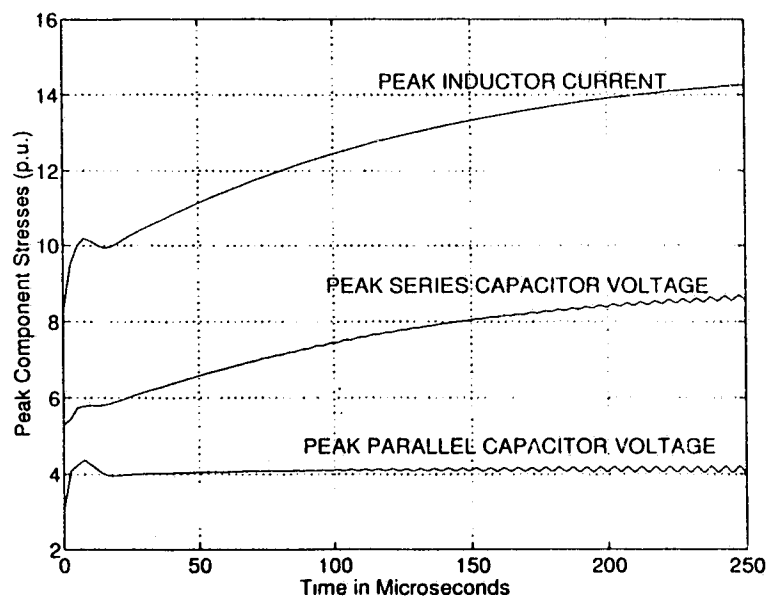
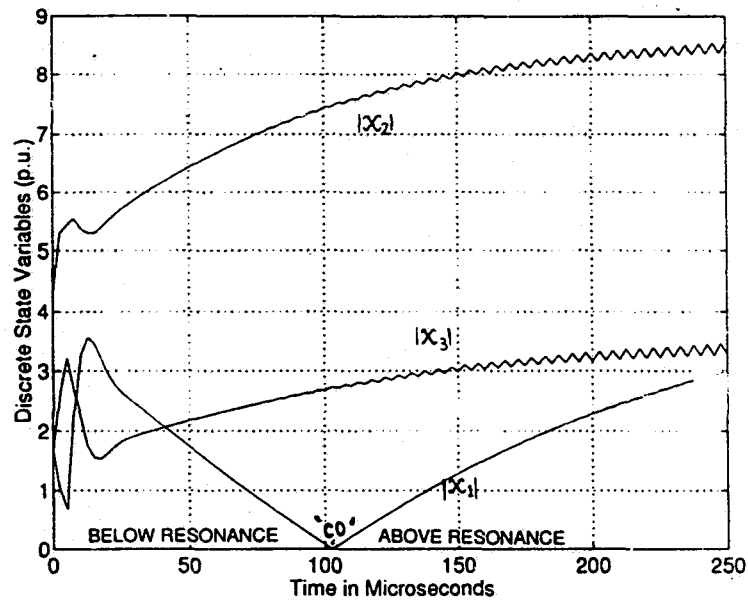
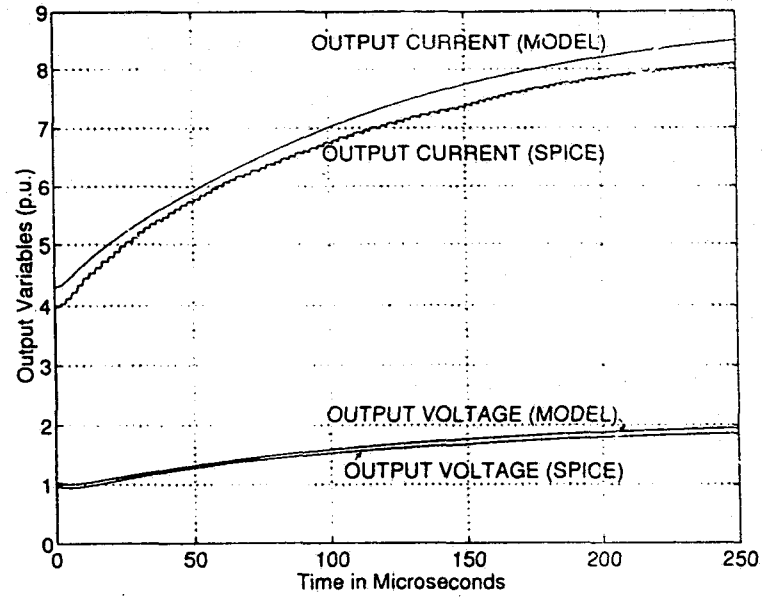


Figure 3.9: Peak component stresses for step change in the input voltage.



(a)



(b)

Figure 3.10: Variation in state variables for step change in the input voltage. (a) Tank state variables. (b) Output state variables. In (b), the SPICE results are also included for the sake of comparison.

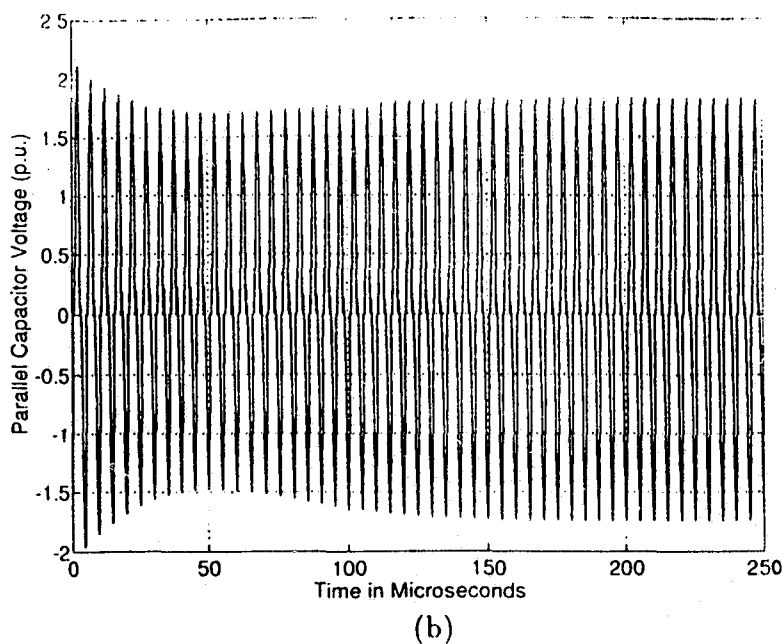
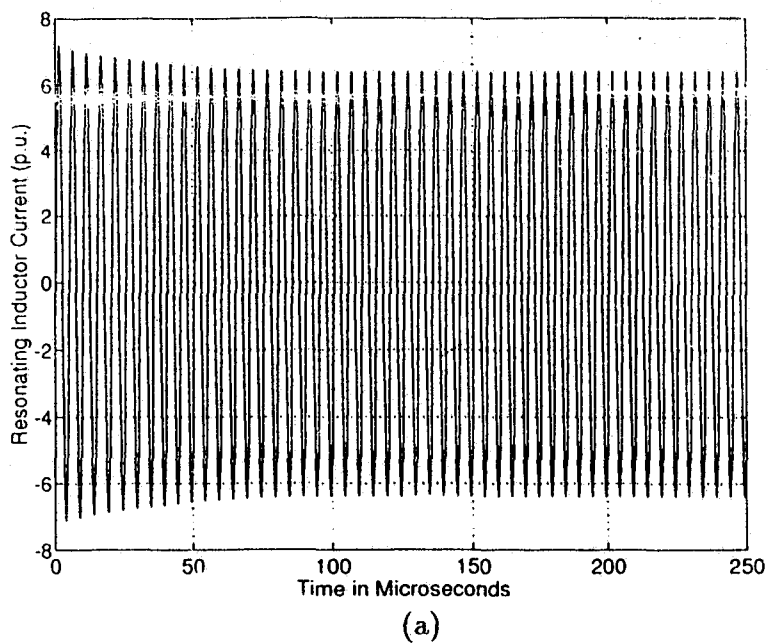


Figure 3.11: Results obtained for a sudden change in the operating frequency from 200 kHz to 210 kHz. (a) Resonant inductor current. (b) Parallel capacitor voltage. (c), (d) SPICE plots corresponding to (a) and (b).

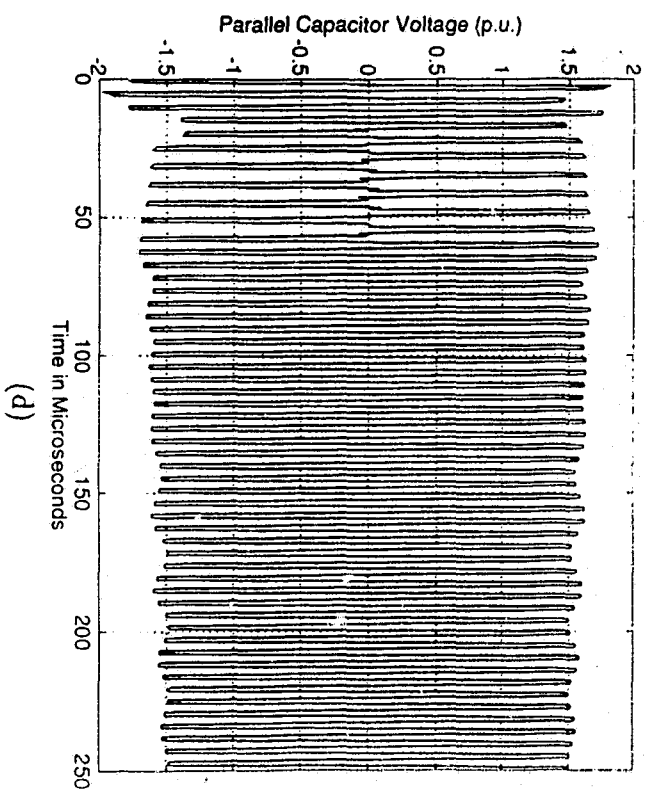
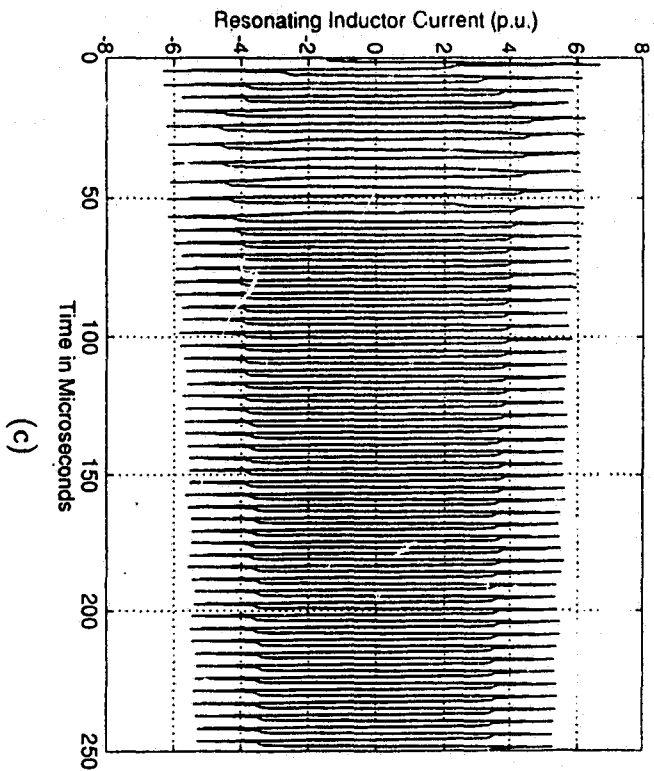


Fig. 3.11 (continued)

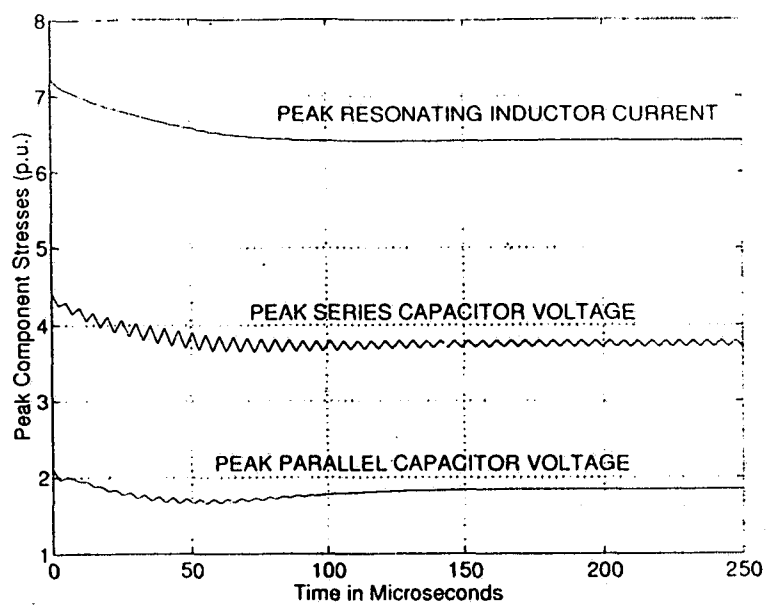


Figure 3.12: Peak component stresses as obtained from the model due to variation in frequency.

of the state variables.

### 3.6.4 Step Change in Load

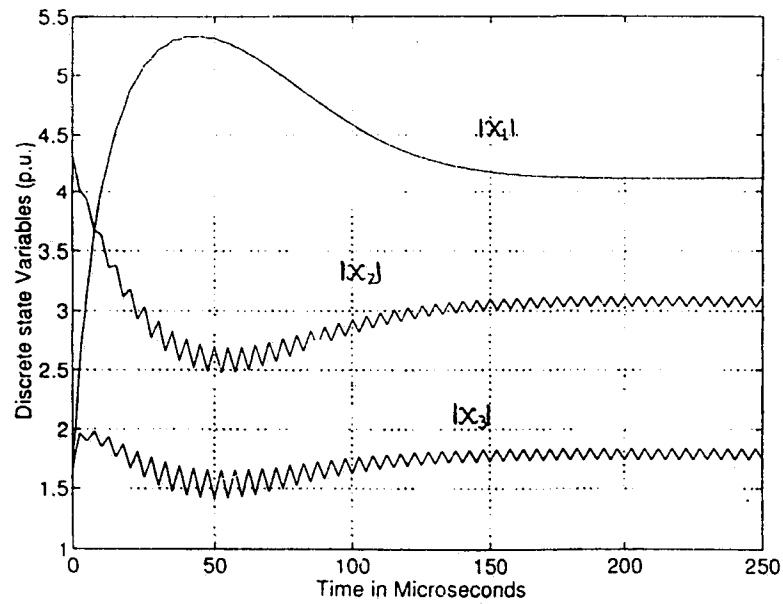
The loading conditions of the converter may change suddenly subject to external factors. This sudden change is bound to cause transients. Here, three examples are considered.

#### **Eg. 1: Load current is suddenly halved (load resistance doubled)**

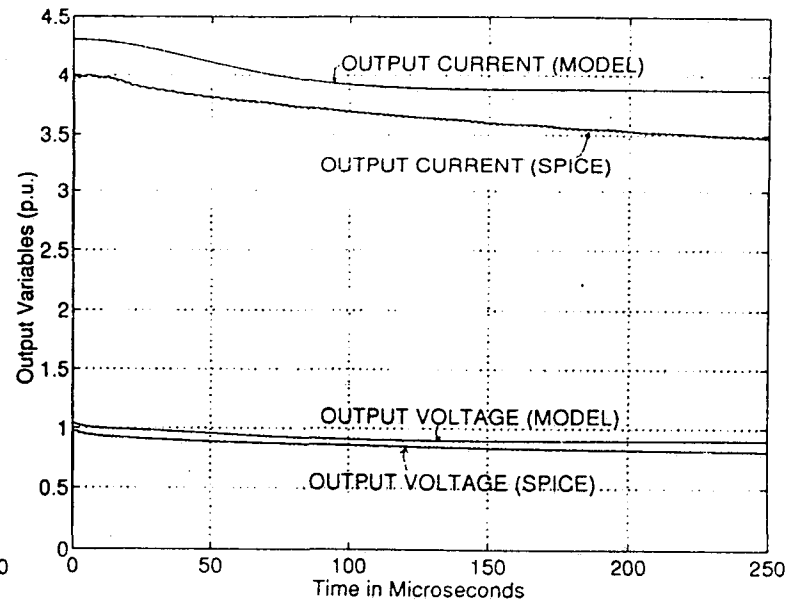
Figs. 3.14(a) and (b) show the variation of the inductor current and the parallel capacitor voltage during the transient phase. The parallel capacitor voltage experiences a small variation. However, the resonating inductor current shows a large variation. Figs. 3.14(c) and (d) show the SPICE plots corresponding to 3.14(a) and (b). Peak stresses have been plotted in Fig. 3.15(a). Unlike the parallel capacitor voltage, the series capacitor voltage shows a large variation. The plots of state variables are given in Figs. 3.15(b) and (c). Fig. 3.15(b) shows that the converter enters below resonance mode. Fig. 3.15(c) shows that the output voltage shoots up to nearly twice the steady state value. Therefore the voltage rating of the output filter capacitor and diodes must be carefully chosen. The output current on the other hand doesn't show any over shoot because of the presence of a large filter inductor.

#### **Eg. 2: Step Change from Full Load to Open Circuit Condition**

From practical point of view, an open circuit condition at the output is very important. The proposed model was used to study the effect of a step change in the load from full load to near open circuit condition. Figs. 3.16(a) and (b) show the variation of the tank current and the parallel capacitor voltage under sudden open circuit conditions. The current waveforms show a marked drop in the peak value before settling down to a new steady-state value. The parallel capacitor voltage shows an additional stress of about 0.5 p.u. for nearly 50  $\mu$ s before settling down to its steady-state value.

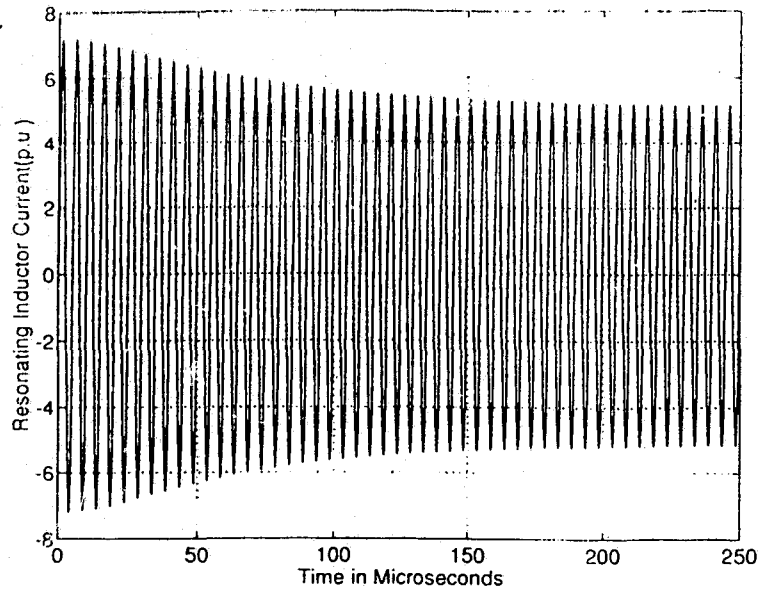


(a)

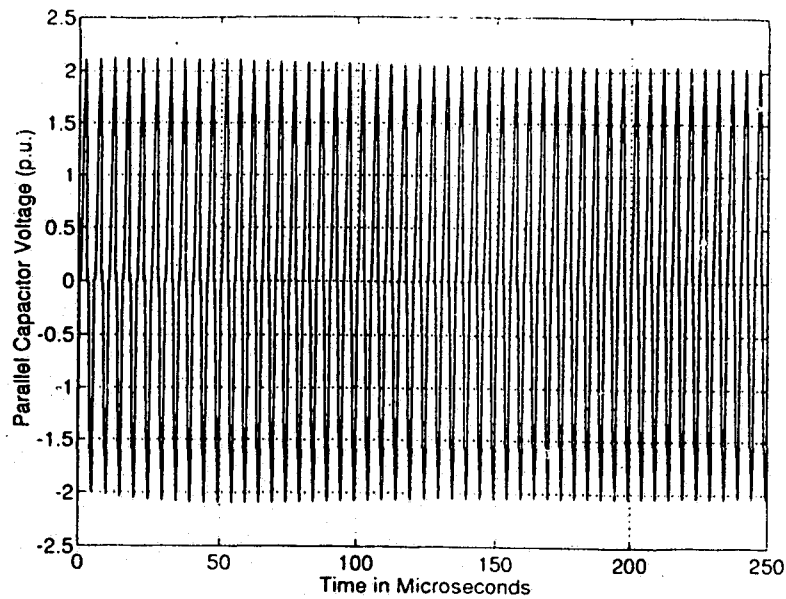


(b)

Figure 3.13: Discrete state variables for step change in the operating frequency. (a) Tank state variables. (b) Output state variables. In (b), SPICE results are also included for comparison.

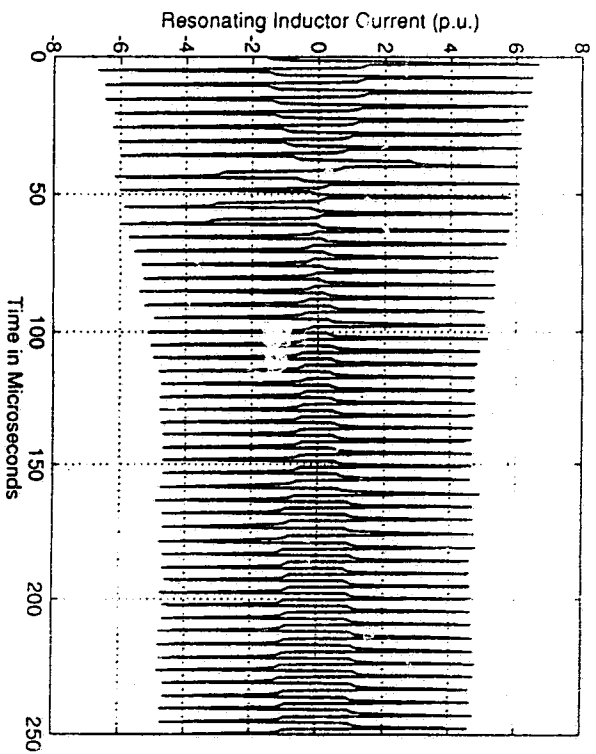


(a)

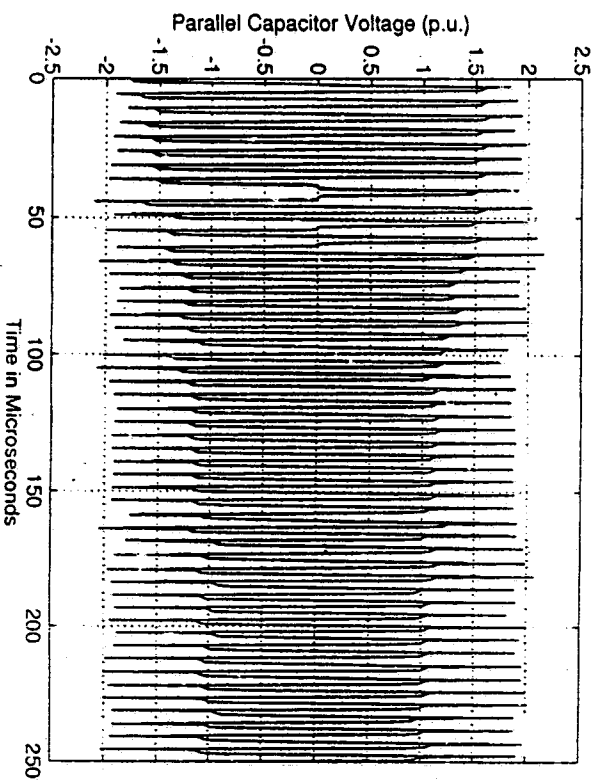


(b)

Figure 3.14: Results obtained for a step change in load resistance to twice the rated value. (a) Resonant inductor current. (b) Parallel capacitor voltage during the transient phase. (c),(d) SPICE plots corresponding to 314(a) and (b) respectively.



(c)



(d)

Fig. 3.14 (continued)

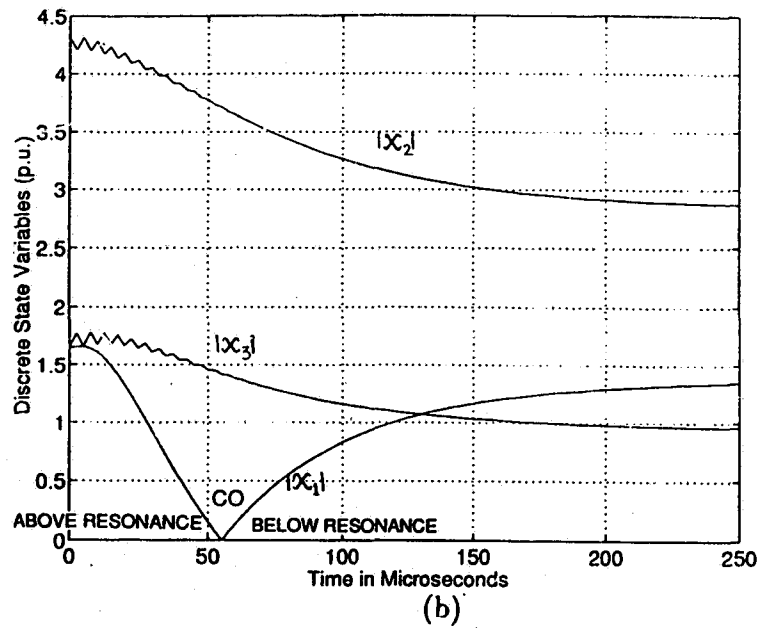
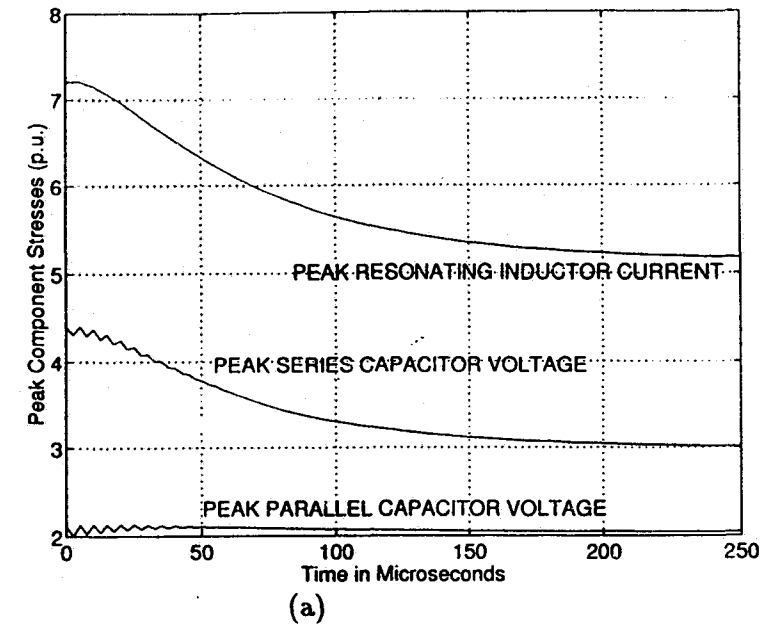


Figure 3.15: (a) Peak component stresses as obtained from the model due to step change in load. (b) The discrete state (tank) variables. (c) Output state variables. In (c), SPICE results are also included for comparison.

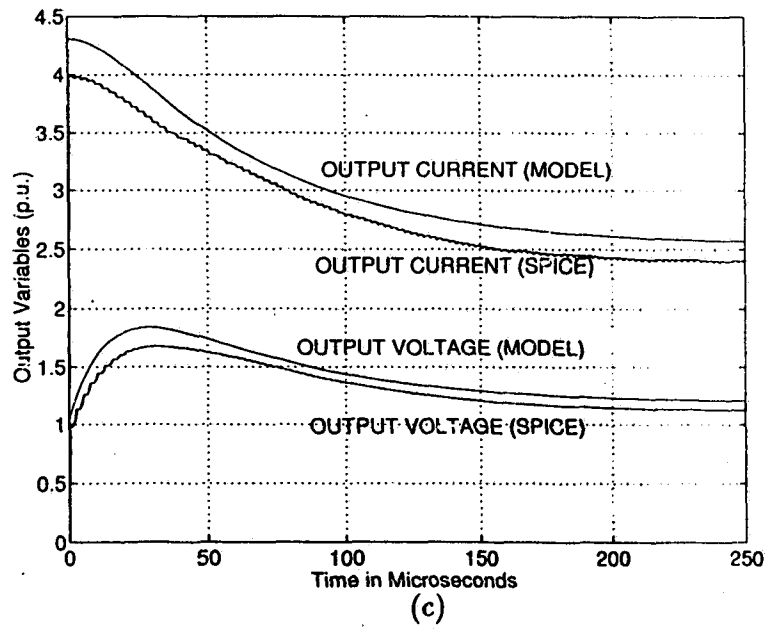


Fig. 3.15 (continued)

Fig. 3.16(c) shows that the converter enters leading p.f. (below resonance) mode of operation. The plot of output variables in Fig. 3.16(d) shows that the current takes about  $50 \mu s$  to reduce to near zero value (it is not exactly zero because of the presence of a high value bleeder resistance). This is affected by the value of the filter inductor. It must be pointed out that the output voltage increases in the absence of a closed loop frequency control.

**Eg. 3: Step Change from Full Load to Short Circuit Condition**

SPICE was used to study this effect as the proposed model can not be applied in this case. This is because under these conditions, the duration for which all the diodes in the output bridge rectifier get shorted (causing more discontinuity in the parallel capacitor voltage), is increased causing operating waveforms that are significantly different from those shown in Fig. 3.2. Fig. 3.17(a) shows how the tank current appears just after a short circuit has been induced. There is an additional over stress of about 2 p.u. for about  $180 \mu s$ , before it attains the steady-state value. It has been observed that the lagging p.f. mode of operation is maintained during the short circuit conditions. In Fig. 3.17(b), the parallel capacitor voltage drops to zero in about  $180 \mu s$ . The output current settles down to a new higher value which is determined by the short circuit resistance. But the load current doesn't shoot up suddenly due to a large filter inductor at the output. It is shown in section 3.7, that many disadvantages of the open loop operation can be overcome by operating the converter in a closed loop manner.

### 3.6.5 Effect of the Output Filter

Define the characteristic impedance of the output filter [76] as:

$$Z_f = \sqrt{\frac{L_f}{C_f}} \quad (3.50)$$

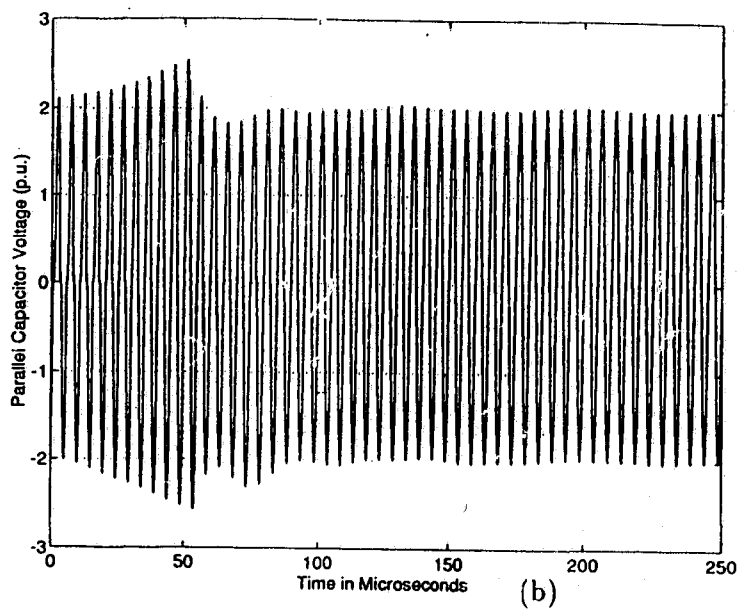
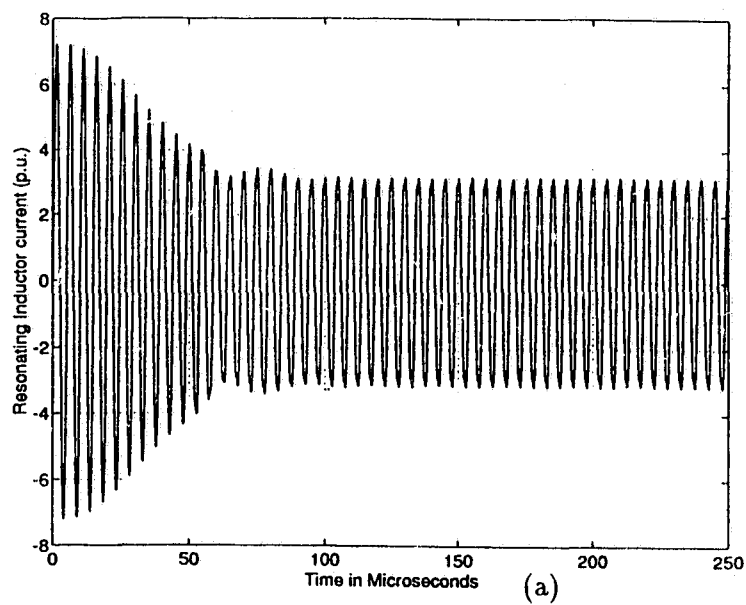
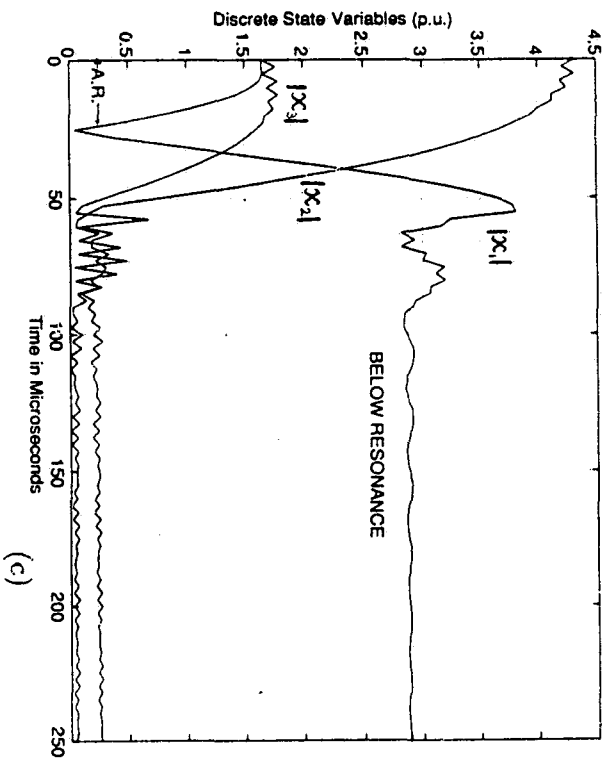
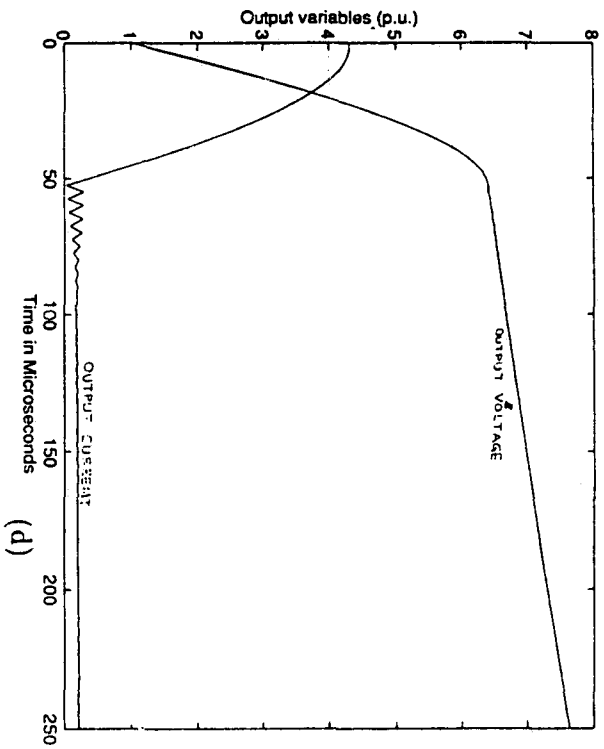


Figure 3.16: Transient waveforms during the step change in load from full load to open circuit condition. (a) Resonating inductor current. (b) Parallel capacitor voltage. (c), (d) Discrete state variables.



(c)



(d)

Fig. 3.16 (continued)

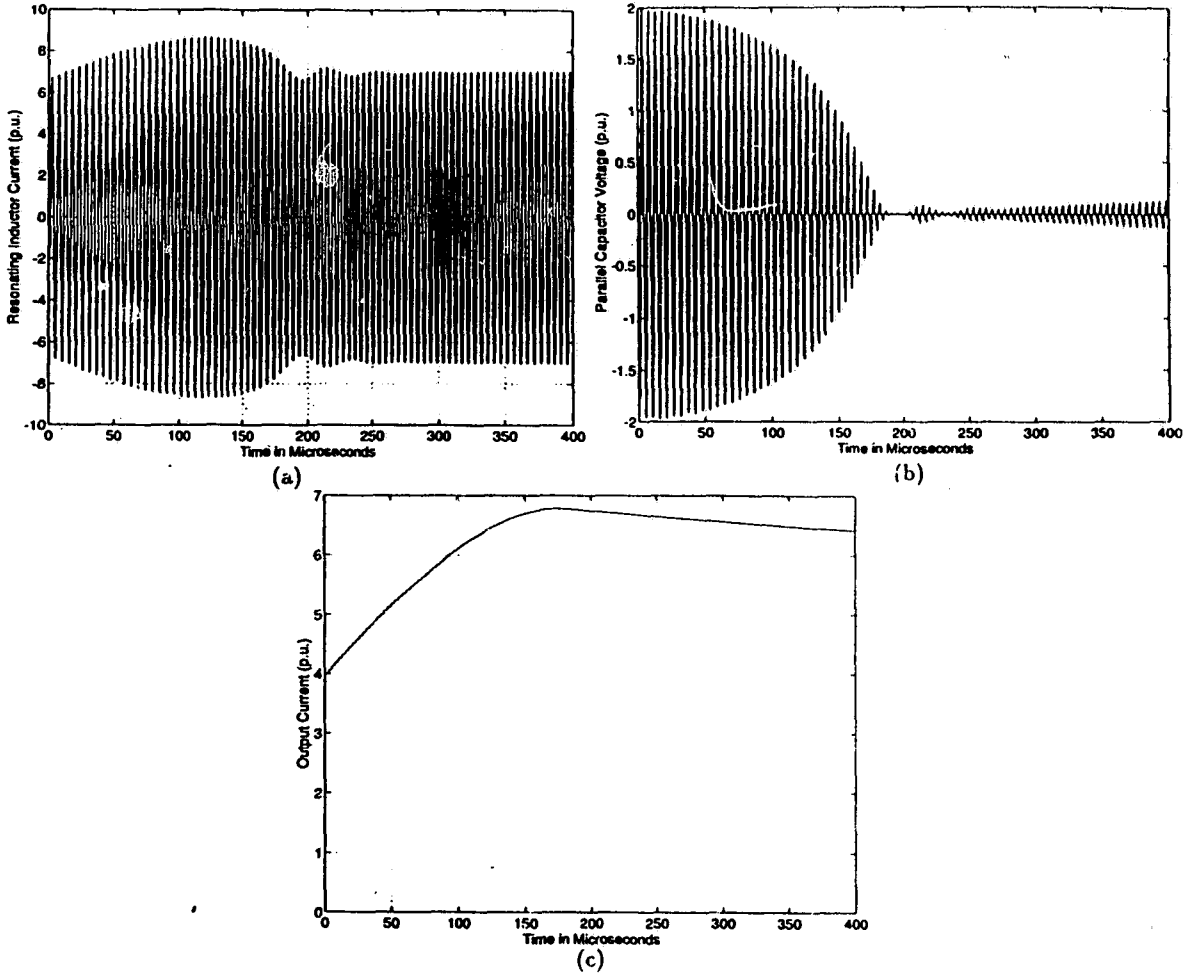


Figure 3.17: Transient waveforms during the step change in load from full load to short circuit condition. (a) Resonating inductor current. (b) Parallel capacitor voltage. (c) Output Current.

The response of the converter is affected by this value. The proposed model has been used to show the effect of  $Z_f$  on the converter response at the time of switching ON. Two different values  $L_f$  ( $1000 \mu H$  and  $300 \mu H$ ) were used corresponding to  $Z_{f1}$  and  $Z_{f2}$ . Results have been obtained for different values of  $Z_{f1}$  and  $Z_{f2}$  corresponding to different values of filter capacitor. Fig. 3.18(a) shows variation of peak resonant current for different values of  $Z_{fi}$ 's. The response becomes faster and the peak goes higher as  $Z_f$  is decreased (either by decreasing  $L_f$  or by increasing  $C_f$ ). Fig. 3.18(b) on the other hand shows that, the peak parallel capacitor voltage during the transient phase decreases with a decrease in the value of  $L_f$  and is independent of  $C_f$  for a given value of  $L_f$ . Fig. 3.18(c) shows the state response of the converter corresponding to tank current. The time instants at which the converter "crosses over" from below resonance (leading p.f. mode) to above resonance (lagging p.f. mode) mode of operation are marked as CO1, CO2 etc. It can be seen that the lagging power factor mode of operation is restored faster as the value of  $L_f$  is decreased. Fig. 3.18(d) shows a similar trend in the speed of response. The output voltage response for different values of  $Z_f$  are plotted in Fig. 3.18(e). It is clear that there is a trade off between the peak component stresses and the transient response time with respect to the output filter design, which is normally done according to ripple specifications of the output quantities. Most suitable filter component values can be chosen based on the specifications of peak stresses, transient response time and output ripple. The curves presented in this section can be used for this purpose.

### 3.7 Experimental Results

An experimental converter was built, whose specifications are given in section 3.5. This set up was used to verify the results of theory. Figs 3.19 - 3.22 show

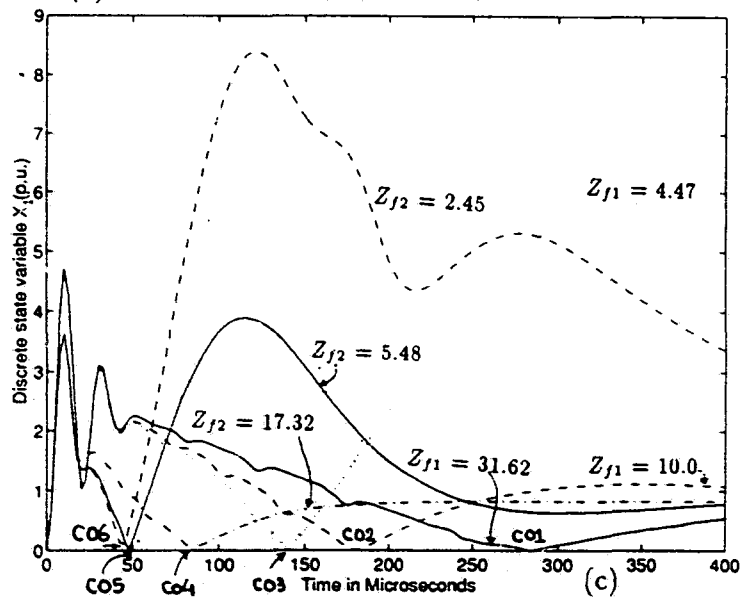
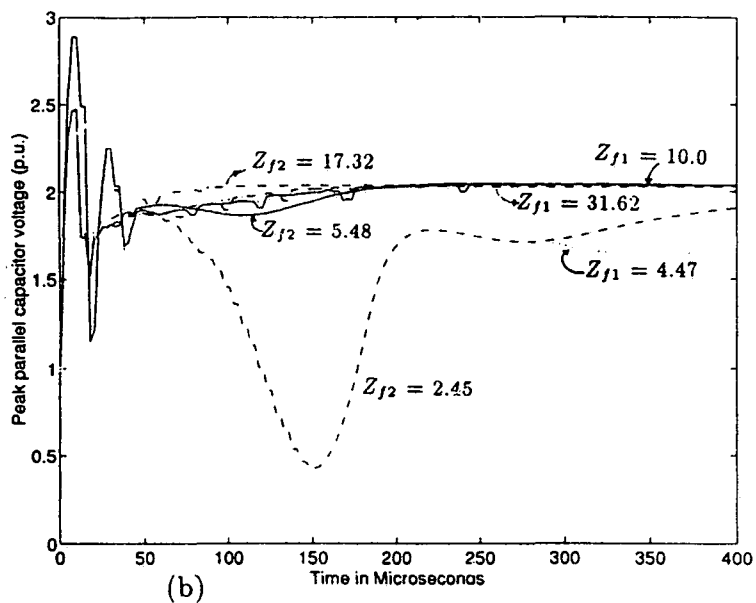
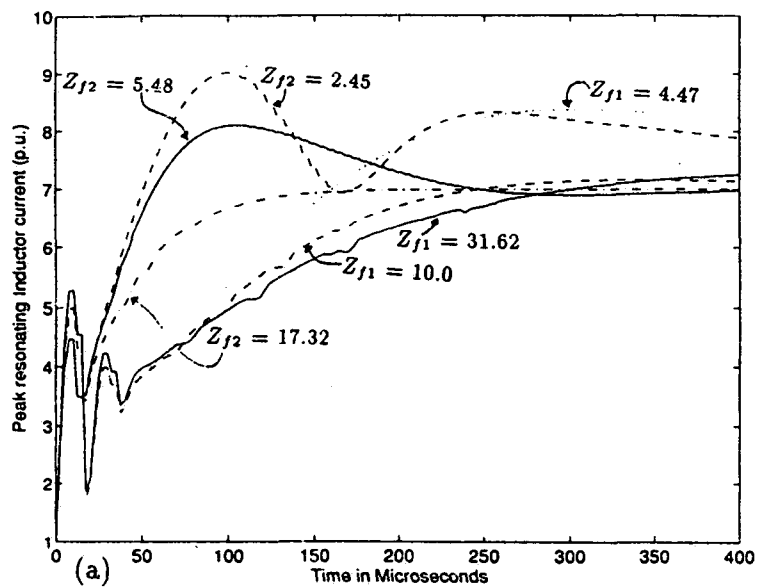


Fig.3.18 Effect of the characteristic impedance of the output filter section on the response of the converter during switching ON.

(a),(b) The peak resonating inductor current and the parallel capacitor voltage.

Discrete state variables

(c)  $x_1$  corresponding to tank current.

(d)  $x_3$  corresponding to parallel capacitor voltage.

(e)  $x_5$  corresponding to output voltage.

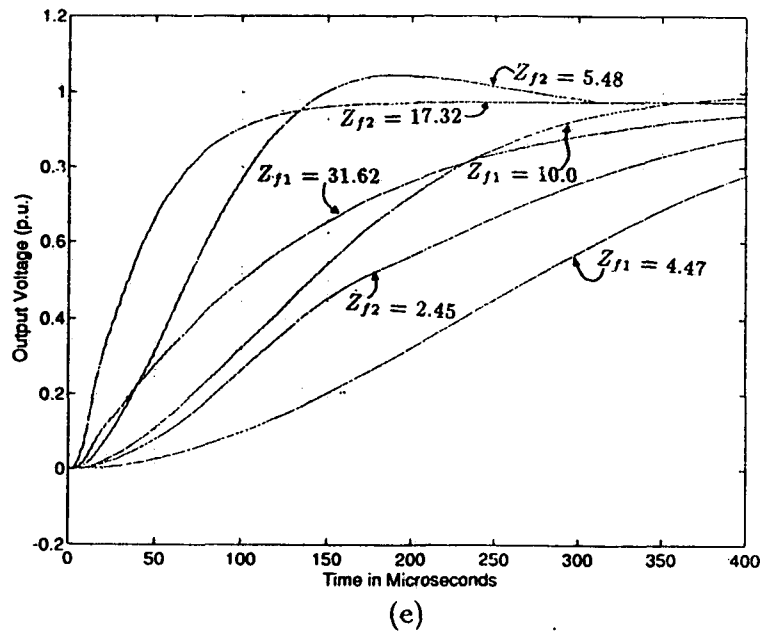
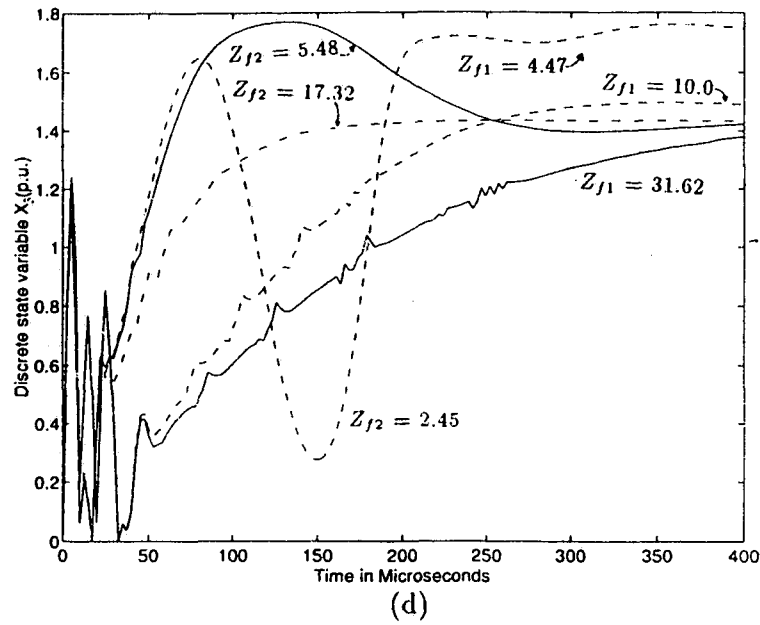


Fig. 3.18 (continued)

the experimental plots corresponding to the analytical plots of section 3.6. All the experimental waveforms are reasonably close to those obtained from theory. However, some deviation in the values is expected as the drops and losses have been neglected in the theoretical analysis.

As was stated in section 3.6.4, many drawbacks of the open loop operation can be overcome when the converter is operated in closed loop fashion. Fig 3.22(d) shows the waveforms of output voltage along with those of  $v_{ab}$  and  $i_L$ , in the event when the load current is reduced to 50 % full load value in a step manner. Contrary to the open loop result of Fig. 3.15(b), it is observed that the converter does not enter the “below resonance” mode of operation due to the corrective action of the controller on the operating frequency. The operating frequency goes up to prevent the output voltage from going up. It was observed that the converter enters discontinuous capacitor voltage mode during this phase. It can also be seen that the peak tank current is also reduced due to the closed loop control. This peak rises gradually to its new (lower) steady-state value when the converter recovers from the transient condition.

### **3.8 Discontinuous Current Mode (DCM)**

In this section, a discrete time domain model for the LCC-type parallel resonant converter, operating in discontinuous current mode (DCM) has been derived. All the equations representing the discrete time domain model are given. This model is useful in predicting some of the basic design constraints (peak component stresses etc.), which are governed by the dynamics of the converter during transients. However, due to the presence of three interval operating mode, the analysis is more complex than the CCM case and numerical solution is required. The analytical results, obtained using PRO-MATLAB are discussed and verified by SPICE simulation and experiments.

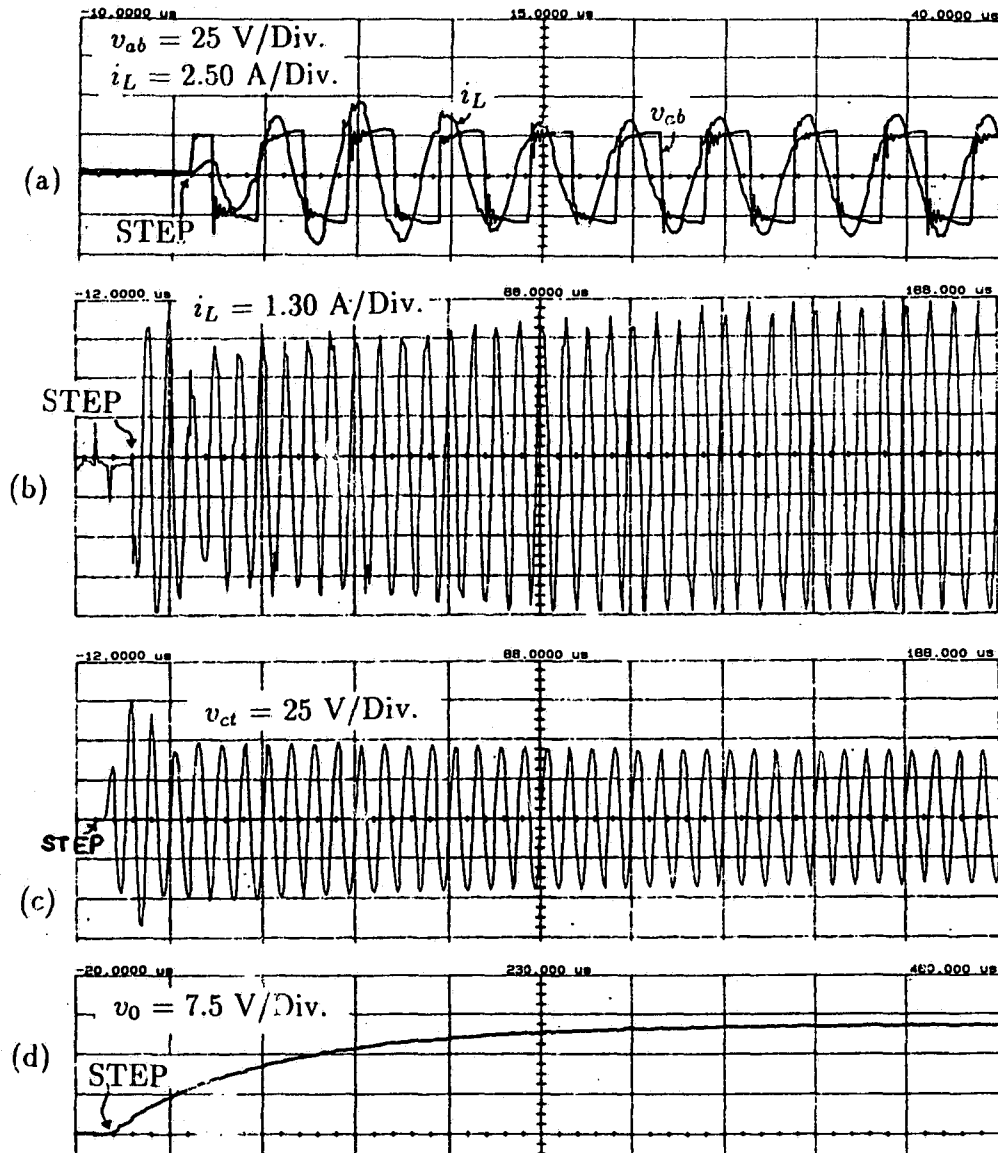


Figure 3.19: Experimental waveforms during the transients caused by switching ON the dc supply of the converter (0 to 25 Volts). The instant where the step change occurs is shown by an arrow.: (a) The very initial stage of the resonant inductor current. This Figure corresponds to Fig. 5(a). (b) Resonating inductor current during the entire transient phase. (c) Parallel capacitor voltage during the transient phase. (d) Output voltage. Details of the converter:  $L_s = 17.74 \mu\text{H}$ ;  $C_s = 0.047 \mu\text{F}$ ;  $C_t = 0.047 \mu\text{F}$ ;  $C_f = 1 \mu\text{F}$ ;  $L_f = 1000 \mu\text{H}$ ; Input dc voltage,  $2E = 50$  Volts; Switches used: IRF 640 MOSFET's

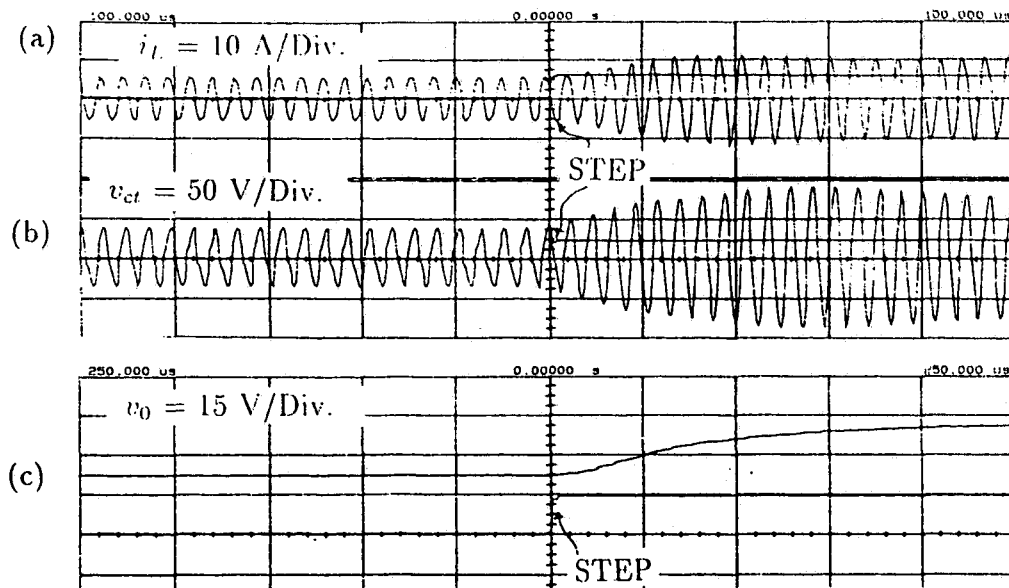


Figure 3.20: Experimental waveforms during the transients caused by a step change in the input supply from 25 Volts to 50 Volts: (a) Resonant inductor current. (b) Parallel capacitor voltage. (c) Output voltage.

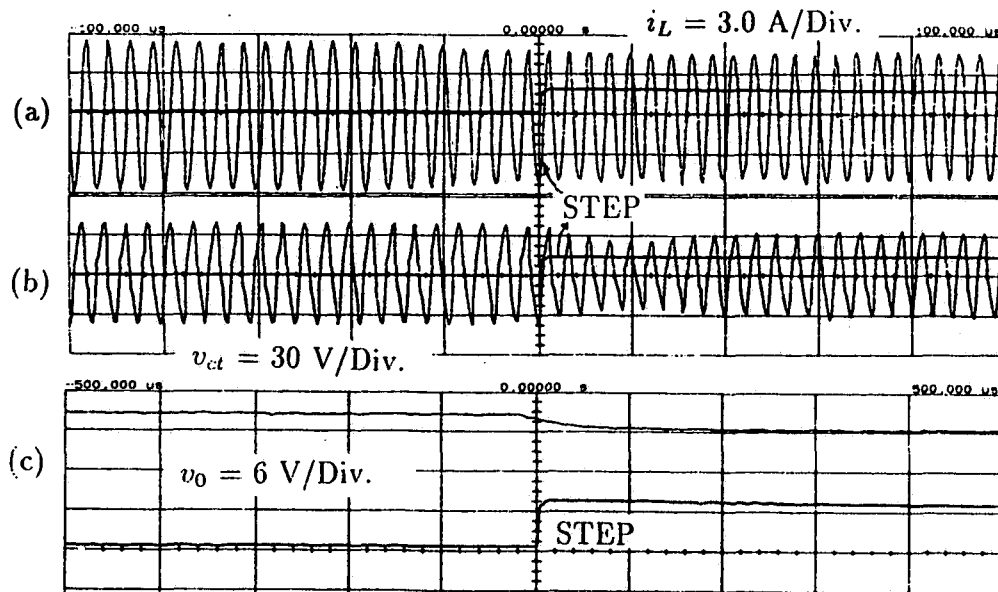


Figure 3.21: Experimental waveforms during the transients caused by a step change in the operating frequency from 200 kHz to 210 kHz. (a) Resonant inductor current. (b) Parallel capacitor voltage. (c) Output voltage.

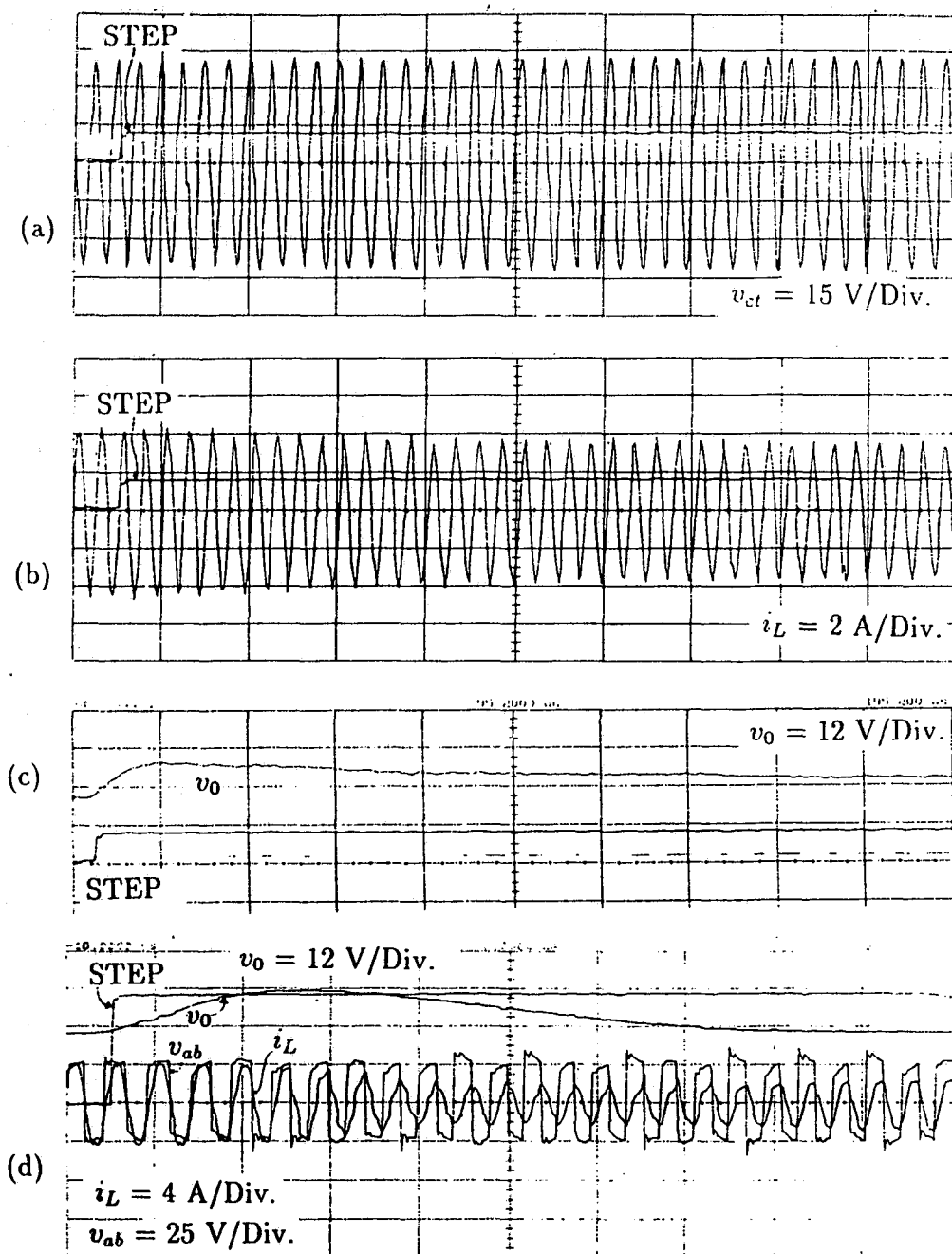
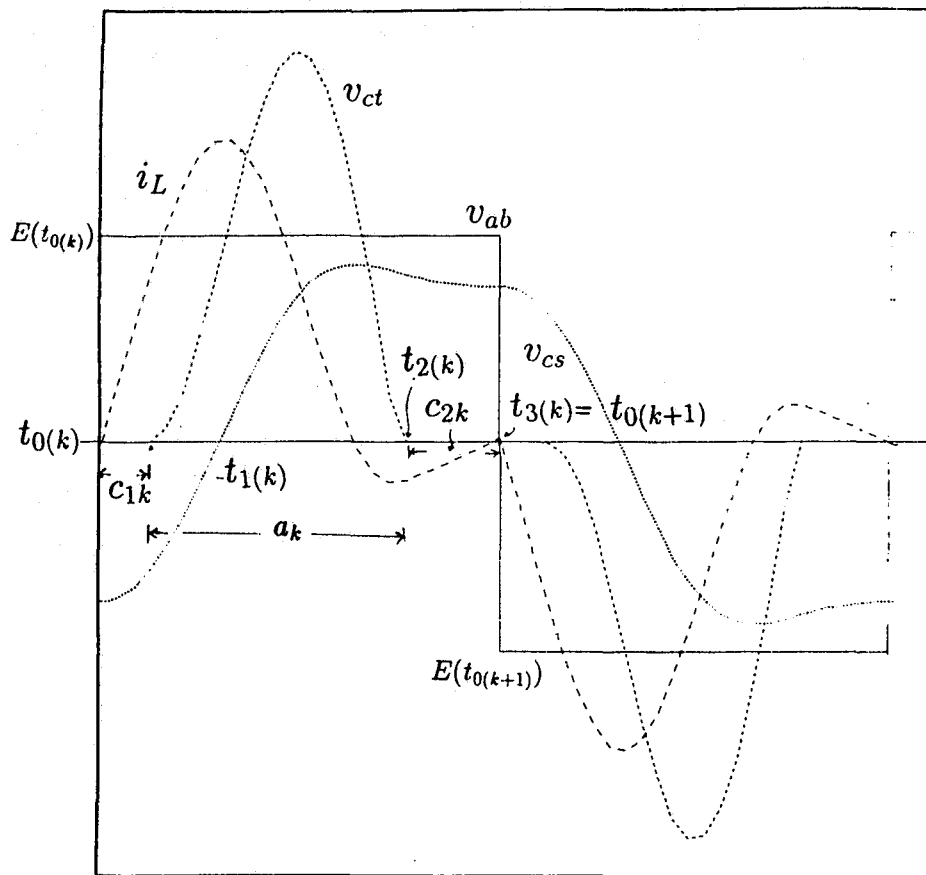


Figure 3.22: Experimental waveforms for a step change in the load from full load to half full load current (load resistance doubled). (a) Parallel capacitor voltage. (b) Resonant inductor current. (c) Output voltage. (d) Closed loop results for a step change in the load from full load to half load.

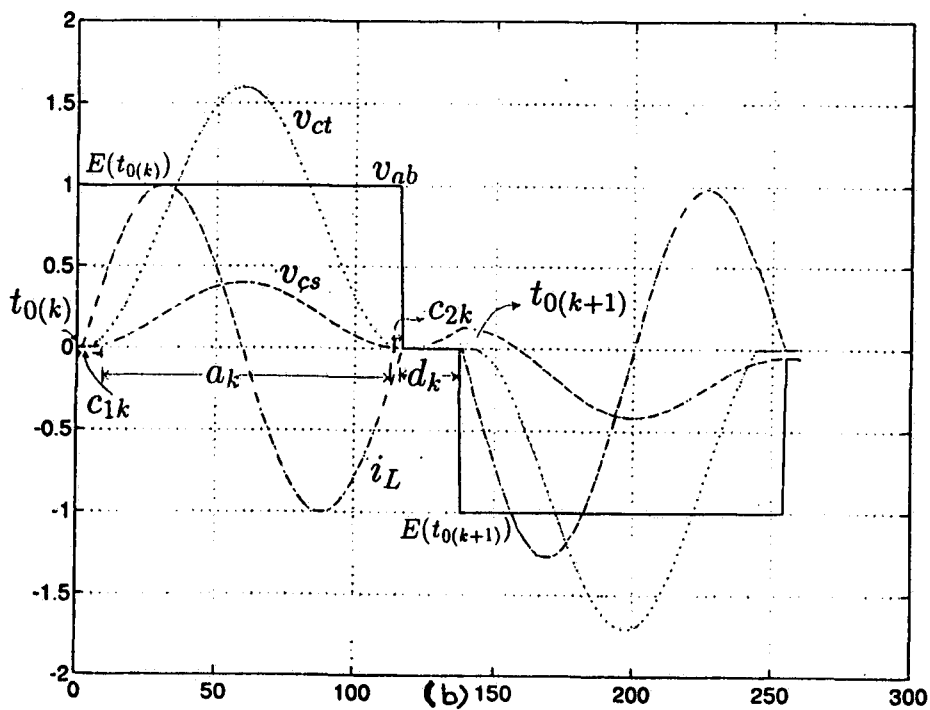
### 3.8.1 Converter Operation in DCM

In the discontinuous current mode (DCM) [13], the current flowing through the switches is zero at the time of switching. Thus the switching power losses are negligible, thereby increasing the efficiency of the converter and allowing high operating frequency. This leads to a reduction in size of the magnetic components of the circuit. Also, the resonant tank current and voltage waveforms are nearly sinusoidal [13], reducing the problems of EMI. Indeed, an SPRC operating in the DCM under steady state is very promising in terms of efficiency and size of the magnetic components. But what about the transient phase? How does a converter designed to operate in DCM, behaves during the transients? Does it maintain zero current switchings? How do the waveforms look like? What kind of peak stresses are experienced by the resonant tank components? What kind of external control is required during the transients and how should it be designed?

Fig. 3.23(a) illustrates typical waveforms from  $k^{\text{th}}$  instant onwards, for *just* DCM and the discontinuous capacitor voltage mode (DCVM) operation of the SPRC. These waveforms correspond to the rated output power and minimum supply voltage, with an “A interval” occurring between two “C intervals” marked  $a_k$ ,  $c_{1k}$  and  $c_{2k}$  respectively. The equivalent circuits of the SPRC during these intervals are shown in Fig. 3.24. During the intervals  $c_{1k}$ ,  $c_{2k}$ , the parallel capacitor voltage is zero, since all the diodes of the output rectifier bridge conduct. During interval  $a_k$ , only two output diodes are conducting and the polarity of capacitor voltage and the direction of rectifier input current are as shown. Fixed “ON time” and variable frequency gating is used to control the power output for load (or line) variations, resulting in a fourth interval ( $d_k$ ) next to  $c_{2k}$  (Fig. 3.23(b)) for reduced output power. The equivalent circuit of the SPRC during this fourth interval is shown in Fig. 3.24(c). During this interval, since all the switches are off, both the parallel capacitor voltage and the resonant



(a)



(b)

Figure 3.23: (a) Typical waveforms of the SPRC circuit operating in *just* DCM and DCVM mode of operation starting from the  $k^{\text{th}}$  instant. (b) Discontinuous current mode waveforms showing the presence of a fourth interval ( $d_k$ ) during the “fixed ON time, variable frequency” gating control of the output power. The various intervals are marked in both the figures.

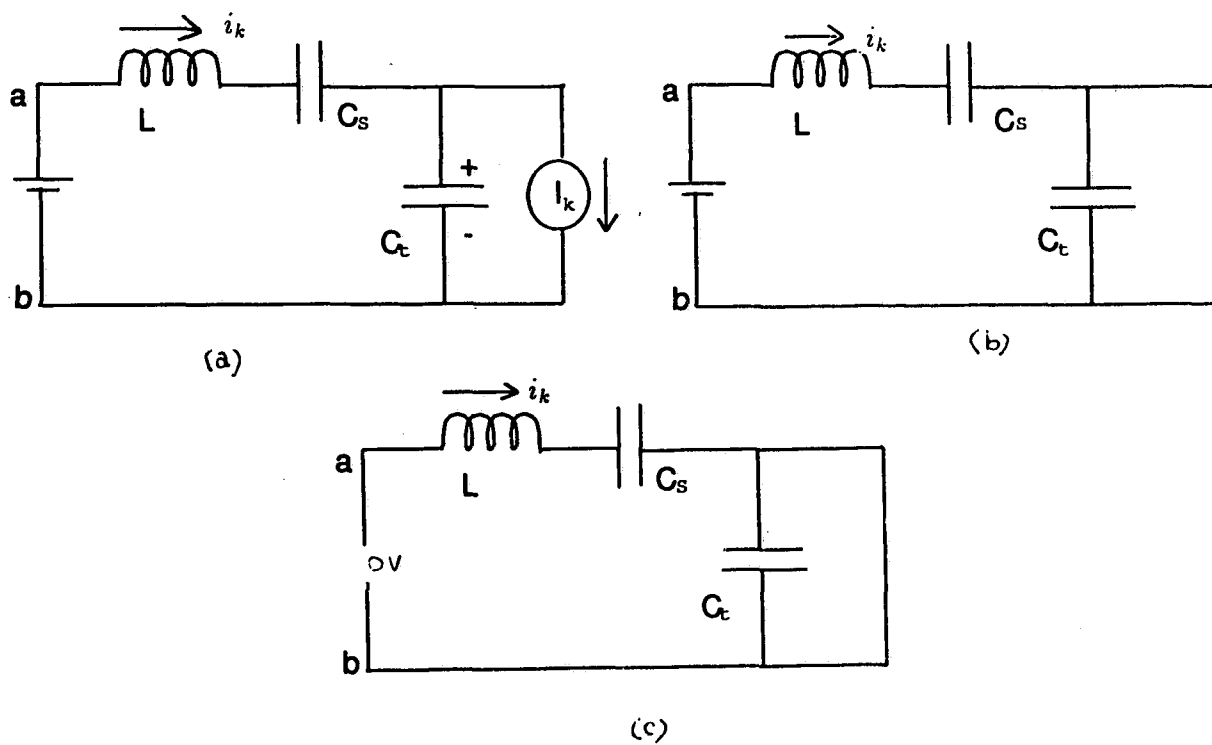


Figure 3.24: The equivalent circuits of the SPRC during the various intervals of DCVM and just DCM mode, using the constant current model. (a) During interval  $a_k$ . (b) During interval  $c_k$ . (c) During interval  $d_k$ .

tank current are zero, while the voltage  $v_{ab}$  is equal to the series capacitor voltage (since terminals “a” and “b” are open) till the complementary switch is turned ON.

It must be pointed out that for any half cycle, the gating signal to the conducting MOSFET may be withdrawn once its anti-parallel diode begins to conduct. The resonant current sinusoidally goes to zero and remains so till the next half cycle begins.

### 3.8.2 Discrete Time Domain Model for DCM

The discrete time domain model is obtained with respect to Fig. 3.23(a) for *just* DCM and DCVM operation. The assumptions used are the same as for the CCM case.

In Fig. 3.23(a), the total conduction angle (switch + diode) is denoted by  $\gamma_k$ ,

$$\begin{aligned} \text{where } \gamma_k &= c_{1k} + a_k + c_{2k}; & c_{1k} &= \omega_s(t_{1(k)} - t_{0(k)}) \\ a_k &= \omega_0(t_{2(k)} - t_{1(k)}); & c_{2k} &= \omega_s(t_{0(k+1)} - t_{2(k)}) \\ & & \text{and } \omega_s &= \frac{1}{\sqrt{LC_s}} \end{aligned}$$

The other quantities have already been defined earlier.

#### $k^{\text{th}}$ Event

Interval  $C_1$  equations;  $t_{0(k)} < t < t_{1(k)}$ ;  $t' = t - t_{0(k)}$

$$i_L(t') = A_{1c_{1k}} \sin(\omega_s t') + B_{1c_{1k}} \cos(\omega_s t') + C_{1c_{1k}} \quad (3.51)$$

$$v_{cs}(t') = A_{2c_{1k}} (1 - \cos(\omega_s t')) + B_{2c_{1k}} \sin(\omega_s t') + C_{2c_{1k}} (\omega_s t') + v_{cs}(t_{0(k)}) \quad (3.52)$$

$$v_{ct}(t') = 0 \quad (3.53)$$

**Interval A equations;  $t_{1(k)} < t < t_{2(k)}$ ;  $t'' = t - t_{1(k)}$**

$$i_L(t'') = A_{1a_k} \sin(\omega_0 t'') + B_{1a_k} \cos(\omega_0 t'') + C_{1a_k} \quad (3.54)$$

$$v_{cs}(t'') = A_{2a_k}(1 - \cos(\omega_0 t'')) + B_{2a_k} \sin(\omega_0 t'') + C_{2a_k}(\omega_0 t'') + v_{cs}(t_{1(k)}) \quad (3.55)$$

$$v_{ct}(t'') = A_{3a_k}(1 - \cos(\omega_0 t'')) + B_{3a_k} \sin(\omega_0 t'') + C_{3a_k}(\omega_0 t'') + v_{ct}(t_{1(k)}) \quad (3.56)$$

**Interval C<sub>2</sub> equations;  $t_{2(k)} < t < t_{3(k)}$ ;  $t''' = t - t_{2(k)}$**

$$i_L(t''') = A_{1c_{2k}} \sin(\omega_s t') + B_{1c_{2k}} \cos(\omega_s t') + C_{1c_{2k}} \quad (3.57)$$

$$v_{cs}(t''') = A_{2c_{2k}}(1 - \cos(\omega_s t')) + B_{2c_{2k}} \sin(\omega_s t') + C_{2c_{2k}}(\omega_s t') + v_{cs}(t_{0(k)}) \quad (3.58)$$

$$v_{ct}(t''') = 0 \quad (3.59)$$

The coefficients  $A_j$ ,  $B_j$  and  $C_j$  used in the above equations are defined in Appendix C.

**$(k+1)^{th}$  Event**

The  $(k+1)^{th}$  interval circuit equations are identical to those of  $k^{th}$  interval with a change in the signs of all the variables.

**Choice of State Variables**

The choice of state variables remains the same as for the CCM, except that the tank state variables are redefined due to their different polarities as compared to the CCM case and are as follows.

$$x_{1(k)} = i_L(t_{0(k)}); x_{2(k)} = -v_{cs}(t_{0(k)}); x_{3(k)} = v_{ct}(t_{0(k)}) \quad (3.60)$$

It should be noted that the state variables  $x_{1(k)}$  and  $x_{3(k)}$  will become zero during the steady state. Discrete state variables for the  $(k+1)^{th}$  event can similarly be chosen.

### Discrete State-Space Model

The discrete state variables of  $(k + 1)^{th}$  event are expressed in terms of the state variables of the  $k^{th}$  event as below:

$$\begin{aligned}
 i_L(t_{0(k+1)}) &= A_{1c_{1k}}(-\cos(a_k)\cos(c_{1k})\sin(c_{2k}) \\
 &+ \frac{1}{\sqrt{r_1}}\sin(a_k)\sin(c_{1k})\sin(c_{2k}) + \sqrt{r_1}\sin(a_k)\cos(c_{1k})\cos(c_{2k}) \\
 &+ \cos(a_k)\sin(c_{1k})\cos(c_{2k})) + C_{1a_k}(\cos(c_{2k})(1 - \cos(a_k)) \\
 &- \frac{1}{\sqrt{r_1}}\sin(a_k)\sin(c_{2k})) \tag{3.61}
 \end{aligned}$$

$$\begin{aligned}
 v_{cs}(t_{0(k+1)}) &= E(t_{0(k)}) + A_{2c_{1k}}(-\cos(a_k)\cos(c_{1k})(1 + \\
 &\cos(c_{2k})) + \frac{1}{\sqrt{r_1}}\sin(a_k)\sin(c_{1k})(1 - \cos(c_{2k}) + r_1) \\
 &+ \cos(c_{1k})(r_1 - 1 - r_1\cos(a_k)) + \sin(c_{2k})(\cos(a_k)\sin(c_{1k}) \\
 &+ \sqrt{r_1}\sin(a_k)\cos(c_{1k})) + Z.C_{1a_{1k}}(\sin(a_k)(\cos(c_{2k}) - 1) \\
 &+ \sqrt{r_1}\sin(c_{2k})(1 - \cos(a_k))) - C_{3a_{1k}}(a_k - \sin(a_k)) \tag{3.62}
 \end{aligned}$$

$$v_{ct}(t_{0(k+1)}) = 0 \tag{3.63}$$

The non linear equation representing the output section is:

$$\begin{aligned}
 I(t_{0(k+1)}) &= I(t_{0(k)}) + \frac{1}{L_f} \left[ \int_{t_{0(k)}}^{t_{0(k+1)}} |(v_{ct}(\tau))| d\tau \right. \\
 &\quad \left. - v_0(t_{0(k)})(t_{0(k+1)} - t_{0(k)}) \right] \tag{3.64}
 \end{aligned}$$

This yields;

$$\begin{aligned}
 I(t_{0(k+1)}) &= I(t_{0(k)}) + \frac{1}{X_{L_f}} [A_{3c_{1k}}(a_k - \sin(a_k)) \\
 &\quad + B_{3c_{1k}}(1 - \cos(a_k)) + \frac{1}{2}C_{3c_{1k}} \cdot (a_k)^2 - v_0(t_{0(k)})\gamma_k] \tag{3.65}
 \end{aligned}$$

where  $X_{L_f} = \omega_0 L_f$ .

Similarly,

$$v_0(t_{0(k+1)}) = v_0(t_{0(k)}) + \frac{(I(t_{0(k)}) - \frac{v_0(t_{0(k)})}{R_L})(t_{0(k+1)} - t_{0(k)})}{C_f} \tag{3.66}$$

By inserting the state variables in equations (3.61), (3.62), (3.63), (3.65) and (3.66), a discrete state-space model is attained for the DCM operation. By matching the boundary conditions, steady state solutions can be obtained by using (3.61) - (3.66).

### 3.8.3 Analytical Results for DCM

Two kinds of transients are considered in this section. One caused due to sudden switching on of the converter and the other due to sudden load variation.

The plots showing the variations in peak resonant inductor current and the peak parallel capacitor voltage due to these transients are obtained for the transient phase. Similarly the plots showing the variation of the discrete state variables were also obtained. These plots were obtained with respect to a converter designed to operate in the DCM. The specifications of this converter are given below.

Input Voltage =  $2E = 150$  Volts.

Output power = 150 Watts.

Output Voltage = 54 Volts.

Switching frequency = 122 kHz.

Values of the components obtained are:

$L = 21.47\mu H$ ;  $C_s = 0.0701\mu F$ ;  $C_t = 0.0175\mu F$

It must be pointed out that only the open loop operation of the converter operating in DCM is considered.

#### Transients Due to Switching ON the Supply

Fig. 3.25(a) shows the first few transient cycles of the tank current. The waveforms show that the switches are subjected to non-zero current switchings during this kind of transients. During the first few cycles, the converter operates in DCM and the

interval  $d_k$  is present. Gradually, the tank current becomes continuous (CCM) to accommodate the higher load current that results due to an overshoot in the output voltage and current. It takes about  $160 \mu s$  for the converter to enter the *just* DCM (Fig. 3.25(b)). This duration is directly dependent on the output filter inductance ( $L_f = 1000 \mu H$ ) and the output filter capacitor ( $C_f = 1 \mu F$ ). As can be seen in Fig. 3.25(a), the converter operates in the CCM and the leading power factor mode, during the transient phase. Fig. 3.25(b) shows the tank current waveforms for more cycles, just about when the current is reaching the steady state. The plot shows that the current during the transients is about 0.5 p.u. more than its steady-state value. It was observed that as the value of  $C_f$  is reduced, the peak tank current goes down. For a low value of filter capacitor, it is observed that there is no over stressing of the tank components on account of high current during the transient phase caused by the sudden switching on of the converter. Fig. 3.25(c) shows first few cycles of the parallel capacitor voltage waveforms and it can be observed that the DCVM operation is maintained through out the transient phase. It is observed that there is no significant over stressing of the parallel capacitor during this phase. Figs. 3.26(a) and (b) show the p.u. SPICE plots corresponding to Figs. 3.25(b) and (c). These figures show a good agreement between the theoretical results obtained with the discrete model and SPICE. Fig. 3.27 shows the variation of the state variables obtained from the proposed model. Fig. 3.27(a) shows the tank state variables. The waveform corresponding to  $x_{1(k)}$  verify the observations mentioned earlier in this section. Between the points marked "P" and "Q", the converter operates in the CCM, leading p.f. mode. Duration of CCM depends upon the value of the output filter components. Fig. 3.27(b) shows the output voltage and current. The same figure also shows the corresponding SPICE results, which are found to be in good agreement. Both the waveforms show an oscillatory behavior. This can be attributed to the presence of a filter capacitor. In the absence of a filter capacitor or a low value

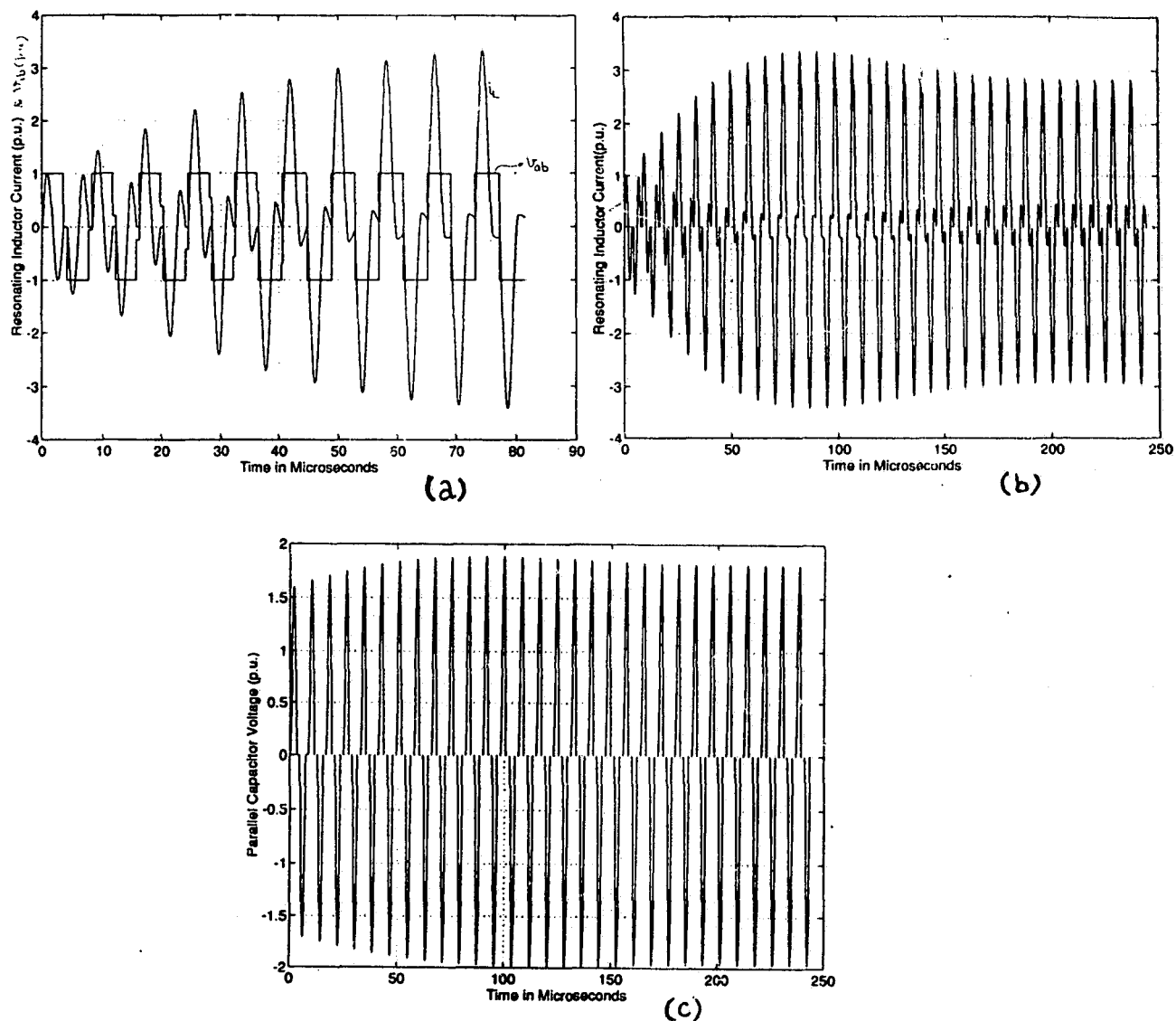


Figure 3.25: Waveforms during the transients caused by switching ON the input supply to the converter from 0 to 75 V.

(a) Resonant inductor current during the very initial transient phase. It shows the DCM is not maintained initially and the converter enters leading p.f. mode during this phase.

(b) Resonant inductor current during the entire transient phase.

(c) Parallel capacitor voltage during the transient phase.

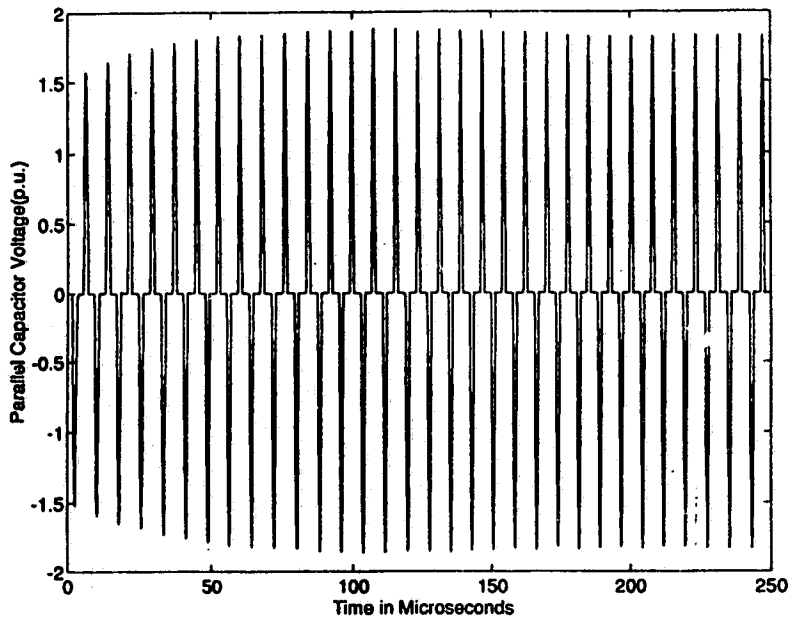
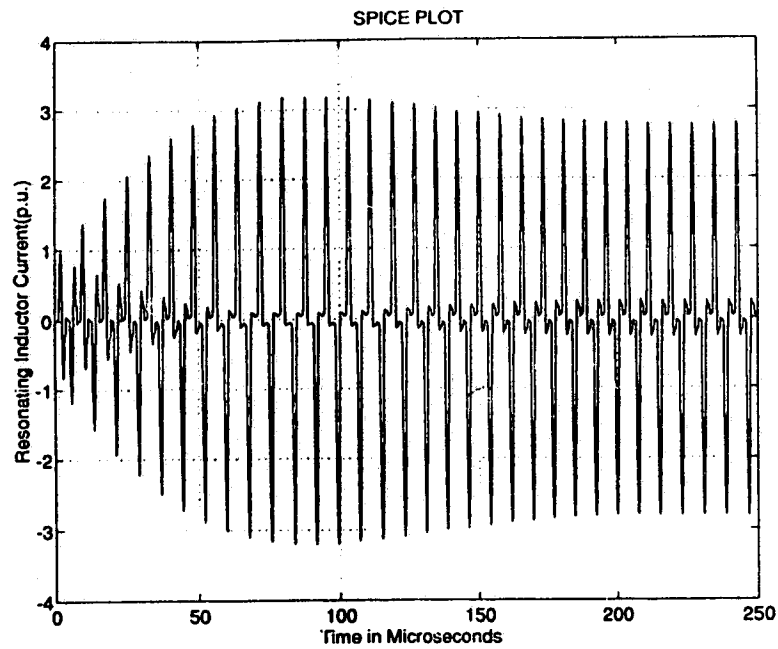


Figure 3.26: SPICE plots during the transients caused by switching ON the input supply from 0 to 75 V. These plots correspond to Figs 3.25(b) and (c).

- (a) The resonating inductor current.
- (b) The parallel capacitor voltage.

of the filter capacitor, the response will be critically damped as the characteristic impedance of the output filter section ( $\sqrt{\frac{L_f}{C_f}}$ ) will be very high. To show the effect of the output filter capacitor value on the converter's large signal response, a case with  $C_f = 0.5 \mu\text{F}$  was considered. The resulting large-signal response is shown in Figs. 3.28(a) - (c). Fig. 3.28(a) shows the tank current for the entire transient phase. Fig. 3.28(b) shows the discrete state variables  $x_{1(k)}$  and  $x_{2(k)}$  for this case and Fig. 3.28(c) shows the output variables as predicted by the proposed model. It can be verified from Fig. 3.28 that as a result of a reduced output filter capacitor, the peak of the tank current has reduced, and the response has become critically damped, without any over stressing of the circuit components during these transients. It can be verified from the plot of  $x_{1(k)}$  that the initial resonant inductor current is very small during the narrow CCM region, unlike the case when a larger filter capacitor is present.

### Transients Due to Sudden Load Change

#### (a) Full Load to Half Full Load

Figs. 3.29(a) and (b) show the tank current and parallel capacitor voltage waveforms during the transient phase caused by sudden halving of the load current. The current waveform shows that there is an appreciable drop in its peak value (nearly 1 p.u.). However the DCM operation is maintained. The dead gap (interval  $d_k$ ) appears as the anti-parallel diode conducts for less time due to a reduction in the load current. The voltage waveform on the other hand do not show an appreciable change in the peak value. Figs. 3.29(c) and (d) show the corresponding SPICE plots. Fig. 3.30 shows the state variables plots. Fig. 3.31 shows the variation of the output voltage and current during these transients from the model. The output voltage shows an oscillatory behavior in the presence of the filter capacitor. The corresponding SPICE plots, included in the same figure, also show a similar trend. Although not explicitly

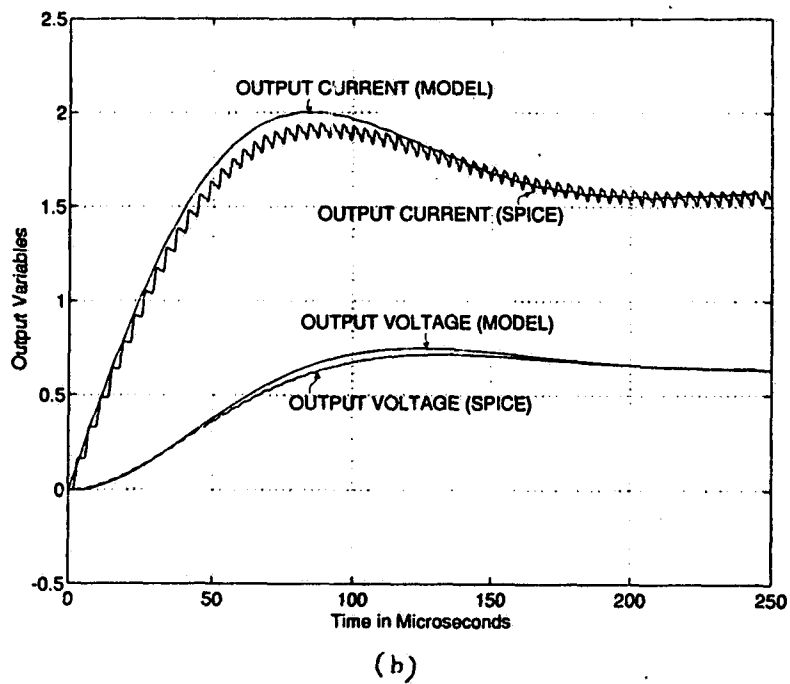
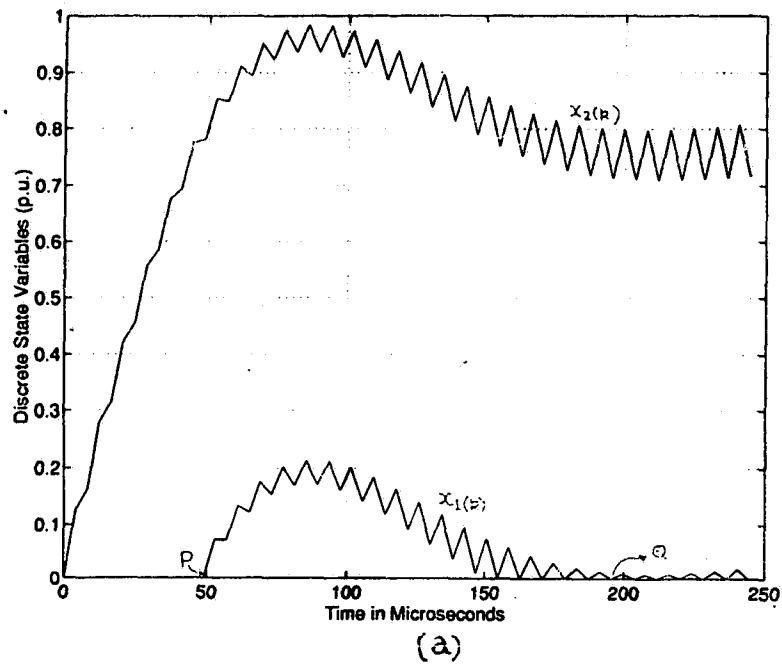
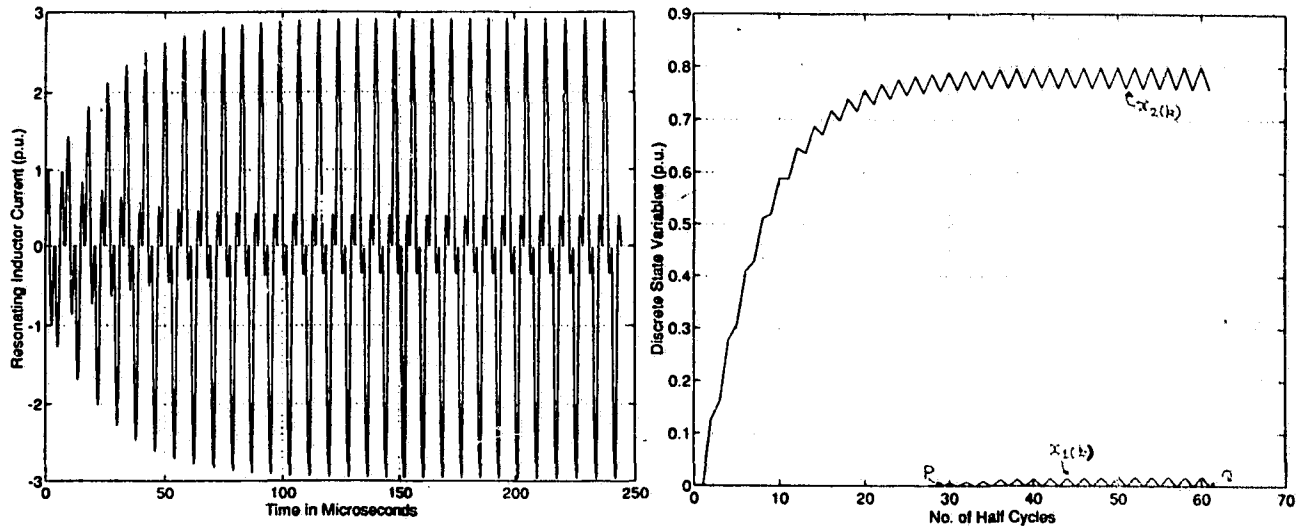
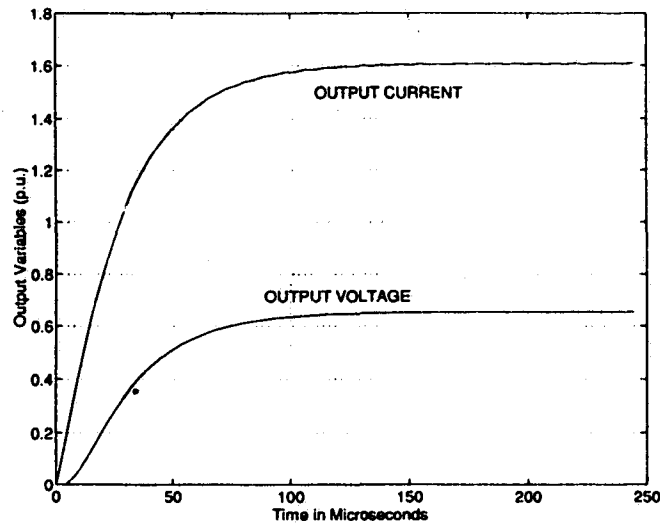


Figure 3.27: The discrete state variables ( $x_{1(k)}$ , and  $x_{2(k)}$ ) and output state variables during the switching ON of the converter. In (a),  $x_{3(k)}$  has not been plotted explicitly as it remains zero through out the transient phase. In (b), SPICE results are also included for comparison.



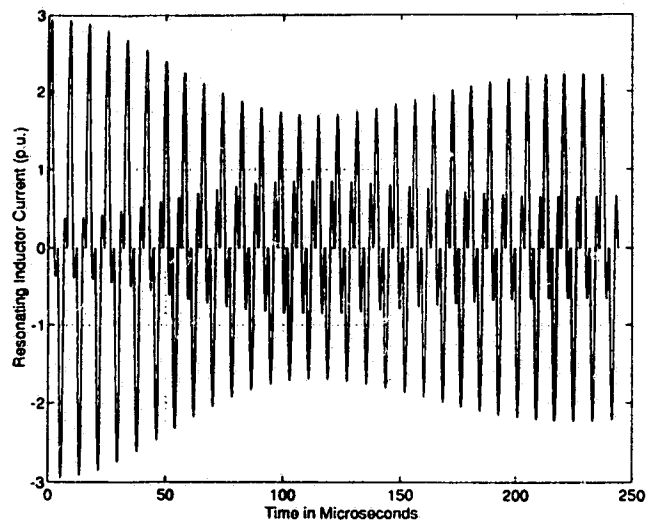
(a)

(b)

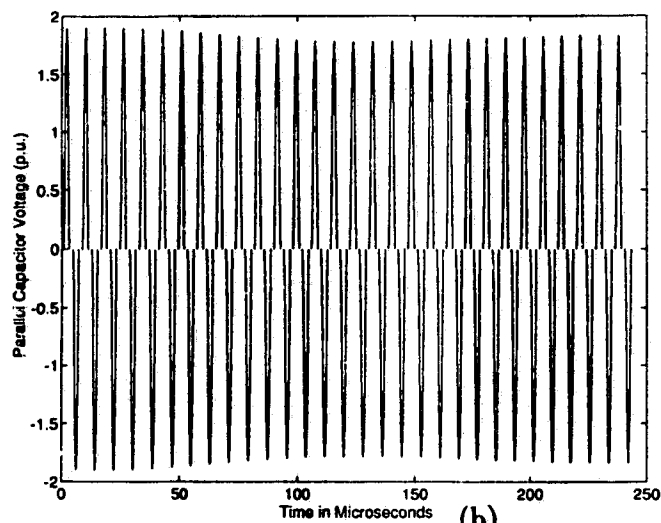


(c)

Figure 3.28: Effect of a smaller filter capacitor ( $C_f = 0.5\mu F$ ) value. (a) Resonating Inductor Current. (b) Discrete state variables. (c) Output Variables.



(a)



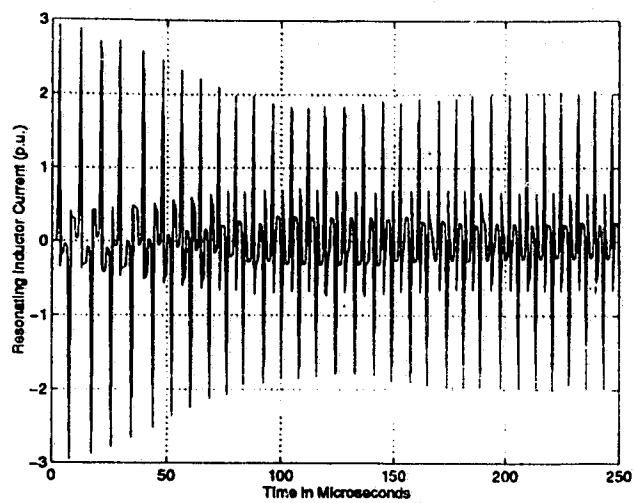
(b)

Figure 3.29: Waveforms during the transients caused by sudden load variation (full load to half load).

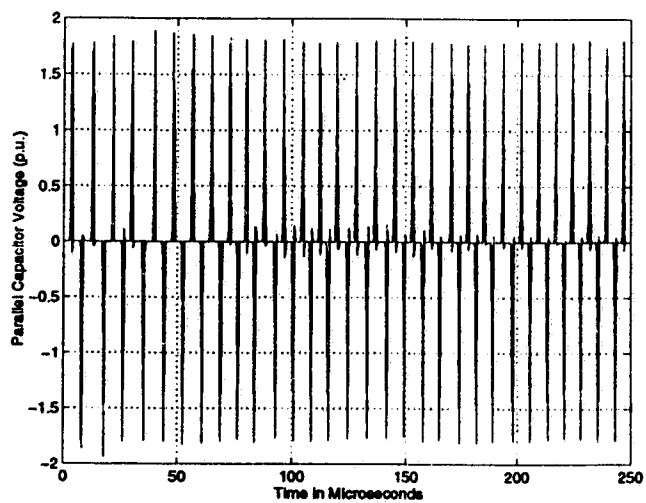
(a) Resonant inductor current during the transient phase.

(b) Parallel capacitor voltage during the transient phase.

(c),(d) SPICE plots corresponding to (a) and (b).



(c)



(d)

Fig. 3.29 (continued)

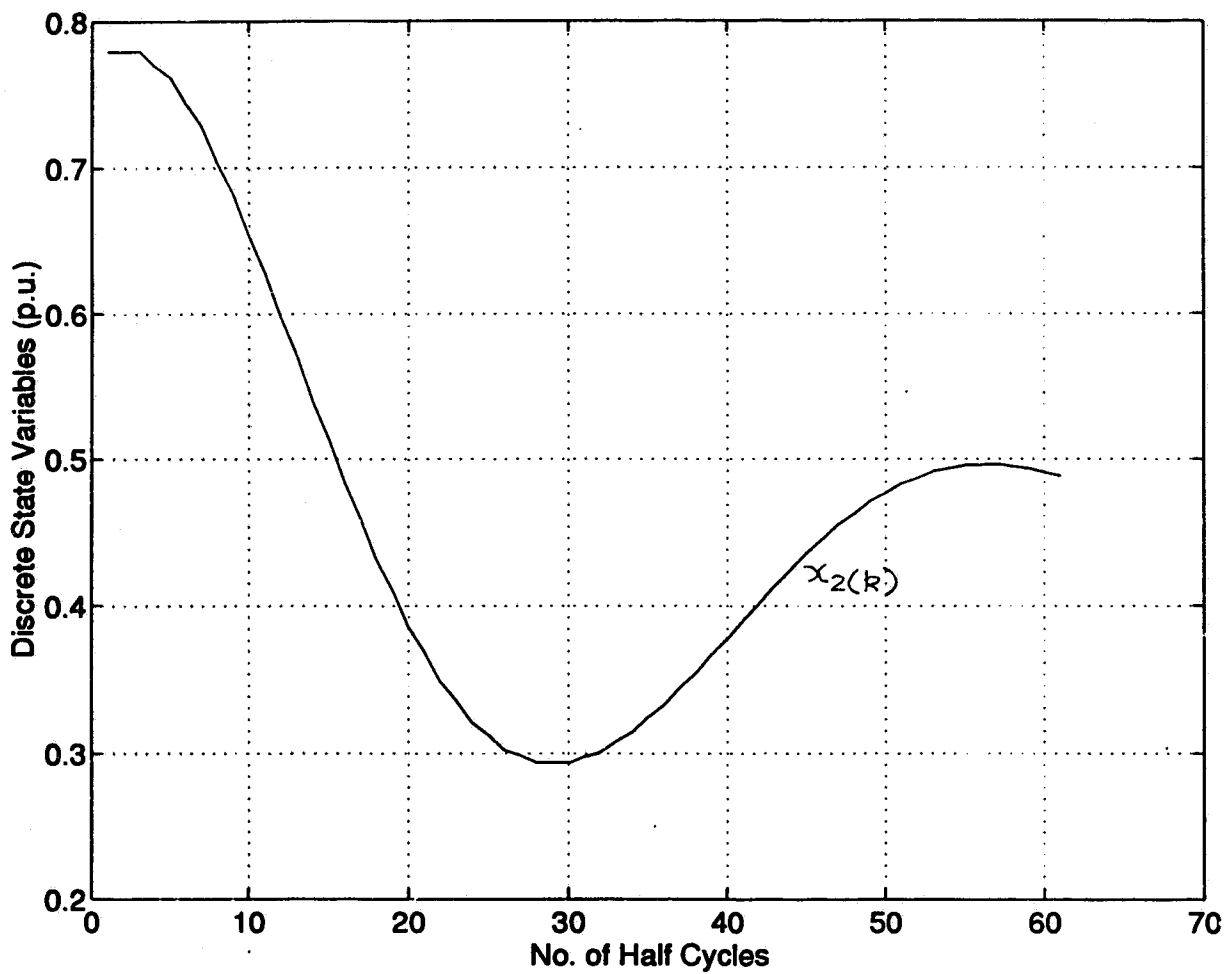


Figure 3.30: The discrete state (tank) variables during sudden variation of load (full load to half load). The variables  $x_{1(k)}$  and  $x_{3(k)}$  are not plotted explicitly, as they remain zero through out the transient phase.

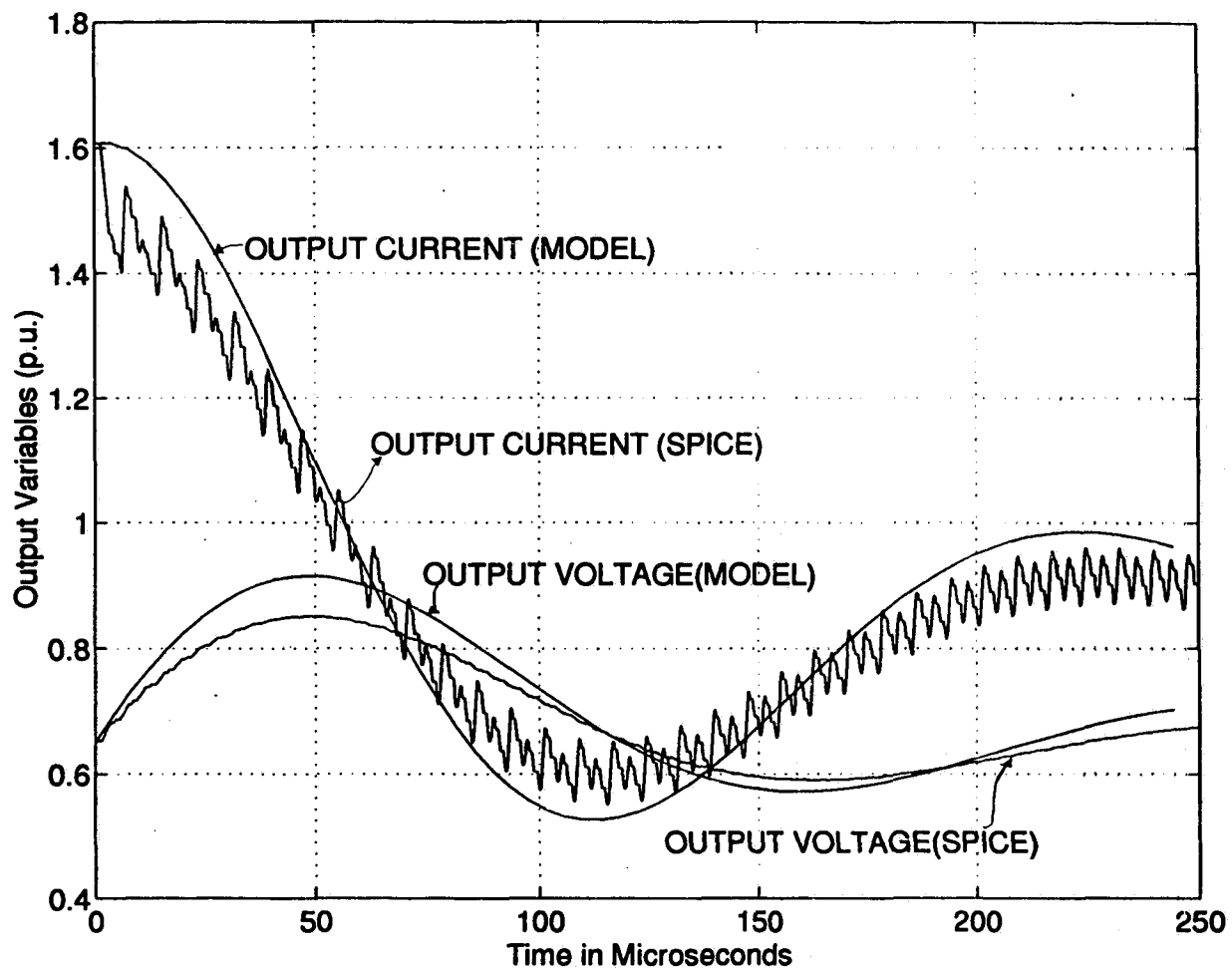


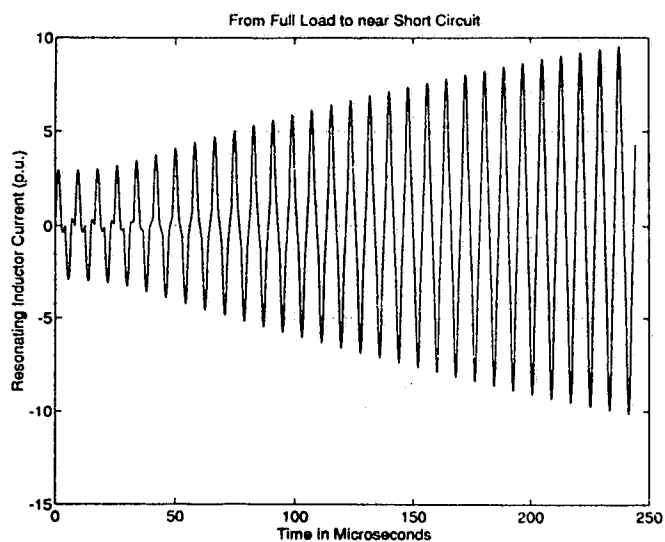
Figure 3.31: Output variables during the transients caused by sudden load variation from full load to half the rated load, as obtained with the model and SPICE.

shown, in the absence of a filter capacitor, the output voltage will show a sudden initial rise in its value because the load current goes down, where as the switching frequency has not been changed (open loop operation). As the converter recovers, the voltage comes down gradually and settles to a new steady-state value. The response will be critically damped.

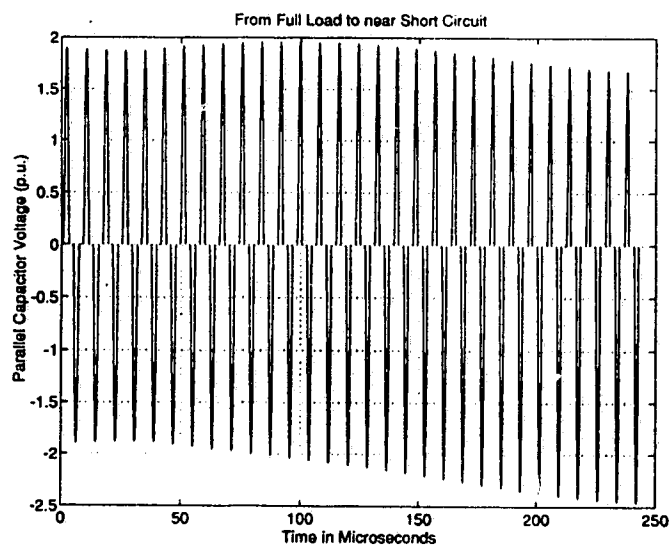
### (b) Full Load to Short Circuit Condition

Figs. 3.32(a) and (b) show the transient phase waveforms of the inverter output current and the parallel capacitor voltage for a sudden change in load from the rated (full load) value to short circuit condition. Figs. 3.32(c), (d) show the corresponding SPICE plots. The state variables are plotted in Fig. 3.33. It can be seen from the plot of  $x_{1(k)}$  (Fig. 3.33) and the resonating inductor current waveform (Fig. 3.32), that the DCM is disturbed during the short circuit causing increased stresses on the switches and more losses. The converter operates in CCM, leading p.f. mode of operation. The peak tank current builds up to a large value. This is directly affected by the presence of a huge filter inductor at the output. The voltage  $v_{ct}$  (Fig. 3.32(b)) does not show an appreciable change in its peak value. Output variables are plotted in Fig. 3.34. It can be seen that due to a large value of  $L_f$  the output current does not rise suddenly. The output voltage on the other hand falls down to zero rather quickly with a response time determined by the filter capacitor value.

It can be concluded that the absence of a closed loop corrective action, causes large currents in the circuit during the short circuit and therefore an open loop SPRC, operating in DCM should not be short circuited.

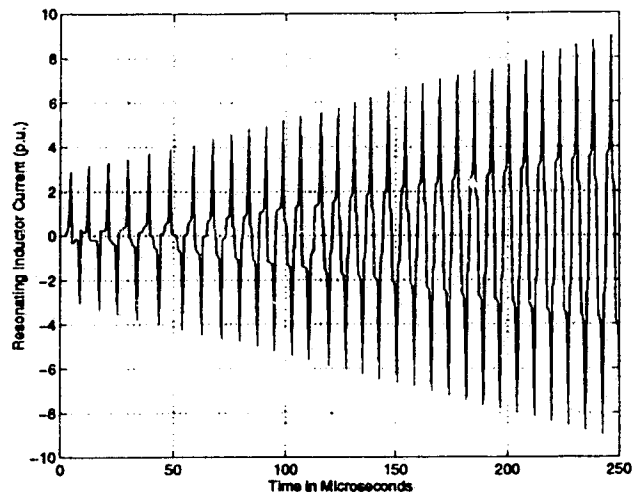


(a)

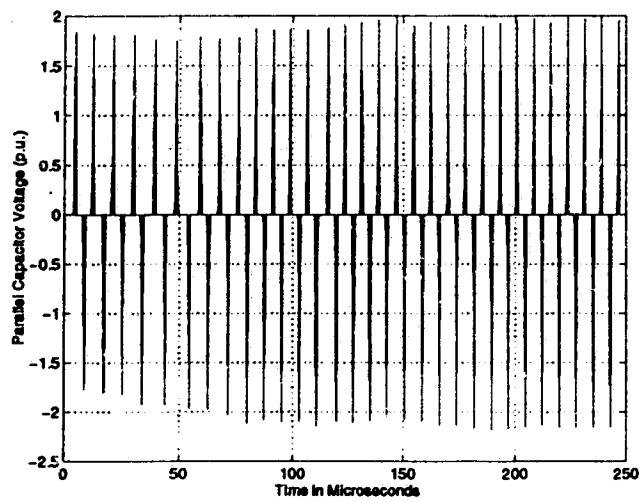


(b)

Figure 3.32: Transient waveforms during the step change in load from full load to short circuit condition. (a) Resonating inductor current. (b) Parallel capacitor voltage. (c),(d) SPICE plots corresponding to (a) and (b), respectively.



(c)



(d)

Fig. 3.32 (continued)

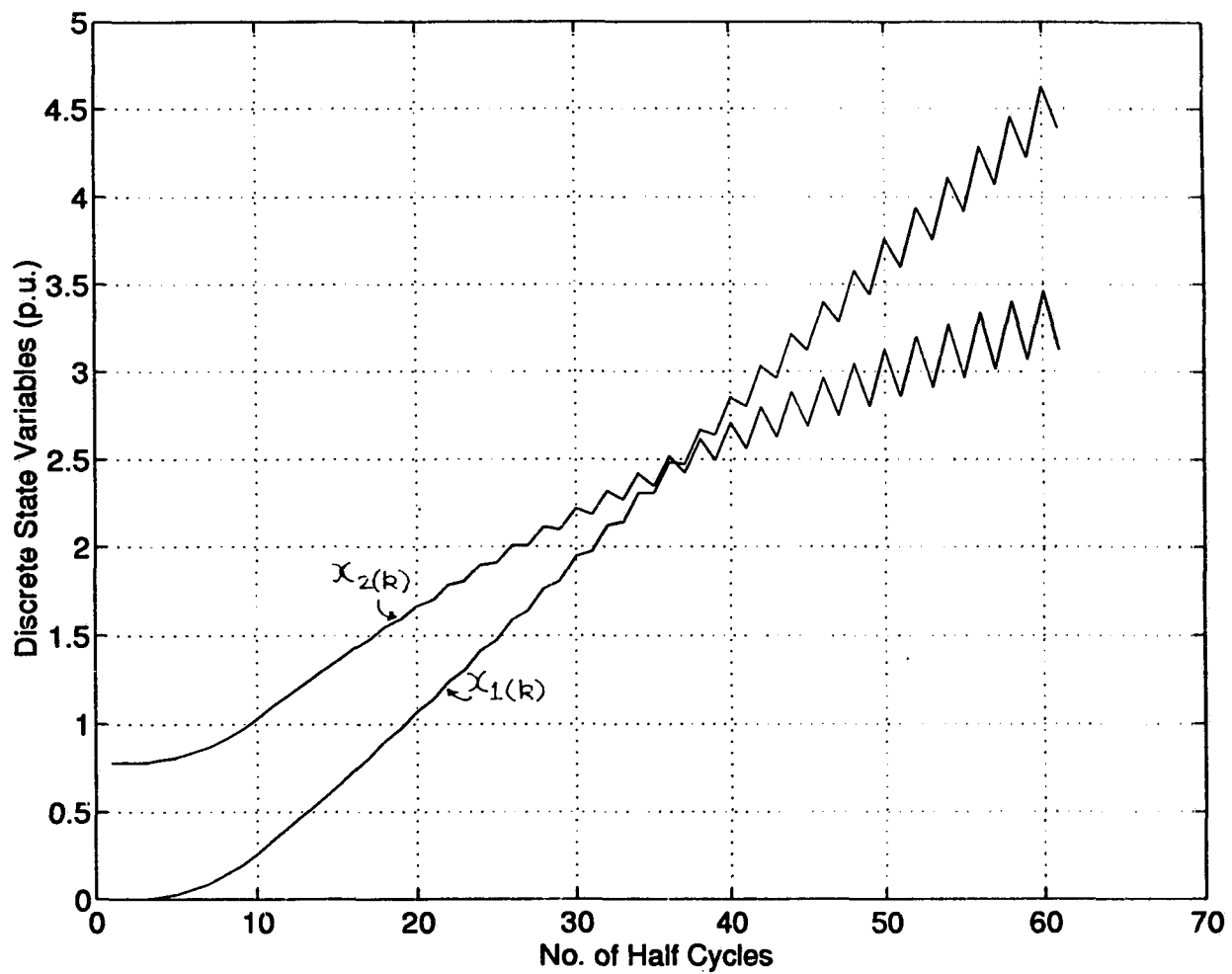


Figure 3.33: Discrete state (tank) variables during the step change from full load to short circuit conditions.

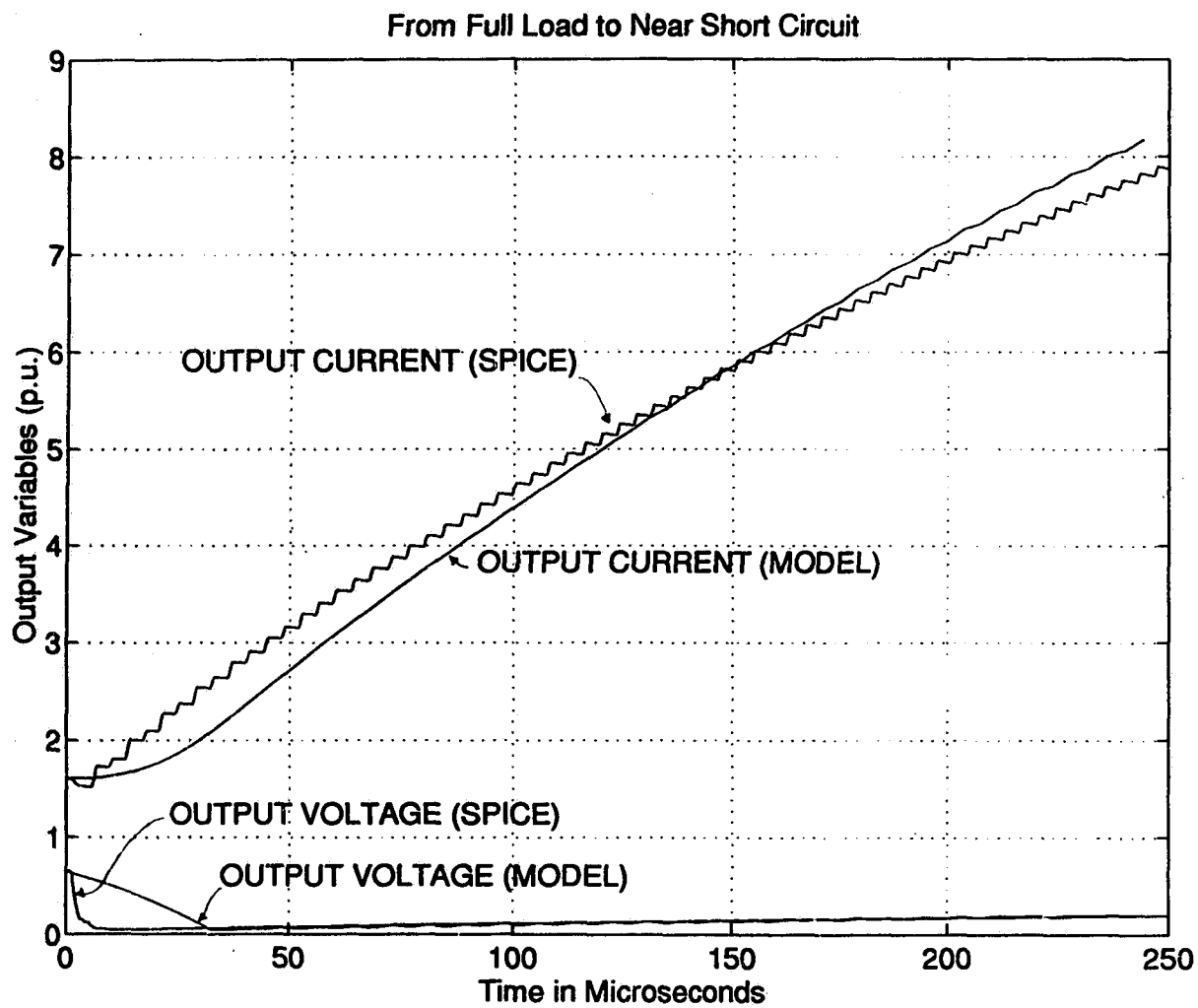


Figure 3.34: Output variables, current and voltage during a step change from full load to short circuit conditions. SPICE results are also included for the sake of comparison.

### Experimental Results for DCM

A 150 Watts converter was used to verify the theoretical results. Fig. 3.35(a) shows the very initial stage of the tank quantities during the transients caused by switching ON the converter. Fig. 3.35(b) shows how the tank current recovers from these transients and how its peak varies. These waveforms confirm that as soon as the converter is switched ON, DCM is maintained for the first few cycles. Later, however, the converter enters CCM. It remains in that mode for several cycles before DCM is restored (also refer to Fig. 3.25(a) and 3.27(a)). Fig. 3.35(c) and (d) show the parallel capacitor voltage waveforms and the output voltage waveforms during the transients. Fig. 3.36 show the various waveforms during the transients caused by a sudden variation in load. The load resistance was changed to twice its value (full load to half the rated load condition).

## 3.9 Observations and Conclusions

### For CCM

- (1) A discrete time domain model has been derived for the SPRC for continuous conduction mode and lagging power factor mode of operation.
- (2) The effectiveness of this model in predicting the transient behavior of an SPRC has been shown.
- (3) Using this model, a few calculations are sufficient to predict the transient behavior of the converter from a designer's point of view. Only the initial conditions at the beginning of every half cycle (initial state vector) are required per half cycle to arrive at the curves for peak stresses and the state behavior. Thus, this approach can be used to obtain the crucial design parameters fairly easily.

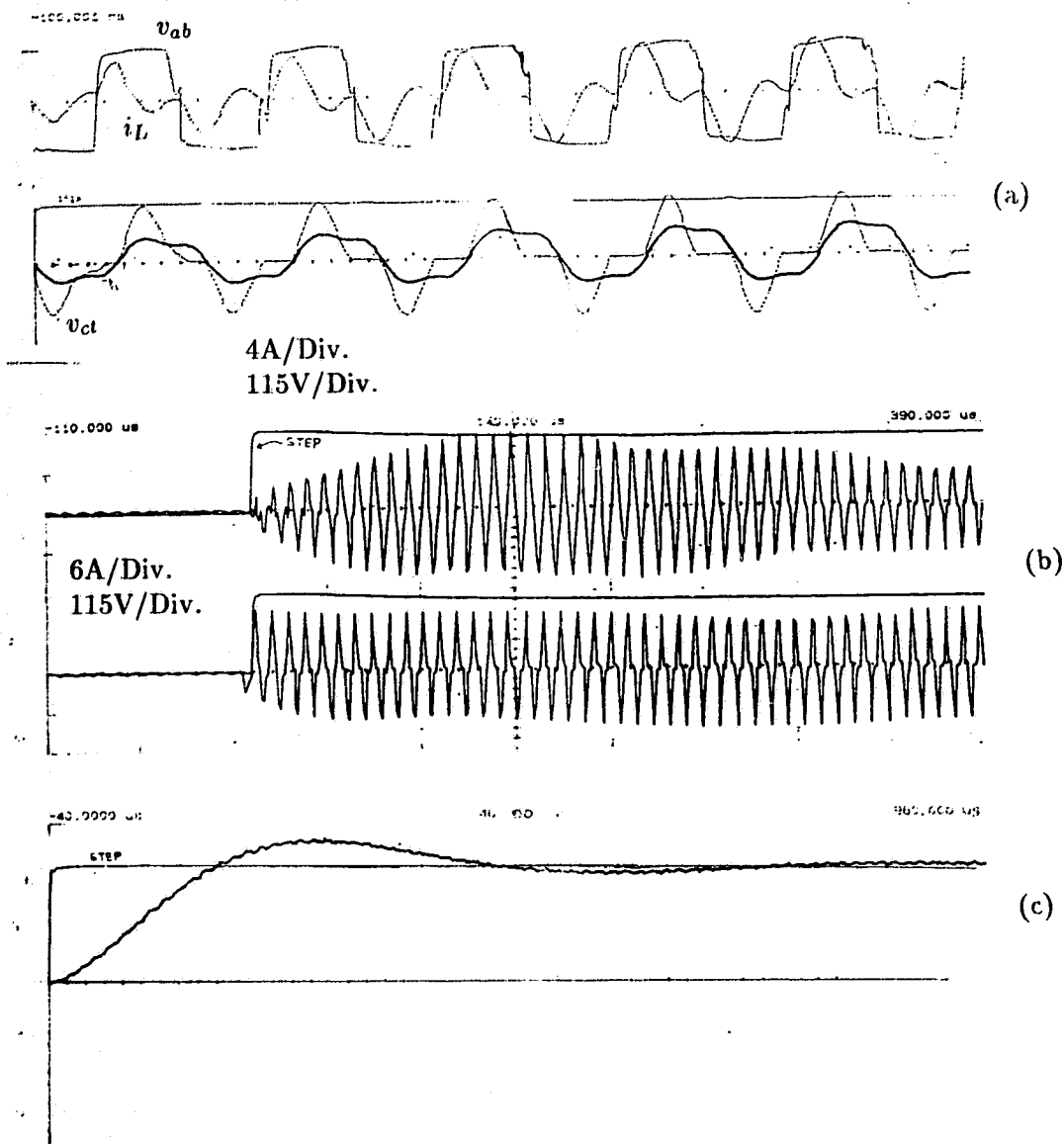


Figure 3.35: Experimental waveforms during the transients caused by switching ON the supply to the converter.

(a) The very initial stage of the resonant inductor current. This figure corresponds to Fig. 3.25(a). Parallel and series capacitor voltage waveforms are also included. The time instant where the external disturbance is induced is shown by a step voltage in all the experimental waveforms.

(b) Resonant inductor current and parallel capacitor voltage during the entire transient phase.

(c) Output voltage.

[ Details of the converter:  $L_s = 21.47\mu H$ ;  $C_s = 0.07\mu F$ ;  $C_t = 0.018\mu F$ ; Input dc voltage,  $2E = 150$  Volts;  $L_f = 1000\mu H$ ;  $C_f = 1.0\mu F$ ; Switches used: IRF 740 MOSFET's ]

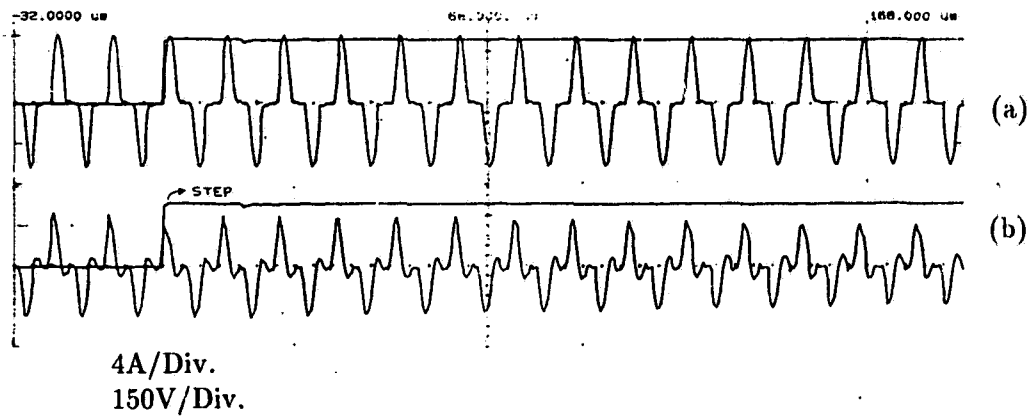


Figure 3.36: Experimental waveforms during the transients caused by a sudden load variation (from full load to half load). (a) Resonant inductor current. (b) Parallel capacitor voltage.

(4) The proposed model can be used to theoretically predict the large-signal behavior of the converter and then SPICE simulation program can be used to verify the results. Usually, SPICE requires large computer memory, even if the information required from the simulation may be small. The proposed model can give crucial design parameters and state behavior with simple calculations.

(5) The model presented has been derived based on the assumption of CCVM (continuous capacitor voltage mode) for  $v_{ct}$  [Fig. 3.2]. However, the converter is designed to operate with slight discontinuity in the parallel capacitor voltage. The results show that the proposed model based on two interval CCV mode (in which the effect of slight discontinuity has been neglected) is good enough to predict the behavior of the designed converter, although some slight deviations are observed. This avoids the use of a more complicated model involving a third interval (in DCV mode), which does not have closed form solutions [12]. If the converter operates with a larger discontinuity in the parallel capacitor voltage then it is essential to derive a model for DCVM, which is more complex.

(6) All the plots are given in p.u. and are therefore general. The results of theory, SPICE simulation and experiments have been presented and compared.

(7) During switching ON, only the parallel capacitor experiences additional stress for the design presented in this chapter and the converter enters below resonance. The anti-parallel diode has to undergo additional peak current stress (Fig. 3.5(f)). Therefore closed loop frequency control is necessary.

(8) It has been observed that the SPRC, designed to operate slightly above resonance and with slight discontinuity in the parallel capacitor voltage (as in this chapter), does not show pronounced stresses on resonant inductor and the series capacitor during switching ON.

(9) The response of the converter is dependent on the output filter design. Characteristic impedance of the output filter is a convenient parameter to evaluate this

dependence. It is observed that the switching ON response becomes faster (oscillatory) as  $Z_f$  is decreased. The peak tank current during the transient phase increases with an increase in the value of  $C_f$  and a decrease in the value of  $L_f$ . However, the peak parallel capacitor voltage during the transient phase decreases with a decrease in the value of  $L_f$  and is independent of  $C_f$  for a given value of  $L_f$ .

(10) The transients caused due to sudden short circuit and open circuit conditions have been studied.

(11) The advantages of closed loop operation have been investigated experimentally, by considering the example of the transients caused due to step change in the load condition from full load to half full load condition. It is found that the drawbacks of the open loop operation are overcome. The converter does not enter the leading p.f. mode of operation and the peak stresses are less. It was observed that the parallel capacitor voltage becomes discontinuous due to the closed loop control action, as the operating frequency is corrected.

### **For DCM**

Following are the main observations from the large-signal analysis of the SPRC operating in DCM:

(1) The discrete time domain model is quite effective in predicting the state behavior of the converter during transients. It reduces the computation time drastically.

(2) The large-signal response of the converter during sudden switching ON of the supply voltage, is affected by the value of filter components. For a small value of the filter capacitor, the converter maintains DCM and the transient response is critically damped. For a larger value of filter capacitor, the converter enters the CCM, leading p.f. mode to accommodate an overshoot of the output current which shows an oscillatory response. This may result in more losses during transients. Clearly, since the

choice of filter components is based on the ripple specifications, there is a trade off.

(3) During a step change from full load to half full load conditions, the dead gap is present due to a reduction in the load current.

(4) During sudden short circuiting of the output at full load conditions, the converter enters the leading p.f. mode (CCM), which it maintains. The current in the resonant tank as well in the output section rises to very high values in the absence of a close loop corrective action. Thus, the converter should not be short circuited while in open loop.

(5) The DCM model presented has limitations in predicting the large-signal behavior for full load to open circuit operating conditions. This is because of the occurrence of operating modes not analyzed in this chapter.

For the CCM case, both the open loop and closed loop operations have been investigated in this chapter, however, only the large-signal behavior has been studied. Small-signal analysis of the LCC-type converter operating in the CCM [77], using the large-signal model presented in this chapter is considered in the next chapter. For the DCM case, only open loop results are discussed in this chapter. These results can be used to design the closed loop controller to control the operating frequency of the converter whenever load or supply voltage variations occur.

## Chapter 4

# Small-Signal Analysis using Discrete Time Domain Modeling

The large-signal state equations were obtained in the previous chapter. In this chapter, those equations are linearized about a steady-state operating point to perform the small-signal modeling of the SPRC. Multiple loops have been used. An outer voltage loop, which takes care of the voltage regulation and an inner, state variable feedback loop to improve the dynamics. State variable feedback control has been integrated with the linear small-signal state-space model and the associated control aspects are studied. The small-signal state-space model has been used to study the small signal behavior of the converter for open loop and closed loop operation for parameters like control to output transfer function, audio-susceptibility and output impedance. Key theoretical results have been experimentally verified.

## 4.1 Introduction

In order to make best use of any power converter configuration, it is necessary to formulate proper design procedures. Clearly, these design procedures are governed by the conditions under which a converter has to operate. Before an actual converter is built, it is desirable to know how the converter will behave under these conditions? This has led to three kinds of analysis depending upon the operating state of the converter.

- (1) The steady-state or DC analysis.
- (2) The large-signal analysis.
- (3) The small-signal analysis.

The first two have been presented in chapters 2 and 3, respectively. Small-signal analysis, to which this chapter is devoted, is concerned with the response of the converter to small perturbations in its steady state operating conditions.

The traditional sampled data modeling approach or the discrete time domain modeling approach has been applied to the lesser order resonant converters, the SRC and the PRC. However such an approach was considered to be difficult to apply in the case of SPRC, which is a third order system. Therefore, attempts were made to circumvent this complexity by making approximations. The extended describing function was used in [73], where in all the tank waveforms have been approximated by their fundamental harmonics. However, the resonant tank has a *sampled* response owing to the fact that the converter operation itself is discrete (due to the square wave that appears across the resonant tank). Moreover, since the switching frequency is of the same order as the natural frequency of the tank circuit, both are significant with respect to each other and none can be neglected in favour of the other. Thus, a continuous time domain model is not an *exact* representation [42,49]. The objective of this chapter is to present small-signal analysis based on discrete time domain modeling

method and to study the control aspects of the SPRC. The constant current model has been used to arrive at the discrete time domain model.

The state variable feedback or the pole placement method of control has many advantages over the conventional ones [44, 79, 80]. With this technique, it is possible to place the closed loop poles of the system anywhere in the  $s$  plane. Since the location of its poles determines the behavior of any system, it is possible to achieve the stability and desired dynamic response using the state variable feedback. Further more, since this kind of control is based on feeding back the "states", it can be easily integrated with a small-signal discrete state-space model, the type derived in this chapter. This helps the analytical prediction. The control is done with two feedback loops, a "minor" inner feedback loop and a "major" outer voltage feedback loop [54,81].

The remaining of this chapter is divided into the following sections. Section 4.2 derives the discrete state-space (large signal) model of the SPRC. In section 4.3 the large-signal model described in section 4.2 has been linearized about the steady-state operating point to obtain the small-signal, state-space model. The state feedback control is discussed in section 4.4. The modified small-signal model, with the state variable feedback incorporated into it, is also given in the same section. Dynamic performance parameters (control to output gain, audio susceptibility, etc.) obtained with the model described in sections 4.3 are presented in section 4.5. The results are also compared with those of [73]. Experimental verification of the key theoretical results is presented in section 4.6. Finally, section 4.7 states the conclusions.

## 4.2 The Discrete State-Space Model of the SPRC

Fig. 3.2 shows the discrete time model waveforms for lagging power factor mode of operation of the SPRC. Various intervals are marked in the figure. The total conduction angle (switch + diode), for the  $k^{th}$  event is given by

$$\gamma_k = \alpha_k + \beta_k \quad (4.1)$$

$$\text{where } \alpha_k = \omega_0(t_{1(k)} - t_{0(k)}); \quad \beta_k = \omega_0(t_{0(k+1)} - t_{1(k)}) \quad (4.2)$$

“ $\alpha_k$ ” and “ $\beta_k$ ” stand for the lengths of intervals B and A respectively.

$$\text{Further } \omega_0 = \frac{1}{\sqrt{LC_e}}; \quad C_e = \frac{C_s C_t}{C_s + C_t}; \quad Z = \sqrt{\frac{L}{C_e}} \quad (4.3)$$

Both intervals B and A [Fig. 3.3], are described by two separate sets of equations given in Appendix A. The discrete time domain model obtained using these equations can be found in chapter 3. Equating the final values of the  $k^{th}$  event to the initial values of the  $(k+1)^{th}$  event, the latter can be determined in terms of the initial values of the  $k^{th}$  event [78]. The low ripple approximation, wherein the input and output voltages are assumed constant during an event (one half period), is followed in this chapter. The variations in these voltages during an event are negligible as compared to the step changes they undergo at the beginning or end of an event.

The following state variables were chosen (corresponding to the storage elements in the circuit) for the  $k^{th}$  and  $(k+1)^{th}$  events. It was mentioned earlier that the converter operation is discrete. Since the operating frequency is comparable to the converter's natural frequency, the tank states are discrete. Hence the following state variables are discrete quantities.

$$x_{1(k)} = -i_L(t_{0(k)}); \quad x_{2(k)} = -v_{cs}(t_{0(k)}); \quad x_{3(k)} = -v_{ct}(t_{0(k)}) \quad (4.4)$$

$$x_{1(k+1)} = i_L(t_{0(k+1)}); \quad x_{2(k+1)} = v_{cs}(t_{0(k+1)}); \quad x_{3(k+1)} = v_{ct}(t_{0(k+1)}) \quad (4.5)$$

For the output section of the SPRC (Fig. 3.4), two additional discrete state variables were introduced for the  $k^{th}$  event.

$$x_{4(k)} = I(t_{0(k)}); \quad x_{5(k)} = v_0(t_{0(k)}) \quad (4.6)$$

Using the state variables defined in (4.4) to (4.6), the following discrete state-space model was obtained.

$$\begin{aligned} x_{1(k+1)} = & A_{1B_k} \cdot \sin(\gamma_k) + B_{1B_k} \cdot \cos(\gamma_k) \\ & + C_{1B_k}(2\cos(\beta_k) - 1) \end{aligned} \quad (4.7)$$

$$\begin{aligned} x_{2(k+1)} = & A_{2B_k}(1 - \cos(\gamma_k)) + B_{2B_k} \sin(\gamma_k) \\ & + C_{2B_k}(\alpha_k - \beta_k + 2\sin(\beta_k)) + x_{2(k)} \end{aligned} \quad (4.8)$$

$$\begin{aligned} x_{3(k+1)} = & A_{3B_k}(1 - \cos(\gamma_k)) + B_{3B_k} \sin(\gamma_k) + C_{3B_k}(\alpha_k - \beta_k \\ & + 2\frac{C_e}{C_t} C_{1B_k} \sin(\beta_k)) + x_{3(k)} \end{aligned} \quad (4.9)$$

$$\begin{aligned} x_{4(k+1)} = & x_{4(k)} + 1/X_{Lf} \cdot A_{3B_k}((\beta_k - \alpha_k) + 2 \cdot \sin(\alpha_k) - \sin(\gamma_k)) \\ & + \frac{1}{X_{Lf}} \cdot B_{3B_k}(2 \cdot \cos(\alpha_k) - 1 - \cos(\gamma_k)) - \frac{1}{2X_{Lf}} \cdot C_{3B_k}(\alpha_k - \beta_k)^2 \\ & + \frac{2Z}{X_{Lf}} \frac{C_e}{C_t} C_{1B_k}(1 - \cos(\beta_k)) - \frac{x_{3(k)}}{X_{Lf}}(\beta_k - \alpha_k) - \frac{1}{X_{Lf}} \cdot x_{5(k)}\gamma_k \end{aligned} \quad (4.10)$$

$$x_{5(k+1)} = x_{5(k)} + \gamma_k X_{Cf}(x_{4(k)} + i_{out(k)} - \frac{x_{5(k)}}{R_L}) \quad (4.11)$$

where  $X_{Lf} = \omega_0 L_f$  and  $X_{Cf} = \frac{1}{\omega_0 C_f}$

### 4.3 Linearization of SPRC about the Equilibrium Point

The discrete state-space equations (4.7) to (4.11) are non linear with the following general form:

$$x_{i(k+1)} = f_i(x_1(k), x_2(k), x_3(k), x_4(k), x_5(k), \gamma_k, E(k), i_{out(k)}) \quad (4.12)$$

Where “ $f_i$ ” represents some non-linear function of the relevant independent variables specified on the right hand side of the above equation and  $i = 1 \dots 5$ .

These equations can be linearized using the Taylor’s expansion about the equilibrium point. This equilibrium point or the steady-state operating point of the converter can be determined by applying the following symmetry condition to equations (4.7) through (4.11).

$$x_{i(k)} = x_{i(k+1)} \quad (4.13)$$

Simultaneous solution of the resultant equations yields the following steady-state solution, which is the same as derived in continuous time domain in [12].

$$\begin{aligned} x_{1(k)} = & -(E_{(k)}/Z) \cdot \sin(\gamma_k)/(1 + \cos(\gamma_k)) - \frac{C_e}{C_t} \cdot I_{0(k)} \\ & + \frac{C_e}{C_t} \cdot I_{0(k)} \cdot [\cos(\alpha_k) + \cos(\beta_k)]/(1 + \cos(\gamma_k)) \end{aligned} \quad (4.14)$$

$$\begin{aligned} x_{2(k)} = & Z \cdot I_{0(k)} \left(\frac{C_e}{C_s}\right) \left(\frac{C_e}{C_t}\right) [\sin(\beta_k) - \sin(\alpha_k)]/(1 + \cos(\gamma_k)) \\ & - Z \left(\frac{C_e}{C_t}\right) \left(\frac{C_e}{C_s}\right) I_{0(k)} \cdot (\gamma_k - 2\alpha_k)/2 \end{aligned} \quad (4.15)$$

$$\begin{aligned} x_{3(k)} = & Z \cdot I_{0(k)} \left(\frac{C_e}{C_t}\right)^2 [\sin(\beta_k) - \sin(\alpha_k)]/(1 + \cos(\gamma_k)) \\ & + Z \left(\frac{C_e}{C_t}\right) \left(\frac{C_e}{C_s}\right) \cdot I_{0(k)} \cdot (\gamma_k - 2\alpha_k)/2 \end{aligned} \quad (4.16)$$

$$x_{4(k)} = x_{5(k)}/R_L \quad (4.17)$$

$$x_{5(k)} = \frac{2}{\gamma_k} \cdot \frac{C_e}{C_t} E_{(k)} \cdot \left( \frac{-\sin(\gamma_k/2 - \alpha_k)}{\cos(\gamma_k/2)} + (\gamma_k/2 - \alpha_k) \right) \quad (4.18)$$

The subscript “ $k$ ” may be dropped while representing steady-state expressions as above, a convention followed through out this chapter. Taylor’s expansion of (4.7) to (4.11) about the equilibrium point (defined by equations (4.14) - (4.18)), yields five linearized small-signal equations of the following general form ( $i = 1 \dots 5$ ).

$$\delta x_{i(k+1)} = \left. \frac{\partial f_i}{\partial x_{1(k)}} \right|_{eq} \cdot \delta x_{1(k)} + \left. \frac{\partial f_i}{\partial x_{2(k)}} \right|_{eq} \cdot \delta x_{2(k)} + \left. \frac{\partial f_i}{\partial x_{3(k)}} \right|_{eq} \cdot \delta x_{3(k)}$$

$$\begin{aligned}
& + \left. \frac{\partial f_i}{\partial x_{4(k)}} \right|_{eq} \cdot \delta x_{4(k)} + \left. \frac{\partial f_i}{\partial x_{5(k)}} \right|_{eq} \cdot \delta x_{5(k)} + \left. \frac{\partial f_i}{\partial E(k)} \right|_{eq} \cdot \delta E(k) + \left. \frac{\partial f_i}{\partial \gamma_k} \right|_{eq} \cdot \delta \gamma_k \\
& \left. \frac{\partial f_i}{\partial i_{out(k)}} \right|_{eq} \cdot \delta i_{out(k)} \tag{4.19}
\end{aligned}$$

In the above equation “|<sub>eq</sub>” implies “at equilibrium”.

All the small-signal equations can be clubbed together and represented in the matrix form as below:

$$[\delta x_{i(k+1)}] = [A] \cdot [\delta x_{i(k)}] + [B] \cdot [\delta u_{(k)}]$$

Or

$$\begin{aligned}
\begin{bmatrix} \delta x_{1(k+1)} \\ \delta x_{2(k+1)} \\ \delta x_{3(k+1)} \\ \delta x_{4(k+1)} \\ \delta x_{5(k+1)} \end{bmatrix} &= \begin{bmatrix} a_{11} & a_{12} & a_{13} & a_{14} & a_{15} \\ a_{21} & a_{22} & a_{23} & a_{24} & a_{25} \\ a_{31} & a_{32} & a_{33} & a_{34} & a_{35} \\ a_{41} & a_{42} & a_{43} & a_{44} & a_{45} \\ a_{51} & a_{52} & a_{53} & a_{54} & a_{55} \end{bmatrix} \cdot \begin{bmatrix} \delta x_{1(k)} \\ \delta x_{2(k)} \\ \delta x_{3(k)} \\ \delta x_{4(k)} \\ \delta x_{5(k)} \end{bmatrix} \\
&+ \begin{bmatrix} b_{11} & b_{12} & b_{13} \\ b_{21} & b_{22} & b_{23} \\ b_{31} & b_{32} & b_{33} \\ b_{41} & b_{42} & b_{43} \\ b_{51} & b_{52} & b_{53} \end{bmatrix} \cdot \begin{bmatrix} \delta \gamma_k \\ \delta E(k) \\ \delta i_{out(k)} \end{bmatrix} \tag{4.20}
\end{aligned}$$

The elements  $a_{ij}$ s and  $b_{ij}$ s of matrix A and B can be determined by using the following:

$$a_{ij} = \left. \frac{\partial f_i}{\partial x_{j(k)}} \right|_{eq} \tag{4.21}$$

$$b_{i1} = \left. \frac{\partial f_i}{\partial \gamma_k} \right|_{eq} ; b_{i2} = \left. \frac{\partial f_i}{\partial E(k)} \right|_{eq} ; b_{i3} = \left. \frac{\partial f_i}{\partial i_{out(k)}} \right|_{eq} \tag{4.22}$$

where  $i = 1 \dots 5; j = 1 \dots 5$ .

In the following equations  $r_1 = C_e/C_s$  and  $r_2 = C_e/C_t$ :

$$a_{11} = -\cos(\gamma) + \left[ \frac{\partial \alpha_k}{\partial x_{1(k)}} \cdot \frac{\partial f_1}{\partial \alpha_k} \right]_{eq} \quad (4.23)$$

$$a_{12} = (1/Z)\sin(\gamma) + \left[ \frac{\partial \alpha_k}{\partial x_{2(k)}} \cdot \frac{\partial f_1}{\partial \alpha_k} \right]_{eq} \quad (4.24)$$

$$a_{13} = (1/Z)\sin(\gamma) + \left[ \frac{\partial \alpha_k}{\partial x_{3(k)}} \cdot \frac{\partial f_1}{\partial \alpha_k} \right]_{eq} \quad (4.25)$$

$$a_{14} = r_2 \cdot \cos(\gamma) + r_2 \cdot (1 - 2\cos(\beta)) + \left[ \frac{\partial \alpha_k}{\partial x_{4(k)}} \cdot \frac{\partial f_1}{\partial \alpha_k} \right]_{eq} \quad (4.26)$$

$$a_{21} = -Z \cdot r_1 \cdot \sin(\gamma) + \left[ \frac{\partial \alpha_k}{\partial x_{1(k)}} \cdot \frac{\partial f_2}{\partial \alpha_k} \right]_{eq} \quad (4.27)$$

$$a_{22} = -r_1 \cdot \cos(\gamma) + r_1 - 1 + \left[ \frac{\partial \alpha_k}{\partial x_{2(k)}} \cdot \frac{\partial f_2}{\partial \alpha_k} \right]_{eq} \quad (4.28)$$

$$a_{23} = -r_1 \cdot \cos(\gamma) + r_1 + \left[ \frac{\partial \alpha_k}{\partial x_{3(k)}} \cdot \frac{\partial f_2}{\partial \alpha_k} \right]_{eq} \quad (4.29)$$

$$a_{24} = Z \cdot r_1 \cdot r_2 \cdot \sin(\gamma) + Z \cdot r_1 \cdot r_2 \cdot (\beta - \alpha - 2\sin(\beta)) + \left[ \frac{\partial \alpha_k}{\partial x_{4(k)}} \cdot \frac{\partial f_2}{\partial \alpha_k} \right]_{eq} \quad (4.30)$$

$$a_{31} = -Z \cdot r_2 \cdot \sin(\gamma) + \left[ \frac{\partial \alpha_k}{\partial x_{1(k)}} \cdot \frac{\partial f_3}{\partial \alpha_k} \right]_{eq} \quad (4.31)$$

$$a_{32} = -r_2 \cdot \cos(\gamma) + r_2 + \left[ \frac{\partial \alpha_k}{\partial x_{2(k)}} \cdot \frac{\partial f_3}{\partial \alpha_k} \right]_{eq} \quad (4.32)$$

$$a_{33} = -r_2 \cdot \cos(\gamma) + r_2 - 1 + \left[ \frac{\partial \alpha_k}{\partial x_{3(k)}} \cdot \frac{\partial f_3}{\partial \alpha_k} \right]_{eq} \quad (4.33)$$

$$a_{34} = Z \cdot (r_2)^2 \sin(\gamma) - Z \cdot r_2 \cdot (2 \cdot r_2 \cdot \sin(\beta) + r_1 \cdot (\beta - \alpha)) + \left[ \frac{\partial \alpha_k}{\partial x_{4(k)}} \cdot \frac{\partial f_3}{\partial \alpha_k} \right]_{eq} \quad (4.34)$$

$$a_{41} = -\frac{Z \cdot r_2}{X_{Lf}} \cdot (2\cos(\alpha) - 1 - \cos(\gamma)) + \left[ \frac{\partial \alpha_k}{\partial x_{1(k)}} \cdot \frac{\partial f_4}{\partial \alpha_k} \right]_{eq} \quad (4.35)$$

$$a_{42} = \frac{r_2}{X_{Lf}} \cdot ((\beta - \alpha) + 2 \cdot \sin(\alpha) - \sin(\gamma)) + \left[ \frac{\partial \alpha_k}{\partial x_{2(k)}} \cdot \frac{\partial f_4}{\partial \alpha_k} \right]_{eq} \quad (4.36)$$

$$a_{43} = \frac{r_2}{X_{Lf}} \cdot ((\beta - \alpha) + 2 \cdot \sin(\alpha) - \sin(\gamma)) - \frac{(\beta - \alpha)}{X_{Lf}} + \left[ \frac{\partial \alpha_k}{\partial x_{3(k)}} \cdot \frac{\partial f_4}{\partial \alpha_k} \right]_{eq} \quad (4.37)$$

$$a_{44} = 1 + \frac{Z \cdot r_2^2}{X_{Lf}} (2 \cos(\alpha) - 1 - \cos(\gamma)) - \frac{Z \cdot r_1 \cdot r_2 \cdot (\alpha - \beta)^2}{2 \cdot X_{Lf}} + \frac{2 \cdot Z \cdot r_2^2}{X_{Lf}} (\cos(\beta) - 1) + \left[ \frac{\partial \alpha_k}{\partial x_{4(k)}} \cdot \frac{\partial f_4}{\partial \alpha_k} \right]_{eq} \quad (4.38)$$

$$a_{45} = -\frac{\gamma}{X_{Lf}} \quad (4.39)$$

$$a_{54} = \gamma X_{Cf} \quad (4.40)$$

$$a_{55} = 1 - \frac{\gamma X_{Cf}}{R_L} \quad (4.41)$$

$$b_{11} = A_{1B} \cos(\gamma) - B_{1B} \sin(\gamma) - 2 \cdot C_{1B} \sin(\beta) \quad (4.42)$$

$$b_{21} = A_{2B} \cdot \sin(\gamma) + B_{2B} \cdot \cos(\gamma) + 2 \cdot C_{2B} \cos(\beta) \quad (4.43)$$

$$b_{31} = A_{3B} \sin(\gamma) + B_{3B} \cos(\gamma) - C_{3B} + 2 \cdot \left( \frac{C_e}{C_t} \right) \cdot C_{1B} \cos(\beta) \quad (4.44)$$

$$b_{41} = \frac{1}{X_{Lf}} A_{3B} (1 - \cos(\gamma)) + \frac{1}{X_{Lf}} B_{3B} \sin(\gamma) + \frac{C_{3B}}{X_{Lf}} (2\alpha - \gamma) + \frac{2}{X_{Lf}} \left( \frac{C_e}{C_t} \right) \cdot C_{1B} \sin(\beta) - \frac{x_3}{X_{Lf}} - \frac{x_5}{X_{Lf}} \quad (4.45)$$

$$b_{12} = \frac{\sin(\gamma)}{Z} + \left[ \frac{\partial \alpha_k}{\partial E_{(k)}} \cdot \frac{\partial f_1}{\partial \alpha_k} \right]_{eq} \quad (4.46)$$

$$b_{22} = -r_1 \cdot \cos(\gamma) + r_1 + \left[ \frac{\partial \alpha_k}{\partial E_{(k)}} \cdot \frac{\partial f_2}{\partial \alpha_k} \right]_{eq} \quad (4.47)$$

$$b_{32} = -r_2 \cdot \cos(\gamma) + r_2 + \left[ \frac{\partial \alpha_k}{\partial E_{(k)}} \cdot \frac{\partial f_3}{\partial \alpha_k} \right]_{eq} \quad (4.48)$$

$$b_{42} = \frac{r_2}{X_{Lf}} ((\beta - \alpha) + 2 \sin(\alpha) - \sin(\gamma)) + \left[ \frac{\partial \alpha_k}{\partial E_{(k)}} \cdot \frac{\partial f_4}{\partial \alpha_k} \right]_{eq} \quad (4.49)$$

$$b_{53} = \gamma X_{Cf} \quad (4.50)$$

$$a_{15} = a_{25} = a_{35} = a_{51} = a_{52} = a_{53} = 0 \quad (4.51)$$

$$b_{13} = b_{23} = b_{33} = b_{43} = b_{51} = b_{52} = 0 \quad (4.52)$$

The partial derivatives involved in the above equations are evaluated next. For this the parallel capacitor voltage is equated to zero at the end of interval B, which leads to the following equation:

$$\begin{aligned} r_2 \cdot (E_k + x_2(k) + x_3(k)) \cdot (1 - \cos(\alpha_k)) + Z \cdot r_2 \cdot (-x_1(k) \\ + r_2 \cdot x_4(k)) \sin(\alpha_k) + Z \cdot r_1 \cdot r_2 \cdot x_4(k) \cdot \alpha_k - x_3(k) = 0 \end{aligned} \quad (4.53)$$

Then, using (4.53), the partial derivatives (evaluated at the equilibrium point) obtained are given by:

$$\frac{\partial \alpha_k}{\partial x_1(k)} = \frac{Z \cdot \sin(\alpha)}{D} \quad (4.54)$$

$$\frac{\partial \alpha_k}{\partial x_2(k)} = \frac{-(1 - \cos(\alpha))}{D} \quad (4.55)$$

$$\frac{\partial \alpha_k}{\partial x_3(k)} = \frac{1 - r_2 \cdot (1 - \cos(\alpha))}{r_2 \cdot D} \quad (4.56)$$

$$\frac{\partial \alpha_k}{\partial x_4(k)} = \frac{-(r_2 \cdot Z \cdot \sin(\alpha) + Z \cdot r_1 \cdot \alpha)}{D} \quad (4.57)$$

$$\frac{\partial \alpha_k}{\partial E_k} = \frac{\cos(\alpha) - 1}{(E + x_2 + x_3) \sin(\alpha)} \quad (4.58)$$

$$\begin{aligned} \text{where } D = (E + x_2 + x_3) \sin(\alpha) + Z \cdot (-x_1 + r_2 \cdot x_4) \cos(\alpha) \\ + Z \cdot r_1 \cdot x_4 \end{aligned} \quad (4.59)$$

Using (4.7) - (4.10) (also refer to (4.12)) yield the following:

$$\frac{\partial f_1}{\partial \alpha_k} = -2 \cdot r_2 \cdot x_4 \cdot \sin(\beta) \quad (4.60)$$

$$\frac{\partial f_2}{\partial \alpha_k} = Z \cdot r_1 \cdot r_2 \cdot x_4 [2 \cos(\beta) - 2] \quad (4.61)$$

$$\frac{\partial f_3}{\partial \alpha_k} = Z \cdot r_2 \cdot x_4 [2 \cdot r_2 \cdot \cos(\beta) + 2 \cdot r_1] \quad (4.62)$$

$$\begin{aligned} \frac{\partial f_4}{\partial \alpha_k} = \frac{r_2}{X_{Lf}} (E + x_2 + x_3) \cdot (-2 + 2 \cos(\alpha)) \\ - \frac{2Z \cdot r_2}{X_{Lf}} (-x_1 + r_2 \cdot x_4) (\cos(\alpha)) - \frac{2Z \cdot r_1 \cdot r_2 \cdot x_4}{X_{Lf}} (2\alpha - \gamma) \end{aligned}$$

$$+\frac{2Z.r_2^2.x_4}{X_{Lf}}.\sin(\beta) + \frac{x_3\alpha}{X_{Lf}} \quad (4.63)$$

The small-signal model derived in this section can be used to predict the small signal behavior of the frequency controlled SPRC.

## 4.4 State Feedback Control

This section describes the implementation of the “state feedback” or the “pole placement method” [44,79,80] for improving the dynamics of the SPRC. The results obtained with state feedback control are compared with the  $\gamma$  or frequency control discussed in the previous section. Results are also compared with those obtained in [73].

### 4.4.1 State Variable Feedback

It is well known [79, pp. 188] that stabilization of an unstable system may not necessarily be achieved by the use of “cascade compensators”. Such compensators may provide minimal improvement to the system’s time response. This is because although the compensator’s transfer function cancels the undesired poles and zeros of the plant’s transfer function, the “unstable” natural frequency of the system may still exist, rendering an unstable control system. This kind of compensation may also accentuate the noise problems when a higher gain is required. It is therefore desirable to introduce some kind of “feedback” compensation [79,80] which has the following advantages.

- (1) Faster Response
- (2) Noise problems are minimal.
- (3) For the control systems, such as the one developed in this chapter, which require

a tight loop stabilization to isolate the dynamics of converter from the outer voltage loop, an inner “feedback loop” is desirable.

The “states” of the system are the natural choice as feedback variables as they summarize all the current information about the system. All that is required to implement this technique is that the system should be “state controllable”, which means its controllability matrix must be non singular. State variable feedback allows us to place the poles of the system at arbitrary locations (and thus achieving the desired dynamic response) without disturbing the internal stability of the system. Thus the choice of state variable feedback is justified.

#### 4.4.2 Control Law

The fed back “states” need to be mixed in proper proportion to constitute the proper control signal. This requires an appropriate control law. The following control law has been used in this work.

$$V_{control} = S_1.Z.x_{1(k+1)} + S_2.x_{2(k+1)} + S_3.x_{3(k+1)} \quad (4.64)$$

This control law can be linearized about the equilibrium point as below:

$$\delta V_{control} = S_1.Z.\delta x_{1(k+1)} + S_2.\delta x_{2(k+1)} + S_3.\delta x_{3(k+1)} \quad (4.65)$$

Substituting the values of  $\delta x_{i(k+1)}$  from (4.20), and solving for  $\delta \gamma_k$  yields the following:

$$\begin{aligned} \delta \gamma_k = & h_1.\delta x_{1(k)} + h_2.\delta x_{2(k)} + h_3.\delta x_{3(k)} + h_4.\delta x_{4(k)} \\ & + h_5.\delta x_{5(k)} + h_6.\delta E(k) + h_7.\delta i_{out(k)} + h_8.\delta V_{control} \end{aligned} \quad (4.66)$$

where;

$$h_1 = -\frac{S_1.Z.a_{11} + S_2.a_{21} + S_3.a_{31}}{d} \quad (4.67)$$

$$h_2 = -\frac{S_1.Z.a_{12} + S_2.a_{22} + S_3.a_{32}}{d} \quad (4.68)$$

$$h_3 = -\frac{S_1.Z.a_{13} + S_2.a_{23} + S_3.a_{33}}{d} \quad (4.69)$$

$$h_4 = -\frac{S_1.Z.a_{14} + S_2.a_{24} + S_3.a_{34}}{d} \quad (4.70)$$

$$h_5 = -\frac{S_1.Z.a_{15} + S_2.a_{25} + S_3.a_{35}}{d} \quad (4.71)$$

$$h_6 = -\frac{S_1.Z.b_{12} + S_2.b_{22} + S_3.b_{32}}{d} \quad (4.72)$$

$$h_7 = -\frac{S_1.Z.b_{13} + S_2.b_{23} + S_3.b_{33}}{d} \quad (4.73)$$

$$h_8 = \frac{1}{d} \quad (4.74)$$

$$d = S_1.Z.b_{11} + S_2.b_{21} + S_3.b_{31} \quad (4.75)$$

### 4.4.3 Integration with SPRC Model

The linearized small-signal state-space model of the SPRC can be integrated with the linearized state feedback control law by substituting the value of  $\delta\gamma_k$  from (4.66) into (4.20), the state-space model gets modified as below:

$$[\delta x_{i(k+1)}] = [A_{new}] \cdot [\delta x_{i(k)}] + [B_{new}] \cdot [\delta u_{new(k)}] \quad (4.76)$$

where;

$$[A_{new}] = \begin{bmatrix} a_{11} + b_{11}.h_1 & a_{12} + b_{11}.h_2 & a_{13} + b_{11}.h_3 & a_{14} + b_{11}.h_4 & a_{15} + b_{11}.h_5 \\ a_{21} + b_{21}.h_1 & a_{22} + b_{21}.h_2 & a_{23} + b_{21}.h_3 & a_{24} + b_{21}.h_4 & a_{25} + b_{21}.h_5 \\ a_{31} + b_{31}.h_1 & a_{32} + b_{31}.h_2 & a_{33} + b_{31}.h_3 & a_{34} + b_{31}.h_4 & a_{35} + b_{31}.h_5 \\ a_{41} + b_{41}.h_1 & a_{42} + b_{41}.h_2 & a_{43} + b_{41}.h_3 & a_{44} + b_{41}.h_4 & a_{45} + b_{41}.h_5 \\ a_{51} + b_{51}.h_1 & a_{52} + b_{51}.h_2 & a_{53} + b_{51}.h_3 & a_{54} + b_{51}.h_4 & a_{55} + b_{51}.h_5 \end{bmatrix}$$

$$[B_{new}] = \begin{bmatrix} b_{11} \cdot i_8 & b_{11} \cdot h_6 + b_{12} & b_{11} \cdot h_7 + b_{13} \\ b_{21} \cdot h_8 & b_{21} \cdot h_6 + b_{22} & b_{21} \cdot h_7 + b_{23} \\ b_{31} \cdot h_8 & b_{31} \cdot h_6 + b_{32} & b_{31} \cdot h_7 + b_{33} \\ b_{41} \cdot h_8 & b_{41} \cdot h_6 + b_{42} & b_{41} \cdot h_7 + b_{43} \\ b_{51} \cdot h_8 & b_{51} \cdot h_6 + b_{52} & b_{51} \cdot h_7 + b_{53} \end{bmatrix}$$

$$[\delta u_{new(k)}] = \begin{bmatrix} \delta V_{control} \\ \delta E_{(k)} \\ \delta i_{out(k)} \end{bmatrix}$$

#### 4.4.4 The Complete Control Scheme

Fig. 4.1 shows the overall control structure realized in this chapter. There are two feedback loops in the system. An inner state feedback loop, which feeds back the “perturbations in states” according to the control law described in section 4.4.2 and an outer voltage feedback loop which regulates the output voltage. The feedback signals from these loops are compared and used to drive the voltage controlled oscillator, which controls the operating frequency of the input inverter.

### 4.5 Dynamic Performance Parameters

The dynamic performance parameters like the control to output gain, audio susceptibility and output impedance are useful in evaluating the dynamic performance of a converter. All these parameters are studied in this section. The converter can be controlled by controlling the frequency ( $\gamma$  control). Both the open loop and closed loop control aspects have been investigated using the models developed in the earlier sections.

An SPRC with the following design specifications has been designed. The analysis presented is used to predict the small-signal behavior of the converter designed.

Input supply voltage,  $2E_{min} = 50 \text{ V}$

Output voltage of the converter,  $V_0 = 24 \text{ V}$

Maximum output power,  $P_o = 100 \text{ Watts}$ ,

Switching frequency,  $f_t = 200 \text{ kHz}$ .

Equivalent resonant frequency ( $f_0$ ) = 250 kHz.

Designed values are:

$L_s = 17.74\mu\text{H}$  ;  $C_s = 0.047\mu\text{F}$  ;  $C_t = n^2 C'_t = 0.047\mu\text{F}$ ;  $n = 1$ .

$R_{L(\text{rated})} = 6.74 \Omega$ .

$L_f = 1000\mu\text{H}$ ;  $C_f = 1.0\mu\text{F}$ .

The control to output gain, audio susceptibility and output impedance with and without state feedback, were obtained using (4.20) and (4.76), respectively with the help of PRO-MATLAB.

Fig. 4.2 shows the magnitude and phase plot of the open loop control to output transfer function obtained using the proposed discrete small-signal model (Eq. 4.20).

No feedback loops are used. Because of the power stage, a -40 dB roll off can be observed starting at the corner frequency of the power stage filter. For the purpose of comparison, plots obtained using the model of [73] are also included in the same figure (also refer to Table 4.1). Fig. 4.3 shows the bode plots for the audio-susceptibility and output impedance from the proposed model. The audio-susceptibility plot is useful in determining the effect of perturbations of the input supply voltage on the converter output. Fig. 4.3(a) shows that for low perturbation frequencies, the input supply variations appear at the converter output with an approximate gain of unity. However, as the perturbation frequency goes up, this effect becomes less and less

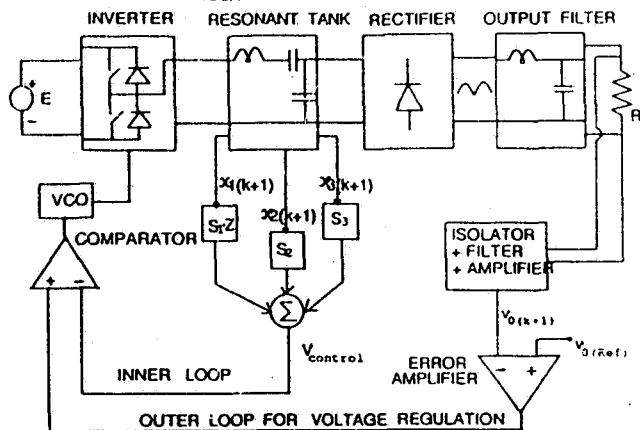


Figure 4.1: Complete control scheme of the SPRC. Note that the terms  $x_1(k+1)$ ,  $x_2(k+1)$  etc. represent the sampled values.

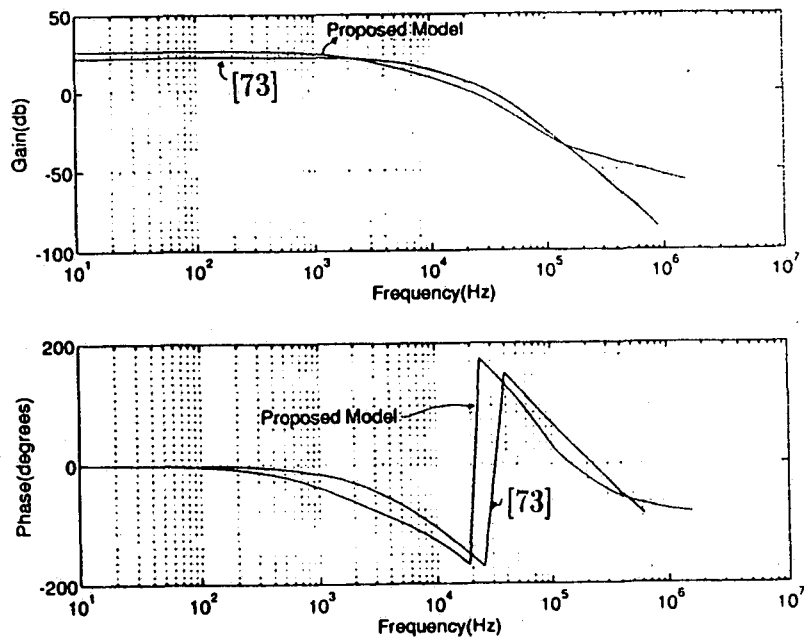


Figure 4.2: Control to output bode plots for frequency controlled, open loop, without state feedback case. Details of the converter: Half bridge configuration with the details given in section 4.5. The plots obtained with the model of [73] are also included for comparison.

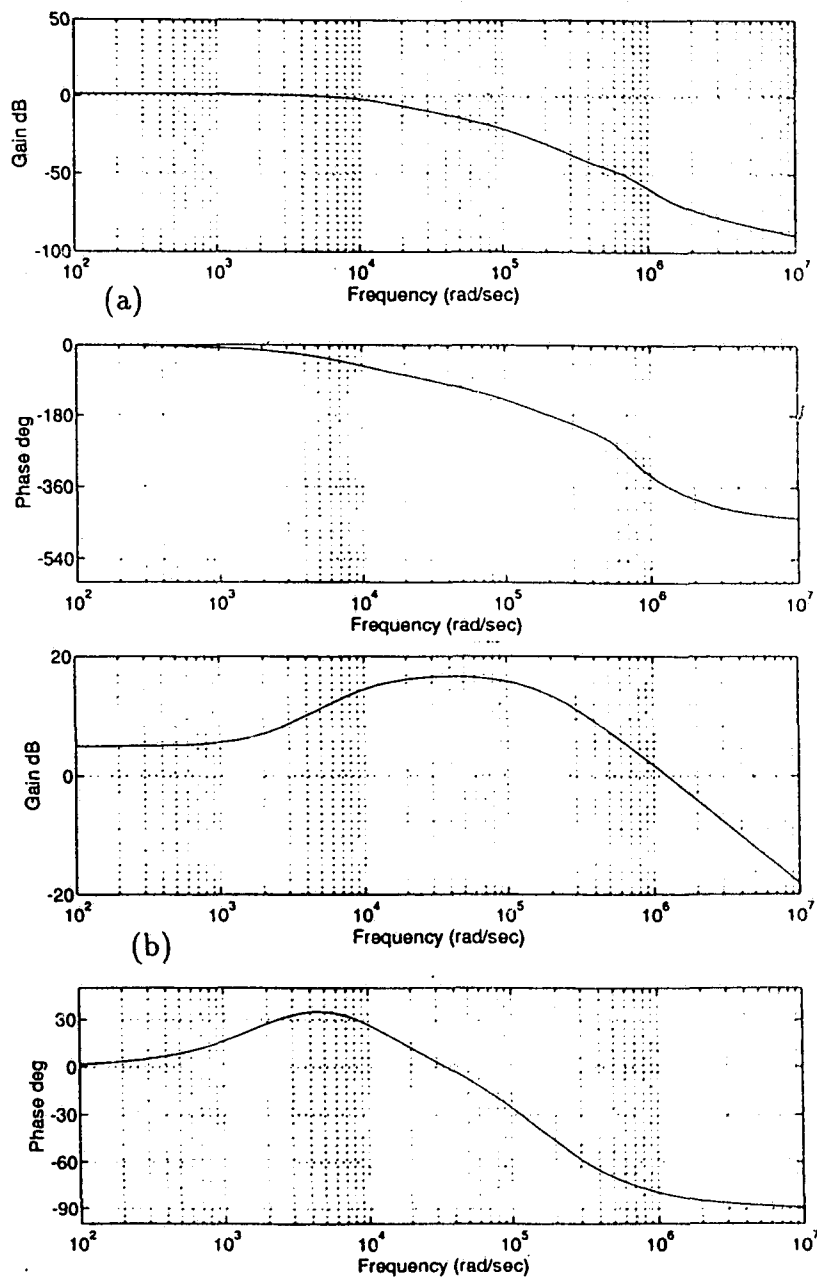


Figure 4.3: (a) Open loop audio-susceptibility bode plot obtained with the proposed model. (b) Output impedance transfer function.

Table 4.1: Comparison with [73]

	GM(db)	PM(deg)	Bandwidth(kHz)
Proposed Model	0.25	1.39	24
Method of [73]	0.10	0.25	30
Experiment	0.50	2.20	26

pronounced. Output impedance plot is useful in determining the transient response of the converter. It is desirable that the gain plot does not show a peaking nature and the magnitude is as low as possible in order to have a good transient response.

Fig. 4.4 shows the control to output transfer function for half the rated load condition obtained with the model. For this condition, the switching frequency was increased to  $245\text{ kHz}$  to regulate the output voltage. The audio-susceptibility and output impedance plots are given in Fig. 4.5

#### 4.5.1 Stability Aspects and Closed Loop Operation

Using (4.20), the open loop eigen values for the given SPRC are found to be:

$$-0.0232 + 0.4931j; \quad -0.0232 - 0.4931j; \quad 0.9765; \quad 0.6456; \quad 0.6038$$

Clearly the dynamics of the open loop system are controlled by a dominant pair of complex poles. The other poles are too far to affect significantly. Also all the values lie inside a unit circle, which satisfies the stability condition of a discrete system. Therefore the system is stable. But the phase margin is only 1.39 degrees and the system is "barely stable". This however is dependent on the DC gain of the control to output transfer function, which depends on the slope of the converter gain versus the normalized operating frequency curve and also on the gain of the VCO.

Further, when the outer feedback loop is included for output voltage regulation,

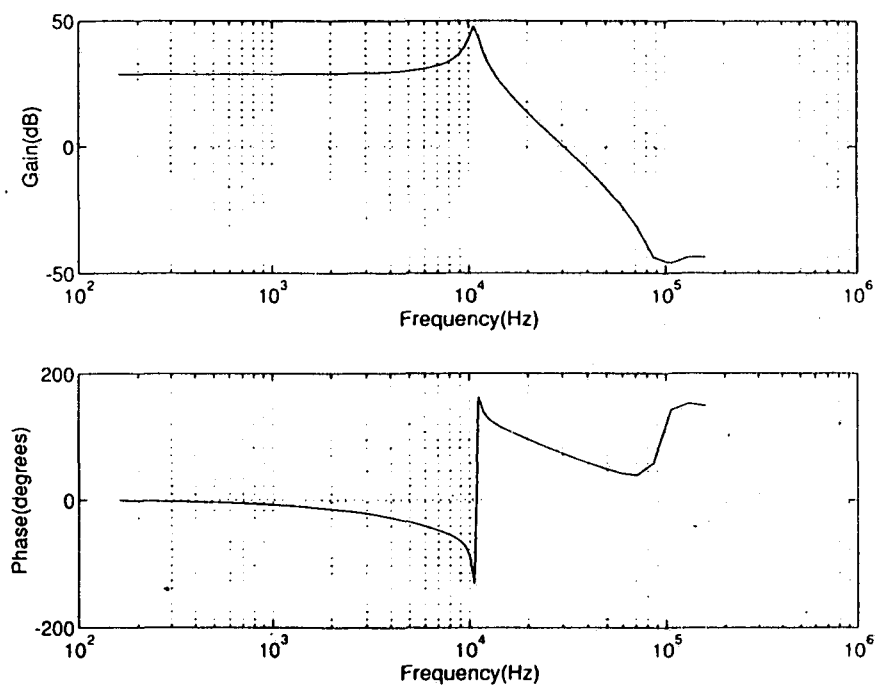


Figure 4.4: Open loop control to output transfer function at half the rated load condition. Load resistance =  $13.4 \Omega$ ,  $f_{switching} = 245 \text{ kHz}$

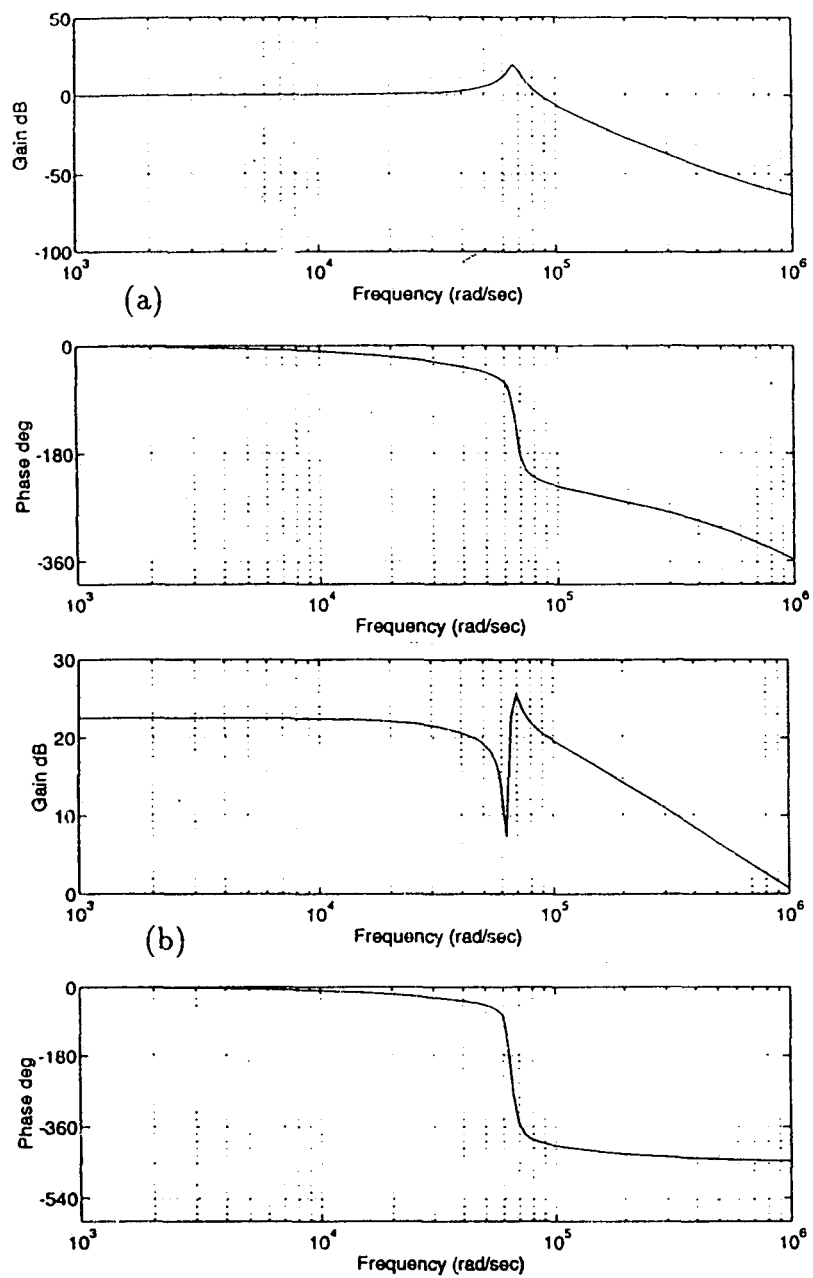


Figure 4.5: (a) Open loop audio-susceptibility bode plot obtained with the proposed model for half the rated load condition. (b) Output impedance transfer function.

the question of stability and desirable phase and gain margins arises. A phase margin of at least  $50^\circ$  is desirable for stability. As the results obtained in this section show, the addition of state feedback greatly improves the performance of a closed loop frequency controlled SPRC.

### (a) Closed Loop Control

Loop gain  $T$  is most important for a feedback system, as it determines the stability aspects of the closed loop system. The loop gain transfer function is given by  $A_{sprc} \cdot A_{error} \cdot A_{fb}$  where  $A_{sprc}$  is the open loop control to output transfer function of the SPRC,  $A_{error}$  is the transfer function of the error amplifier and  $A_{fb}$  is the transfer function of the feedback block. Matrices  $A$  and  $A_{new}$  are used depending on whether one is dealing with the frequency controlled SPRC or with the state feedback controlled SPRC. The loop gain crossover frequency determines the phase margin and the control bandwidth. For stability, magnitude plot of the loop gain, must cross the 0 db line before the total phase shift reaches  $360^\circ$ . A higher phase margin restricts the control bandwidth which limits the advantages of the feedback. On the other hand, a higher control bandwidth restricts the phase margin, reducing the stability of the system. The midband loop gain, on the other hand is simply the product of the dc gain terms of individual transfer functions around the closed loop.

If the desired closed loop properties are not met, then proper compensation need be designed. For the frequency controlled SPRC, without state feedback, only external compensation can be used. However, with the state feedback controlled SPRC, we can achieve the desired closed loop response by varying the feedback gain matrix. External compensation may still be used, if desired. An integral/lead-lead/lag compensator has been recommended by some authors [50,76].

The state feedback aspects are considered next.

### (b) Control with State Feedback

The rank of the controllability matrix is found by using the “rank” command of MATLAB and is found to be 5 for our system and therefore the system is controllable. Thus by the definition of controllability, it is possible to assign the closed loop poles of the system to arbitrary locations by adjusting the feedback gain matrix  $S = [S_1 S_2 S_3 S_4 S_5]$  to any desired value. It must be pointed out here that in the state feedback loop we are only feeding back three of the (tank) states. The output voltage, which is also a state, is fed back through an outer feedback loop. Matrix  $S$  is adjusted until the desired performance is obtained. The three variables  $S_1, S_2, S_3$  can be suitably tuned. For convenience, one of the variables ( $S_3$ ) was kept constant and the other two variables were tuned. Thus the design was done by varying the ratio  $\frac{S_1}{S_2}$ . Fig. 4.6 shows the open loop eigen values of matrix  $A_{new}$  in the  $z$  plane for  $S_3 = 1.0$ . There are five roots  $\lambda_1 \dots \lambda_5$ . It is found that  $\lambda_1$  always remains at the origin.  $\lambda_4$  is nearly independent of  $S_i$  variation.  $\lambda_5$  moves out of the unit circle as the ratio  $\frac{S_1}{S_2}$  is decreased, thus rendering the system unstable. The complex pair ( $\lambda_2, \lambda_3$ ) also moves towards the positive side of the real axis, with a gradual reduction in the magnitude of the imaginary part of the roots. This is not desirable, as such a system will be slow in recovering from the transient disturbances. Fig. 4.7 shows the trajectory of the poles of the system when the ratio  $\frac{S_1}{S_2}$  is made negative. As this ratio is reduced,  $\lambda_5$  moves towards the origin on the real axis and the complex pair moves left, acquiring more negative real part. This is a more desirable situation.

Fig. 4.8 shows the “MATLAB” realization of the controlled SPRC. The blocks are numbered for convenience. They can be combined to form an aggregate system and study the closed loop operation of the SPRC with and without state feedback. The segment of the “MATLAB” program used to achieve this is also shown in Fig. 4.8. The format of the commands “nblocks”, “blkbuild” and “connect” is available in

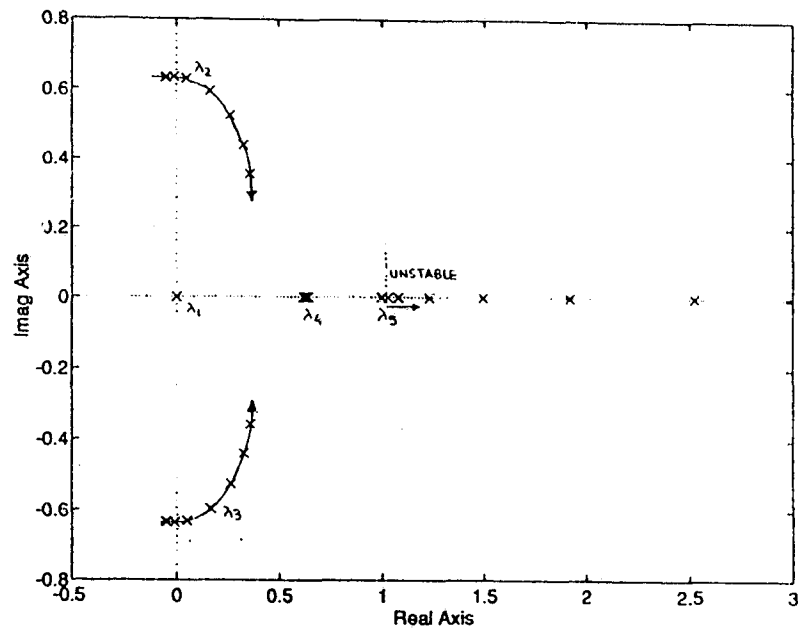


Figure 4.6: Trajectory of the open loop poles of the state feedback controlled SPRC.  $S_3 = 1.0$ , while the ratio  $\frac{S_1}{S_2}$  is varied.

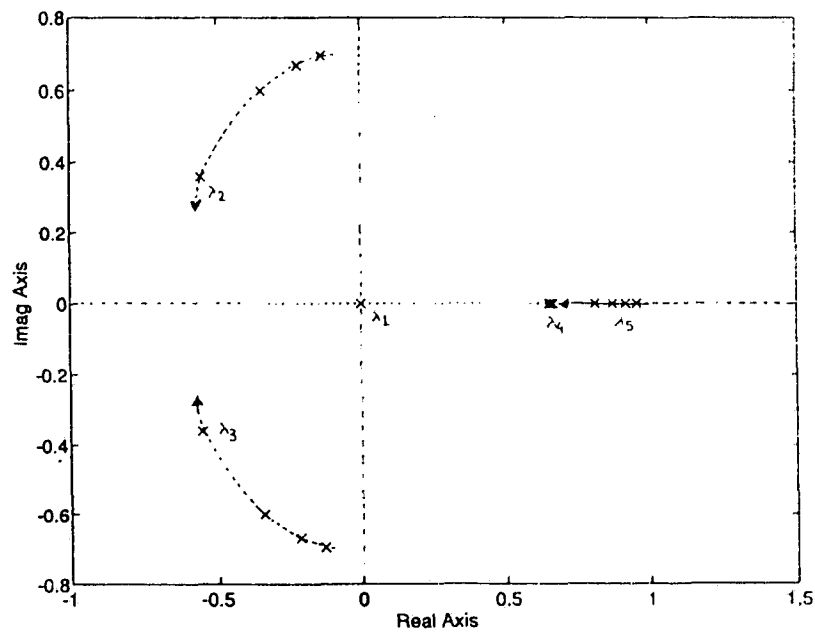


Figure 4.7: Trajectory of the open loop poles of the state feedback controlled SPRC.  $S_3 = 1.0$ , while the ratio  $\frac{S_1}{S_2}$  is made negative. As the magnitude of this ratio becomes smaller, the roots (except  $\lambda_1$  and  $\lambda_4$ ) move towards the left of the origin.

“MATLAB” manual. The block marked ‘3’, which represents the linearized, discrete small-signal model of the SPRC will have the form given by (4.20) or (4.76), depending on whether the state feedback is incorporated or not. Matrices  $A_c$  and  $B_c$  represent the continuous time domain representation of matrices  $A$  and  $B$  obtained by using the command “d2c”. Each of these blocks can be manipulated, eliminated or retained depending on the situation and configuration of the circuit.

The closed loop audio-susceptibility  $A_{gf}$  and output impedance  $Z_{of}$  have been evaluated using the following relations [81].

$$A_{gf} = \frac{A_g}{1+T} \quad (4.77)$$

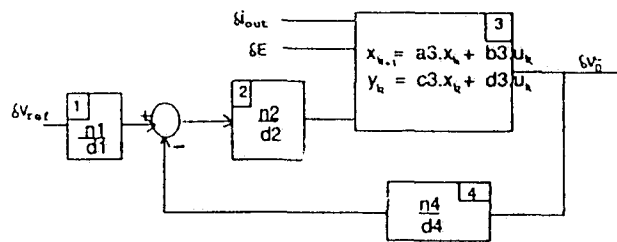
$$Z_{of} = \frac{Z_o}{1+T} \quad (4.78)$$

Where  $A_g$  and  $Z_o$  denote the open loop line to output transfer function and output impedance respectively. Fig. 4.9 shows the closed loop audio-susceptibility with and without the state feedback for the same phase margin.

As can be seen, state feedback controlled SPRC is better adapted to perturbations in the supply voltage. Fig. 4.10 shows the corresponding plot for the output impedance.

## 4.6 Experimental Results

The converter prototype, whose design details are given in the previous section was realized in the laboratory. The tank variables were sensed and sampled using the sample and hold circuits. These signals were added in an operational amplifier and were used to form the state feedback loop. The output voltage was separately sensed and formed the outer feedback loop.



```

% Dummy Block
n1 = [1];
d1 = [1];
% Error Amplifier
ti = 1/100;
kp = 10.0;
n2 = [kp, ti];
d2 = [ti, 0];
% Model of SPRC
a3 = Ac;
b3 = Bc;
c3 = Cc;
d3 = Dc;

% Butterworth Filter, fb block
a0 = 1;
r = 1000;
cf = 10e-06;
n4 = [a0];
d4 = [(r^2).*(cf^2) (3-a0).r.cf 1];
nblocks = 4;
blkbuild;
Q = [2 1 -4;
      3 2 0;
      6 3 0];
inputs = [3 4 5];
outputs = [3];
[ac, bc, cc, dc] = connect(a, b, c, d, Q, inputs, outputs)

```

Figure 4.8: MATLAB realization of the controlled SPRC. The commands used are standard and can be found in MATLAB manual. Note that disturbances  $\delta E$  and  $\delta i_{out}$  are treated as inputs to the system.

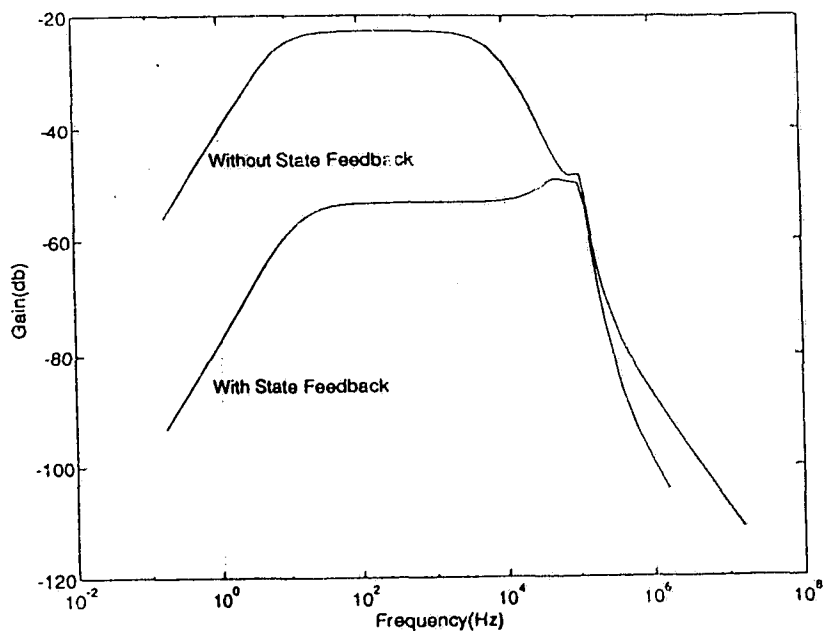


Figure 4.9: Comparison of the state feedback controlled SPRC's audio-susceptibility gain with a frequency controlled SPRC.

Figs. 4.11(a) and (b) show the open loop (without state feedback) magnitude and phase plots of the control to output transfer function obtained experimentally at full load condition.

Figs. 4.11(c) and (d) are those for half the rated load condition. During this part of the experiment both the feedback loops were disconnected. Use was made of a network analyzer (HP 3577A) to obtain these results. Figs. 4.12(a) and (b) shows the magnitude and phase plot of the control to output transfer function for the frequency controlled, closed loop operation. Fig. 4.13 shows the plot corresponding to Fig. 4.12, with the inner state feedback loop incorporated in the closed loop system.

## 4.7 Conclusions

Small-signal analysis of the SPRC has been presented using discrete time domain modeling. A switching converter being inherently discrete, the choice of discrete domain modeling is justified. This model has been modified by integrating it with the state feedback control law. The resulting multiple feedback loop controlled SPRC has been analyzed and the advantages of having an inner state feedback control have been shown. Introduction of state feedback improves the small-signal dynamic response of the converter. The open loop results obtained with the proposed model have been compared with those predicted by the model of [73] based on the extended describing function method. The results compare well. However, at reduced load conditions, for regulated output voltage, where the converter is operated much above resonance, the proposed model gives more accurate results, as they are closer to the experimental results. The advantages of state feedback control have been shown.

Although the analysis and results have been presented for the converter designed to operate in lagging power factor mode under steady-state conditions, it can be

modified for leading power factor mode of operation with some minor changes.

Following are important observations and conclusions of this work:

- (1) The dynamics of the slower, output (continuous time) section of the converter are controlled by a complex pair of poles determined by the filter elements, which determine the corner frequency for the -40 dB roll off point.
- (2) Fast poles occurring at *beat frequency*, which is roughly the difference between the operating frequency and the resonant frequency [87], govern the dynamics of the converter for perturbation frequencies in the vicinity of the operating frequency.
- (3) It was verified that the audio-susceptibility transfer function shows the same pattern as the control to output transfer function [73].
- (4) The loop gain  $T$  of the outer voltage loop determines the stability factor of the converter. It must be suitably designed for a proper phase margin and bandwidth.
- (5) It was observed that for lagging p.f. mode, the initial phase lag is  $0^\circ$  for low perturbation frequencies. For leading p.f. mode, it was observed that the initial phase leads by  $180^\circ$ .
- (6) Parameters like the output impedance and the audio-susceptibility can be controlled by the state feedback gain matrix, which in turn controls the dynamics of the resonant tank portion of the converter.

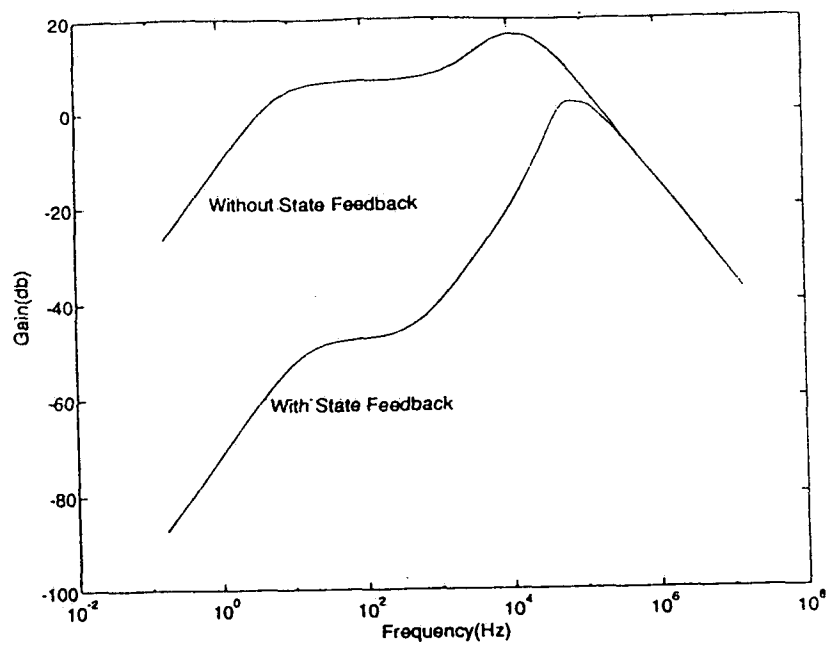


Figure 4.10: Comparison of the state feedback controlled SPRC's output impedance gain with an ordinary frequency controlled SPRC.

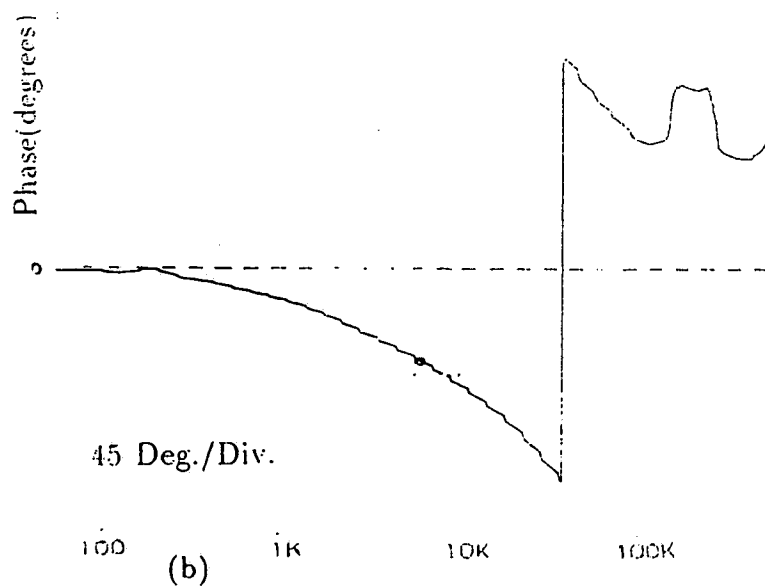
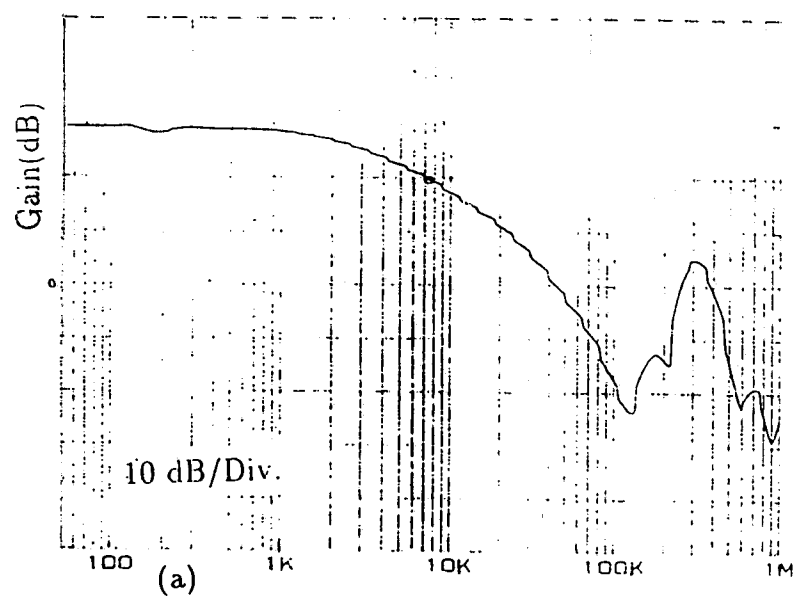


Figure 4.11: Experimental bode plots, obtained with the help of Hewlett Packard's 3577A network analyzer, for the control to output transfer function of the SPRC. These plots are for the open loop case. (a),(b): Gain and phase plots for the full load case. (c),(d) Gain and phase plots for the half full load case

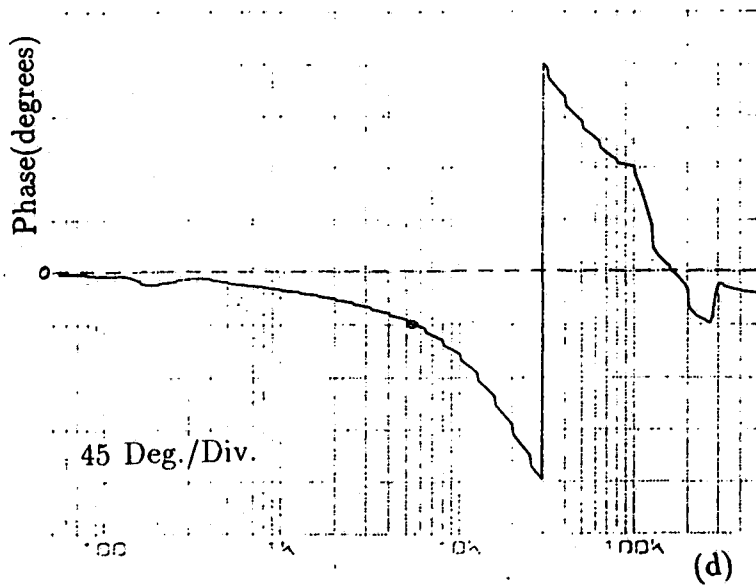
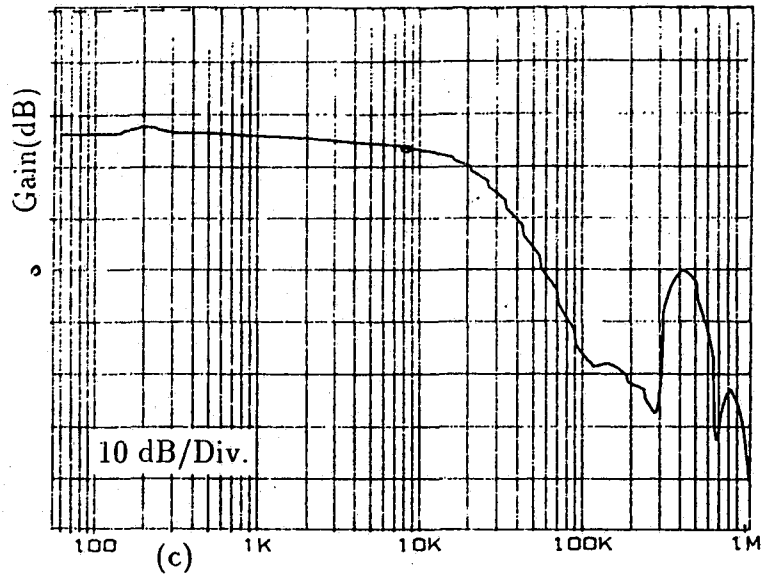


Fig. 4.11 (continued)

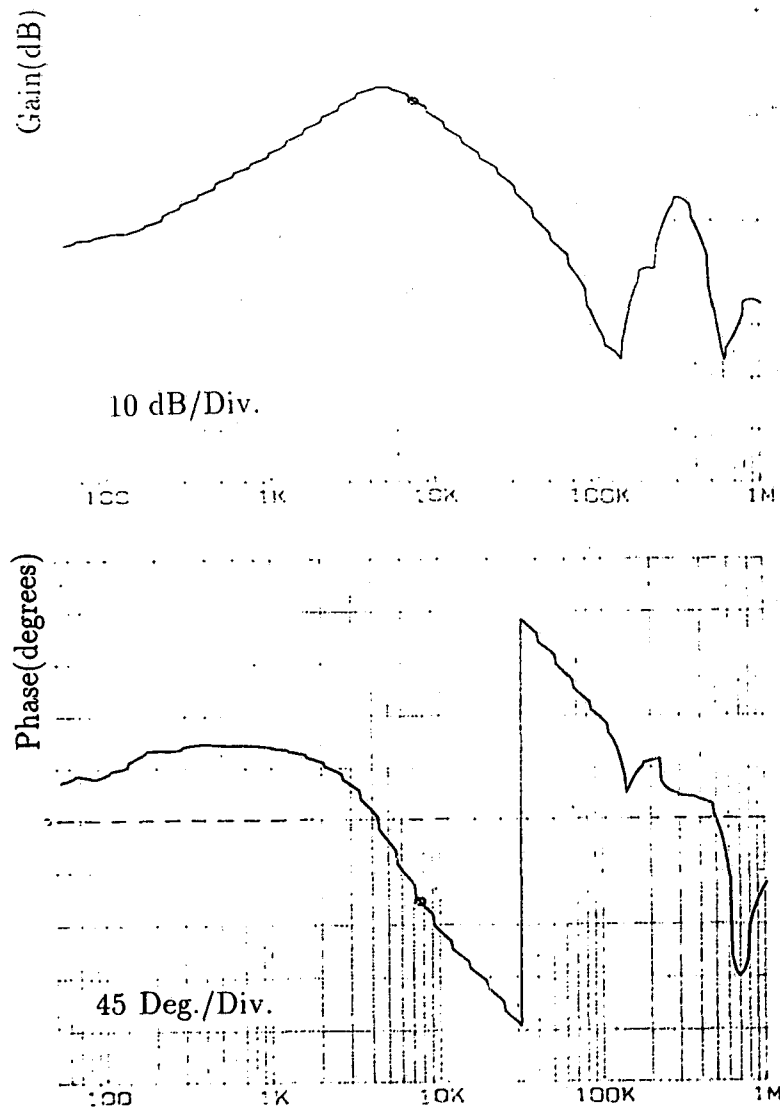


Figure 4.12: Experimental bode plot for the control to output transfer function for the closed loop operation of the frequency controlled SPRC, without state feedback

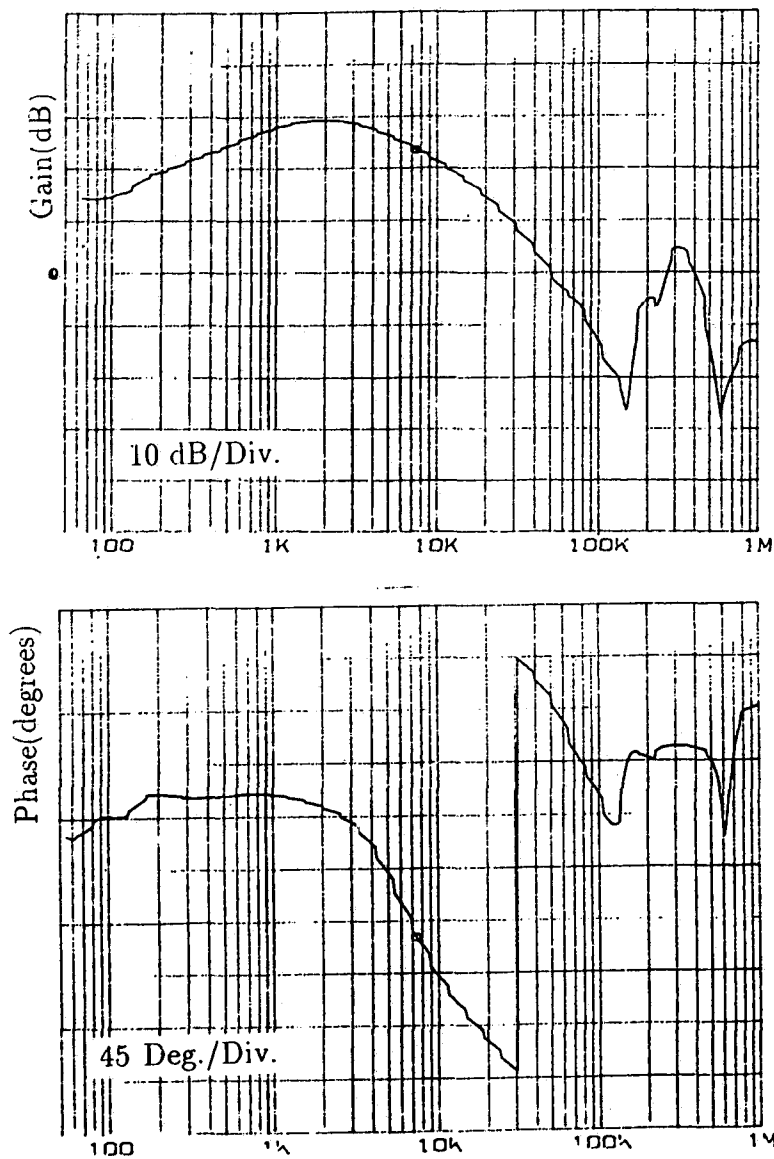


Figure 4.13: Experimental bode plot for the control to output transfer function corresponding to Fig. 4.12, with the inner state feedback loop incorporated.

## Chapter 5

# Small-Signal Equivalent Circuit Model

In this chapter, a small-signal equivalent circuit model is obtained for the LCC-type parallel resonant converter in the form of a two port hybrid parameter model using discrete time domain analysis. This model is used to study the small-signal behavior of the converter. Dynamic performance parameters like the control to output transfer function, audio-susceptibility, output impedance and input admittance have been plotted. Both exact (discrete time domain) and approximate (continuous time domain) models are obtained. When the exact model is used, the results are found to be accurate up to the switching frequency. Experimental verification of the key results is presented.

### 5.1 Introduction

While performing the small-signal analysis of the resonant converters, mainly two approaches have been followed in the literature.

- (1) Obtaining a purely theoretical model, based on the state-space method or the transfer function approach [51,77,83].
- (2) Obtaining a somewhat more practical equivalent circuit model [49,73].

In this context, the small-signal equivalent circuit models of the resonant converters such as those given in [49,73] are more convenient, both for the design calculation purpose as well as for the understanding of the dynamic behavior of the circuit. The small-signal model developed in chapter 4 was based on (1). Although that model is accurate, it is purely theoretical and does not give any physical insight into the small-signal dynamics of the converter. The equivalent circuit modeling approach, presented in this chapter, offers the following advantages:

- (1) It represents the converter dynamics in a more accessible and flexible format and therefore can be used as a design tool for small-signal dynamics of a converter.
- (2) The input and output impedances of the converter along with other transfer functions (such as the control to output transfer function and the audio-susceptibility) can be determined using simple rules of circuit theory.
- (3) It gives more physical insight into the converter dynamics than a state-space model given in [42, 51, 77].

However, equivalent circuit modeling of the resonant converters is not easy. One of the main reasons being that the resonant converters are inherently discrete (sampled) in nature. Physically, this can be understood from the input voltage square wave that appears across the tank of a resonant converter, as a result of the opening and closing of the transistor switches of the input inverter. Clearly, the control of the converter is restricted to the instants where either a falling or rising edge of this square wave occurs. In addition to being inherently discrete, these converters are non-linear and time varying too. What adds to the complexity of the small-signal modeling of the resonant converters is the fact that *state-space averaging* can not be applied in this

case. This is because the switching frequency of a resonant converter is comparable to its natural frequency (determined by the resonant tank component values). Thus, the former can not be neglected in comparison to the latter. However, the input and output (filter) sections of the converter, which have a much lower natural frequency (slower response) than the switching frequency, can be treated as continuous time sections.

The traditional sampled data approach [42] was considered difficult to be applied in the case of SPRC and therefore in [73], a small-signal equivalent circuit model was obtained using an approximate mathematical model based on the extended describing function method. This model, though elegant and simple, was not exact because the resonant tank waveforms were approximated by their fundamental harmonics and the analysis was done in continuous time domain. To obtain more exact model, the tank states must be treated as “sampled quantities” [49] necessitating a discrete time domain modeling. The small-signal analysis based on sampled data modeling has been presented in chapter 4 [77].

The objective of this chapter is to present a two port hybrid lumped parameter small-signal equivalent circuit model of the SPRC based on the discrete time domain modeling method and to study the control aspects of the SPRC. Both exact (discrete time domain) and approximate (continuous time domain) versions of the model are considered.

The remaining of this chapter is divided into the following sections. The converter operation and the various terminology used in this chapter are described in section 5.2. A step by step derivation of the small-signal equivalent circuit model is given in section 5.3. In section 5.4, the equivalent circuit is used to predict the small-signal behavior of the converter. Dynamic performance parameters (control to output gain, audio-susceptibility, etc.) have been obtained. Experimental verification of the theoretical

results is presented in section 5.5, while the main contributions and conclusions of this chapter are summarized in section 5.6.

## 5.2 Converter Operation and Terminology

Fig. 3.2 in chapter 3, shows typical waveforms, from  $k^{th}$  instant onwards, for the SPRC operating in the lagging power factor mode. The tank current lags the voltage  $v_{ab}$ . To give more meaning to the “sampled nature” of the converter operation, it is customary to call the half period of the switching frequency as an *event*. Each event consists of two sub-events,  $\alpha_k$  and  $\beta_k$  (also called intervals B and A respectively) corresponding to the circuit topology of the converter. The various intervals are marked in Fig. 3.2.

For each of the intervals ( $\alpha_k$  and  $\beta_k$ ) marked in Fig. 3.2, the equivalent circuit representation is shown in Fig. 3.3. The equations representing these equivalent circuits are given in Appendix A

Since the  $k^{th}$  event described above represents any arbitrary half period of the switching frequency, the subscript  $k$  will no longer be used explicitly in the rest of the chapter. This will simplify the notation.

The choice of state variables and the notation used are presented in sections 5.2.1 and 5.2.2, respectively.

### 5.2.1 Choice of State Variables

To appropriately represent the resonant tank of the converter, it is necessary that suitable state variables are identified. If the values of the resonant inductor current, series capacitor voltage and the parallel capacitor voltage, at the beginning of a

half cycle of the operating frequency are known, all the subsequent waveforms can be constructed using the appropriate circuit equations. Hence they can be chosen as state variables. As was mentioned earlier, the converter operating frequency is comparable to the natural frequency of the resonant tank. Therefore, the response time of the tank states is comparable to the sampling time. Consequently they must be treated as *discrete* state variables.

### 5.2.2 Notation Used

The small-signal dynamics are investigated in the neighborhood of the dc or steady state operating point of the converter. Fig. 5.1 shows the steady state parallel capacitor voltage waveform along with a perturbed one. Table 5.1 summarizes the notation used to define the instantaneous, steady-state and perturbed quantities. Table 5.2 summarizes the steady-state expressions [7, 12] for the lagging p.f. mode of operation of the SPRC corresponding to Fig. 3.2.  $f_n$  denotes the normalized switching frequency.

Table 5.1: Notation

Running Variable	Steady State value	Disturbance
$E$	$E_0$	$\hat{e}$
$i_0$	$I_0$	$\hat{i}_0$
$i_{L0}$	$I_{L0}$	$\hat{i}_{L0}$
$v_{cs0}$	$V_{cs0}$	$\hat{v}_{cs0}$
$v_{ct0}$	$V_{ct0}$	$\hat{v}_{ct0}$
$\alpha$	$A$	$\hat{\alpha}$
$\gamma$	$\Gamma$	$\hat{\gamma}$

Table 5.2: Steady-State Expressions

$I_{L0} = \frac{-\frac{E_0}{Z} \sin(\Gamma)}{1 + \cos(\Gamma)} - r_2 I_0 + \frac{r_2 I_0}{1 + \cos(\Gamma)} (\cos(A) + \cos(\Gamma - A))$
$V_{cs0} = \frac{Z I_0 r_1 r_2 (\sin(\Gamma - A) - \sin(A))}{1 + \cos(\Gamma)} - Z r_1 r_2 I_0 \frac{\Gamma - 2A}{2}$
$V_{ct0} = \frac{Z I_0 r_2^2 (\sin(\Gamma - A) - \sin(A))}{1 + \cos(\Gamma)} + Z r_1 r_2 I_0 \frac{\Gamma - 2A}{2}$
$V_0 = \frac{2}{\Gamma} r_2 \cdot E_0 \cdot \left( \frac{-\sin(\frac{\Gamma}{2} - A)}{\cos(\frac{\Gamma}{2})} + (\frac{\Gamma}{2} - A) \right)$
$A = l \cdot \pi - \sin^{-1} \left( \frac{h}{\sqrt{f^2 + g^2}} \right) - \tan^{-1} \left( \frac{g}{f} \right)$
<p>where <math>f = E_0 \cdot \sin(\Gamma)</math>,</p>
<p><math>g = E_0 \cdot (1 + \cos(\Gamma))</math>,</p>
<p>and <math>h = g - Z \cdot C_{1B} \cdot \sin(\Gamma) + Z \cdot I_0 \cdot (C_e / C_s) \cdot (\Gamma / 2) \cdot (g / E_0)</math>,</p>
<p><math>l = 1</math> for <math>f_n &gt; 1</math> and <math>0</math> for <math>f_n &lt; 1</math>,</p>
<p><math>r_1 = \frac{C_e}{C_s}</math> and <math>r_2 = \frac{C_s}{C_i}</math>,</p>
<p><math>C_e = \frac{C_s C_i}{C_s + C_i}</math>, <math>Z = \sqrt{L / C_e}</math></p>

### 5.3 Small-Signal Equivalent Circuit Modeling

In this section, a two port, lumped parameter, small-signal equivalent circuit model has been obtained for the SPRC operating in lagging power factor mode (Fig. 3.2).

Referring to Fig. 3.1, the three major sections of the SPRC can be identified. The resonant tank portion of the converter is a discrete system, as explained previously. The input and output (filter) sections can be treated as continuous systems. Low frequency approximation can not be used for the resonant tank and hence its modeling is more complex. We assume that the resonant tank is a *two-port* network specified by four terminal quantities. The inverter input current ( $i_{in}$ ) and the rectified parallel capacitor voltage ( $v_{out}$ ) are chosen as dependent quantities while the input dc voltage ( $E$ ) and the output current ( $i_o$ ) are considered as independent quantities. To interface the input and output sections with the resonant section, the dependent quantities are averaged. It is assumed that the independent quantities ( $E$  and  $i_o$ ) change only at the beginning or end of an event and remain constant during an event.

Inspection of the resonant tank and the choice of dependent and independent variables, reveals that a hybrid parameter model is most suitable for representing the resonant tank. Two equations (an input current equation and an output voltage equation) are required for this purpose. The dependent quantities are expressed in terms of the independent quantities. However, these relations are non-linear. To be able to obtain a linearized two port hybrid model, we linearize this system of equations about a steady-state operating point and obtain a small-signal representation of the resonant tank of the SPRC, as shown in Fig. 5.2. The governing small-signal equations are given by

$$\hat{v}_{out} = h_{11} \cdot \hat{e} + h_{22} \cdot \hat{i}_o + h_{2c} \hat{v}_\gamma \quad (5.1)$$

$$\hat{i}_{in} = h_{21} \cdot \hat{e} + h_{12} \cdot \hat{i}_o + h_{1c} \hat{v}_\gamma \quad (5.2)$$

To accommodate the role of the voltage controlled oscillator, which controls the

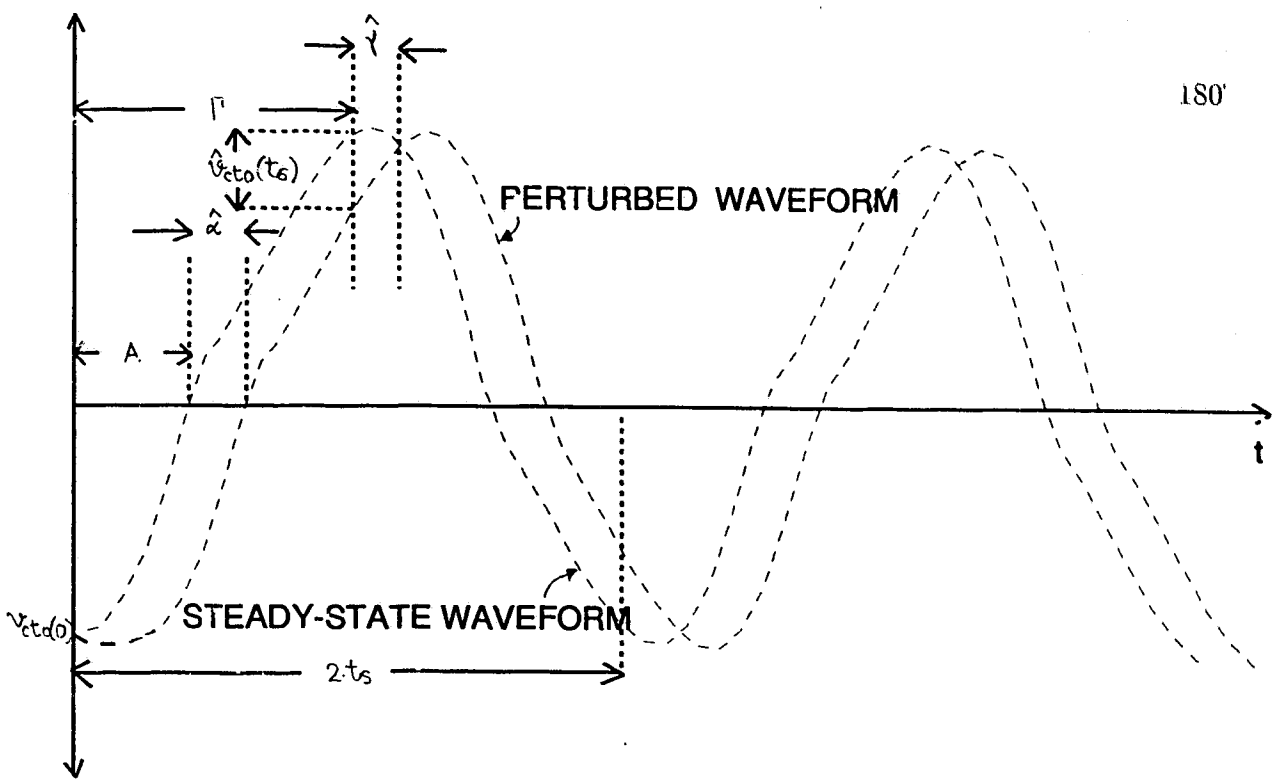


Figure 5.1: Waveforms showing the effect of perturbation on the circuit variables. The notation used is clearly marked and followed through out the paper.

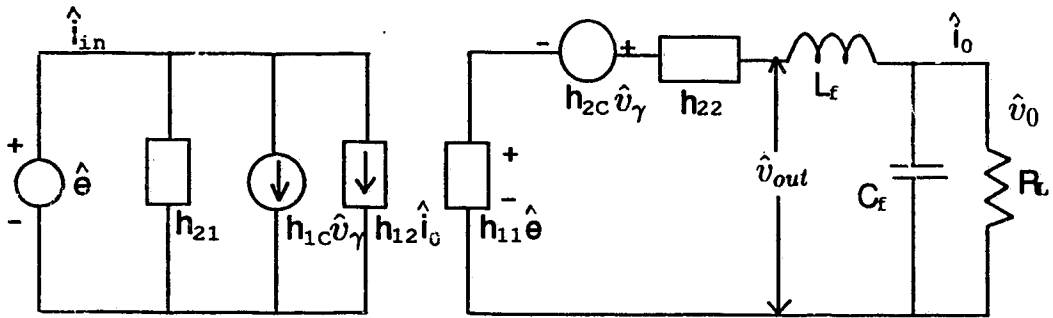


Figure 5.2: Two port hybrid parameter, small signal equivalent circuit model of the SPRC developed in this paper. The hybrid parameters have been defined in section 5.3. The output section of the SPRC is shown connected to the linearized small signal model of the resonant tank.

converter operating frequency (another independent variable), additional independent sources have been inserted in the last two equations denoted by coefficients with subscript "c".  $v_\gamma$  stands for the control voltage of the VCO. Following seven steps are followed in obtaining the two port hybrid parameter small-signal equivalent circuit model.

### 5.3.1 Large-Signal State Equations for Resonant Tank (Step 1)

The first step in the derivation of the model is writing the large-signal state equations for the resonant tank, which is in discrete time domain. The large-signal equation corresponding to the tank current state is given by

$$\frac{\Delta i_{L0}}{t_s} = \frac{-i_L(t_s) - i_L(0)}{t_s} \quad (5.3)$$

$i_L(t_s)$  denotes the tank current at the end of the half period ( $k^{th}$  event) and is same as  $i_L(t_{0(k+1)})$  (Fig. 2). A large-signal expression is required giving  $i_L(t_s)$  in terms of  $i_L(0)$ . This, along with those for the other two states, were derived in [78]. These relations are summarized in the Appendix B. Substituting the value of  $i_L(t_s)$  from Appendix B into the last equation;

$$\frac{\Delta i_{L0}}{t_s} = \frac{-A_{1B} \sin(\omega_0 t_s) - B_{1B} \cos(\omega_0 t_s) - C_{1B}(2\cos(\omega_0 t_\beta) - 1) - i_L(0)}{t_s} \quad (5.4)$$

Similarly,

$$\frac{\Delta v_{cs0}}{t_s} = \frac{-v_{cs}(t_s) - v_{cs}(0)}{t_s} \quad (5.5)$$

$$= \frac{A_{2B}(1 - \cos(\omega_0 t_s)) + B_{2B} \sin(\omega_0 t_s) + C_{2B}(\omega_0 t_\alpha - \omega_0 t_\beta + 2\sin(\omega_0 t_\beta)) + 2v_{cs}(0)}{t_s} \quad (5.6)$$

$$\frac{\Delta v_{ct0}}{t_s} = \frac{-v_{ct}(t_s) - v_{ct}(0)}{t_s} \quad (5.7)$$

$$= \frac{X_1 + X_2}{t_s} \quad (5.8)$$

where

$$X_1 = A_{3B}(1 - \cos(\omega_0 t_s)) + B_{3B} \sin(\omega_0 t_s) + C_{3B}(2\omega_0 t_\alpha - \omega_0 t_s)$$

$$X_2 = 2Z.r_2.C_{1B} \sin(\omega_0 t_s - \omega_0 t_\alpha) + 2v_{ct}(0)$$

### 5.3.2 Input and Output Equations (Step 2)

The next step is to obtain the large-signal state equations for the dependent quantities. As stated previously, the dependent quantities  $v_{out}$  and  $i_{in}$  should be averaged over the switching period following the low frequency approximation. These averaged quantities then serve to link the discrete resonant tank portion to the other two slower (continuous time) sections.

We begin with the current equation. Referring to Fig. 3.2, it can be seen that the current  $i_{in}$  flowing into the resonant tank can be obtained by averaging the charges during the two sub-intervals  $\alpha$  and  $\beta$ . Thus:

$$i_{in} = \frac{q_\alpha + q_\beta}{t_s} \quad (5.9)$$

where

$$q_\alpha = \int_0^{t_\alpha} (A_{1B} \sin(\omega_0 t') + B_{1B} \cos(\omega_0 t') + C_{1B}) dt' \quad (5.10)$$

$$q_\beta = \int_0^{t_s - t_\alpha} (A_{1A} \sin(\omega_0 t'') + B_{1A} \cos(\omega_0 t'') + C_{1A}) dt'' \quad (5.11)$$

The above expressions are evaluated by substituting the values of the A,B,C constants from the Appendix A and integrating between the specified intervals.

$$q_\alpha = \frac{E - v_{cs0} - v_{ct0}}{\omega_0 Z} (1 - \cos(\alpha)) + \frac{i_{L0} + r_2 i_0}{\omega_0} \sin(\alpha) - \frac{r_2 i_0}{\omega_0} \alpha \quad (5.12a)$$

$$q_\beta = \frac{E - v_{cs1} - v_{ct1}}{\omega_0 Z} (1 - \cos(\gamma - \alpha)) + \frac{i_{L1} - r_2 i_0}{\omega_0} \sin(\gamma - \alpha) - \frac{r_2 i_0}{\omega_0} (\gamma - \alpha) \quad (5.12b)$$

where  $i_{L1}$ ,  $v_{cs1}$  and  $v_{ct1}$  are given by (A.1), (A.2) and (A.3) in Appendix A.

For the other dependent quantity, i.e. output voltage of the resonant tank, the parallel capacitor voltage equations for the intervals  $\alpha$  and  $\beta$  (see Appendix A) are integrated. This yields;

$$v_{out} = \frac{1}{t_s} \int_0^{t_s} |v_{ct}(\tau)| d\tau = \frac{1}{t_s} \left( - \int_0^{t_\alpha} v_{ct_\alpha}(\tau) d\tau + \int_0^{t_s - t_\alpha} v_{ct_\beta}(\tau) d\tau \right) \quad (5.13)$$

The expressions for  $v_{ct_\alpha}$  and  $v_{ct_\beta}$  are given by (A.3) and (A.11) respectively in Appendix A.

$$\begin{aligned} v_{out} = & \frac{r_2}{\omega_0 t_s} (E - v_{cs0} - v_{ct0}) \cdot (\gamma - 2\alpha + 2\sin(\alpha) - \sin(\gamma)) \\ & + \frac{Z \cdot r_2}{\omega_0 t_s} (i_{L0} + r_2 \cdot i_0) \cdot (2\cos(\alpha) - 1 - \cos(\gamma)) - \frac{Z r_1 r_2 i_0}{2\omega_0 t_s} (2\alpha - \gamma)^2 \\ & + \frac{2Z \cdot r_2^2 i_0}{\omega_0 t_s} (\cos(\gamma - \alpha) - 1) + \frac{v_{ct0}}{\omega_0 t_s} (\gamma - 2\alpha) \end{aligned} \quad (5.14)$$

At this point we have all the large-signal state equations necessary to represent the system. But these are non-linear equations. To model the small-signal dynamics of the converter, they must be linearized in the neighborhood of the stable operating point (Table 5.2). This is done in the next section.

### 5.3.3 Perturbation and Linearization (Step 3)

The equations (5.4), (5.6), (5.8), (5.9) and (5.14) are perturbed and linearized about the steady state operating point. The perturbation and linearization of these state equations is shown below.

$$\begin{aligned} -\frac{\Delta(I_{L0} + \hat{i}_{L0})}{t_s} &= \omega_0 \frac{E_0 + \hat{e} - V_{cs0} - \hat{v}_{cs0} - V_{ct0} - \hat{v}_{ct0}}{Z(\Gamma + \hat{\gamma})} \sin(\Gamma + \hat{\gamma}) \\ &+ \omega_0 \frac{(I_{L0} + \hat{i}_{L0} + r_2 I_0 + r_2 \hat{i}_0) \cos(\Gamma + \hat{\gamma}) - 2\omega_0 r_2 (I_0 + \hat{i}_0) \cos(\Gamma + \hat{\gamma} - A - \hat{\alpha})}{\Gamma + \hat{\gamma}} \\ &+ \frac{\omega_0 r_2 (I_0 + \hat{i}_0) + \omega_0 I_{L0} + \hat{i}_{L0} \omega_0}{\Gamma + \hat{\gamma}} \end{aligned} \quad (5.15a)$$

$$-\frac{\Delta(V_{cs0} + \hat{v}_{cs0})}{t_s} = \omega_0 r_1 \frac{E_0 + \hat{e} - V_{cs0} - \hat{v}_{cs0} - V_{ct0} - \hat{v}_{ct0}}{(\Gamma + \hat{\gamma})} (1 - \cos(\Gamma + \hat{\gamma}))$$

$$\begin{aligned}
& +\omega_0 Z r_1 \frac{(I_{L0} + \hat{i}_{L0} + r_2 I_0 + r_2 \hat{i}_0) \sin(\Gamma + \hat{\gamma}) - 2\omega_0 r_1 r_2 Z (I_0 + \hat{i}_0) \sin(\Gamma + \hat{\gamma} - A - \hat{\alpha})}{\Gamma + \hat{\gamma}} \\
& + \frac{-Z r_1 r_2 \omega_0 (I_0 + \hat{i}_0) (2A + 2\hat{\alpha} - \Gamma - \hat{\gamma}) + 2\omega_0 (V_{cs0} + \hat{v}_{cs0})}{\Gamma + \hat{\gamma}} \quad (5.15b)
\end{aligned}$$

$$\begin{aligned}
-\frac{\Delta(V_{ct0} + \hat{v}_{ct0})}{t_s} & = \omega_0 r_2 \frac{E_0 + \hat{e} - V_{cs0} - \hat{v}_{cs0} - V_{ct0} - \hat{v}_{ct0}}{(\Gamma + \hat{\gamma})} (1 - \cos(\Gamma + \hat{\gamma})) \\
& + \omega_0 Z r_2 \frac{(I_{L0} + \hat{i}_{L0} + r_2 I_0 + r_2 \hat{i}_0) \sin(\Gamma + \hat{\gamma}) - 2\omega_0 r_2^2 Z (I_0 + \hat{i}_0) \sin(\Gamma + \hat{\gamma} - A - \hat{\alpha})}{\Gamma + \hat{\gamma}} \\
& + \frac{Z r_1 r_2 \omega_0 (I_0 + \hat{i}_0) (2A + 2\hat{\alpha} - \Gamma - \hat{\gamma}) + 2\omega_0 (V_{ct0} + \hat{v}_{ct0})}{\Gamma + \hat{\gamma}} \quad (5.15c)
\end{aligned}$$

The above equations can be simplified using the following.

$$\sin(\Gamma + \hat{\gamma}) = \sin(\Gamma) + \hat{\gamma} \cos(\Gamma) \quad (5.16)$$

$$\text{with } \cos(\hat{\gamma}) = 1$$

$$\cos(\Gamma + \hat{\gamma}) = \cos(\Gamma) - \hat{\gamma} \sin(\Gamma) \quad (5.17)$$

$$\text{with } \sin(\hat{\gamma}) = \hat{\gamma}$$

$$\text{Similarly } \cos(\Gamma + \hat{\gamma} - A - \hat{\alpha}) = \cos(\Gamma - A) - (\hat{\gamma} - \hat{\alpha}) \sin(\Gamma - A) \quad (5.18)$$

$$\begin{aligned}
\text{and the denominator } \frac{1}{\Gamma + \hat{\gamma}} & = \frac{1}{\Gamma} \left(1 + \frac{\hat{\gamma}}{\Gamma}\right)^{-1} \\
& \approx \frac{1}{\Gamma} \left(1 - \frac{\hat{\gamma}}{\Gamma}\right) \quad (5.19)
\end{aligned}$$

Using the above simplifications, the small-signal terms can be separated from the dc terms to yield the following small-signal equations.

$$\frac{\Delta \hat{i}_{L0}}{t_s} = p'_{11} \hat{i}_{L0} + p'_{12} \hat{v}_{cs0} + p'_{13} \hat{v}_{ct0} + p'_{14} \hat{i}_0 + p'_{15} \hat{e} + p'_{16} \hat{\gamma} + p'_{17} \hat{\alpha} \quad (5.20a)$$

$$\frac{\Delta \hat{v}_{cs0}}{t_s} = p'_{21} \hat{i}_{L0} + p'_{22} \hat{v}_{cs0} + p'_{23} \hat{v}_{ct0} + p'_{24} \hat{i}_0 + p'_{25} \hat{e} + p'_{26} \hat{\gamma} + p'_{27} \hat{\alpha} \quad (5.20b)$$

$$\frac{\Delta \hat{v}_{ct0}}{t_s} = p'_{31} \hat{i}_{L0} + p'_{32} \hat{v}_{cs0} + p'_{33} \hat{v}_{ct0} + p'_{34} \hat{i}_0 + p'_{35} \hat{e} + p'_{36} \hat{\gamma} + p'_{37} \hat{\alpha} \quad (5.20c)$$

where  $p'_{ij}$  are some intermediate coefficients introduced as a matter of convenience. At this point, we have obtained the small-signal equations, but they still have one dependent quantity  $\hat{\alpha}$ . This must be eliminated, as shown in the next section.

### 5.3.4 Elimination of $\hat{\alpha}$ (Step 4)

To eliminate the dependent quantity  $\hat{\alpha}$ , we note that the parallel capacitor voltage goes to zero at the end of B ( $\alpha$ ) interval. Therefore;

$$A_{3B}(1 - \cos(\alpha)) + B_{3B}\sin(\alpha) + C_{3B}\alpha + v_{ct0} = 0 \quad (5.21)$$

$$\text{or } r_2(E - v_{cs0} - v_{ct0})(1 - \cos(\alpha)) + Zr_2(i_{L0} + r_2i_0)\sin(\alpha) + Zr_1r_2i_0\alpha + v_{ct0} = 0 \quad (5.22)$$

The above equation, which is of the form  $f(\alpha, E, v_{cs0}, v_{ct0}, i_{L0}, i_0) = 0$  can be expanded and linearized using the Taylor's expansion to yield the following:

$$\begin{aligned} 0 = & f(A, E_0, V_{cs0}, V_{ct0}, I_{L0}, I_0) + \left. \frac{\partial f}{\partial \alpha} \right|_{eq} \hat{\alpha} + \left. \frac{\partial f}{\partial E} \right|_{eq} \hat{e} \\ & + \left. \frac{\partial f}{\partial v_{cs0}} \right|_{eq} \hat{v}_{cs0} + \left. \frac{\partial f}{\partial v_{ct0}} \right|_{eq} \hat{v}_{ct0} + \left. \frac{\partial f}{\partial i_{L0}} \right|_{eq} \hat{i}_{L0} + \left. \frac{\partial f}{\partial i_0} \right|_{eq} \hat{i}_0 \end{aligned} \quad (5.23)$$

Noting that the first term on the right hand side in the last equation is zero, we get;

$$\hat{\alpha} = - \frac{DE.\hat{e} + DVCS.\hat{v}_{cs0} + DVCT.\hat{v}_{ct0} + DVIL.\hat{i}_{L0} + DIO.\hat{i}_0}{DA} \quad (5.24)$$

where

$$\begin{aligned} DA (= \left. \frac{\partial f}{\partial \alpha} \right|_{eq}) &= r_2(E_0 - V_{cs0} - V_{ct0})\sin(A) + Zr_2(I_{L0} + r_2I_0)\cos(A) + Zr_1r_2I_0 \\ &= A_{3B}\sin(A) + B_{3B}\cos(A) + C_{3B} \end{aligned}$$

The quantities  $DE$ ,  $DVCS$  etc. are summarized in Table 5.3 and the A, B, C constant are same as given in the Appendix A with subscript "k" dropped and the state variables replaced with their steady-state values as per Table 5.1.

### 5.3.5 Final Small-Signal Equations (Step 5)

Once  $\hat{\alpha}$  is evaluated in terms of the independent quantities, we can eliminate it from (5.20). To give more meaning to the modified equation, it is multiplied by  $L$ , the

Table 5.3: Partial Derivatives

Symbol	Meaning	Expression
DE	$\left. \frac{\partial f}{\partial E} \right _{eq}$	$(1 - \cos(A)) \cdot r_2$
DVCS	$\left. \frac{\partial f}{\partial v_{cs0}} \right _{eq}$	-DE
DVCT	$\left. \frac{\partial f}{\partial v_{ct0}} \right _{eq}$	DVCS + 1
DVIL	$\left. \frac{\partial f}{\partial i_{L0}} \right _{eq}$	$Z \cdot r_2 \sin(A)$
DIO	$\left. \frac{\partial f}{\partial i_0} \right _{eq}$	$Z \cdot r_2^2 \sin(A) + Z r_1 r_2 A$

resonating inductance, resulting in the following equation.

$$L \cdot \frac{\Delta \hat{i}_{L0}}{t_s} = R_1 \hat{i}_{L0} + K_1 \hat{v}_{cs0} + K_2 \hat{v}_{ct0} + R_2 \hat{i}_0 + K_3 \hat{e} + K_{1c} \hat{v}_\gamma \quad (5.25)$$

The remaining two equations for the tank states can also be suitably modified. They, along with the other two for the dependent quantities ( $v_{out}$  and  $i_{in}$ ) are given below:

$$C_s \cdot \frac{\Delta \hat{v}_{cs0}}{t_s} = K_4 \hat{i}_{L0} + g_1 \hat{v}_{cs0} + g_2 \hat{v}_{ct0} + K_5 \hat{i}_0 + g_3 \hat{e} + g_{1c} \hat{v}_\gamma \quad (5.26)$$

$$C_t \cdot \frac{\Delta \hat{v}_{ct0}}{t_s} = K_6 \hat{i}_{L0} + g_4 \hat{v}_{cs0} + g_5 \hat{v}_{ct0} + K_7 \hat{i}_0 + g_6 \hat{e} + g_{2c} \hat{v}_\gamma \quad (5.27)$$

$$\hat{v}_{out} = R_3 \hat{i}_{L0} + K_8 \hat{v}_{cs0} + K_9 \hat{v}_{ct0} + R_4 \hat{i}_0 + K_{10} \hat{e} + K_{2c} \hat{v}_\gamma \quad (5.28)$$

$$\hat{i}_{in} = K_{11} \hat{i}_{L0} + g_7 \hat{v}_{cs0} + g_8 \hat{v}_{ct0} + K_{12} \hat{i}_0 + g_9 \hat{e} + g_{3c} \hat{v}_\gamma \quad (5.29)$$

In the above equations,  $g$ 's have dimensions of conductance,  $R$ 's have dimensions of resistance, and  $K$ 's are dimensionless. The coefficients of small-signal equations (5.25) - (5.29) are defined in Tables (5.4) and (5.5).

### 5.3.6 Elimination of Intermediate Variables (Step 6)

Equations (5.25) - (5.29) represent a small-signal multi-port model of the SPRC shown in Fig. 5.3. This model might give some physical insight into the small-signal

Table 5.4: Small Signal Coefficients for the Resonant Tank Equations

$R_1$	$-(Z \frac{1+\cos(\Gamma)}{\Gamma}) - Z \frac{r_2 I_0}{\Gamma} \sin(\Gamma - A) \frac{DVIL}{DA}$
$K_1$	$\frac{\sin(\Gamma)}{\Gamma} - \frac{2r_2 I_0 Z}{\Gamma} \sin(\Gamma - A) \frac{DVCS}{DA}$
$K_2$	$\frac{\sin(\Gamma)}{\Gamma} - \frac{2r_2 I_0 Z}{\Gamma} \sin(\Gamma - A) \frac{DVCT}{DA}$
$R_2$	$-\frac{r_2 Z \cos(\Gamma)}{\Gamma} + \frac{2Z r_2 \cos(\Gamma - A)}{\Gamma} - \frac{r_2 Z}{\Gamma} - \frac{2Z r_2 I_0}{\Gamma} \sin(\Gamma - A) \frac{DIO}{DA}$
$K_3$	$-\frac{\sin(\Gamma)}{\Gamma} - \frac{2Z r_2 I_0}{\Gamma} \sin(\Gamma - A) \frac{DE}{DA}$
$K_{1c}$	$\frac{(E(0) - V_{cs0} - V_{ct0}) \cdot (\sin(\Gamma) - \Gamma \cos(\Gamma))}{\Gamma^2} + Z \frac{(I_{L0} + r_2 I_0) \cdot (\cos(\Gamma) + \Gamma \sin(\Gamma))}{\Gamma^2}$ $+ Z \frac{r_2 I_0 (-2\Gamma \sin(\Gamma - A) + 1 - 2\cos(\Gamma - A))}{\Gamma^2} + Z \frac{I_{L0}}{\Gamma^2}$
$K_4$	$-\frac{\sin(\Gamma)}{\Gamma} + \frac{2r_2 I_0}{\Gamma} \cos(\Gamma - A) \frac{DVIL}{DA} - \frac{2r_2 I_0}{\Gamma} \frac{DVIL}{DA}$
$g_1$	$\frac{1}{Z\Gamma} - \frac{1}{Z\Gamma} \cos(\Gamma) - \frac{2}{Zr_2\Gamma} + \frac{2r_2 I_0}{\Gamma} (\cos(\Gamma - A) - 1) \frac{DVCS}{DA}$
$g_2$	$\frac{1}{Z\Gamma} - \frac{1}{Z\Gamma} \cos(\Gamma) + \frac{2r_2 I_0}{\Gamma} (\cos(\Gamma - A) - 1) \frac{DVCT}{DA}$
$K_5$	$-\frac{r_2 \sin(\Gamma)}{\Gamma} + \frac{r_2}{\Gamma} (2A - \Gamma) + \frac{2r_2}{\Gamma} \sin(\Gamma - A) + \frac{2r_2 I_0}{\Gamma} (\cos(\Gamma - A) - 1) \frac{DIO}{DA}$
$g_3$	$-\frac{1}{Z\Gamma} + \frac{1}{Z\Gamma} \cos(\Gamma) + \frac{2r_2 I_0}{\Gamma} (\cos(\Gamma - A) - 1) \frac{DE}{DA}$
$g_{1c}$	$\frac{1}{Z\Gamma} (E(0) - V_{cs0} - V_{ct0}) \cdot (-\sin(\Gamma) + \frac{1}{\Gamma} - \frac{\cos(\Gamma)}{\Gamma}) + \frac{1}{\Gamma} (I_{L0} + r_2 I_0) \cdot (\frac{\sin(\Gamma)}{\Gamma} - \cos(\Gamma))$ $+ \frac{r_2 I_0}{\Gamma} (-1 + 2\cos(\Gamma - A) - \frac{2A - \Gamma}{\Gamma} - 2\frac{\sin(\Gamma - A)}{\Gamma}) + \frac{2 \cdot V_{ct0}}{Zr_2 \Gamma^2}$
$K_6$	$-\frac{1}{\Gamma} \sin(\Gamma) + \frac{2I_0}{\Gamma} \frac{DVIL}{DA} (r_2 \cos(\Gamma - A) + r_1)$
$g_4$	$\frac{1}{Z\Gamma} (1 - \cos(\Gamma)) + \frac{2I_0}{\Gamma} \frac{DVCS}{DA} (r_2 \cos(\Gamma - A) + r_1)$
$g_5$	$\frac{1}{Z\Gamma} (1 - \cos(\Gamma)) - \frac{2}{Zr_2\Gamma} + \frac{2I_0}{\Gamma} \frac{DVCT}{DA} (r_2 \cos(\Gamma - A) + r_1)$
$K_7$	$-\frac{r_2}{\Gamma} \sin(\Gamma) - \frac{r_2}{\Gamma} (2A - \Gamma) + \frac{2r_2}{\Gamma} \sin(\Gamma - A) + \frac{2I_0}{\Gamma} \frac{DIO}{DA} (r_2 \cos(\Gamma - A) + r_1)$
$g_6$	$-\frac{1}{Z\Gamma} + \frac{1}{Z\Gamma} \cos(\Gamma) + \frac{2I_0}{\Gamma} \frac{DE}{DA} (r_2 \cos(\Gamma - A) + r_1)$
$g_{2c}$	$\frac{1}{Z\Gamma} (E(0) - V_{cs0} - V_{ct0}) \cdot (-\sin(\Gamma) + \frac{1}{\Gamma} - \frac{\cos(\Gamma)}{\Gamma}) + \frac{1}{\Gamma} (I_{L0} + r_2 I_0) \cdot (\frac{\sin(\Gamma)}{\Gamma} - \cos(\Gamma))$ $+ \frac{I_0}{\Gamma} (2r_2 \cos(\Gamma - A) + r_1 + \frac{r_1(2A - \Gamma)}{\Gamma} - \frac{2r_2 \sin(\Gamma - A)}{\Gamma}) + \frac{2 \cdot V_{ct0}}{Zr_2 \Gamma^2}$

Table 5.5: Small Signal Coefficients for the Input and Output Equations

$R_3$	$P'_{41} + P'_{47} \frac{DVIL}{DA}$
$K_8$	$P'_{42} + P'_{47} \frac{DVCS}{DA}$
$K_9$	$P'_{43} + P'_{47} \frac{DVCT}{DA}$
$R_4$	$P'_{44} + P'_{47} \frac{DIO}{DA}$
$K_{10}$	$P'_{45} + P'_{47} \frac{DE}{DA}$
$K_{2c}$	$P'_{46}$
$K_{11}$	$P'_{51} + P'_{57} \frac{DVIL}{DA}$
$g_7$	$P'_{52} + P'_{57} \frac{DVCS}{DA}$
$g_8$	$P'_{53} + P'_{57} \frac{DVCT}{DA}$
$K_{12}$	$P'_{54} + P'_{57} \frac{DIO}{DA}$
$g_9$	$P'_{55} + P'_{57} \frac{DE}{DA}$
$g_{3c}$	$P'_{56}$
$P'_{41}$	$\frac{Zr_2(2\cos(A) - 1 - \cos(\Gamma))}{\Gamma}$
$P'_{42}$	$\frac{-r_2(\Gamma - 2A + 2\sin(A) - \sin(\Gamma))}{\Gamma}$
$P'_{43}$	$P'_{42} + \frac{\Gamma - 2A}{\Gamma}$
$P'_{44}$	$\frac{Zr_2^2(2\cos(A) - 3 - \cos(\Gamma) + 2\cos(\Gamma - A))}{\Gamma^2} \cdot \frac{Zr_1r_2(2A - \Gamma)^2}{2\Gamma}$
$P'_{45}$	$-P'_{42}$
$P'_{46}$	$\frac{r_2(E(0) - V_{c10} - V_{c10})(2A - 2\sin(A) + \sin(\Gamma) - \Gamma \cos(\Gamma))}{\Gamma^2} + \frac{Zr_2(I_{L0} + r_2I_0)(1 - 2\cos(A) + \cos(\Gamma) + \Gamma \sin(\Gamma))}{\Gamma^2}$ $- Zr_1r_2I_0(\frac{-2A^2}{\Gamma^2} + \frac{1}{2}) + \frac{2Zr_2^2I_0(-\Gamma \sin(\Gamma - A) + 1 - \cos(\Gamma - A))}{\Gamma^2} + \frac{2A}{\Gamma^2}V_{c10}$
$P'_{47}$	$\frac{r_2(E(0) - V_{c10} - V_{c10})(2\cos(A) - 2) + \frac{-2Zr_2\sin(A)}{\Gamma}(I_{L0} + r_2I_0) - 2Zr_1r_2I_0(2A - \Gamma)}{\Gamma^2}$ $+ \frac{2Zr_2^2I_0(\sin(\Gamma - A)) - 2V_{c10}}{\Gamma^2}$
$P'_{51}$	$\frac{\sin(A)}{\Gamma^2} - \frac{\sin(A)}{\Gamma^2}(r_1 + r_2)(1 - \cos(\Gamma - A)) + \frac{\cos(A)\sin(\Gamma - A)}{\Gamma}$
$P'_{52}$	$\frac{-1}{\Gamma^2} + \frac{\cos(A)}{\Gamma^2} + \frac{(r_1 + r_2)(1 - \cos(\Gamma))(1 - \cos(\Gamma - A))}{\Gamma^2} - \frac{1 - \cos(\Gamma - A)}{\Gamma^2} - \frac{\sin(A)\sin(\Gamma - A)}{\Gamma^2}$
$P'_{53}$	$P'_{52}$
$P'_{54}$	$\frac{(1 - \cos(\Gamma - A))(r_1r_2(A - \sin(A)) - \sin(A)r_2^2) - r_1r_2A(1 - \cos(\Gamma - A))}{\Gamma^2}$ $+ r_2\cos(A)\sin(\Gamma - A) - 2r_2\sin(\Gamma - A) + r_2(\Gamma + \sin(A) - 2A)$
$P'_{55}$	$\frac{2 - \cos(A) - \cos(\Gamma - A)}{\Gamma^2} - \frac{(1 - \cos(A))(1 - \cos(\Gamma - A))(r_1 + r_2)}{\Gamma^2} + \frac{\sin(A)\sin(\Gamma - A)}{\Gamma^2}$
$P'_{56}$	$-\frac{A_1B}{\Gamma^2}(1 - \cos(A)) - \frac{B_1B \cdot \sin(A)}{\Gamma^2} - 2 \cdot \frac{C_1B \cdot A}{\Gamma^2}$ $+ PP \cdot ((r_1 + r_2) \cdot (A_1B(\cos(A) - 1) - B_1B \cdot \sin(A)) + B_1B) + QQ \cdot (\sin(A) \cdot A_1B + B_1B + 2C_1B))$
$PP$	$-\frac{1 - \cos(\Gamma - A)}{\Gamma^2} + \frac{\sin(\Gamma - A)}{\Gamma}$
$QQ$	$-\frac{\sin(\Gamma - A)}{\Gamma^2} + \frac{\cos(\Gamma - A)}{\Gamma}$
$P'_{57}$	$-\frac{4 \cdot A_1B}{\Gamma^2}(r_1 + r_2 - 1) \cdot \sin(A/2) \cdot \sin(\frac{\Gamma - A}{2}) \cdot \sin(\frac{\Gamma - 2A}{2}) - \frac{2 \cdot B_1B}{\Gamma}(r_1 + r_2 - 1) \cdot \sin(\frac{3A - \Gamma}{2}) \cdot \sin(\frac{A - \Gamma}{2})$ $- \frac{2C_1B}{\Gamma}(\cos(\Gamma - A) - 1)$

dynamics of the converter, but is far too complex to be used as a control design tool. In an attempt to simplify this model, tank state variables can be eliminated from these equations as they are not of direct use. One is interested in them only to the extent they affect the terminals (dependent quantities) at the two ports and not otherwise. At this point we consider two cases, which give different interpretation to the analysis.

**Case(I) Continuous Time Domain:** If the variation of the *states* of the system is small as compared to the switching frequency, which means they remain more or less constant over a given operating frequency cycle, then the sampled nature of the *states* can be neglected and equations (5.25) - (5.27) can be treated as continuous time domain equations. As a result, the left hand quantities in (5.25) - (5.27) can be converted to continuous time derivatives ( $L \frac{di_{L0}}{dt}$  etc.). Laplace transformation can now be applied and these equations can then be solved simultaneously, to determine the values of  $\hat{i}_{L0}$ ,  $\hat{v}_{cs0}$  and  $\hat{v}_{ct0}$  in terms of the terminal quantities. These values can then be substituted in (5.28) and (5.29) to arrive at the final small-signal equivalent hybrid model (in Laplace domain) as below.

$$\begin{aligned} \hat{V}_{out}(s) = & (R_3\nu_{11} + K_8\nu_{21} + K_9\nu_{31} + R_4)\hat{I}_0(s) + (R_3\nu_{12} + K_8\nu_{22} + K_9\nu_{32} + K_{10})\hat{E}(s) \\ & + (R_3\nu_{13} + K_8\nu_{23} + K_9\nu_{33} + R_4)\hat{V}_\gamma(s) \end{aligned} \quad (5.30)$$

$$\begin{aligned} \hat{I}_{in}(s) = & (K_{11}\nu_{11} + g_7\nu_{21} + g_8\nu_{31} + K_{12})\hat{I}_0(s) + (K_{11}\nu_{12} + g_7\nu_{22} + g_8\nu_{32} + g_9)\hat{E}(s) \\ & + (K_{11}\nu_{13} + g_7\nu_{23} + g_8\nu_{33} + g_{3c})\hat{V}_\gamma(s) \end{aligned} \quad (5.31)$$

The quantities  $\nu_{ij}$  are defined in Table 5.6.

**Case(II) Discrete Time Domain:** If the perturbation frequencies are comparable to the switching frequency, the approximation of case (I) will not give accurate results. Hence (5.25) - (5.27) must be treated as discrete time domain (difference) equations. This case has been further discussed in section 5.4.

Table 5.6: Coefficients  $\nu_{ij}s$ 

$\nu_{11}$	$\frac{1}{D} \cdot (-s^2(R_2) + s.(g_5R_2 + g_1R_2 - K_1K_5 - K_2K_7) + C_{11})$
$\nu_{12}$	$\frac{1}{D} \cdot (-s^2(K_3) + s.(g_5K_3 + g_1K_3 - K_1g_3 - K_2g_6) + C_{12})$
$\nu_{13}$	$\frac{1}{D} \cdot (-s^2(K_{1c}) + s.(g_5K_{1c} + g_1K_{1c} - K_1g_{1c} - K_2g_{2c}) + C_{13})$
$\nu_{21}$	$\frac{1}{D} \cdot (-s^2(K_5) + s.(R_1K_5 + g_5K_5 - g_2K_7 - K_4R_2) + C_{21})$
$\nu_{22}$	$\frac{1}{D} \cdot (-s^2(g_3) + s.(R_1g_3 + g_5g_3 - g_2g_6 - K_4K_3) + C_{22})$
$\nu_{23}$	$\frac{1}{D} \cdot (-s^2(g_{1c}) + s.(R_1g_{1c} + g_5g_{1c} - g_2g_{2c} - K_4K_{1c}) + C_{23})$
$\nu_{31}$	$\frac{1}{D} \cdot (-s^2(K_7) + s.(R_1K_7 + g_1K_7 - g_4K_5 - K_6R_2) + C_{31})$
$\nu_{32}$	$\frac{1}{D} \cdot (-s^2(g_6) + s.(R_1g_6 + g_1g_6 - g_4g_3 - K_6K_3) + C_{32})$
$\nu_{33}$	$\frac{1}{D} \cdot (-s^2(g_{2c}) + s.(R_1g_{2c} + g_1g_{2c} - g_4g_{1c} - K_6K_{1c}) + C_{33})$
$D$	$-s^3 + s^2.(R_1 + g_1 + g_5) + s.(g_2g_4 + K_1K_4 + K_2K_6 - R_{11}g_1 - R_1g_5 - g_1g_5) + C_D$

The coefficients  $C_{ij}s$  are defined in Table 5.7.

### 5.3.7 Interfacing with the Input and Output Sections of the Converter (Step 7)

The input and output port of the resonant tank can be interfaced with the input and output filter sections (slow, continuous time domain) of the converter to obtain the over all small-signal model shown in Fig. 5.2.

## 5.4 Dynamic Performance Parameters

The dynamic performance parameters like the control to output gain, audio susceptibility and output impedance are useful in evaluating the dynamic performance of a converter. As was stated earlier, the equivalent circuit model can be used to obtain these transfer functions fairly easily as linear circuit theory can be applied. It is with this view that the small-signal hybrid model developed in section 5.3, has been used to obtain these transfer functions in this section. First we use the approximate

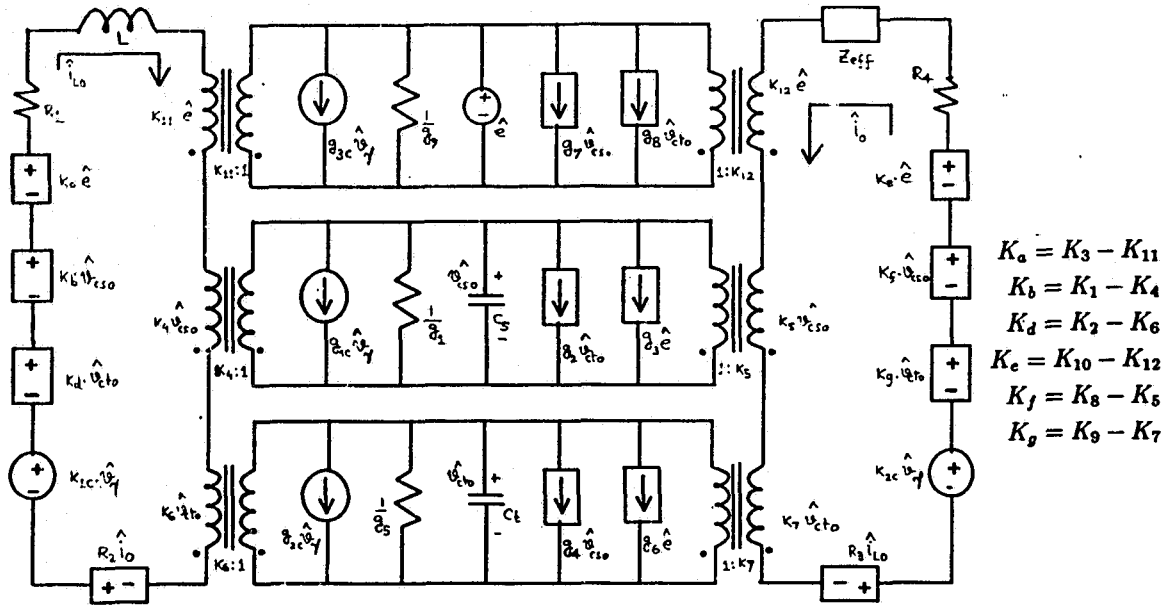


Figure 5.3: Small signal multiple port model of the SPRC

Table 5.7: Coefficients  $C_{ij}$ 's

$C_{11}$	$\frac{1}{D}(-g_1g_5R_2 + g_2g_4R_2 + K_1K_5g_5 - K_1g_2K_7 - K_2g_1K_5 + K_2K_7g_1)$
$C_{12}$	$\frac{1}{D}(-g_1g_5K_3 + g_2g_4K_3 + K_1g_3g_5 - K_1g_2g_6 - K_2g_4g_3 + K_2g_6g_1)$
$C_{13}$	$\frac{1}{D}(-g_1g_5K_{1c} + g_2g_4K_{1c} + K_1g_{1c}g_5 - K_1g_2g_{2c} - K_2g_4g_{1c} + K_2g_{2c}g_1)$
$C_{21}$	$\frac{1}{D}(-R_1g_5K_5 + R_1g_2K_7 + R_2K_4g_5 - R_2g_2K_6 - K_2K_4K_7 + K_2K_6K_5)$
$C_{22}$	$\frac{1}{D}(-R_1g_5g_3 + R_1g_2g_6 + K_3K_4g_5 - K_3g_2K_6 - K_2K_4g_6 + K_2K_6g_3)$
$C_{23}$	$\frac{1}{D}(-R_1g_5g_{1c} + R_1g_2g_{2c} + K_{1c}K_4g_5 - K_{1c}g_2K_6 - K_2K_4g_{2c} + K_2K_6g_{2c})$
$C_{31}$	$\frac{1}{D}(-R_1g_1K_7 + R_1g_4K_5 + K_1K_4K_7 - K_1K_6K_5 - K_4g_4R_2 + K_6g_1R_2)$
$C_{32}$	$\frac{1}{D}(-R_1g_1g_6 + R_1g_4g_3 + K_1K_4g_6 - K_1K_6g_3 - K_4g_4K_3 + K_6g_1K_3)$
$C_{33}$	$\frac{1}{D}(-R_1g_1g_{2c} + R_1g_4g_{1c} + K_1K_4g_{2c} - K_1K_6g_{1c} - K_4g_4K_{1c} + K_6g_1K_{1c})$
$C_D$	$R_1g_1g_5 - R_1g_2g_4 - K_1K_4g_5 + K_1K_6g_2 + K_2K_4g_4 - K_2K_6g_1$

equivalent circuit model, in which the *sampled* nature of the tank states is neglected.

The control to output transfer function and the output impedance are obtained as below.

$$\text{Define } h_{2c}(s) = \left. \frac{\hat{V}_{out}(s)}{\hat{V}_\gamma(s)} \right|_{\hat{I}_0(s)=0, \hat{E}(s)=0} \quad (5.32)$$

$$\text{and } h_{22}(s) = \left. \frac{\hat{V}_{out}(s)}{\hat{I}_0(s)} \right|_{\hat{V}_\gamma(s)=0, \hat{E}(s)=0} \quad (5.33)$$

Referring to Fig. 5.2, the control to output transfer function can be written as below.

$$\frac{\hat{v}_0}{\hat{V}_\gamma}(s) = \frac{h_{2c}(s)R_{parallel}(s)}{R_{parallel}(s) + h_{22}(s) + sL_f} \quad (5.34)$$

$$\text{where } R_{parallel}(s) = \frac{R_L/sC_f}{R_L + 1/sC_f}$$

Similarly, the output impedance is given by

$$Z_o(s) = (h_{22}(s) + sL_f) \parallel (1/sC_f) \parallel R_L \quad (5.35)$$

Two more hybrid parameters are of interest. These are the audio-susceptibility parameter ( $h_{11}(s)$ ) and the input admittance parameter ( $h_{21}(s)$ ) defined below.

$$h_{11}(s) = \left. \frac{\hat{V}_{out}(s)}{\hat{E}(s)} \right|_{\hat{I}_0(s)=0, \hat{V}_\gamma(s)=0} \quad (5.36)$$

$$h_{21}(s) = \left. \frac{\hat{I}_{in}(s)}{\hat{E}(s)} \right|_{\hat{V}_\gamma(s)=0, \hat{I}_0(s)=0} \quad (5.37)$$

An SPRC (Fig. 3.1) has been designed with the following specifications to verify the accuracy of the small-signal models presented.

Input supply voltage,  $2E_{min} = 50 \text{ V}$

Output voltage of the converter,  $V_0 = 24 \text{ V}$

Maximum output power,  $P_o = 100 \text{ Watts}$ ,

Switching frequency,  $f_t = 200 \text{ kHz}$ .

Resonant Frequency ( $f_0$ ) = 250 kHz.

Designed values are:

$$L_s = 17.74\mu H ; C_s = 0.047\mu F ; C_t = n^2 C'_t = 0.047\mu F ; n = 1.$$

$$R_{L(\text{rated})} = 6.74 \Omega.$$

$$L_f = 1000\mu H ; C_f = 1.0\mu F.$$

Fig. 5.4 shows the control to output transfer function bode plot as obtained using (5.34). Fig. 5.5 shows the plots of output impedance and audio-susceptibility transfer functions obtained with the approximate equivalent circuit model. Output impedance plot is useful in determining the transient response of the converter. It is desirable that this plot does not show a peaking nature and the magnitude is as low as possible in order to have a good transient response. The audio-susceptibility plot on the other hand, is useful in determining the effect of the perturbations of the input supply voltage on the converter output. Fig. 5.5(b) shows that for low perturbation frequencies, the input supply variations affect the converter output considerably. However, as the perturbation frequency goes up, this effect becomes less and less pronounced. The bode plots of parameters  $h_{11}(s)$  and  $h_{21}(s)$  are given in Fig. 5.6.

### Observations

- (1) The dynamics of the converter are influenced by complex pole pair (slow) due to the filter elements of the output filter section. They determine the corner frequency for the -40 db roll off point as is clear from Fig. 5.4.
- (2) The dynamics of the converter at perturbation frequencies closer to the switching frequency are governed by the fast (complex) poles due to the resonant tank portion of the converter, which introduce a phase lag of  $180^\circ$ . These poles occur at the *beat frequency* which is approximately the difference of operating frequency and the natural resonant frequency.

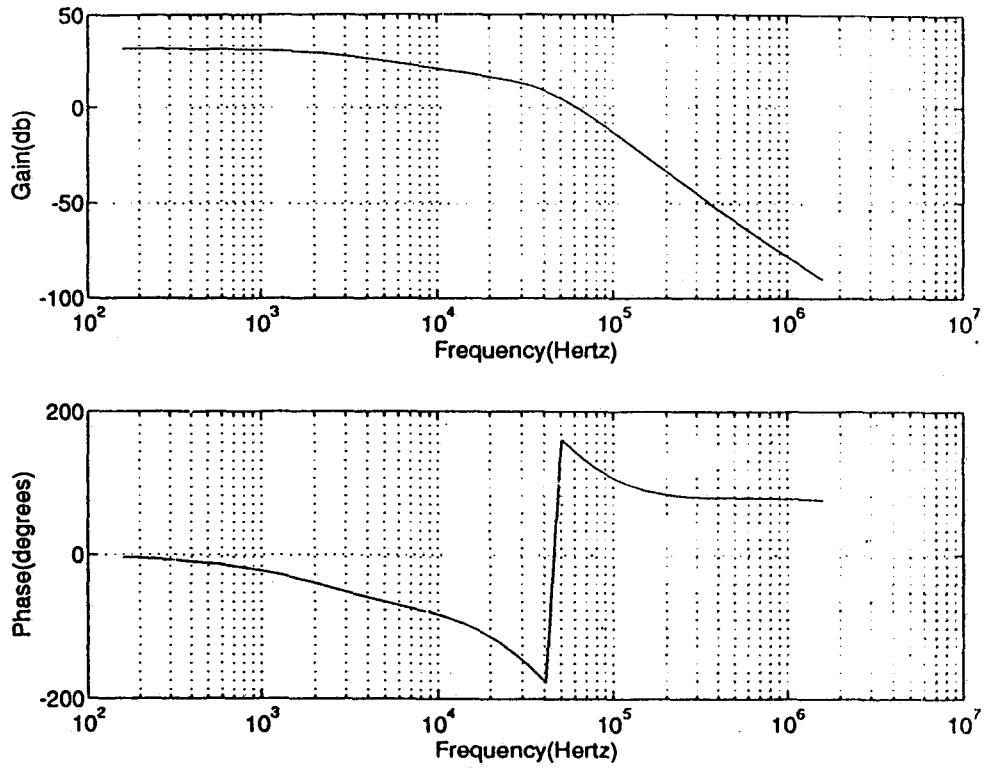


Figure 5.4: Bode plot of control to output transfer function obtained with the approximate small signal equivalent circuit model.

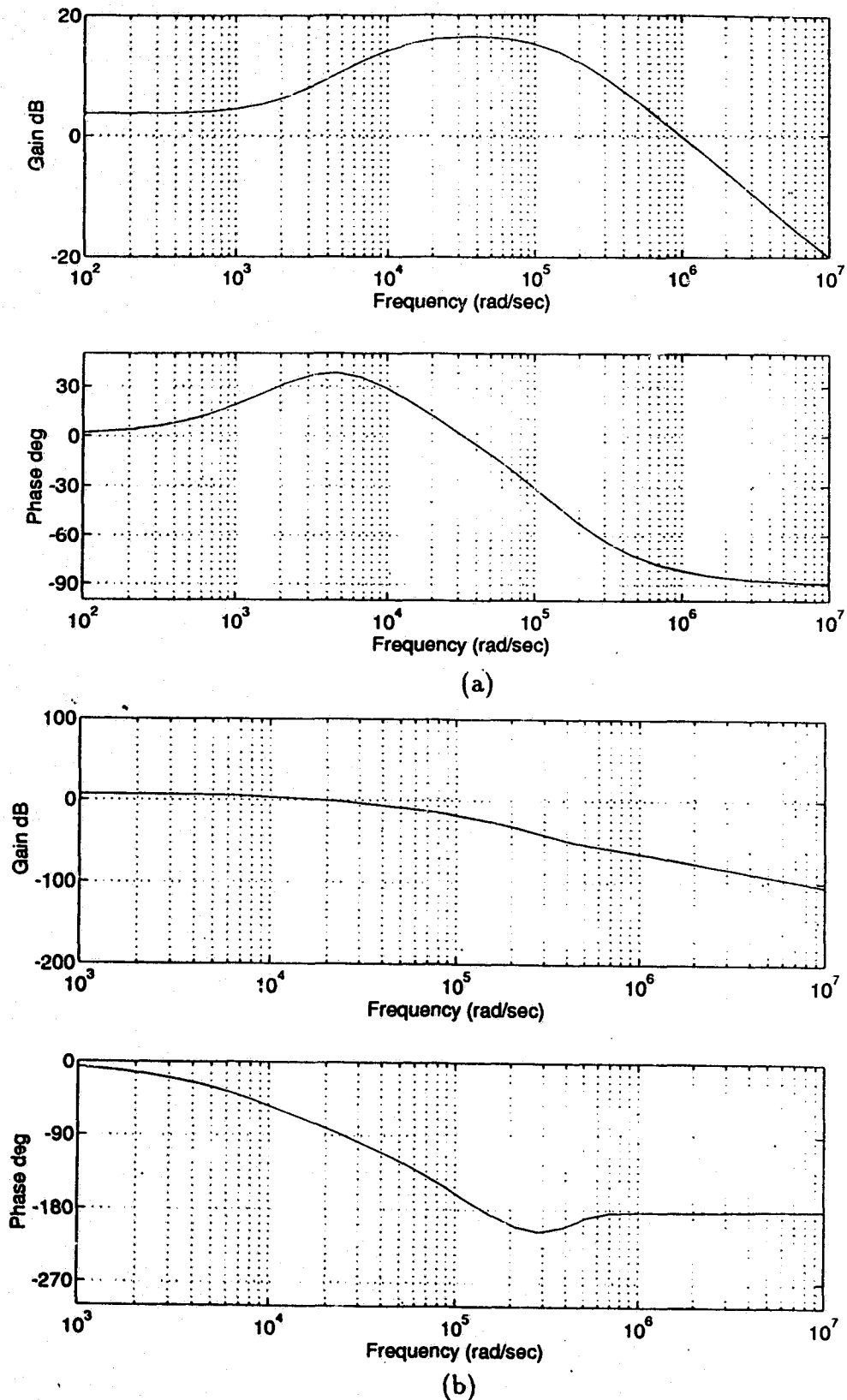


Figure 5.5: (a) Bode plot of output impedance transfer function obtained with the approximate small signal equivalent circuit model. (b) Audio-susceptibility transfer function.

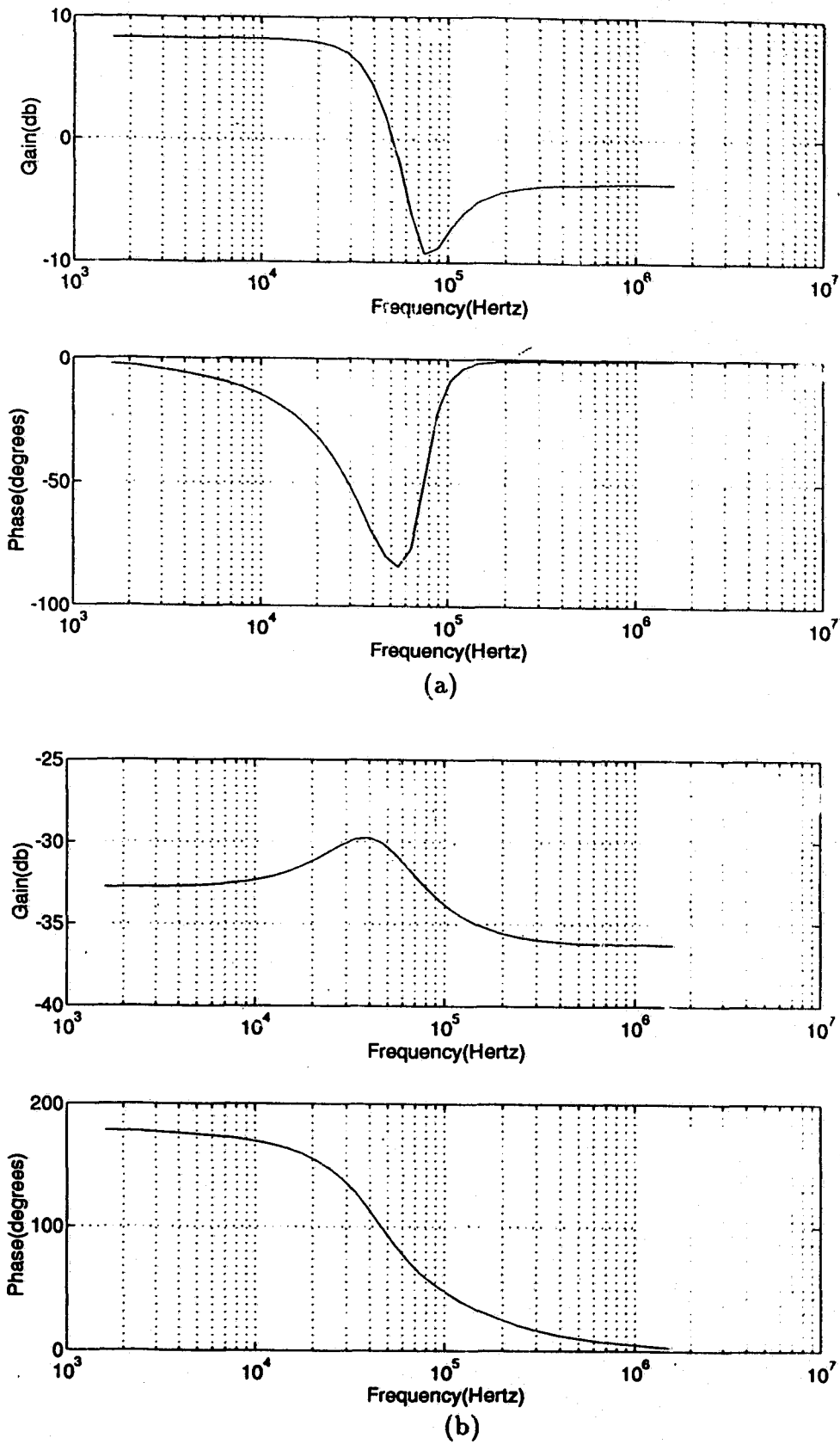


Figure 5.6: (a) The bode plot of the audio-susceptibility parameter. (b) Input admittance parameter.

(3) The lumped parameters of the equivalent circuit model are frequency dependent and can be represented by transfer functions of order 3. This can be verified from (5.32), (5.33), (5.36) and Table 5.6. The lumped parameters are of order 2, in case of series- and parallel- resonant converters. Thus the order of the resonant tank governs the order of the lumped parameter.

(4) The audio-susceptibility transfer function has nearly the same pattern as the control to output transfer function.

So far we have neglected the sampled nature of the converter states. This however is not an accurate representation because the states are in fact discrete. To account for the sampled nature, (5.4), (5.6) and (5.8) must be re-written as difference equations. For example, the equation corresponding to (5.4) will become:

$$\Delta i_{L0} = -A_{1B} \sin(\omega_0 t_s) - B_{1B} \cos(\omega_0 t_s) - C_{1B}(2\cos(\omega_0 t_s) - 1) - i_L(0) \quad (5.38)$$

Equations corresponding to (5.6) and (5.8) can be similarly written. The procedure of obtaining the small-signal model remains essentially the same as described in section 3, except a few changes owing to the discrete nature of the equations. For example, Laplace transform must be replaced by the z-transform. It can be shown that the resultant small-signal model will have the same coefficients as obtained in section 3. The lumped hybrid parameters obtained earlier are redefined in terms of the complex variable  $z$  by making the following substitution.

$$s = \frac{(z - 1)}{T_s} \quad (5.39)$$

where  $T_s$  is the steady-state value of half time period of the operating frequency.

With this substitution, all the s-domain coefficients  $\nu$  in Table 5.6 will now become z-domain coefficients. Fig. 5.7 shows the control to output transfer function obtained using the exact, z domain equivalent circuit model. The results obtained using the

approximate model (Fig. 5.4) are also plotted again for the sake of comparison. It is clear that the approximate model is not able to predict the small-signal dynamics near the switching frequency, a fact confirmed by experimental results in the next section. The “hump” seen with the exact model is actually a result of the “beat frequency dynamics”, a phenomenon resulting from the interaction of the switching frequency and the resonant frequency [87]. Prediction of the beat dynamics is important for proper control loop design as they affect the control bandwidth. To demonstrate the importance of the exact model, the plots of the output impedance and audio-susceptibility transfer functions, obtained using the z domain model, are plotted in Figs. 5.8 and 5.9 respectively. The approximate plots are also plotted. It can be seen that once again the s domain model is unable to predict the dynamics at higher perturbation frequencies. In particular the phase prediction is highly inaccurate when the approximate model is used. Hence, if the knowledge of the small-signal behavior near the switching frequency is desired, *sampled* nature of the tank states can not be ignored.

## 5.5 Experimental Results

An experimental converter was built with the same specifications as given in section 5.4, and was used to verify some of the theoretical results. Figs. 5.10(a) and (b) show the experimental results obtained for the control to output transfer function. These results can be compared to those of Fig. 5.7. These waveforms confirm that the results predicted by the exact equivalent circuit model are reasonably accurate upto the switching frequency, while the approximate, continuous time domain model is good for lower perturbation frequencies only.

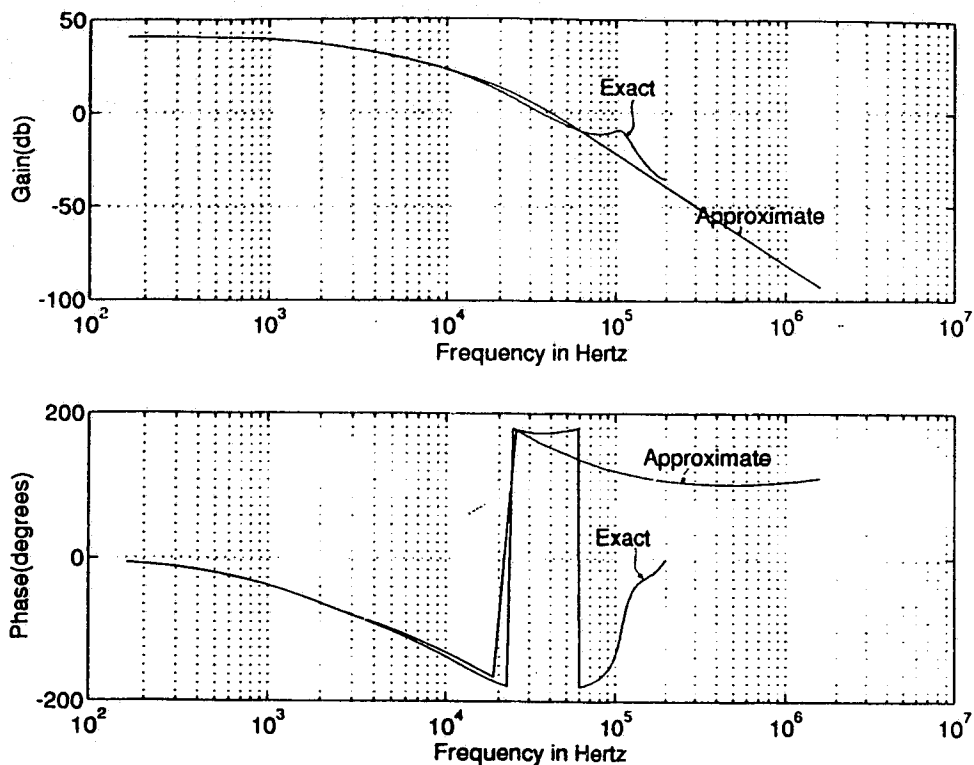


Figure 5.7: Control to output transfer function obtained with *exact* small signal equivalent circuit model. The plot of Fig. 5.4 is included for the sake of comparison.

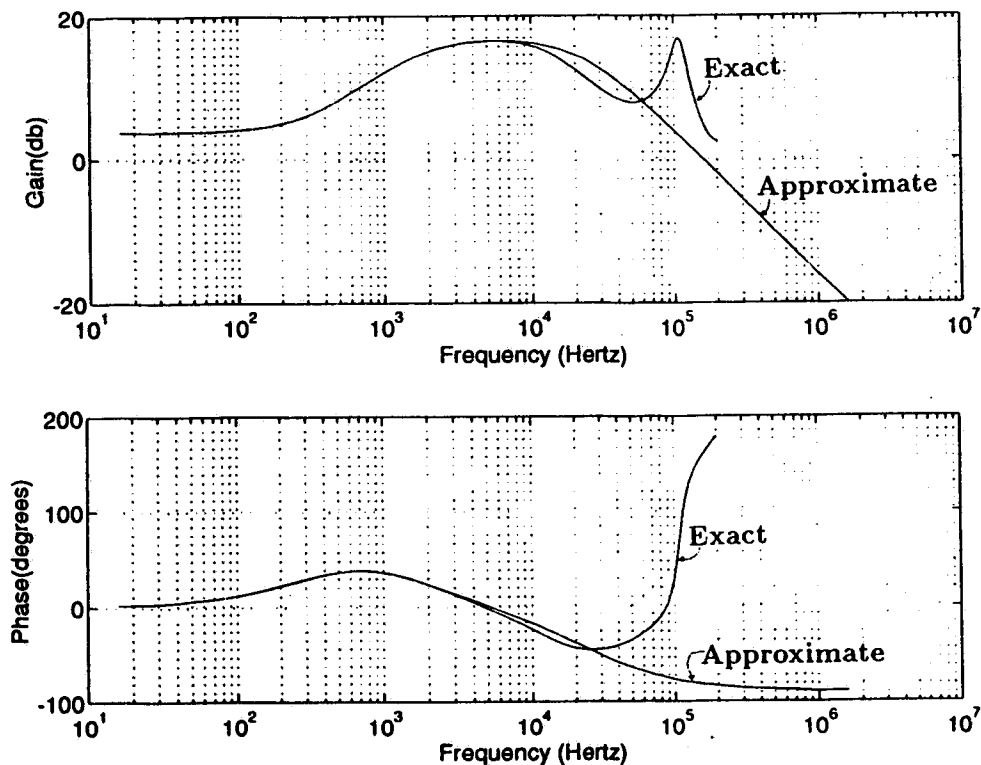


Figure 5.8: Output impedance transfer function obtained with the exact model. The plot of Fig. 5.5(a) is also included for the sake of comparison.

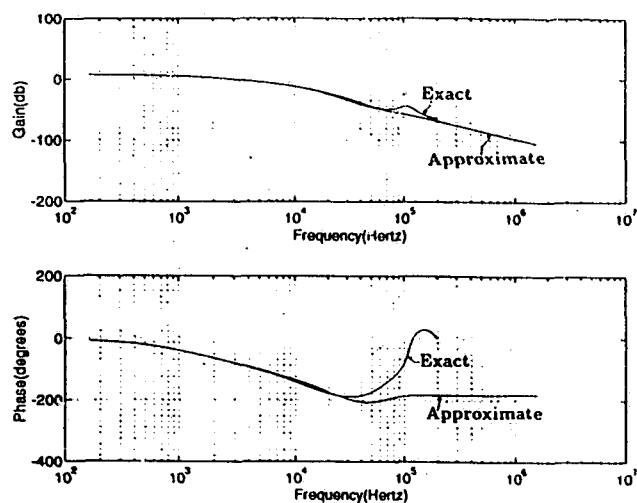


Figure 5.9: Audio-susceptibility transfer function obtained with the exact model. The plot of Fig. 5.5(b) is also included for the sake of comparison.

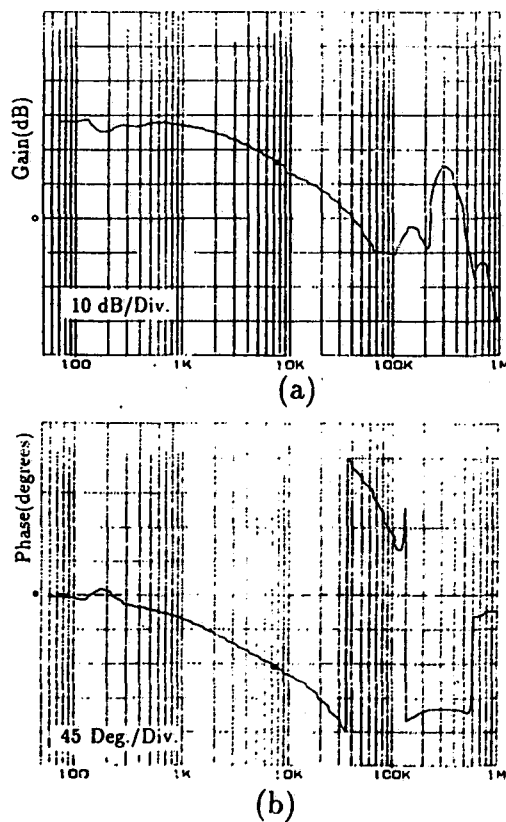


Figure 5.10: Experimental waveforms corresponding to Fig. 5.7 These plots were obtained using a network analyzer (HP 3577A). The details of the converter are the same as given in section 5.4

## 5.6 Conclusions

A two port hybrid small-signal equivalent circuit model has been presented in this chapter. This model is derived using the discrete time domain modeling. Two versions of this model were considered. An approximate one, in which the sampled nature of the tank states was neglected and the analysis was done in continuous time domain. The low frequency approximation, on which the continuous time domain model is based, simplifies the modeling, but the results obtained are good for low perturbation frequencies only. This model fails to predict the “beat frequency dynamics”. The other, exact, z domain model takes into account the sampled nature of the tank states, which in fact is their true nature in a resonant converter. The results obtained with this exact model are more accurate.

Although the equivalent circuit model derived in this chapter is meant for lagging p.f. mode of operation, it can be extended to leading p.f. mode of operation with minor changes. The equivalent circuit model is capable of giving useful dynamic performance parameters in terms of simple transfer functions.

## **Chapter 6**

# **Steady-State and Dynamic Analysis for Fixed Frequency Operation**

In this chapter, steady-state and dynamic analysis of constant frequency pulse-width modulated operation of the LCC-type parallel resonant converter is presented. The full bridge version of this converter, suitable for fixed frequency operation is shown in Fig. 6.1. First, the steady-state analysis is presented and the steady-state solution is obtained. The main purpose of steady-state analysis is to understand the different operating modes and to use the steady-state results for the dynamic analysis. The large-signal behavior is investigated using a large-signal state-space model in the discrete time domain. Key theoretical results are verified using SPICE simulation. A small-signal model is then derived by linearizing the large-signal state equations about a steady-state operating point. The small-signal behavior is predicted using the resulting model.

## 6.1 Introduction

Many techniques have been proposed to control the output power of a resonant converter. Traditionally, the power control in resonant converters has been done by varying the operating frequency of the converter. Although this technique is very popular, it has many drawbacks. These drawbacks are briefly summarized below.

- (1) For below resonance operation, the size of the magnetic components tend to become quite large because they must be designed for the lowest operating frequency.
- (2) There are turn ON losses when the converter is operated below resonance.
- (3) There is a need for lossy RC snubbers,  $\frac{di}{dt}$  limiting inductors and fast recovery diodes.
- (4) For above resonance case, as the frequency goes up, the turn-off switching losses of the switches, the losses in the resonating components and the transformer core losses go up.
- (5) It is more difficult to design the filter components.

To overcome these drawbacks, attempts were made to propose alternate control schemes based on a "fixed" operating frequency. Thus came the idea of fixed frequency pulse-width modulated resonant converters. Some of the initial work in this direction was reported in [58 - 61]. Many techniques have been proposed for the fixed frequency operation. The most popular technique is based on applying phase shifted gating signals to the full bridge converter.

It was stated earlier that in order to make best use of any power converter configuration, it is necessary to formulate proper design procedures which are governed by the conditions under which a converter has to operate. Before an actual converter is built, it is desirable to know how the converter will behave under different operating conditions. This has led to three kinds of analysis depending upon the operating

state of the converter.

- (1) The steady-state or DC analysis.
- (2) The large-signal analysis.
- (3) The small-signal analysis.

Some authors [15,16,18] have reported the fixed frequency operation and its analysis for the SPRC. Reference [15] describes the fixed-frequency PWM control of the SPRC. It is shown that high efficiency for large load variations is achievable along with a narrow range of duty-cycle ratio control and protection against load short circuit conditions. A simple analysis and design procedure based on complex ac circuit theory was presented in [15]. However, this analysis is based on the following approximations.

- (1) The input voltage to the resonant circuit has been represented by the fundamental component of the square wave.
- (2) A sinusoidal rectifier input voltage has been assumed.
- (3) Only the fundamental component of the rectifier input current has been considered and an equivalent value of ac resistance as seen by the parallel capacitor has been used.

This type of analysis loses its accuracy at reduced pulse widths and can not predict the different modes of operation of the converter.

In [18], state-plane technique has been used to analyze the third order SPRC, which has been reduced to a second order system (by transformation of variables) so that a two dimensional state-plane analysis can be applied. Although this technique is very useful, the transformation of the third order system to a second order system, makes it difficult to understand how the various circuit variables are behaving physically. The steady-state analysis of only one of the operating modes of the SPRC, based on the state-plane technique was reported.

Thus a detailed analysis based on the state-space approach giving different modes of operation is not available in literature.

It is well known that the dynamic analysis is very important to know the response of the converter to sudden disturbances. The large-signal analysis determines the response of the converter when its operating conditions undergo *large* variations in their steady-state values. Similarly the small-signal analysis determines the converter's response to small perturbations in its steady-state values. Dynamic analysis is useful for two reasons. First, it helps in designing the closed loop around the converter and second, it helps in choosing appropriate component ratings.

The large-signal analysis of the SPRC, operating in fixed frequency, pulse-width modulated manner is not available in the literature. The small-signal analysis, using an approximate extended describing function method was reported in [73]. Recently, a combination of extended describing function method and state-space approach has been used [84] to perform the small-signal analysis. In the present thesis work this analysis has been carried out independently, using state-space technique.

Thus the main objectives of this chapter are the following:

- (1) To present a steady-state analysis of the fixed frequency pulse-width modulated SPRC (FF PWM SPRC) using the state-space approach. This approach is followed using a constant current model [12] of the SPRC.
- (2) To present a large-signal analysis using a discrete time domain model on the same lines as derived in chapter 3 for the variable frequency operation.
- (3) To present a small-signal analysis by linearizing the large-signal equations about a steady-state operating point.

The remaining of this chapter is divided into the following sections. Section 6.2 identifies the various operating modes and explains the converter operation for these modes. In section 6.3, the state-space equations are developed for the predominant

operating mode and its steady-state solution is obtained. The large-signal discrete time domain modeling of the fixed frequency PWM SPRC is performed in section 6.4. The model obtained is used to predict the large-signal response of the converter to two kinds of external disturbances. One caused due to switching ON the converter and the other due to a sudden step change in the load. Section 6.5 is devoted to the small-signal analysis. The large-signal equations developed in section 6.4, are linearized about a steady-state operating point to obtain a linearized small-signal model. This model is used to study the dynamic parameters like the control to output transfer function and audio-susceptibility. The observations and conclusions are given in section 6.6.

## 6.2 Operating Modes of a FF PWM SPRC

Fig. 6.2 shows all the possible equivalent circuits of the SPRC during the different intervals of the various operating modes of the fixed frequency PWM SPRC discussed in this chapter. During interval A the polarity of the parallel capacitor voltage is positive where as in interval B, it is negative. Accordingly, the polarity of the rectifier input current ( $i_{rect}$  in Fig. 6.1) is also positive or negative. Interval C1 corresponds to the discontinuous capacitor voltage condition in which the parallel capacitor ( $C_t$ ) gets shorted. Interval C2 is same as C1 except that here voltage  $v_{ab}$  is also zero. Intervals T1 and T2 are special cases of A and B in which the input supply  $v_{ab}$  is zero. Fig. 6.3 shows the gating signals for the various switches of the circuit and the resulting waveform across points a & b of the circuit of Fig. 6.1 for a general case. It can be seen that the gating pulses to the switches of the same "arm" are  $180^\circ$  out of phase. The gating signals for the switch pair S3 & S4 are phase shifted with respect to S1 & S2, to obtain the desired zero voltage interval ( $T_{sft}$ ) in  $v_{ab}$ . It should be noted

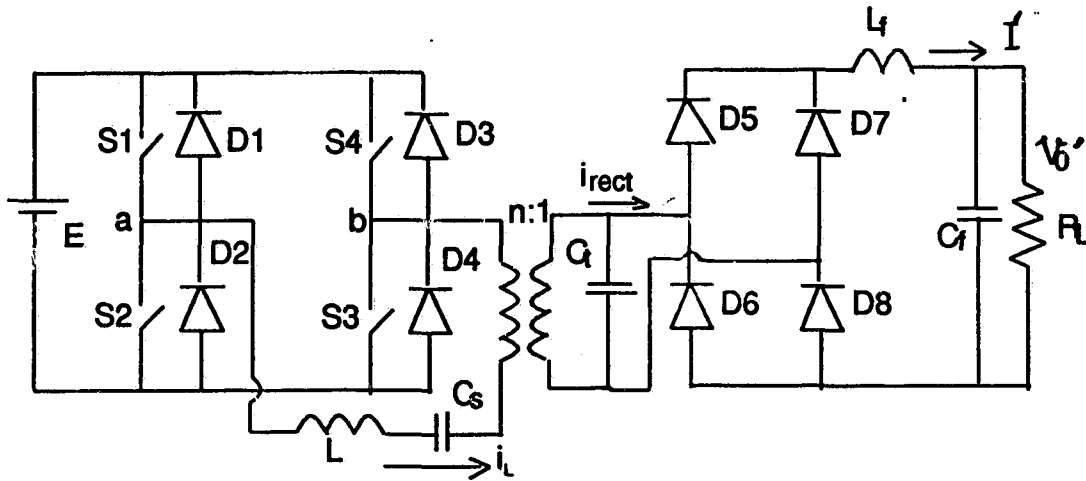


Figure 6.1: The full bridge version of the SPRC suitable for fixed frequency operation. The timing sequence of the gating signals to the various switches is shown in Fig. 6.3.

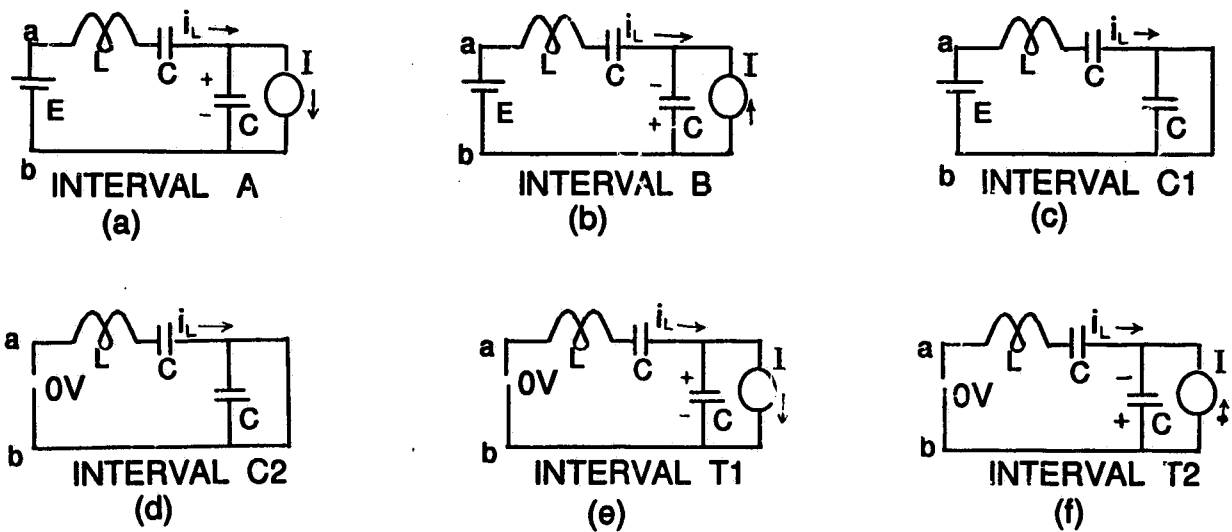


Figure 6.2: Equivalent circuits of the SPRC for various intervals during different operating modes.

that this zero voltage interval corresponds to the duration for which one switch and anti-parallel diode on the other arm in the upper limbs (or the lower limbs) are ON simultaneously. The output voltage regulation for load (or line) variations is obtained by adjusting  $T_{sft}$ .

### 6.2.1 Design of the Converter

The design used is same as used in the earlier chapters based on the method described in [12]. Design is done for the worst case loading conditions i.e. for maximum load current with minimum input voltage. At the rated design conditions given below, the converter operates with full pulse width (i.e.  $T_{sft} = 0$ ) in lagging power factor mode and on the boundary of CCVM and DCVM. As the load current varies due to change in load resistance, the phase shift between gating signals is changed so as to maintain the constant, rated value of the output voltage. The various operating modes encountered in this process are described later in this section. The SPRC designed has the following specifications (same as chapter 3):

Input supply voltage,  $V_{smin}(= 2E) = 50 \text{ V}$ .

Output voltage of the converter,  $V'_0 = 24 \text{ V}$ .

Output voltage ripple,  $V'_{0(p-p)} = \pm 0.025 \text{ V}$ .

Output current ripple,  $I'_{p-p} = \pm 0.010 \text{ A}$ .

Maximum output power,  $P_o = 100 \text{ Watts}$ .

Switching frequency,  $f_t = 200 \text{ kHz}$ .

The design values obtained are:

Normalized load current,  $J = \frac{I}{(E/Z)} = 4.3 \text{ p.u.}; n \approx 1$ .

$L = 17.74 \mu\text{H}; C_s = 0.047 \mu\text{F}; C_t = n^2 C'_t = 0.047 \mu\text{F}$ .

The rated load resistance is,  $R'_L = 5.76 \Omega$ .

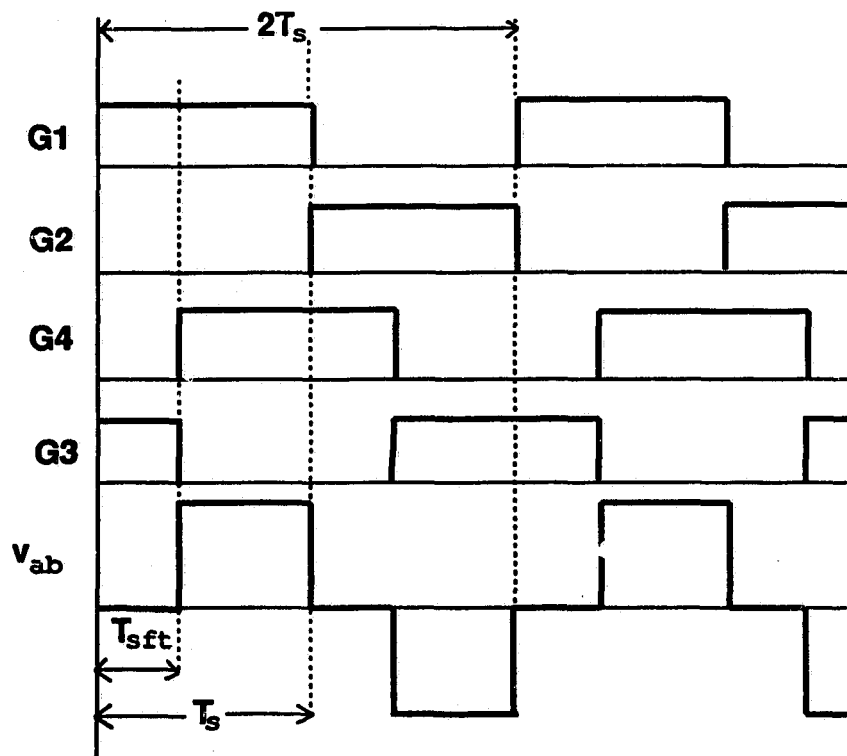


Figure 6.3: Time sequence of the gating pulses to the switches of the inverter bridge for fixed frequency PWM operation of the converter.

Using the above design, the following operating modes were identified for the FF-PWM-SPRC.

**(1) Full pulse width ( $T_{sft} = 0$ ), lagging p.f. mode:** Fig. 6.4(a) shows the typical waveforms for this mode and correspond to the rated operating conditions. The duty ratio is 50 % ( $T_{sft} = 0$ ). The resonating inductor current lags the voltage  $v_{ab}$  and therefore zero voltage switching occurs. The parallel capacitor voltage is continuous and therefore the converter is operating in the CCVM. Thus only two intervals are present in this operating mode, namely intervals A and B.

**(2) Reduced pulse width, lagging p.f. mode:** As the load current decreases, the pulse width is reduced ( $T_{sft}$  is increased) to maintain a constant output voltage. This results in the operating mode shown in Fig. 6.4(b). The tank current still lags the input square-wave voltage,  $v_{ab}$  and the converter is operating in the CCVM. Operation at this reduced value of the duty cycle results in a three interval operating mode as shown in the Figure.

**(3) Reduced pulse width, leading p.f. mode:** As the load current is further reduced, the tank current leads  $v_{ab}$  and the converter is operating in the CCVM. Typical waveforms are shown in Fig. 6.4(c).

It was observed that if the capacitor ratio  $\frac{C_a}{C_t} = 1$  is increased, the converter operates in the DCVM and the converter gain decreases. This results in some more operating modes with more intervals. To highlight these modes, another design is considered [15], with the capacitor ratio  $\frac{C_a}{C_t} = 2$ . The design specifications (referred to as design 2) of the converter used to identify these modes are:

Input voltage = 120V

Output Voltage = 48 V

Output power = 500 Watts

Operating Frequency = 40 kHz

The following component values are used.

$$L = 315.8 \mu H; \quad C_s = 0.0553 \mu F; \quad C_t = 0.02764 \mu F$$

The following additional operating modes are identified with design 2.

**(4) Full pulse width, lagging p.f. and DCV mode:** Fig. 6.5(a) shows the waveforms corresponding to this mode. It comprises of three intervals (an *A* interval between two *C1* intervals). The equivalent circuits of the SPRC during these intervals are given in Fig. 6.2. Full pulse width has been applied with the converter operating at rated load conditions and the tank current is lagging the input square-wave voltage.

**(5) Reduced pulse width, leading p.f. and DCV mode:** When the pulse width is reduced to regulate the output voltage, an operating mode results whose waveforms are shown in Fig. 6.5(b). This mode has four intervals, *C2*, *C1*, *A* and *C1* and the tank current leads the input square-voltage.

As the load decreases further and the pulse width is reduced to a lower value, the converter enters the CCV mode (2), described above.

The steady-state and dynamic analysis of operating mode (1) has already been dealt with in chapters 2 through 5, under variable frequency operation. The state-space analysis of operating modes (4) and (5) is complex due to the presence of more intervals on account of the discontinuity in the parallel capacitor voltage. They have not been dealt further in this thesis. Therefore, in this chapter, the discussion will be confined to (2) and (3) alone. The steady-state analysis for these two modes is presented in the next section.

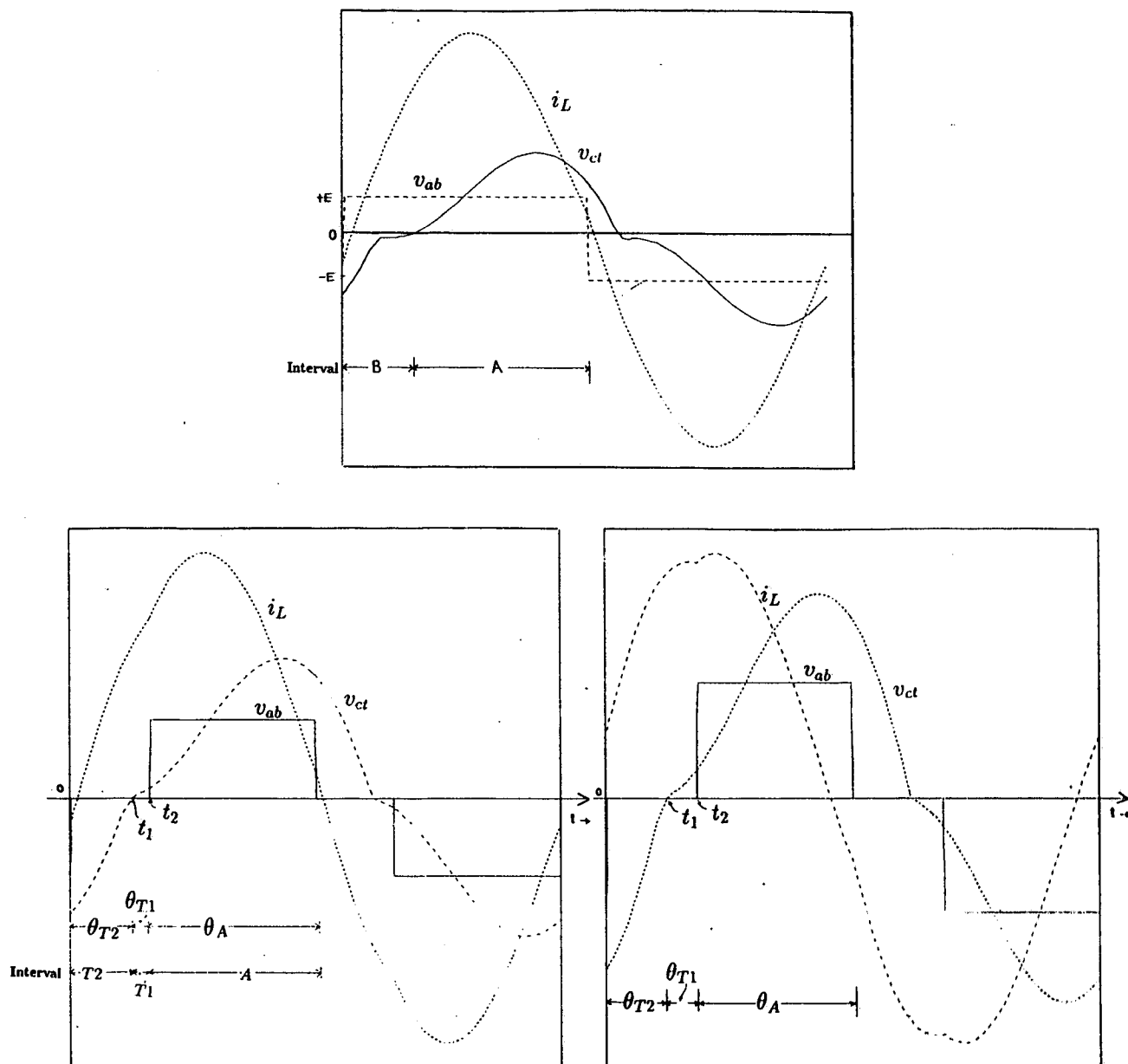
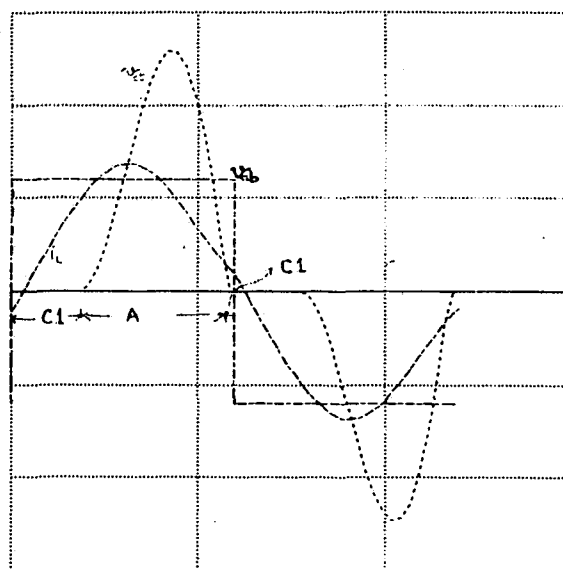
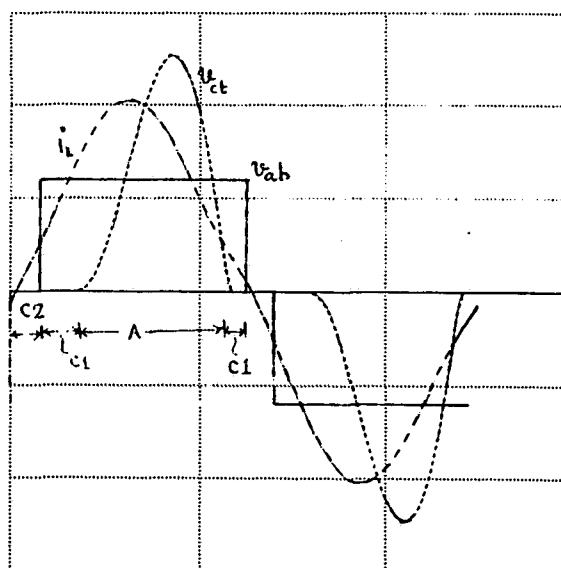


Figure 6.4: The various operating modes of the FF PWM SPRC for the design example with  $C_s/C_t = 1$ .

- Rated load conditions, 50 percent duty cycle,  $T_{sft} = 0$ .
- Reduced pulse width, lagging power factor mode of operation at reduced load current and rated output voltage.
- Reduced pulse width, leading power factor mode of operation for very light load conditions.



(a)



(b)

Figure 6.5: The various operating modes of the FF PWM SPRC for the design example with  $C_s/C_t = 2$ .

(a) Rated load conditions, 50 percent duty cycle,  $T_{sft} = 0$ .

(b) Reduced pulse width, leading power factor mode of operation at reduced load current and rated output voltage.

## 6.3 Steady-State Analysis using State-Space Approach

### 6.3.1 General Solutions

All the equivalent circuits of Fig. 6.2 can be represented by the following general differential equations.

$$\frac{di_L}{dt} = \frac{k_1 E - (v_{csi} + v_{cti})}{L} \quad (6.1)$$

$$C_s \cdot \frac{dv_{cs}}{dt} = i_L \quad (6.2)$$

$$C_t \cdot \frac{dv_{ct}}{dt} = i_L + k_2 \cdot I \quad (6.3)$$

The above equations can be compactly expressed in the following state-space form [7]:

$$\begin{bmatrix} \frac{di_L}{dt} \\ \frac{dv_{cs}}{dt} \\ \frac{dv_{ct}}{dt} \end{bmatrix} = \begin{bmatrix} 0 & \frac{-1}{L} & \frac{-1}{L} \\ \frac{1}{C_s} & 0 & 0 \\ \frac{1}{C_t} & 0 & 0 \end{bmatrix} \begin{bmatrix} i_L \\ v_{cs} \\ v_{ct} \end{bmatrix} + \begin{bmatrix} \frac{1}{L} & 0 \\ 0 & 0 \\ 0 & \frac{-1}{C_t} \end{bmatrix} \begin{bmatrix} k_1 E \\ k_2 \cdot I \end{bmatrix} \quad (6.4)$$

where,  $k_2$  is +1 for intervals A and T1, -1 for intervals B and T2, and zero for intervals C1 and C2.  $k_1$  is zero for intervals C1, C2, T1 and T2. Equation (6.4) has the following general solutions.

$$i_L(t) = A_{1m} \cdot \sin(\omega_q t) + B_{1m} \cdot \cos(\omega_q t) + C_{1m} \quad (6.5)$$

$$v_{cs}(t) = A_{2m}(1 - \cos(\omega_q t)) + B_{2m} \cdot \sin(\omega_q t) + C_{2m}(\omega_q t) + v_{cs(mi)} \quad (6.6)$$

$$v_{ct}(t) = A_{3m}(1 - \cos(\omega_q t)) + B_{3m} \cdot \sin(\omega_q t) + C_{3m}(\omega_q t) + v_{ct(mi)} \quad (6.7)$$

Here,  $m$  denotes the interval of operation (e.g. A, B, C1, C2, T1 or T2) as shown in Fig. 6.2.  $\omega_q = \omega_s = \frac{1}{\sqrt{LC_s}}$  for intervals C1 and C2, while,  $\omega_q = \omega_0 = \frac{1}{\sqrt{LC_e}}$  for intervals A, B, T1 and T2. The steady-state analysis of two operating modes discussed in section 6.2 is presented next.

### 6.3.2 Steady-State Solutions

The waveforms corresponding to this mode are shown in Fig. 6.4(b) and (c). The various intervals are clearly marked. It can be observed that the sequence of equivalent circuits for both modes is the same. Therefore, the analysis presented is valid for both modes.

#### Interval T2; $0 < t < t_1$

Let  $t' = t$  be the running variable for this interval. Then using (6.5) - (6.7), we obtain:

$$i_L(t') = A_{1T2} \cdot \sin(\omega_0 t') + B_{1T2} \cdot \cos(\omega_0 t') + C_{1T2} \quad (6.8)$$

$$v_{cs}(t') = A_{2T2}(1 - \cos(\omega_0 t')) + B_{2T2} \cdot \sin(\omega_0 t') + C_{2T2}(\omega_0 t') + v_{cs(T2i)} \quad (6.9)$$

$$v_{ct}(t') = A_{3T2}(1 - \cos(\omega_0 t')) + B_{3T2} \cdot \sin(\omega_0 t') + C_{3T2}(\omega_0 t') + v_{ct(T2i)} \quad (6.10)$$

#### Interval T1; $t_1 < t < t_2$

Let  $t'' = t - t_1$  be the running variable for this interval.

$$i_L(t'') = A_{1T1} \cdot \sin(\omega_0 t'') + B_{1T1} \cdot \cos(\omega_0 t'') + C_{1T1} \quad (6.11)$$

$$v_{cs}(t'') = A_{2T1}(1 - \cos(\omega_0 t'')) + B_{2T1} \cdot \sin(\omega_0 t'') + C_{2T1}(\omega_0 t'') + v_{cs(T1i)} \quad (6.12)$$

$$v_{ct}(t'') = A_{3T1}(1 - \cos(\omega_0 t'')) + B_{3T1} \cdot \sin(\omega_0 t'') + C_{3T1}(\omega_0 t'') + v_{ct(T1i)} \quad (6.13)$$

#### Interval A; $t_2 < t < T_s$

Let  $t''' = t - t_2$  be the running variable for this interval.

$$i_L(t''') = A_{1A} \cdot \sin(\omega_0 t''') + B_{1A} \cdot \cos(\omega_0 t''') + C_{1A} \quad (6.14)$$

$$v_{cs}(t''') = A_{2A}(1 - \cos(\omega_0 t''')) + B_{2A} \cdot \sin(\omega_0 t''') + C_{2A}(\omega_0 t''') + v_{cs(Ai)} \quad (6.15)$$

$$v_{ct}(t''') = A_{3A}(1 - \cos(\omega_0 t''')) + B_{3A} \cdot \sin(\omega_0 t''') + C_{3A}(\omega_0 t''') + v_{ct(Ai)} \quad (6.16)$$

In the above equations "i" has been used to denote the initial time instant of the interval under consideration. The  $A, B, C$  constants involved in (6.8) - (6.16) are defined in the Appendix D.

To obtain the steady-state solutions, the initial state vector  $[i_{L0} \ v_{cs0} \ v_{ct0}]'$  and the durations of the various intervals are to be evaluated. The procedure remains the same as chapter 2.

### (a) Evaluation of the Initial State Vector

The initial state vector is evaluated using the symmetry conditions of the waveforms according to which the initial state vector is equal and opposite to the value at time instant  $T_s$ . The detailed procedure is presented below:

The final values of the state variables at the end of the interval  $T_2$ , are obtained using (6.8) - (6.10) and is represented in the matrix form as:

$$[x_1] = [A_{T_2}][x_0] + [B_{T_2}][u_{T_2}] \quad (6.17)$$

where;

$$[x_1] = \begin{bmatrix} i_L(t_1) \\ v_{cs}(t_1) \\ v_{ct}(t_1) \end{bmatrix} \quad (6.18)$$

$$[A_{T_2}] = \begin{bmatrix} \cos(\theta_{T_2}) & -\sin(\theta_{T_2})/Z & -\sin(\theta_{T_2})/Z \\ Z.r_2.\sin(\theta_{T_2}) & 1 - r_2.(1 - \cos(\theta_{T_2})) & -r_2.(1 - \cos(\theta_{T_2})) \\ Z.r_1.\sin(\theta_{T_2}) & -r_1.(1 - \cos(\theta_{T_2})) & 1 - r_1.(1 - \cos(\theta_{T_2})) \end{bmatrix} \quad (6.19)$$

$$[B_{T_2}] = \begin{bmatrix} \sin(\theta_{T_2})/Z & r_1.(1 - \cos(\theta_{T_2})) \\ r_2.(1 - \cos(\theta_{T_2})) & Z.r_1.r_2.(\theta_{T_2} - \sin(\theta_{T_2})) \\ r_1.(1 - \cos(\theta_{T_2})) & -Z.r_1.(r_2.\theta_{T_2} + r_1.\sin(\theta_{T_2})) \end{bmatrix} \quad (6.20)$$

$$[u_{T_2}] = \begin{bmatrix} 0 \\ -I \end{bmatrix} \quad (6.21)$$

$$\theta_{T_2} = \omega_0(t_1 - 0) \quad (6.22)$$

$r_1 = C_e/C_s$ ;  $r_2 = C_e/C_t$  and  $C_e = C_s C_t / (C_s + C_t)$ . The final value of interval T1 is obtained using (6.11) - (6.13) with the final values of the state variables of interval T2 as the initial values. This gives:

$$[x_2] = [A_{T1}][x_1] + [B_{T1}][u_{T1}] \quad (6.23)$$

$$[x_2] = [A_{T1}]([A_{T2}][x_0] + [B_{T2}][u_{T2}]) + [B_{T1}][u_{T1}] \quad (6.24)$$

where;

$$[x_2] = \begin{bmatrix} i_L(t_2) \\ v_{cs}(t_2) \\ v_{ct}(t_2) \end{bmatrix} \quad (6.25)$$

$$[A_{T1}] = \begin{bmatrix} \cos(\theta_{T1}) & -\sin(\theta_{T1})/Z & -\sin(\theta_{T1})/Z \\ Z.r_2.\sin(\theta_{T1}) & 1 - r_2.(1 - \cos(\theta_{T1})) & -r_2.(1 - \cos(\theta_{T1})) \\ Z.r_1.\sin(\theta_{T1}) & -r_1.(1 - \cos(\theta_{T1})) & 1 - r_1.(1 - \cos(\theta_{T1})) \end{bmatrix} \quad (6.26)$$

$$[B_{T1}] = \begin{bmatrix} \sin(\theta_{T1})/Z & r_1.(1 - \cos(\theta_{T1})) \\ r_2.(1 - \cos(\theta_{T1})) & Z.r_1.r_2.(\theta_{T1} - \sin(\theta_{T1})) \\ r_1.(1 - \cos(\theta_{T1})) & -Z.r_1.(r_2.\theta_{T1} + r_1.\sin(\theta_{T1})) \end{bmatrix} \quad (6.27)$$

$$[u_{T1}] = \begin{bmatrix} 0 \\ +I \end{bmatrix} \quad (6.28)$$

$$\theta_{T1} = \omega_0(t_2 - t_1) \quad (6.29)$$

Proceeding in a similar manner, we can obtain the final values of the state variables of the third interval (interval A), by using (6.14) - (6.16) with the final value of interval T1 (=  $[x_2]$ ) as the initial value. We obtain.

$$[x_A] = [A_A][x_2] + [B_A][u_A] \quad (6.30)$$

$$[x_A] = [A_A]([A_{T1}]([A_{T2}][x_0] + [B_{T2}][u_{T2}]) + [B_{T1}][u_{T1}]) + [B_A][u_A] \quad (6.31)$$

where;

$$[x_A] = \begin{bmatrix} i_L(T_s) \\ v_{cs}(T_s) \\ v_{ct}(T_s) \end{bmatrix} \quad (6.32)$$

$$[A_A] = \begin{bmatrix} \cos(\theta_A) & \frac{-1}{Z}\sin(\theta_A) & \frac{-1}{Z}\sin(\theta_A) \\ Z.r2.\sin(\theta_A) & 1 - r2.(1 - \cos(\theta_A)) & -r2.(1 - \cos(\theta_A)) \\ Z.r1.\sin(\theta_A) & -r1.(1 - \cos(\theta_A)) & 1 - r1.(1 - \cos(\theta_A)) \end{bmatrix} \quad (6.33)$$

$$[B_A] = \begin{bmatrix} \frac{1}{Z}\sin(\theta_A) & r1.(1 - \cos(\theta_A)) \\ r2.(1 - \cos(\theta_A)) & Z.r1.r2.(\theta_A - \sin(\theta_A)) \\ r1.(1 - \cos(\theta_A)) & -Z.r1.(r2.\theta_A + r1.\sin(\theta_A)) \end{bmatrix} \quad (6.34)$$

$$[u_A] = \begin{bmatrix} E \\ +I \end{bmatrix} \quad (6.35)$$

$$\theta_A = \omega_0(T_s - t_2) \quad (6.36)$$

By symmetry of waveforms (Fig. 6.4(b)),  $[x_A] = -[x_0]$ . Therefore (6.31) can be written as below:

$$-[x_0] = [A_A]([A_{T1}]([A_{T2}][x_0] + [B_{T2}][u_{T2}]) + [B_{T1}][u_{T1}]) + [B_A][u_A] \quad (6.37)$$

which gives

$$[x_0] = -(I_3 + [A_A][A_{T1}][A_{T2}])^{-1}([A_A][A_{T1}][B_{T2}][u_{T2}] + [A_A][B_{T1}][u_{T1}] + [B_A][u_A]) \quad (6.38)$$

### (b) Evaluation of the Interval Durations

The duration of interval A is the pulse width per half cycle and is known. This pulse width can be expressed in terms of the half period ( $T_s$ ) of the operating frequency as  $\zeta.T_s$ , where  $\zeta$  is the duty ratio and  $T_s$  is known. To determine the durations of

intervals of modes T1 and T2, note that time instant  $t_2$  is fixed once the pulse width is fixed, i.e.,

$$t_2 = T_s(1 - \zeta) \quad (6.39)$$

The duration  $t_1$  of interval T2 can be determined by noting that the parallel capacitor voltage is zero at this point. Using (6.10), we obtain the following:

$$\begin{aligned} v_{ct}(t_1) &= A_{3T2}(1 - \cos(\omega_0 t_1)) + B_{3T2} \sin(\omega_0 t_1) + C_{3T2}(\omega_0 t_1) + v_{ct}(T2(0)) \\ &= 0 \end{aligned} \quad (6.40)$$

Equation (6.40) is solved numerically to find  $t_1$ .

### 6.3.3 Design Curves

Once the various interval durations are known the converter gain can be obtained by integrating the parallel capacitor voltage as below:

$$M = \frac{1}{T_s} \left[ \int_0^{t_1} v_{ctT2} d(\omega_0 t') + \int_0^{t_2 - t_1} v_{ctT1} d(\omega_0 t'') + \int_0^{t_A} v_{ctA} d(\omega_0 t''') \right] \quad (6.41)$$

The analysis presented in the previous sections can be used to obtain the design curves for the FF PWM SPRC. Fig. 6.6 shows the plot of normalized load current versus the phase shift for a regulated output voltage. This plot can be used to choose the required duty ratio for a given value of the load current, so that the output voltage remains fixed at the rated value. Fig. 6.7 shows the peak component stresses as the duty ratio is varied to hold the output voltage constant for different load currents.

## 6.4 Large-Signal Analysis

In this section, a large-signal discrete time domain model for the FF PWM SPRC, on the same lines as chapter 3, is presented for the modes discussed in sections 6.2

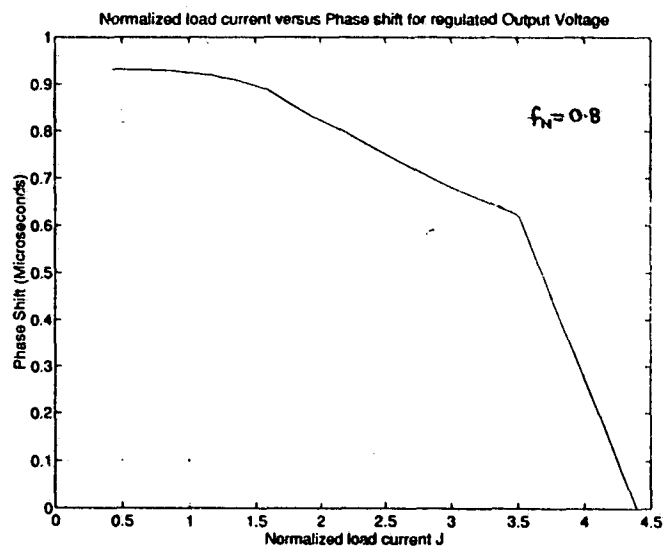


Figure 6.6: Normalized load current versus the phase shift  $T_{sft}$  for regulated output voltage.

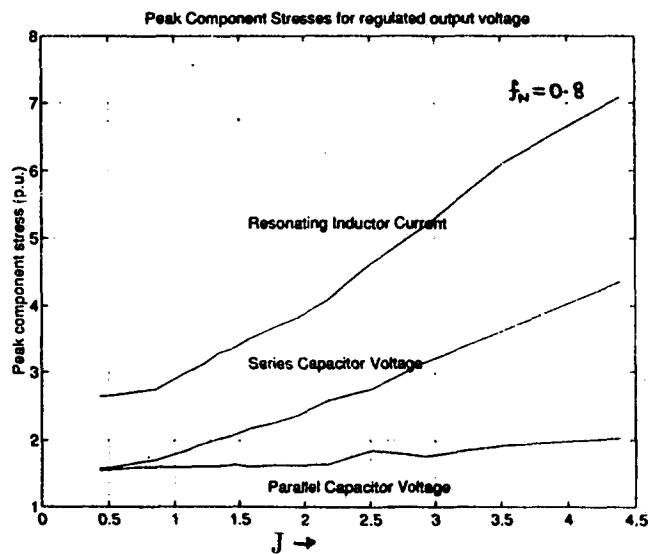


Figure 6.7: Peak component stresses for regulated output voltage.

and 6.3. Details of this modeling are presented next.

### 6.4.1 Terminology

To give a discrete time domain interpretation of the operation of the FF PWM SPRC, Fig. 6.4(b) is drawn again as Fig. 6.8. The converter operation over one cycle of Fig. 6.8, can be represented as a combination of two events, called the  $k^{th}$  and  $(k + 1)^{th}$  events, as in the earlier chapters. Each of the events is composed of three sub-events or the intervals marked in Fig. 6.8 as intervals T2, T1 and A, respectively. These intervals are defined by the following relations.

$$\alpha_k = \omega_0(t_{1(k)} - t_{0(k)}) \quad (6.42)$$

$$\beta_k = \omega_0(t_{2(k)} - t_{1(k)}) \quad (6.43)$$

$$\xi_k = \alpha_k + \beta_k = \omega_0(t_{2(k)} - t_{0(k)}) = (1 - \zeta_k) \cdot T_s \quad (6.44)$$

$$\eta_k = \omega_0(t_{0(k+1)} - t_{2(k)}) = \zeta_k \cdot T_s \quad (6.45)$$

$$\gamma_k = \alpha_k + \beta_k + \eta_k = \omega_0(t_{0(k+1)} - t_{0(k)}) = \omega_0 \cdot T_s \quad (6.46)$$

It should be noted that  $\gamma_k$ , the half period of the operating cycle, is a constant and hence the subscript “ $k$ ” will no longer be used. A careful inspection reveals that the case is analogous to the variable frequency case with  $\zeta_k$  replacing  $\gamma_k$  as the controlling parameter. It should be recalled that in the case of variable frequency operation in chapters 3, 4 and 5,  $\gamma_k$  was considered to be independent of the initial values of the tank variables.

The low ripple approximation is once again assumed. The input supply to the tank circuit is assumed constant either at its *clamped* value of zero or  $\pm E_k$ , for a given event  $k$ . The ripple in its value is considered negligible as compared to the large step changes it makes at instants  $t_{2(k)}$  and  $t_{0(k+1)}$ . The load current is also assumed constant during a given event  $k$  using the same approximation.

## 6.4.2 Discrete Time Domain Model for the FF PWM SPRC

### $k^{th}$ Event

It was seen in section 6.3, that equations (6.8) - (6.16) represent the converter, during the various intervals of the first half of the operating cycle (called  $k^{th}$  event). The same equations are reformulated again, as shown below, with subscript " $k$ " to give a discrete time domain interpretation.

Interval T2;  $t_{0(k)} < t < t_{1(k)}$

$$i_L(t') = A_{1T2k} \cdot \sin(\omega_0 t') + B_{1T2k} \cdot \cos(\omega_0 t') + C_{1T2k} \quad (6.47)$$

$$v_{cs}(t') = A_{2T2k}(1 - \cos(\omega_0 t')) + B_{2T2k} \cdot \sin(\omega_0 t') \\ + C_{2T2k}(\omega_0 t') + v_{cs}(t_{0(k)}) \quad (6.48)$$

$$v_{ct}(t') = A_{3T2k}(1 - \cos(\omega_0 t')) + B_{3T2k} \cdot \sin(\omega_0 t') \\ + C_{3T2k}(\omega_0 t') + v_{ct}(t_{0(k)}) \quad (6.49)$$

Interval T1;  $t_{1(k)} < t < t_{2(k)}$

Let  $t'' = t - t_{1(k)}$ .

$$i_L(t'') = A_{1T1k} \cdot \sin(\omega_0 t'') + B_{1T1k} \cdot \cos(\omega_0 t'') + C_{1T1k} \quad (6.50)$$

$$v_{cs}(t'') = A_{2T1k}(1 - \cos(\omega_0 t'')) + B_{2T1k} \cdot \sin(\omega_0 t'') \\ + C_{2T1k}(\omega_0 t'') + v_{cs}(t_{1(k)}) \quad (6.51)$$

$$v_{ct}(t'') = A_{3T1k}(1 - \cos(\omega_0 t'')) + B_{3T1k} \cdot \sin(\omega_0 t'') \\ + C_{3T1k}(\omega_0 t'') + v_{ct}(t_{1(k)}) \quad (6.52)$$

Interval A;  $t_{2(k)} < t < t_{0(k+1)}$

Let  $t''' = t - t_{2(k)}$ .

$$i_L(t''') = A_{1A_k} \cdot \sin(\omega_0 t''') + B_{1A_k} \cdot \cos(\omega_0 t''') + C_{1A_k} \quad (6.53)$$

$$v_{cs}(t''') = A_{2A_k}(1 - \cos(\omega_0 t''')) + B_{2A_k} \cdot \sin(\omega_0 t''') \\ + C_{2A_k}(\omega_0 t''') + v_{cs}(t_{2(k)}) \quad (6.54)$$

$$v_{ct}(t''') = A_{3A_k}(1 - \cos(\omega_0 t''')) + B_{3A_k} \cdot \sin(\omega_0 t''') \\ + C_{3A_k}(\omega_0 t''') + v_{ct}(t_{2(k)}) \quad (6.55)$$

The coefficients  $A_{1T2_k}$ ,  $B_{1T2_k}$  etc. are defined in Appendix D, with subscript "k" inserted.

### $(k + 1)^{th}$ Event

The  $(k + 1)^{th}$  interval circuit equations are identical to those of  $k^{th}$  interval with a change in the signs of all the variables.

By using the final values of an interval as the initial values of the immediately occurring interval, it is possible to express the initial values of the  $(k + 1)^{th}$  event in terms of the initial values of the  $k^{th}$  event. The resulting expressions have been simplified to yield the following.

$$i_L(t_{0(k+1)}) = \frac{E_{(k)}}{Z} \sin(\eta_k) + A_{1T2_k} \sin(\gamma) + B_{1T2_k} \cos(\gamma) + 2 \cdot C_{1T2_k} \cos(\eta_k \\ + \beta_k) - C_{1T2_k} \quad (6.56)$$

$$v_{cs}(t_{0(k+1)}) = r_1(1 - \cos(\eta_k)) \cdot E_{(k)} + A_{2T2_k}[1 - \cos(\gamma)] + B_{2T2_k} \cdot \sin(\gamma) \\ + C_{2T2_k}[2 \cdot \sin(\eta_k + \beta_k) - \eta_k + \alpha_k - \beta_k] + v_{cs}(t_{0(k)}) \quad (6.57)$$

$$v_{ct}(t_{0(k+1)}) = r_2(1 - \cos(\eta_k)) \cdot E_{(k)} + A_{3T2_k}[1 - \cos(\gamma)] + B_{3T2_k} \cdot \sin(\gamma) \\ - C_{3T2_k}[2 \cdot \frac{r_2}{r_1} \sin(\eta_k + \beta_k) + \eta_k - \alpha_k + \beta_k] + v_{ct}(t_{0(k)}) \quad (6.58)$$

Note that equations (6.56) - (6.58) are the discrete time domain version of (6.31) which is the matrix representation of the same set of equations in continuous time domain.

## Output Equations

The non-linear equations representing the output section of the SPRC are reproduced below:

$$I(t_{0(k+1)}) = I(t_{0(k)}) + 1/L_f \left[ \int_{t_{0(k)}}^{t_{0(k+1)}} |v_{ct}(\tau)| d\tau \right] - 1/L_f [v_0(t_{0(k)})(t_{0(k+1)} - t_{0(k)})] \quad (6.59)$$

$$v_0(t_{0(k+1)}) = v_0(t_{0(k)}) + \frac{(I(t_{0(k)}) - \frac{v_0(t_{0(k)})}{R_L})(t_{0(k+1)} - t_{0(k)})}{C_f} \quad (6.60)$$

The integration interval in (6.59) can be split into three.  $t_{0(k)}$  to  $t_{1(k)}$ ,  $t_{1(k)}$  to  $t_{2(k)}$  and  $t_{2(k)}$  to  $t_{0(k+1)}$ . Value of  $v_{ct}$  can then be substituted using (6.49), (6.52) and (6.55) with an additional negative sign introduced for the interval T2 expression to account for the absolute value of  $v_{ct}$ .

### 6.4.3 The Discrete State-Space Model

#### (a) Selection of Discrete State Variables

As in the earlier chapters, the following discrete state variables are chosen (corresponding to the storage elements in the circuit) for the  $k^{th}$  and  $(k+1)^{th}$  events.

$$x_{1(k)} = -i_L(t_{0(k)}); x_{2(k)} = -v_{cs}(t_{0(k)}); x_{3(k)} = -v_{ct}(t_{0(k)}) \quad (6.61)$$

$$x_{1(k+1)} = i_L(t_{0(k+1)}); x_{2(k+1)} = v_{cs}(t_{0(k+1)}); x_{3(k+1)} = v_{ct}(t_{0(k+1)}) \quad (6.62)$$

For the output section, two additional discrete state variables are introduced for the  $k^{th}$  event.

$$x_{4(k)} = I(t_{0(k)}); x_{5(k)} = v_0(t_{0(k)}) \quad (6.63)$$

### (b) Formulation of the Model

Using the state variables defined in (6.61) to (6.63) and substituting in (6.56) - (6.60), the following discrete state-space model is obtained;

$$x_{1(k+1)} = \frac{E_{(k)}}{Z} \sin(\eta_k) + A_{1T2k} \sin(\gamma) + B_{1T2k} \cos(\gamma) + 2.C_{1T2k} \cos(\eta_k + \beta_k) - C_{1T2k} \quad (6.64)$$

$$x_{2(k+1)} = r_1(1 - \cos(\eta_k)).E_{(k)} + A_{2T2k}[1 - \cos(\gamma)] + B_{2T2k}.\sin(\gamma) + C_{2T2k}[2.\sin(\eta_k + \beta_k) - \eta_k + \alpha_k - \beta_k] + v_{cs}(t_{0(k)}) \quad (6.65)$$

$$x_{3(k+1)} = r_2(1 - \cos(\eta_k)).E_{(k)} + A_{3T2k}[1 - \cos(\gamma)] + B_{3T2k}.\sin(\gamma) - C_{3T2k}[2.\frac{r_2}{r_1}\sin(\eta_k + \beta_k) + \eta_k - \alpha_k + \beta_k] + v_{ct}(t_{0(k)}) \quad (6.66)$$

$$x_{4(k+1)} = x_{4(k)} + \frac{r_2}{X_{Lf}}(x_{2(k)} + x_{3(k)}).(\beta_k + \eta_k - \alpha_k + 2.\sin(\alpha_k) + \sin(\eta_k) - \sin(\gamma)) + \frac{Z.r_2}{X_{Lf}}(-x_{1(k)} + r_2.x_{4(k)})(2.\cos(\alpha_k) - 1 - \cos(\gamma)) + \frac{2Zr_2^2x_{4(k)}}{X_{Lf}}.(\cos(\beta_k + \eta_k) - 1) - \frac{Zr_1r_2x_{4(k)}}{2X_{Lf}}.(\beta_k + \eta_k - \alpha_k)^2 + \frac{r_2.E_{(k)}}{X_{Lf}}.(\eta_k - \sin(\eta_k)) - \frac{x_{3(k)}}{X_{Lf}}.(\beta_k - \alpha_k + \eta_k) - \frac{x_{5(k)}\gamma}{X_{Lf}} \quad (6.67)$$

$$x_{5(k+1)} = x_{5(k)} + \gamma X_{Cf}(x_{4(k)} + i_{out(k)} - \frac{x_{5(k)}}{R_L}) \quad (6.68)$$

where  $X_{Lf} = \omega_0 L_f$  and  $X_{Cf} = \frac{1}{\omega_0 C_f}$ .

### 6.4.4 Results of the Analysis

The discrete time domain model described in section 6.4.2 was used in predicting the transient behavior of the designed converter operating under open loop conditions. PRO-MATLAB was used to solve the discrete time domain equations on the computer. These results are also verified using SPICE software. Results obtained for different transient conditions are explained next.

### **(a) Sudden Switching ON of the Supply Voltage**

The large-signal analysis of the full load case, has already been considered in chapter 3. Here we consider another operating condition corresponding to half the rated load current and rated output voltage. The duty ratio is  $\approx 70\%$ . The operating mode is shown in Fig. 6.8. In this section, effect of switching ON the input supply is studied. Figs. 6.9(a) and (b) show the plots of the tank current and the parallel capacitor voltage obtained for this step change using the large-signal model. Figs. 6.9(c) and (d) show the corresponding SPICE plots. Fig. 6.10 shows the peak component stresses. Figs. 6.11(a) and (b) show the plots of tank state variables and output state variables (current and voltage) as obtained with the model. Fig. 6.11(b) also shows the corresponding SPICE plot for the switch ON transient conditions.

### **(b) Step Change in Load**

In this section the effect of a sudden step change in load is considered. The converter is operating at half the rated load condition with 70 % duty cycle, when the load changes to quarter of rated load in a step manner. For the open loop condition, the duty cycle remains at 70 %. These results are explained next.

Figs. 6.12(a) and (b) show the plots of the tank current and the parallel capacitor voltage obtained for this step change using the large-signal model. Figs. 6.12(c) and (d) show the corresponding SPICE plots. Fig. 6.13 shows the peak component stresses. Figs. 6.14(a) and (b) show the plots of tank state variables and output state variables (current and voltage) as obtained with the model. Fig. 6.14(b) also shows the corresponding SPICE plot for the switch ON transient conditions.

### 6.4.5 Closed Loop Example:

In this section, a typical example of closed loop operation is considered. The converter is operating at half the rated load with rated output voltage value and 70 % duty cycle, when the load suddenly changes to quarter the rated load in a step manner. However, unlike in the previous section, where the open loop operation was considered (and so the duty ratio was not altered), the duty ratio is altered to regulate the output voltage (as a result of closed loop operation) to  $\approx 63$  %. The results obtained for this case are discussed next. It is assumed that the closed loop action is instantaneous. Figs. 6.15(a) and (b) show the plots of the tank current and the parallel capacitor voltage obtained using the large-signal model. Figs. 6.15(c) and (d) show the corresponding SPICE plots. Fig. 6.16 shows the peak component stresses. Figs. 6.17(a) and (b) shows the plots of tank state variables and output state variables (current and voltage) as obtained with the model. Fig. 6.17(b) also shows the corresponding SPICE plots.

## 6.5 Small-Signal Analysis of FF PWM SPRC

The small-signal dynamic behavior of the converter was analyzed for the variable frequency operation in chapter 4, by using a small-signal state-space model, acquired by linearizing the large-signal equations of chapter 3. In this section the small-signal modeling of FF PWM SPRC is performed using the large-signal model obtained in section 6.4. As was stated earlier, the small-signal analysis is concerned with the response of the converter to small perturbations in its steady state operating conditions.

### 6.5.1 Linearization of SPRC About the Equilibrium Point

The first step is to determine the equilibrium point of operation. This is done by applying the following symmetry condition to (6.64) - (6.68).

$$x_{i(k)} = x_{i(k+1)} \quad (6.69)$$

It can be verified that this will yield the steady-state operating point given by (6.38). The large-signal state-space model represented by (6.64) - (6.68) has the following general form;

$$x_{i(k+1)} = f_i(x_{1(k)}, x_{2(k)}, x_{3(k)}, x_{4(k)}, x_{5(k)}, \zeta_k, E_{(k)}, i_{out(k)}) \quad (6.70)$$

where “ $f_i$ ” represents some non-linear function of the relevant independent variables specified on the right hand side of the above equation and  $i = 1 \dots 5$ .

These equations can be linearized using the Taylor's expansion about the equilibrium point resulting in five linearized small-signal equations of the following general form.

$$\begin{aligned} \delta x_{i(k+1)} = & \left. \frac{\partial f_i}{\partial x_{1(k)}} \right|_{eq} \cdot \delta x_{1(k)} + \left. \frac{\partial f_i}{\partial x_{2(k)}} \right|_{eq} \cdot \delta x_{2(k)} + \left. \frac{\partial f_i}{\partial x_{3(k)}} \right|_{eq} \cdot \delta x_{3(k)} \\ & + \left. \frac{\partial f_i}{\partial x_{4(k)}} \right|_{eq} \cdot \delta x_{4(k)} + \left. \frac{\partial f_i}{\partial x_{5(k)}} \right|_{eq} \cdot \delta x_{5(k)} + \left. \frac{\partial f_i}{\partial E_{(k)}} \right|_{eq} \cdot \delta E_{(k)} + \left. \frac{\partial f_i}{\partial \gamma_k} \right|_{eq} \cdot \delta \zeta_k \\ & + \left. \frac{\partial f_i}{\partial i_{out(k)}} \right|_{eq} \cdot \delta i_{out(k)} \end{aligned} \quad (6.71)$$

In the above equation “ $|_{eq}$ ” implies “at equilibrium”.

All the small-signal equations can be clubbed together and represented in the matrix form as below:

$$[\delta x_{i(k+1)}] = [A] \cdot [\delta x_{i(k)}] + [B] \cdot [\delta u_{(k)}]$$

Or

$$\begin{aligned}
 \begin{bmatrix} \delta x_{1(k+1)} \\ \delta x_{2(k+1)} \\ \delta x_{3(k+1)} \\ \delta x_{4(k+1)} \\ \delta x_{5(k+1)} \end{bmatrix} &= \begin{bmatrix} a_{11} & a_{12} & a_{13} & a_{14} & a_{15} \\ a_{21} & a_{22} & a_{23} & a_{24} & a_{25} \\ a_{31} & a_{32} & a_{33} & a_{34} & a_{35} \\ a_{41} & a_{42} & a_{43} & a_{44} & a_{45} \\ a_{51} & a_{52} & a_{53} & a_{54} & a_{55} \end{bmatrix} \cdot \begin{bmatrix} \delta x_{1(k)} \\ \delta x_{2(k)} \\ \delta x_{3(k)} \\ \delta x_{4(k)} \\ \delta x_{5(k)} \end{bmatrix} \\
 &+ \begin{bmatrix} b_{11} & b_{12} & b_{13} \\ b_{21} & b_{22} & b_{23} \\ b_{31} & b_{32} & b_{33} \\ b_{41} & b_{42} & b_{43} \\ b_{51} & b_{52} & b_{53} \end{bmatrix} \cdot \begin{bmatrix} \delta \zeta_k \\ \delta E(k) \\ \delta i_{out(k)} \end{bmatrix} \quad (6.72)
 \end{aligned}$$

The elements  $a_{ij}$ s and  $b_{ij}$ s of matrices [A] and [B] can be determined using the following:

$$a_{ij} = \left. \frac{\partial f_i}{\partial x_{j(k)}} \right|_{eq} \quad (6.73)$$

$$b_{i1} = \left. \frac{\partial f_i}{\partial \zeta_k} \right|_{eq}; \quad b_{i2} = \left. \frac{\partial f_i}{\partial E(k)} \right|_{eq}; \quad b_{i3} = \left. \frac{\partial f_i}{\partial i_{out(k)}} \right|_{eq} \quad (6.74)$$

where  $i = 1 \dots 5$ ;  $j = 1 \dots 5$ .

$$a_{11} = -\cos(\gamma) + \left[ \frac{\partial \alpha_k}{\partial x_{1(k)}} \cdot \frac{\partial f_1}{\partial \alpha_k} \right]_{eq} \quad (6.75)$$

$$a_{12} = (1/Z)\sin(\gamma) + \left[ \frac{\partial \alpha_k}{\partial x_{2(k)}} \cdot \frac{\partial f_1}{\partial \alpha_k} \right]_{eq} \quad (6.76)$$

$$a_{13} = (1/Z)\sin(\gamma) + \left[ \frac{\partial \alpha_k}{\partial x_{3(k)}} \cdot \frac{\partial f_1}{\partial \alpha_k} \right]_{eq} \quad (6.77)$$

$$a_{14} = r_2 \cdot \cos(\gamma) + r_2 \cdot (1 - 2\cos(\beta + \eta)) + \left[ \frac{\partial \alpha_k}{\partial x_{4(k)}} \cdot \frac{\partial f_1}{\partial \alpha_k} \right]_{eq} \quad (6.78)$$

$$a_{21} = -Z \cdot r_1 \cdot \sin(\gamma) + \left[ \frac{\partial \alpha_k}{\partial x_{1(k)}} \cdot \frac{\partial f_2}{\partial \alpha_k} \right]_{eq} \quad (6.79)$$

$$a_{22} = -r_1 \cdot \cos(\gamma) + r_1 - 1 + \left[ \frac{\partial \alpha_k}{\partial x_{2(k)}} \cdot \frac{\partial f_2}{\partial \alpha_k} \right]_{eq} \quad (6.80)$$

$$a_{23} = -r_1 \cdot \cos(\gamma) + r_1 + \left[ \frac{\partial \alpha_k}{\partial x_{3(k)}} \cdot \frac{\partial f_2}{\partial \alpha_k} \right]_{eq} \quad (6.81)$$

$$a_{24} = Z \cdot r_1 \cdot r_2 \cdot \sin(\gamma) + Z \cdot r_1 \cdot r_2 \cdot (\beta + \eta - \alpha - 2 \sin(\beta + \eta)) + \left[ \frac{\partial \alpha_k}{\partial x_{4(k)}} \cdot \frac{\partial f_2}{\partial \alpha_k} \right]_{eq} \quad (6.82)$$

$$a_{31} = -Z \cdot r_2 \cdot \sin(\gamma) + \left[ \frac{\partial \alpha_k}{\partial x_{1(k)}} \cdot \frac{\partial f_3}{\partial \alpha_k} \right]_{eq} \quad (6.83)$$

$$a_{32} = -r_2 \cdot \cos(\gamma) + r_2 + \left[ \frac{\partial \alpha_k}{\partial x_{2(k)}} \cdot \frac{\partial f_3}{\partial \alpha_k} \right]_{eq} \quad (6.84)$$

$$a_{33} = -r_2 \cdot \cos(\gamma) + r_2 - 1 + \left[ \frac{\partial \alpha_k}{\partial x_{3(k)}} \cdot \frac{\partial f_3}{\partial \alpha_k} \right]_{eq} \quad (6.85)$$

$$a_{34} = Z \cdot (r_2)^2 \sin(\gamma) - Z \cdot r_2 \cdot (2 \cdot r_2 \cdot \sin(\beta + \eta) + r_1 \cdot (\eta + \beta - \alpha)) + \left[ \frac{\partial \alpha_k}{\partial x_{4(k)}} \cdot \frac{\partial f_3}{\partial \alpha_k} \right]_{eq} \quad (6.86)$$

$$a_{41} = -\frac{Z \cdot r_2}{X_{Lf}} \cdot (2 \cos(\alpha) - 1 - \cos(\gamma)) + \left[ \frac{\partial \alpha_k}{\partial x_{1(k)}} \cdot \frac{\partial f_4}{\partial \alpha_k} \right]_{eq} \quad (6.87)$$

$$a_{42} = \frac{r_2}{X_{Lf}} \cdot ((\eta + \beta - \alpha) + 2 \cdot \sin(\alpha) + \sin(\eta) - \sin(\gamma)) + \left[ \frac{\partial \alpha_k}{\partial x_{2(k)}} \cdot \frac{\partial f_4}{\partial \alpha_k} \right]_{eq} \quad (6.88)$$

$$a_{43} = \frac{r_2}{X_{Lf}} \cdot ((\beta + \eta - \alpha) + 2 \cdot \sin(\alpha) + \sin(\eta) - \sin(\gamma)) - \frac{(\eta + \beta - \alpha)}{X_{Lf}} + \left[ \frac{\partial \alpha_k}{\partial x_{3(k)}} \cdot \frac{\partial f_4}{\partial \alpha_k} \right]_{eq} \quad (6.89)$$

$$a_{44} = 1 + \frac{Z \cdot r_2^2}{X_{r,f}} (2 \cos(\alpha) - 1 - \cos(\gamma) + 2 \cos(\beta + \eta) - 2) - \frac{Z \cdot r_1 \cdot r_2 \cdot (\beta + \eta - \alpha)^2}{2 \cdot X_{Lf}} + \left[ \frac{\partial \alpha_k}{\partial x_{4(k)}} \cdot \frac{\partial f_4}{\partial \alpha_k} \right]_{eq} \quad (6.90)$$

$$a_{45} = -\frac{\gamma}{X_{I,f}} \quad (6.91)$$

$$a_{54} = \gamma \cdot X_{Cf} \quad (6.92)$$

$$a_{55} = 1 - \frac{\gamma X_{cf}}{R_L} \quad (6.93)$$

$$b_{11} = \gamma \cdot \frac{E}{Z} \cos(\zeta\gamma) \quad (6.94)$$

$$b_{21} = r_1(\gamma \sin(\zeta\gamma)) \cdot E \quad (6.95)$$

$$b_{31} = r_2(\gamma \sin(\zeta\gamma)) \cdot E \quad (6.96)$$

$$b_{41} = \frac{r_2\gamma}{X_{Lf}}(x_2 + x_3) \cdot \cos(\zeta\gamma) + \frac{r_2 \cdot E}{X_{Lf}}(\gamma - \gamma \cdot \cos(\zeta\gamma)) \quad (6.97)$$

$$b_{12} = \frac{\sin(\zeta\gamma)}{Z} + \left[ \frac{\partial \alpha_k}{\partial E_{(k)}} \cdot \frac{\partial f_1}{\partial \alpha_k} \right]_{eq} \quad (6.98)$$

$$b_{22} = -r_1 \cdot \cos(\zeta\gamma) + r_1 + \left[ \frac{\partial \alpha_k}{\partial E_{(k)}} \cdot \frac{\partial f_2}{\partial \alpha_k} \right]_{eq} \quad (6.99)$$

$$b_{32} = -r_2 \cdot \cos(\zeta\gamma) + r_2 + \left[ \frac{\partial \alpha_k}{\partial E_{(k)}} \cdot \frac{\partial f_3}{\partial \alpha_k} \right]_{eq} \quad (6.100)$$

$$b_{42} = \frac{r_2}{X_{Lf}}(\zeta\gamma - \sin(\zeta\gamma)) + \left[ \frac{\partial \alpha_k}{\partial E_{(k)}} \cdot \frac{\partial f_4}{\partial \alpha_k} \right]_{eq} \quad (6.101)$$

$$b_{53} = \gamma X_{Cf} \quad (6.102)$$

$$a_{15} = a_{25} = a_{35} = a_{51} = a_{52} = a_{53} = 0 \quad (6.103)$$

$$b_{13} = b_{23} = b_{33} = b_{43} = b_{51} = b_{52} = 0 \quad (6.104)$$

The partial derivatives involved in the above equations are evaluated next. For this the parallel capacitor voltage is equated to zero at the end of interval B, which leads to the following equation:

$$\begin{aligned} & r_2 \cdot (x_{2(k)} + x_{3(k)}) \cdot (1 - \cos(\alpha_k)) + Z \cdot r_2 \cdot (-x_{1(k)} \\ & + r_2 \cdot x_{4(k)}) \sin(\alpha_k) + Z \cdot r_1 \cdot r_2 \cdot x_{4(k)} \cdot \alpha_k - x_{3(k)} = 0 \end{aligned} \quad (6.105)$$

Then, using (6.105), the partial derivatives (evaluated at the equilibrium point) obtained are given by:

$$\frac{\partial \alpha_k}{\partial x_{1(k)}} = \frac{Z \cdot \sin(\alpha)}{D} \quad (6.106)$$

$$\frac{\partial \alpha_k}{\partial x_{2(k)}} = \frac{-(1 - \cos(\alpha))}{D} \quad (6.107)$$

$$\frac{\partial \alpha_k}{\partial x_{3(k)}} = \frac{1 - r_2 \cdot (1 - \cos(\alpha))}{r_2 \cdot D} \quad (6.108)$$

$$\frac{\partial \alpha_k}{\partial x_{4(k)}} = \frac{-(r_2 \cdot Z \cdot \sin(\alpha) + Z \cdot r_1 \cdot \alpha)}{D} \quad (6.109)$$

$$\frac{\partial \alpha_k}{\partial E_k} = 0 \quad (6.110)$$

$$\begin{aligned} \text{where } D &= (x_2 + x_3) \sin(\alpha) + Z \cdot (-x_1 + r_2 \cdot x_4) \cos(\alpha) \\ &\quad + Z \cdot r_1 \cdot x_4 \end{aligned} \quad (6.111)$$

Use of (6.64) - (6.66) and (6.70), yields the following:

$$\frac{\partial f_1}{\partial \alpha_k} = -2 \cdot r_2 \cdot x_4 \cdot \sin(\beta + \eta) \quad (6.112)$$

$$\frac{\partial f_2}{\partial \alpha_k} = Z \cdot r_1 \cdot r_2 \cdot x_4 [2 \cos(\beta + \eta) - 2] \quad (6.113)$$

$$\frac{\partial f_3}{\partial \alpha_k} = Z \cdot r_2 \cdot x_4 [2 \cdot r_2 \cdot \cos(\eta + \beta) + 2 \cdot r_1] \quad (6.114)$$

$$\begin{aligned} \frac{\partial f_4}{\partial \alpha_k} &= \frac{r_2}{X_{Lf}} (x_2 + x_3) \cdot (-2 + 2 \cos(\alpha)) \\ &\quad - \frac{2Z \cdot r_2}{X_{Lf}} (-x_1 + r_2 \cdot x_4) (\sin(\alpha)) - \frac{2Z \cdot r_1 \cdot r_2 \cdot x_4}{X_{Lf}} (2\alpha - \gamma) \\ &\quad + \frac{2Z \cdot r_2^2 \cdot x_4}{X_{Lf}} \cdot \sin(\beta + \eta) + \frac{2x_3}{X_{Lf}} \end{aligned} \quad (6.115)$$

Which completes the derivation of the small-signal model for a FF PWM SPRC. Equation (6.72), with coefficients of matrices A and B given by  $a_{ij}$  and  $b_{ij}$ , respectively, represents the model in matrix form. This model can be used to predict the small-signal behavior of the FF PWM SPRC.

### 6.5.2 Dynamic Performance Parameters

The dynamic performance parameters like the control to output gain, audio susceptibility and output impedance, which are useful in evaluating the dynamic behavior of the converter are studied in this section. Fig. 6.18 (a) shows the plot of control

to output transfer function as obtained with the help of the proposed model. Fig. 6.18(b) shows the corresponding plot for the audio-susceptibility transfer function. Importance of such plots was explained in Chapters 4 and 5. The output impedance transfer function plot is shown in Fig. 6.18(c).

## 6.6 Observations and Conclusions

The steady-state analysis of FF PWM SPRC shows that the designed FF PWM SPRC operates in three major modes for  $\frac{C_s}{C_t} = 1$ , and two major (both DCVM) modes for  $\frac{C_s}{C_t} = 2$ . The converter is designed to operate on the boundary of CCVM and DCVM, lagging p.f. mode for full load conditions. As the load current reduces, the pulse width is adjusted to regulate this output voltage. This results in operating modes 2 and 3 and the discontinuity in parallel capacitor voltage is negligible. The discontinuity in the parallel capacitor voltage increases with an increase in  $C_s/C_t$  ratio. The curve of  $T_{sft}$  versus normalized load current is non-linear. This, however, does not matter because in actual practice the converter is operated in closed loop manner. The required variation in  $T_{sft}$  is much larger for load current variation from full load to half load than for half load to very light load conditions.

The large-signal analysis provided the following results. During switch ON conditions, the converter enters leading p.f mode of operation before reaching the steady state where it is designed to operate in lagging p.f. mode. All the tank components are over stressed during the switch ON transients. During step change in load from half the rated load condition to quarter load condition, the converter enters leading p.f. mode within 30 microseconds (Fig. 6.14(a)). For the closed loop operation however, the converter stays longer in the lagging p.f. mode (50 microseconds). During step change from half the rated load to quarter the rated load conditions, the tank

components do not experience an over stress.

Small-signal analysis shows that the control to output transfer for the FF PWM SPRC has nearly the same pattern as the one for frequency controlled SPRC, obtained in Chapter 4. The audio-susceptibility transfer function shows the same pattern as the control to output transfer function. However, the phase plot does not show as much lag as it did in the case of frequency controlled SPRC.

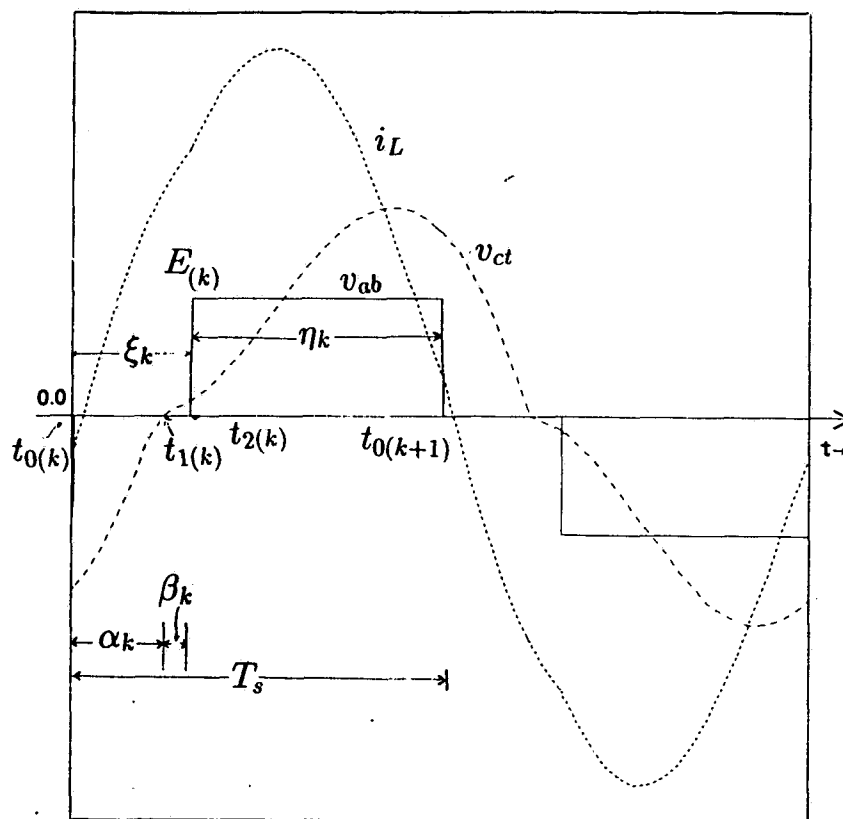


Figure 6.8: Typical waveforms of the FF PWM SPRC circuit starting from the  $k^{\text{th}}$  instant for lagging power factor mode of operation. The various intervals are marked.

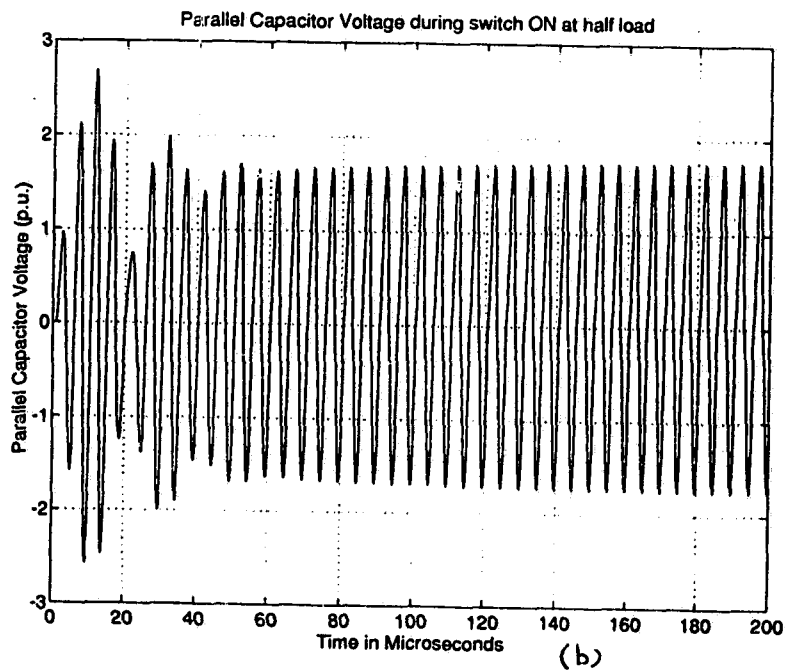
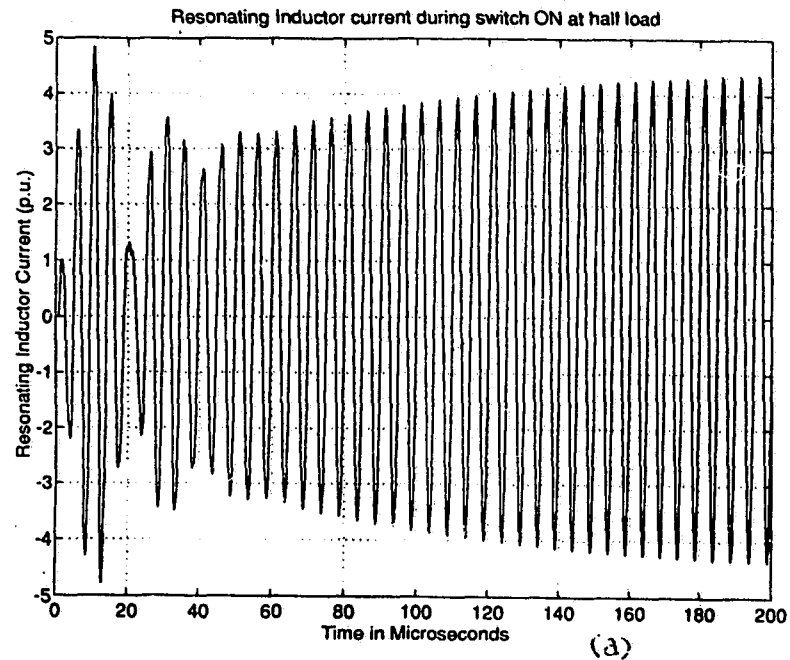
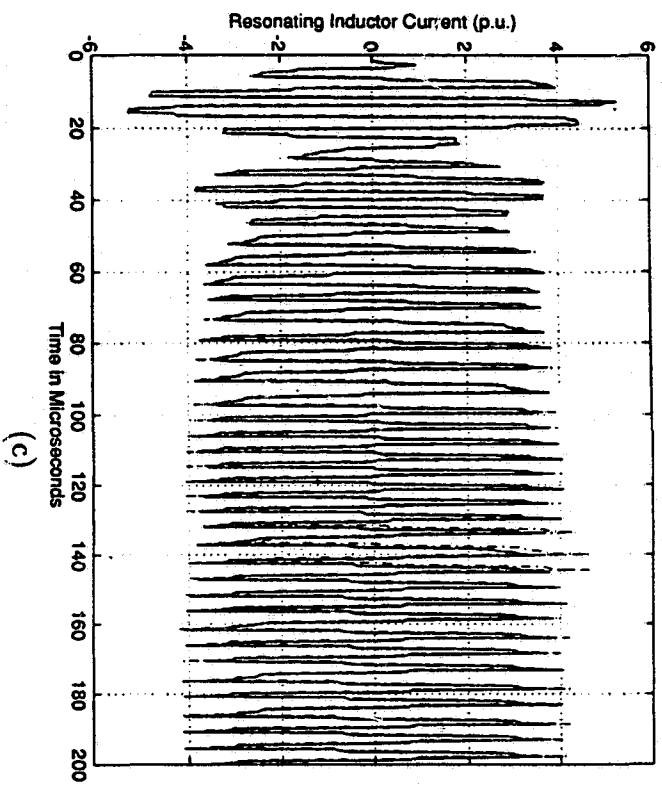
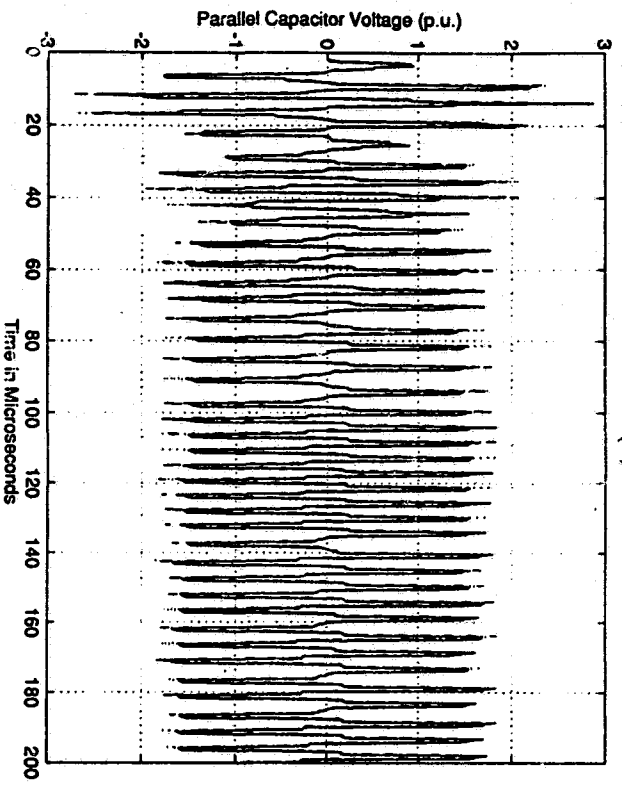


Figure 6.9: (a) Resonating inductor and (b) parallel capacitor voltage, for step change in input voltage supply from 0V to 25V at half the rated load conditions. In all the plots the step change occurs at the origin. (c),(d): SPICE plots corresponding to (a) and (b).



(c)



(d)

Fig. 6.9 (continued)

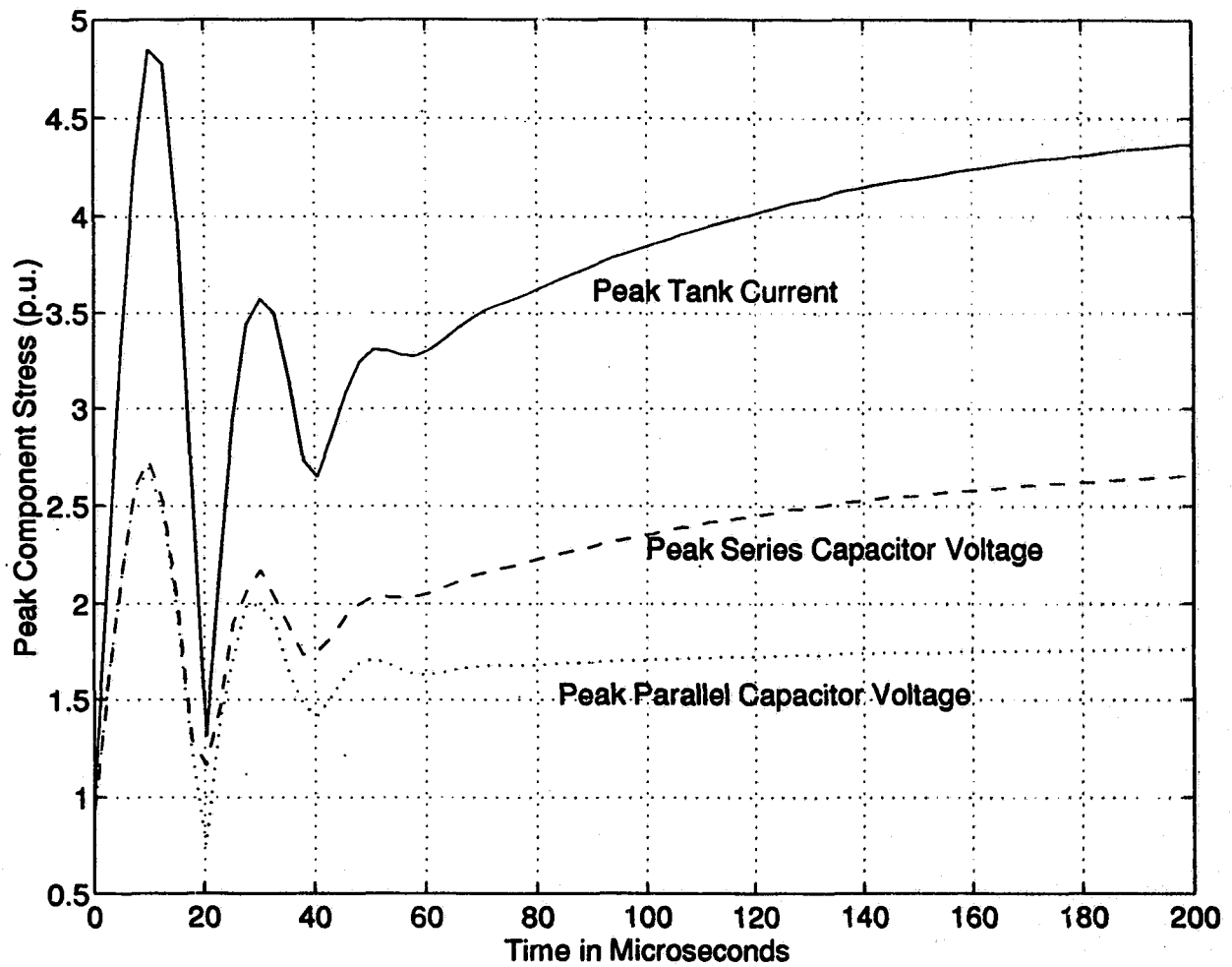
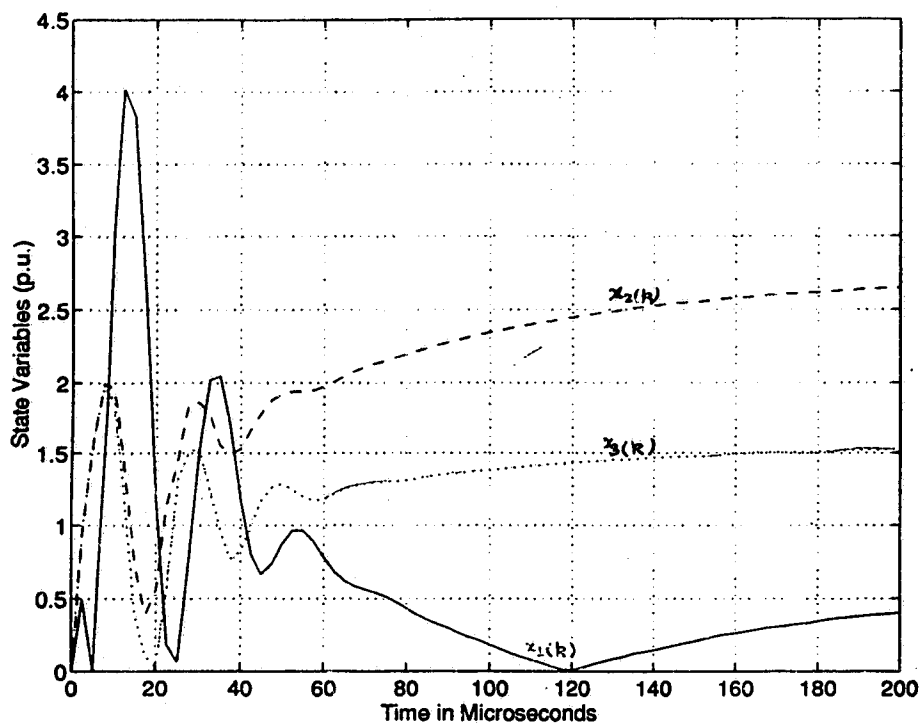
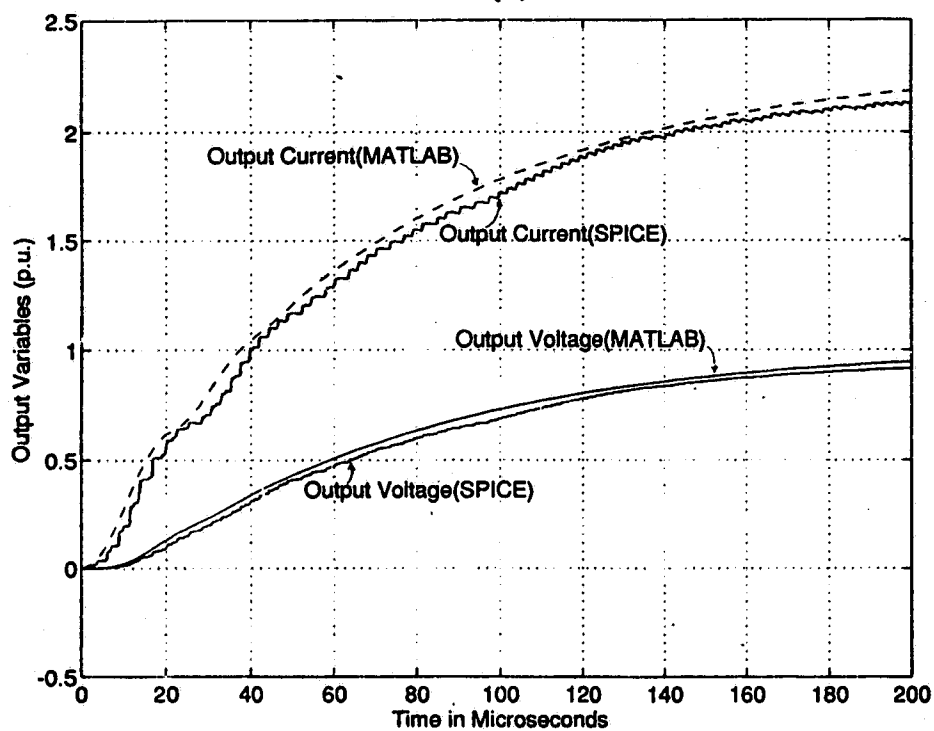


Figure 6.10: Peak component stresses (p.u.) for step change in input supply. Note that all these plots have been obtained with discrete set of points obtained one per half cycle, and connected to give an over all continuous picture.



(a)



(b)

Figure 6.11: Discrete state variables: (a) Tank state variables. (b) Output state variables. SPICE results are also plotted for the sake of comparison.

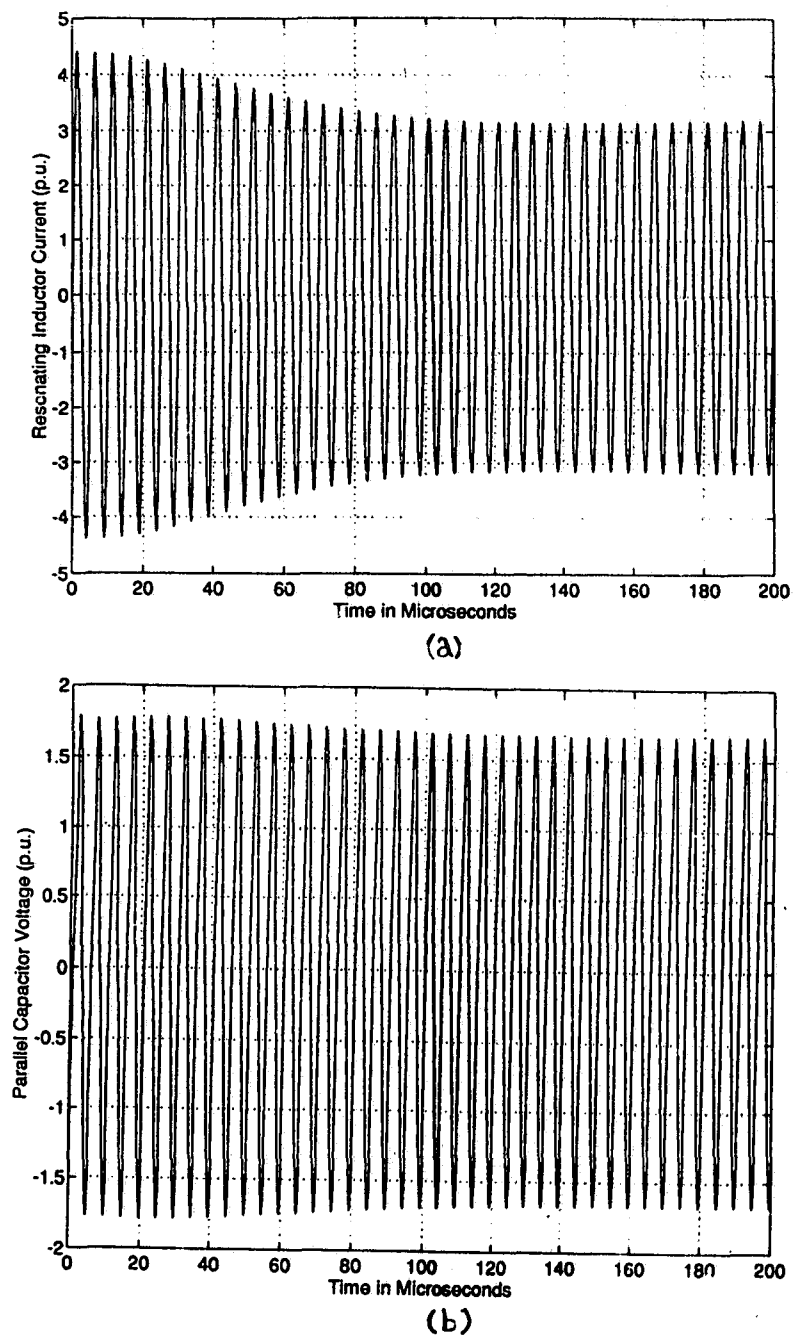


Figure 6.12: (a) Resonating inductor and (b) parallel capacitor voltage, for step change in load from half the rated load to quarter the rated load. (c),(d): SPICE plots corresponding to (a) and (b).

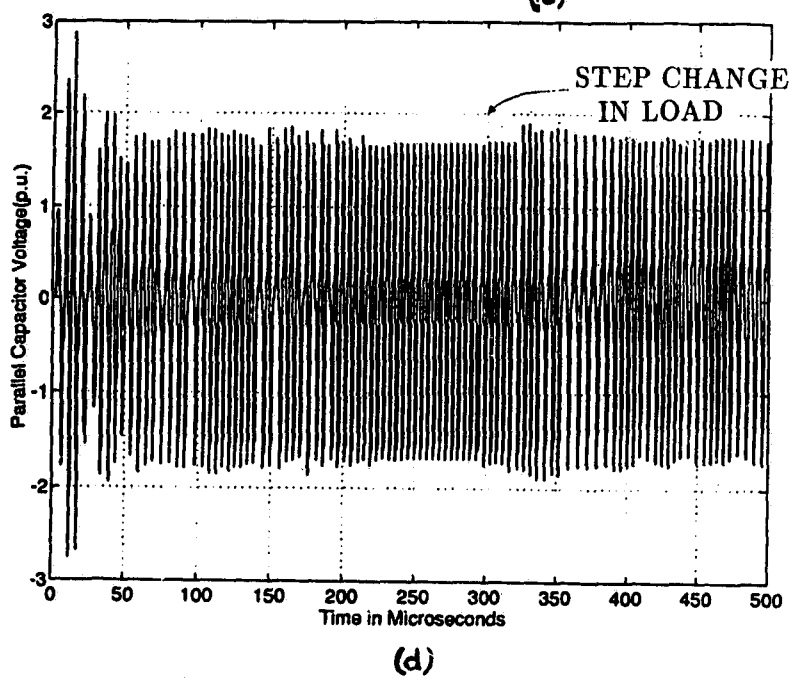
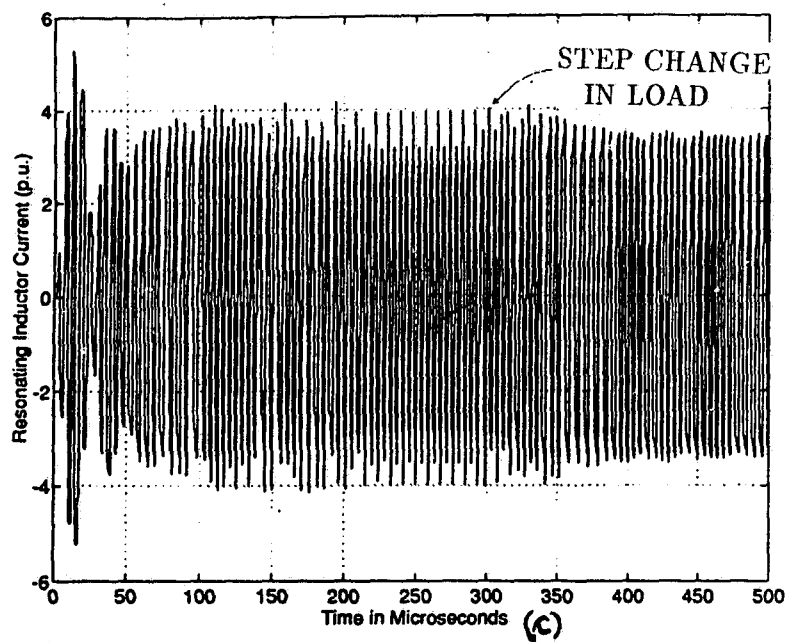


Fig. 6.12 (continued)

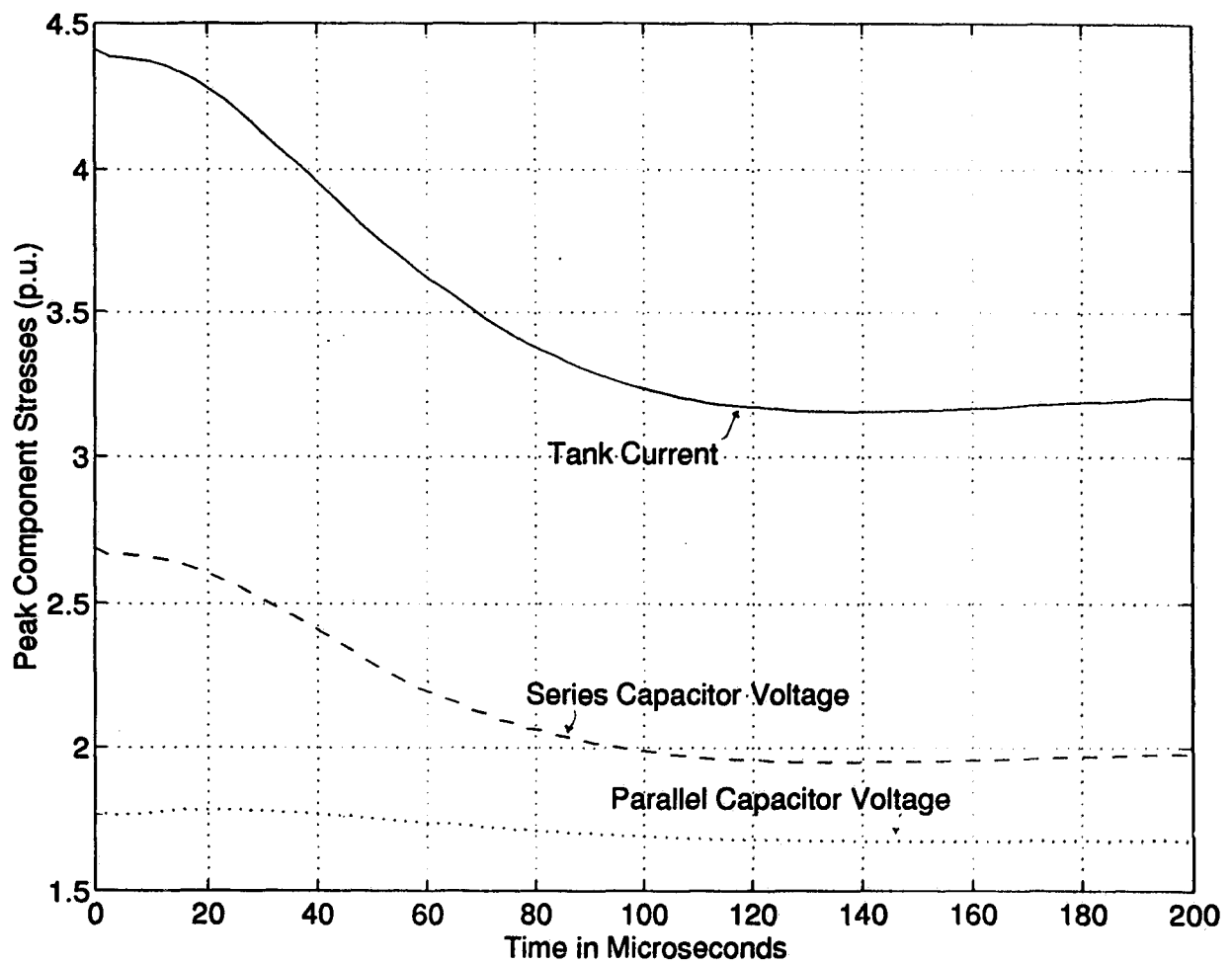
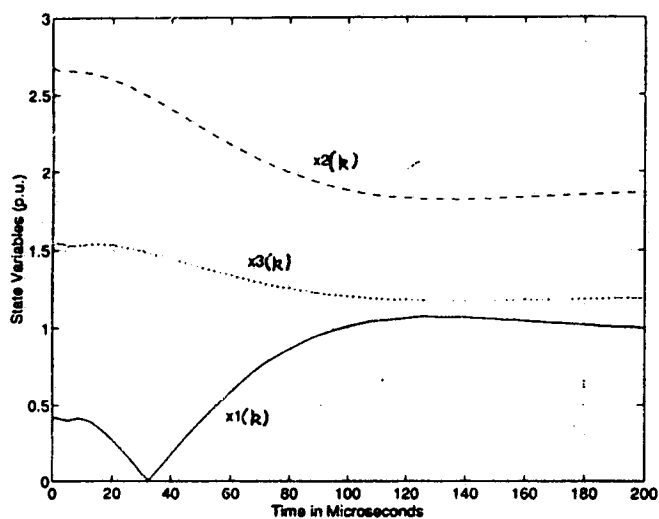
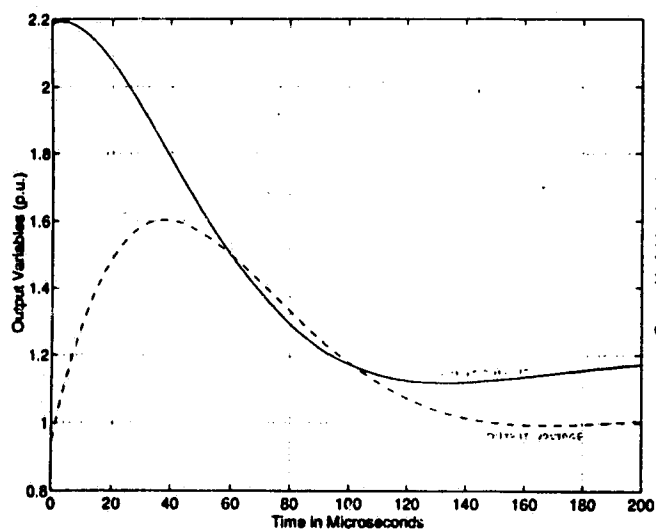


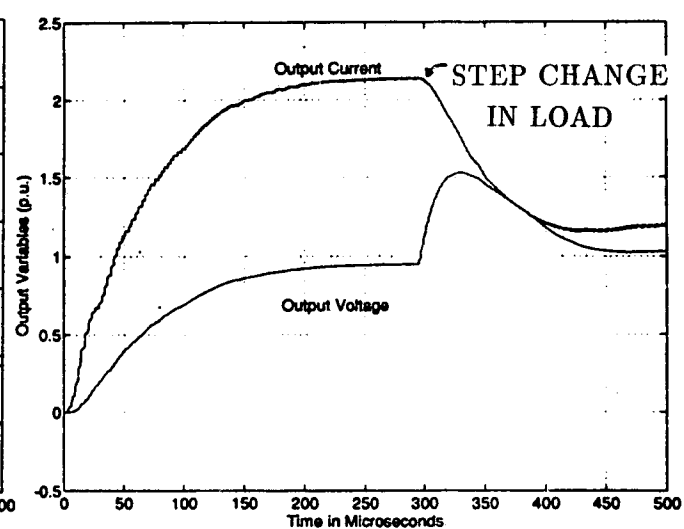
Figure 6.13: Peak component stresses (p.u.) for step change in load from half the rated load to quarter the rated load.



(a)



b(i)

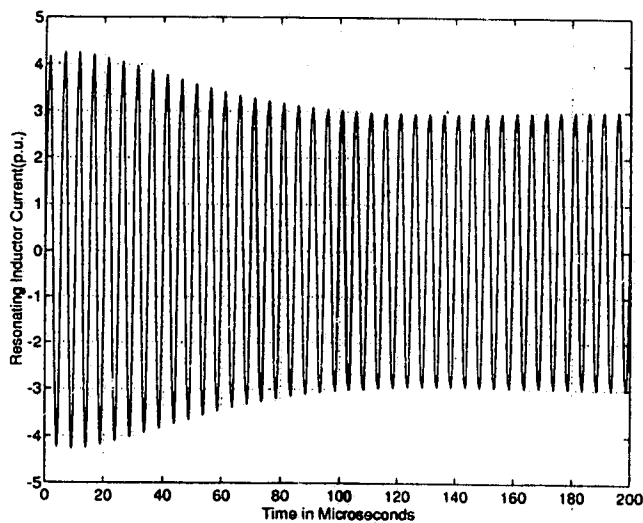


b(ii)

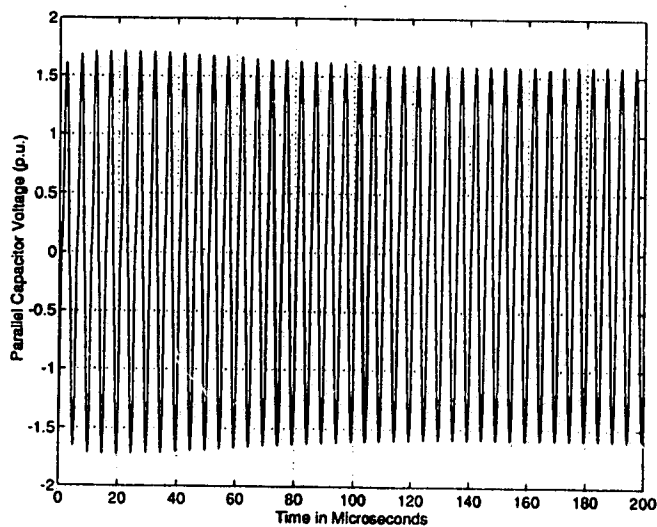
Figure 6.14: Discrete state variables for step change in load from half the rated load to quarter the rated load:

(a) Tank state variables.

(b) Output state variables: b(i) From the model; b(ii) from SPICE.

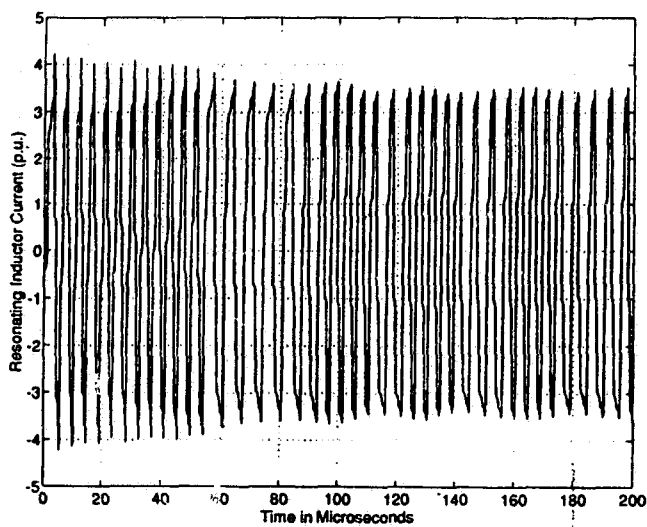


(a)

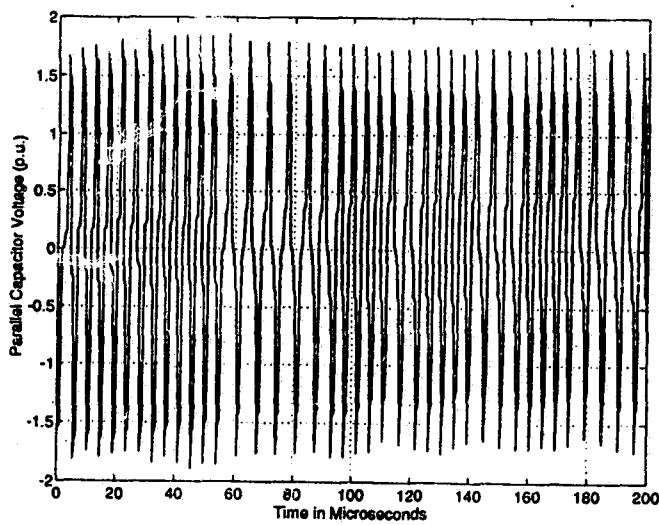


(b)

Figure 6.15: (a) Resonating inductor and (b) Parallel capacitor voltage for closed loop operation example where the duty cycle changes in response to a step change in load from half the rated load to quarter the rated load. (c),(d): SPICE plots corresponding to (a) and (b).



(c)



(d)

Fig. 6.15 (continued)

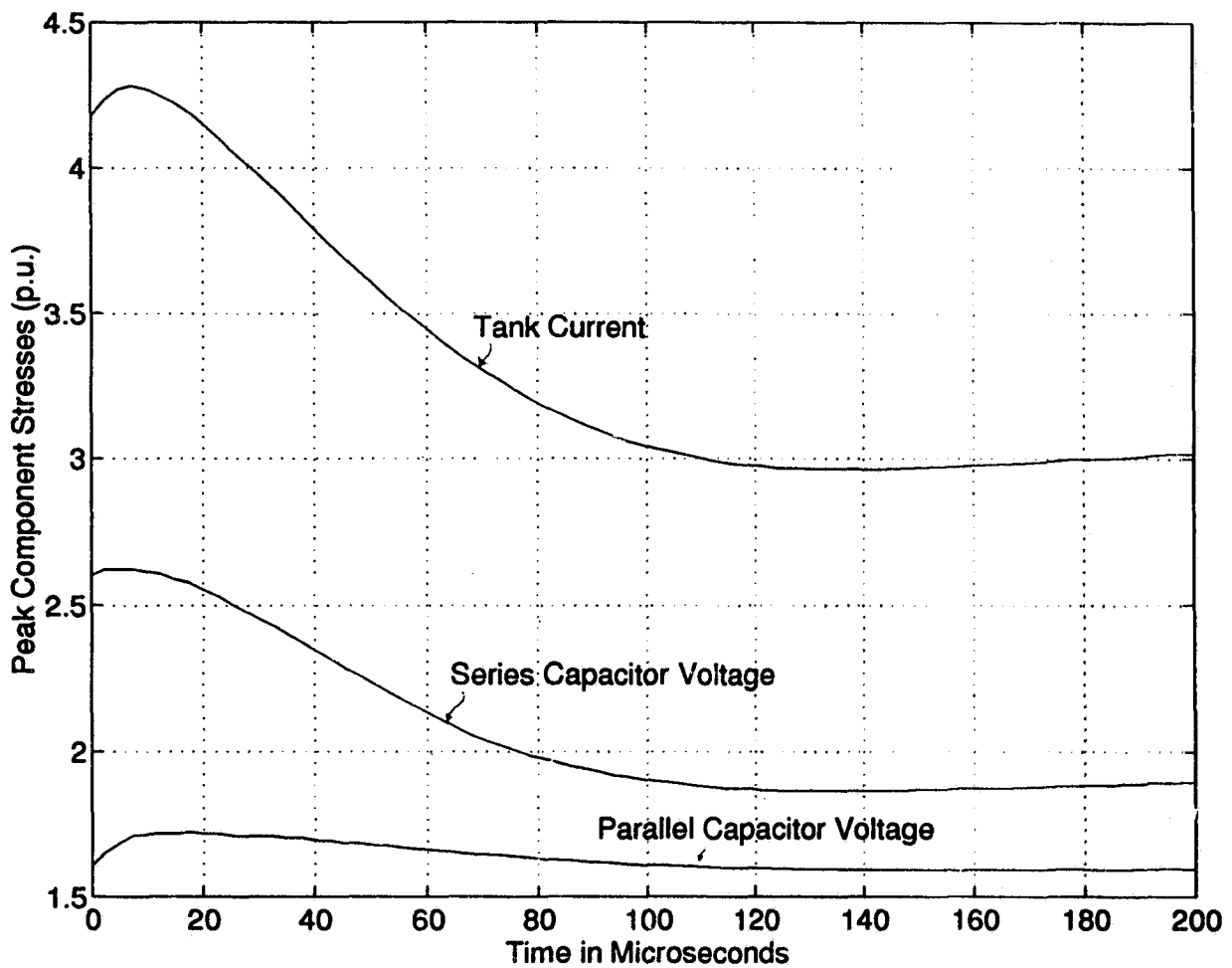
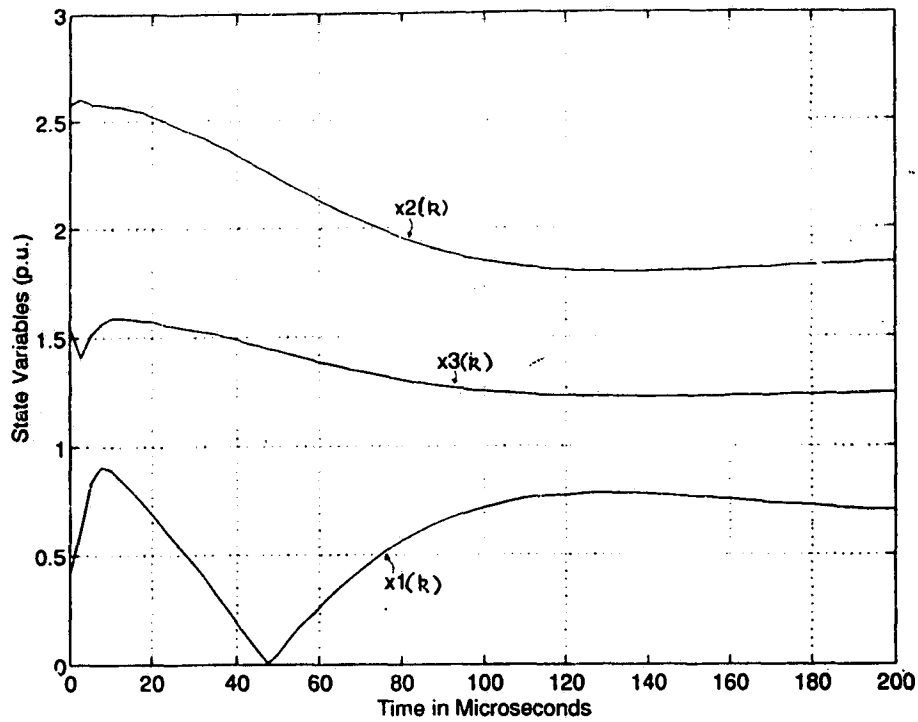
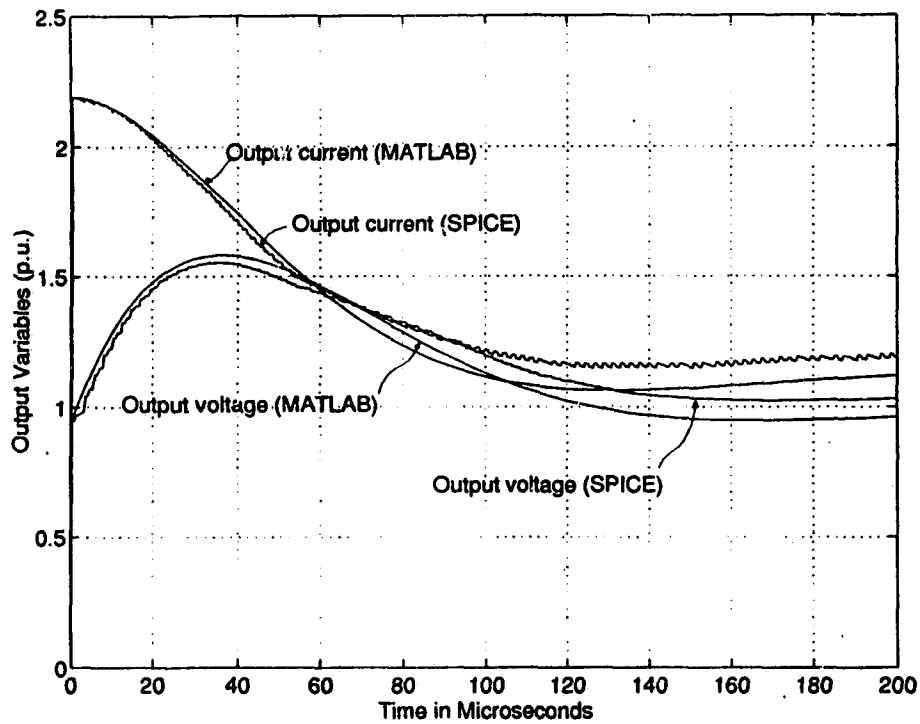


Figure 6.16: Peak component stresses (p.u.) for closed loop operation example where the duty cycle changes in response to a step change in load from half the rated load to quarter the rated load.



(a)



(b)

Figure 6.17: Discrete state variables for closed loop operation example where the duty cycle changes in response to a step change in load from half the rated load to quarter the rated load: (a) Tank state variables. (b) Output state variables. SPICE results are also plotted for the sake of comparison.

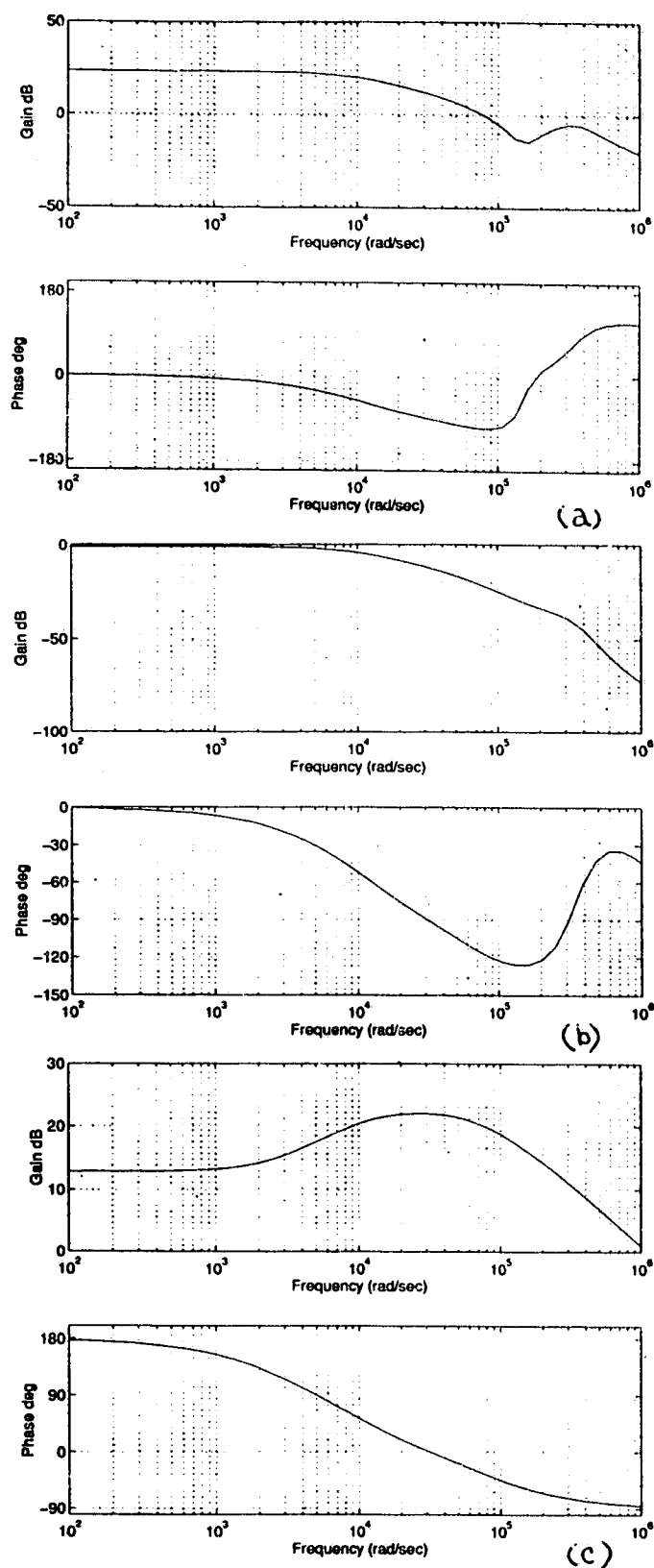


Figure 6.18: Results of the small signal analysis: (a) The plot of control to output transfer function. (b) Plot of audio-susceptibility. (c) Plot of output impedance transfer function as obtained with the small signal model obtained in this chapter.

# Chapter 7

## Conclusions

This chapter summarizes the main contributions and results of this thesis work. It begins with section 7.1 where the major contributions are outlined. Section 7.2 summarizes the results of the thesis. The chapter ends with suggestions for future work in this area in section 7.3.

### 7.1 Major Contributions

One of the major challenges of this thesis work was to deal with a third order system, namely the SPRC. The analysis of the converter is complex due to the various operating modes it enters. This was reflected in the limited attention this converter's analysis had received at the time the present thesis work began. Although, the advantages of this converter over the other two configurations were understood and accepted, there was not much literature available on this configuration except for steady-state analysis [7,8]. Dynamic behavior of this converter in particular, was not studied.

Recently, during the course of this thesis work itself, some authors [73,84] came up with small-signal analysis of this converter. However, they were all based on some *major* approximations, where the square-wave voltages and currents were approximated by their fundamental components.

The most important contribution of this thesis work is the extensive treatment to both the steady-state and dynamic analysis of this third order converter for the various operating modes and operating conditions using the state-space approach based on the constant current model [7]. The analysis presented assumes no approximations (like approximating the square waveforms with their sinusoidal, fundamental components) except a few more practical ones. The main contributions of the thesis can be summarized as below.

- (1) A complete steady-state analysis of the SPRC has been presented for the variable frequency operation. Various operating modes have been identified and general solutions for all the modes of operation have been presented based on the state-space approach.
- (2) Large-signal modeling and analysis has been presented for variable frequency and fixed frequency operation using discrete time domain modeling.
- (3) Small-signal analysis has been presented using the large-signal models for both variable frequency and fixed frequency control.
- (4) A small-signal equivalent circuit model has been derived which gives more physical insight into the dynamics of the converter and is more convenient to use.
- (5) The different operating modes have been identified for the fixed frequency pulse-width modulated control of the SPRC, and the steady-state analysis of the predominant modes has been presented.

A more detailed summary is presented in the next section.

## 7.2 Summary of the Thesis Work

Various aspects of the series-parallel resonant converter were studied during the course of this thesis work. All three kinds of analysis have been performed for both the variable frequency operation and the fixed frequency operation of the SPRC.

A complete steady-state analysis of the series-parallel resonant converter has been carried out in chapter 2. Various operating modes (including multiple conduction modes) were identified using computer simulation. These modes were classified on the basis of different criteria like nature of the parallel capacitor (DCVM and CCVM operation), resonant tank current (DCM and CCM operation) and also on the basis of the way the tank current is related in phase to the square-wave voltage that is impressed across the resonant tank (leading and lagging p.f. modes of operation). General solutions for all the modes of operation have been presented. As an example, two of the predominant modes, with four and two intervals respectively, have been selected as the particular cases and the converter gain for those modes have been analytically obtained. The converter gain and peak component stresses have been plotted against per unit load current. Boundaries between the various modes, CCVM and DCVM as well as between leading and lagging p.f. modes, have been obtained and plotted. The theoretical and simulation results have been compared with the experimental results. To control the output voltage, the operating frequency can be varied in two directions. The range of frequency variation is slightly higher (upto  $f_n = 2.0$ ) for lagging p.f. case (as compared to the leading p.f. operation) for a full range output voltage control. The type of converter control discussed in this chapter (including multiple conduction modes) can be utilized in power supplies meant to serve a wide range of voltage requirements. Multiple conduction modes are capable of supplying variable voltage for very low output current values.

Chapter 3 was devoted to the large-signal analysis of the SPRC using a discrete time domain model for both CCM and DCM. The main contributions of this chapter are summarized below:

**For CCM**

- (1) A discrete time domain model has been derived for the SPRC for lagging power factor mode of operation.
- (2) The effectiveness of this model in predicting the transient behavior of an SPRC has been shown.
- (3) Using this model, a few calculations are sufficient to predict the transient behavior of the converter from a designer's point of view. Only the initial conditions at the beginning of every half cycle (initial state vector) are required per half cycle to arrive at the curves for peak stresses and the state behavior.
- (4) The proposed model can be used to theoretically predict the large-signal behavior of the converter and then SPICE simulation program can be used to verify the results. Usually, SPICE requires large computer memory, even if the information required from the simulation may be small. The proposed model can give crucial design parameters and state behavior with simple calculations.
- (5) The model presented has been derived based on the assumption of CCVM (continuous capacitor voltage mode) for  $v_{ct}$  [Fig. 3.2]. However, the converter is designed to operate with slight discontinuity in the parallel capacitor voltage. The results show that the proposed model based on two interval CCV mode (in which the effect of slight discontinuity has been neglected) is good enough to predict the behavior of the designed converter, although some slight deviations are observed. This avoids the use of a more complicated model involving a third interval (in DCV mode), which does not have closed form solutions [12].
- (6) All the plots are given in p.u. and are therefore general. The results of theory, SPICE simulation and experiments have been presented and compared.

(7) During switching ON, only the parallel capacitor experiences additional stress for the design presented in this thesis and the converter enters below resonance. The anti-parallel diode has to undergo additional peak current stress (Fig. 3.5(f)).

(8) It has been observed that the SPRC, designed to operate slightly above resonance and with slight discontinuity in the parallel capacitor voltage (as in this thesis), does not show pronounced stresses on resonant inductor and the series capacitor during switching ON.

(9) The response of the converter is dependent on the output filter design. Characteristic impedance of the output filter is a convenient parameter to evaluate this dependence. It is observed that the switching ON response becomes faster (oscillatory) as  $Z_f$  is decreased. The peak tank current during the transient phase increases with an increase in the value of  $C_f$  and a decrease in the value of  $L_f$ . However, the peak parallel capacitor voltage during the transient phase decreases with a decrease in the value of  $L_f$  and is independent of  $C_f$  for a given value of  $L_f$ .

(10) The transients caused due to sudden short circuit and open circuit conditions have been studied.

(11) The advantages of closed loop operation have been investigated experimentally, by considering the example of the transients caused due to a step change in the load condition from full load to half full load condition. It is found that the drawbacks of the open loop operation are overcome. The converter does not enter the leading p.f. mode of operation and the peak stresses are less. It was observed that the parallel capacitor voltage becomes discontinuous due to the closed loop control action, as the operating frequency is corrected.

#### **For DCM**

(1) The discrete time domain model for the SPRC operating in the DCM has been derived and used to predict the large-signal behavior of the converter.

(2) The large-signal response of the converter during sudden switching ON of the

supply voltage, is affected by the value of filter components. For a small value of the filter capacitor, the converter maintains DCM and the transient response is critically damped. For a larger value of filter capacitor, the converter enters the CCM, leading p.f. mode to accommodate an overshoot of the output current which shows an oscillatory response. This may result in more losses during transients. Clearly, since the choice of filter components is based on the ripple specifications, there is a trade off.

(3) During a step change from full load to half full load conditions, the dead gap is present due to a reduction in the load current.

(4) During sudden short circuiting of the output at full load conditions, the converter enters the leading p.f. mode (CCM), which it maintains. Therefore the losses are higher and the currents in the circuit rise to high values in the absence of a corrective action. Therefore, the output of an open loop SPRC operating in the DCM should not be short circuited.

(5) The proposed model is not adequate to accurately predict the large-signal response during a step change from full load to open circuit conditions because the converter enters those operating modes which are not analyzed in this thesis.

Closed loop operation can overcome many drawbacks of the open loop operation.

Chapter 4 presented the small-signal modeling of the converter. For this purpose the large-signal state equations derived in chapter 3 have been linearized about a steady-state operating point to obtain a linearized small-signal model. This model has been used to study the small-signal dynamic behavior of the converter and to predict the dynamic performance parameters like the control to output transfer functions, audio-susceptibility, and output impedance transfer functions. The plot of these transfer functions are essential for the control loop design.

A multiple feedback loop based control system was developed which uses *inner* state variable feedback control loop. This kind of control is found to be very useful

for controlling the fast dynamics of the resonant tank portion of the SPRC. It was observed that a converter with state feedback control gives better audio-susceptibility and output impedance performance. Following are some of the major observations of this chapter.

- (1) The dynamics of the slower, output (continuous time) section of the converter are controlled by a complex pair of poles determined by the filter elements, which determine the corner frequency for the -40 dB roll off point.
- (2) Fast poles occurring at *beat frequency*, which is roughly the difference between the operating frequency and the resonant frequency [87], govern the dynamics of the converter for perturbation frequencies in the vicinity of the operating frequency.
- (3) It was verified that the audio-susceptibility transfer function shows the same pattern as the control to output transfer function [73].
- (4) The loop gain  $T$  of the outer voltage loop determines the stability factor of the converter. It must be suitably designed for a proper phase margin and bandwidth.
- (5) It was observed that for lagging p.f. mode, the initial phase lag is  $0^\circ$  for low perturbation frequencies. For leading p.f. mode, it was observed that the initial phase leads by  $180^\circ$ .
- (6) Parameters like the output impedance and the audio-susceptibility can be controlled by the state feedback gain matrix, which in turn controls the dynamics of the resonant tank portion of the converter.

Although the analysis and results in chapter 4, have been presented for the converter designed to operate in lagging power factor mode under steady-state conditions, it can be modified for leading power factor mode of operation with some minor changes.

A more convenient way of predicting the small-signal behavior of the converter is to use a small-signal equivalent circuit model. A small-signal equivalent circuit model for

the SPRC has been derived in chapter 5. This model is more convenient because the various dynamic performance transfer functions (control to output transfer function etc.) can be solved fairly easily by using the simple rules of the linear circuit theory. This model is also capable of giving more physical insight into the converter dynamics. To summarize chapter 5, a two-port hybrid small-signal equivalent circuit model has been presented in this chapter. This model is derived using the discrete time domain modeling. Two versions of this model were considered. An approximate one, in which the sampled nature of the tank states was neglected and the analysis was done in continuous time domain. The low frequency approximation, on which the continuous time domain model is based, simplifies the modeling, but the results obtained are good for low perturbation frequencies only. This model fails to predict the “dynamics” of the converter near the switching frequency. The other, more exact,  $z$  domain model takes into account the sampled nature of the tank states, which in fact is their true nature in a resonant converter. The results obtained with this exact model are more accurate. The main observations are same as those of chapter 4. However, the  $z$  domain equivalent circuit model gives more accurate results. It was observed that the lumped parameters of the equivalent circuit model are frequency dependent and can be represented by transfer functions of order 3. This can be verified from (5.32), (5.33), (5.36) and Table 5.6. The lumped parameters are of order 2, in case of series- and parallel- resonant converters. Thus the order of the resonant tank governs the order of the lumped parameter.

Although the equivalent circuit model derived in Chapter 5 is meant for lagging p.f. mode of operation, it can be extended to leading p.f. mode of operation with minor changes.

To overcome some of the disadvantages of the variable frequency operation, the converter was operated in fixed frequency PWM mode in Chapter 6. Various op-

erating modes for this operation have been identified. Steady-state analysis for the predominant mode has been carried out. It is found that the converter operate in three major modes when the capacitor ratio  $\frac{C_s}{C_t} = 1$ , while it operates in two major modes (both discontinuous capacitor voltage modes) when the capacitor ratio  $\frac{C_s}{C_t} = 2$ . The steady-state and dynamic analysis of the predominant mode for the ratio of  $\frac{C_s}{C_t} = 1$  was carried out. The large-signal analysis showed that during switch ON conditions, the converter enters the leading p.f mode of operation before reaching the steady-state where it is designed to operate in the lagging p.f. mode. All the tank components are over stressed during the switch ON transients. During step change in load from half the rated load condition to quarter load condition, the converter enters leading p.f. mode within 30 microseconds (Fig. 6.14(a)). For the closed loop operation however, the converter stays longer in the lagging p.f. mode (50 microseconds). During step change from half the rated load to quarter the rated load conditions, the tank components do not experience an over stress. From the small-signal analysis it was observed that the control to output transfer function for the FF PWM SPRC has nearly the same pattern as the one for frequency controlled SPRC, obtained in Chapter 4. The audio-susceptibility transfer function shows the same pattern as the control to output transfer function. However, the phase plot does not show as much lag as it did in the case of frequency controlled SPRC.

### 7.3 Suggestions for Future Work

Various aspects of the steady-state and dynamic analysis of the SPRC were addressed in this thesis. Some of the topics that still need to be studied are as follows:

- (1) The large-signal and small-signal analysis for only CCVM have been presented in this thesis. Large and small-signal analysis for DCVM case have to be considered.

- (2) For the fixed frequency operation, in chapter 6, only two of the operating modes have been analyzed corresponding to capacitor ratio  $\frac{C_2}{C_1} = 1$ . Different operating modes are encountered as the capacitor ratio  $\frac{C_2}{C_1}$  is increased and the converter enters DCVM. These modes have to be analyzed for steady-state and dynamic analysis.
- (3) Closed loop models for the large-signal analysis for CCM and DCM have to be developed.
- (4) It was observed in the case of variable frequency operation that the inclusion of an inner state variable feedback loop improves the dynamics of the converter. Effect of such a feedback loop has to be investigated for the fixed frequency pulse-width modulated operation of the SPRC.
- (5) Experimental results for the fixed frequency control of the SPRC have to be obtained.

## Bibliography

- [1] F.C. Schwartz, "An Improved Method of Resonant Current Pulse Modulation for Power Converters," IEEE Trans. Ind. Electron. Contr. Instrum. , Vol. IECI-23, May 1976.
- [2] F.C. Schwartz and J. Ben Klassens, "A 95-Percent Efficient 1-kW DC Converter with an Internal Frequency of 50 kHz," IEEE Trans. Ind. Electron. Contr. Instrum. Vol.. IECI, Nov. 1978, pp. 326-333.
- [3] N. Mapham, "An SCR Inverter with Good Regulation and Sinewave Output," IEEE Transactions on Industry and General Application, Vol. IGA-3, pp. 176-187, March/April 1967.
- [4] R. Myeres and R. D. Peck, "200-kHz power FET technology in new modular power supplies," Hewlett Packard Journal (Aug. 1981), 3-11.
- [5] J. Chen and R. Bonert, "Load Independent AC/DC Power Supply for high Frequencies with Sine-wave Output," IEEE Transactions on Industry Applications, IA-19, 2 (Mar./Apr. 1983), 223-227.
- [6] R. Bonert and P. Blanchard, "Design of a Resonant Inverter with Variable Voltage and Fixed Frequency," IEEE IAS conference Record, 1988, pp. 1003-1008.

- [7] A.K.S. Bhat and S.B. Dewan, "*Analysis and design of a high-frequency resonant converter using LCC-Type commutation,*" IEEE transactions on Power Electronics, Vol. PE-2, No. 4, October 1987, pp. 291-301.
- [8] R.L. Steigerwald, "*A Comparison of half-bridge resonant converter topologies,*" IEEE transactions on Power Electronics, Vol. PE-3, No. 2, April 1988, pp. 174-182.
- [9] K.D.T. Ngo, R.L. Steigerwald, A.J. Yerman and M.H. Kuo, "*A High Density Resonant Power Supply using High Voltage IC,*" Conference on High Frequency Conversion, HFPC, April 1987 proceedings, pp. 244-257.
- [10] I. Batarseh and C.Q. Lee, "*High frequency high-order parallel resonant converter,*" IEEE transactions on Industrial Electronics, Vol. 36, No. 4, November 1989, pp. 485-498.
- [11] A.K.S. Bhat and S.B. Dewan, "*A Generalised approach for the Steady-State Analysis of Resonant Inverters*" IEEE Transactions on Industry Applications, Vol. 25, No. 2, March/April 1989.
- [12] A.K.S. Bhat, "*Analysis and design of a series parallel resonant converter,*" IEEE Transactions on Power Electronics, Vol. 8, No. 1, Jan. 1993. pp. 1 - 11.
- [13] Sandip Shah and Anand K. Upadhyay, "*Analysis and Design of a half-bridge series-parallel resonant converter operating in discontinuous conduction mode,*" Applied Power Electronics Conference., 1990, pp. 165-174.
- [14] A.K.S. Bhat, "*Analysis and Design of Series-Parallel Resonant Power Supply,*" IEEE Transactions on Aerospace and Electronic Systems, Vol. 28, No. 1, Jan. 1992.

- [15] A.K.S. Bhat, " *Fixed Frequency PWM Series-Parallel Resonant Converter,*" IEEE IAS, Oct. 1989, pp. 1115-1121.
- [16] Praveen Jain, " *Performance Comparison of Pulse Width Modulated Resonant Mode DC/DC Converters for Space Applications,*" IEEE IAS, Oct. 1989, pp. 1106-1114.
- [17] R.L. Steigerwald, W. Roshan and C.F. Saj, " *A High-Density 1-kW Resonant Power Converter with a Transient Boost Function,*" IEEE Applied Power Electronics Conference Record, APEC-92, pp. 693-702.
- [18] C.Q. Lee, S. Sooksatra and R. Liu, " *Constant Frequency Controlled Full Bridge LCC Type Resonant Converter,*" IEEE APEC-91 pp. 587-600.
- [19] I. Batarseh, R. Liu, C.Q. Lee and A. Upadhyay, " *150 Watts and 140 kHz Multi-Output LCC-Type Parallel Resonant Converter,*" IEEE Applied Power Electronics Conference Record, 1989, pp. 221-230.
- [20] N. Frohlike, J.Kunze, A. Fiedler and H. Grotstollen, " *Contribution to the AC-Analysis of Resonant Converters; Analysis of the Series-Parallel Resonant Converter including Effects of Parasitics and Lossless Snubbers for Optimized Design,*" IEEE Applied Power Electronics Conference Record, APEC-92, pp. 219-228.
- [21] Barry C. Pollard and R.M. Nelms, " *Using the Series-Parallel Resonant Converter in Capacitor Charging Applications,*" IEEE Applied Power Electronics Conference Record, APEC-92, pp. 245-252.
- [22] R.A. Fisher *et al*, " *Performance of Low Loss Synchronous Rectifiers in a Series-Parallel Resonant DC-DC Converter,*" IEEE Applied Power Electronics Society, APEC-89, pp. 240-246.

- [23] I. Batarseh and C.Q. Lee, "*Design of Parallel Resonant Converter with LCC-Type commutation,*" Electronics Letters, Vol. 24 No. 3, Feb. 1988, pp. 177-179.
- [24] V. Vorperian and Slobodan Cuk, "*A complete DC analysis of the series resonant converter,*" IEEE Power Electronics Conference, 1982 record, pp. 85-100.
- [25] A.F. Witulski and R.W. Erickson, "*Steady-state analysis of the series resonant converter,*" IEEE transactions on aerospace and electronic systems, Vol. AES-21, No. 6, November 1985, pp. 791-799.
- [26] M. Mamon, R. Hiramatsu, K. Harada and H. Sakamoto, "*A Resonant Converter with PWM Control,*" IEEE INTELEC, 1981, pp. 247-249.
- [27] W.J. Gu and K. Harada, "*A New Method to Regulate Resonant Converters,*" IEEE Transactions on Power Electronics, Vol. 3, No. 4, Oct. 1988, pp. 430-439.
- [28] R.J. King and T.A. Stuart, "*A Normalized model for the Half-Bridge Series Resonant Converter,*" IEEE Trans. Aero and Electr. Systems, Vol. AES-17, No. 2, March 1981, pp. 190-198.
- [29] V.T. Ranganathan, P.D. Ziogas and V.R. Stefanovic, "*A Regulated DC-DC Voltage Source Converter Using High Frequency Link,*" IEEE Trans. on Industry Application, Vol IA-18, No. 3, May/ June 1982, pp. 279-287.
- [30] A.K.S. Bhat and M.M. Swamy, "*Analysis and Design of a Parallel Resonant Converter including the effect of a High Frequency Transformer,*" IEEE Transactions on Industrial Electronics, Vol. 37, No. 4, PP. 297-306.
- [31] V.T. Ranganathan, P.D. Ziogas and V.R. Stefanovic, "*Performance Characteristics of High Frequency Links Under Forward and Regenerative Power Flow Conditions,*" IEEE Industry Application Society Conf. Record, IAS-1983, pp. 831-839.

- [32] R.L. Steigerwald, " *High Frequency Resonant Transistor DC-DC Converters*" IEEE Trans. on Industrial Electronics, Vol. IE-31, No. 2, May 1984, pp. 181-191.
- [33] S.D. Johnson and R.W. Erickson, " *Steady-State Analysis and Design of Parallel Resonant Converter,* " IEEE Applied Power Electronics Conference Record, APEC-1987, pp. 135-144.
- [34] S.D. Johnson, A.F. Witulski and R.W. Erickson, " *A Comparison of Resonant Topologies in High Voltage DC Applications,*" IEEE Applied Power Electronics Conference Record, APEC-1987, pp. 145-156.
- [35] R.L. Steigerwald, " *Analysis of a Resonant Transistor DC-DC Converter with Capacitive Output Filter,*" IEEE Trans. on Industrial Electronics, Vol. IE-32, No. 4, November 1985, pp. 439-448.
- [36] Young Goo Kang and A.K Upadhyay, " *Analysis and Design of a Half-Bridge Parallel Resonant Converter,*" IEEE Power Electronics Specialist Conference Record, PESC -1987, pp. 231-243.
- [37] R. Oruganti and F.C. Lee, " *State-Plane Analysis of Parallel Resonant Converter,*" IEEE Power Electronics Specialist Conference Record, PESC-1985, pp. 56-73.
- [38] Y. Lin and R. Unnikrishnan, " *State-Plane Analysis and Control strategies for Parallel Resonant Converters,*" IEEE MONTECH, 1986, pp. 224-227.
- [39] R. Oruganti and F.C. Lee, " *Resonant Power Processors: Part I- state-Plane Analysis,*" IEEE Industry Application Society Conference Record, IAS-1984, pp. 860-867.

- [40] R. Oruganti and F.C. Lee, " *Resonant Power Processors: Part II- Methods of Control*," IEEE Industry Application Society Conference Record, IAS-1984, pp. 868-874.
- [41] R.J. King and T.A. Stuart, " *Modelling the Full-Bridge Series-Resonant Power Converter*," IEEE Trans. Aero. and Electr. Systems, Vol. AES-18, No. 4, July 1982, pp. 449-459.
- [42] R.J. King and T.A. Stuart, " *Small-Signal Model for the series Resonant Converter*," IEEE Trans. Aero. and Electr. Systems, Vol. AES-21, No. 3, May 1985, pp. 301-319.
- [43] Eric X. Yang, Fred C. Lee and Milan M. Jovanovic, " *Small Signal Modelling of Series and Parallel Resonant Converters*," IEEE Applied Power Electronics Conference Record, APEC-92, pp. 785-792.
- [44] Malik E. Elbuluk, " *Closed-Loop Digital Control of Resonant Converters*," IEEE Power Electronics Specialist Conference Records, PESC-1987, pp. 567-576.
- [45] K.Al Haddad, A. Bellahmid and V. Rajagopalan, " *Novel Control Strategy to improve the Dynamic Performance of a Series Resonant Converter*," Can. Elect. Eng. Journal, Vol. 12, No. 4, 1987, pp. 806-813.
- [46] K.A.Haddad, Y. Cheron and H. Foch, " *Static and Small Signal Analysis of a Series- Resonant Converter Operating above Resonance*," Can. Elect. Eng. Journal, Vol. 12, No. 4, 1987 pp. 158-164.
- [47] S.W.H. De Haan , " *A New Integral Pulse Module for the Series-Resonant Converter*," IEEE Transactions on Industrial Electronics, Vol. IE-31, No. 3, August 1984.

- [48] R.J. King and T.A. Stuart, " *A Large-Signal Dynamic Simulation for the Series Resonant Converter,*" IEEE Trans. on Aerospace and Electronic Systems, Vol. AES-19, No.6, Nov. 1983.
- [49] A.F. Witulski, A.F. Hernandez and R.W. Erickson, " *Small Signal Equivalent Circuit Modelling of the Resonant Converters,*" IEEE Trans. on Power Electronics, Vol. 6, No. 1, Jan. 1991.
- [50] Scott L. Smith and S.M. Robinson, " *An Off-Line, One MHz 350-Watt Parallel Resonant Converter (PRC) utilizing an RF Transformer,*" IEEE High Frequency Power Conversion Conference, May 1988, pp. 446-466.
- [51] V. Vorperian and S. Cuk, " *Small Signal Analysis of Resonant Converters,*" IEEE Power Electronics Specialist Conference, PESC-83, pp. 269-282.
- [52] M.G. Kim and M.J. Youn, " *A discrete Time Domain Modeling and Analysis of Controlled Series Resonant Converter,*" IEEE Transactions on Industrial Electronics, Vol. 38, No. 1, Feb. 1991.
- [53] C. Cutrona, C. D. Miceli and L. Fiorella, " *A Mathematical Model for a Series Resonant Converter,*" IEEE INTELEC-90, pp. 330-335.
- [54] M.G. Kim, J.H. Lee, J.H. Ko and M.J. Youn, " *A Discrete Time Domain Modeling and Analysis of Controlled Parallel Resonant Converter,*" IEEE Power Electronics Specialist Conference, PESC-91, pp. 730-736.
- [55] M. Rico, J. Sebastian , J. Uceda , M.A. Perez and F. Aldana , " *Dynamic Modelling of the Parallel Resonant Converters,*" IEEE Power Electronics Specialist Conference, PESC-89, pp. 728-735.

- [56] V. Vorperian , “ *High-Q Approximation in the Small-Signal Analysis of Resonant Converters,*” IEEE Power Electronics Specialist Conference, PESC-85, pp. 707-715.
- [57] M. Nakahara, T. Higashi, T. Ninomiya and K. Harada, “*Dynamic Characteristics and Stability Analysis of Resonant Converter,*” IEEE Power Electronics Specialist Conference, PESC-89, pp. 752-759
- [58] Ira J. Pitel, “*Phase-Modulated Resonant Power Conversion Techniques for High-Frequency Link Inverters,*” IEEE Trans. on Industry Applications. Vol. IA-22, No. 6, Nov./Dec. 1986, pp. 1044-1051.
- [59] Fu-Sheng Tsai and Fred C. Lee, “ Constant-Frequency Phase-controlled Resonant Power Processor,” IEEE Industry Application Society Conference Record, IAS-1986, pp. 617-622.
- [60] J.P. Vandelac and P.D. Ziogas, “ A DC to DC PWM Series Resonant Converter,” Proc. of the Twelfth International SATECH Conference, PCI Oct. 1986, pp. 17-34.
- [61] Fu-Sheng Tsai, Peter Materu and Fred C. Lee, “ *Constant-Frequency, Clamped-Mode Resonant Converters,*” IEEE Power Electronics Specialist Conference Record, PESC-87,pp. 557-566.
- [62] Fu-Sheng Tsai, “ *Small-Signal and Transient Analysis of a Zero-Voltage-Switched, Phase Controlled PWM Converter Using Averaged Switched Model,*” IEEE Industry Applications Society, IAS-91, pp. 1010-1016.
- [63] Khai D.T. Ngo, “*Analysis of a Series Resonant Converter Pulsewidth-Modulated or Current-Controlled for Low Switching Loss,*” IEEE Power Electronics Specialist Conference Record, PESC-87, pp. 527-536.

- [64] R.L. Steigerwald, W. Roshan and C.F. Saj, " *A High-Density 1-kW Resonant Power Converter with a Transient Boost Function,*" IEEE Applied Power Electronics Conference Record, APEC-92, pp. 693-702.
- [65] O.P. Mandhana and R.G. Hoft, " *Steady State Analysis of DC to DC Resonant Converters,*" IEEE Applied Power Electronics Conference, APEC 91, pp. 580-586.
- [66] R.M. Nemes, B.W. Evans and L.L. Grigsby, " *Simulation of AC Spacecraft Power Systems,*" IEEE Transactions on Industrial Electronics, Vol. 36, No. 3, pp. 398-402.
- [67] A.K.S. Bhat, " *High Frequency Link Photovoltaic Power Conditioning System,*" M.A.Sc. Thesis, Dept. of Electrical Engineering, University of Toronto, Toronto, Sept. 1982.
- [68] W.E. Frank and C.F. Der, " *Solid State RF Generators for Induction Heating Application,*" IEEE Industry Application Society Conference Record, 1982, pp. 931-944.
- [69] M.M. Swamy, " *Analysis and Design of Parallel Resonant Converters operating in the Lagging Power Factor Mode,*" Ph.D. Dissertation, University of Victoria, Victoria, Nov. 1991.
- [70] S. Deb, A. Joshi and S.R. Doradla, " *A Novel Frequency-Domain Model for a Parallel-Resonant Converter,*" IEEE transactions on Power Electronics, Vol. 3, No. 2, April 1988, pp. 208-215.
- [71] Vivek Agarwal and A.K.S. Bhat, " *A Complete DC Analysis of LCC Type Parallel Resonant Converter,*" IEEE IECON-1992, pp. 179-184.

- [72] A.K.S. Bhat and Vivek Agarwal, " *Operating Modes and Simulation of the Series-Parallel Resonant Converter*," IEEE ISCAS-1992, pp. 1883-1886.
- [73] E.X. Yang, F.C. Lee, M.M. Jovanovic, " *Small-Signal Modeling of LCC Resonant Converter*," Power Electronics Specialist Conference, 1992, pp. 941-948.
- [74] T. Higashi and T. Ninomiya, " *Large signal transient response of resonant converters*," PESC-92, pp. 807-813.
- [75] A.F. Hernandez, R.W. Erickson, S. Lofton and P. Anderson, " *A large signal computer model for the series resonant converter*," PESC-91. pp. 737-744.
- [76] E.X. Yang, B. Choi, F.C. Lee and Bo H. Cho, " *Dynamic analysis and control design of LCC resonant converter*," Power Electronics Specialist Conference, 1992, pp. 362-369.
- [77] Vivek Agarwal and A.K.S. Bhat, " *Small Signal Analysis of the LCC-Type Parallel Resonant Converter using Discrete Time Domain Modeling*," IEEE PESC-1994, Vol. 2, pp. 805-813.
- [78] Vivek Agarwal and A.K.S. Bhat, " *Large Signal Analysis of LCC-Type parallel resonant converter using discrete time domain analysis*", IEEE IECON, 1993, pp. 836-841.
- [79] T. Kailath, " *Linear Systems*," Prentice-Hall, Inc., 1980.
- [80] J.J. D'Azzo and C.H. Houpis, " *Linear control system. analysis and design, conventional and modern*," McGraw Hill 1981.
- [81] R.D. Middlebrook, " *Modeling Current-Programmed Buck and Boost Regulators*," IEEE Transactions on Power Electronics, Vol. 4, No. 1, January 1989, pp. 36-52.

- [82] V. Vorperian, "*Equivalent Circuit Models for Resonant and PWM switches,*" IEEE International Symposium on Circuits and Systems 1987, pp. 1080-1087.
- [83] I. Batarseh and K. Siri, "*Generalized approach to the small signal modeling of DC-to-DC resonant converters,*" IEEE transactions on aerospace and electronic systems, Vol. 29, No. 3, July 1993, pp. 894-909.
- [84] J.L. Duarte and J.M.A. Willaert, "*A fully digitized phase-shift modulated LCC resonant converter,*" IEEE PESC 1994, Vol. 2, pp. 1303-1308.
- [85] R. King, "*A fourier analysis for a fast simulation algorithm,*" IEEE Transactions on Power Electronics, Vol. 4, pp. 434-441.
- [86] M. Kazimierczuk, N. Thirunarayan and S. Wang, "*Analysis of series-parallel resonant converter,*", IEEE Tran. on Aerospace and Electronic Systems, Vol. 29, No. 1, Jan. 1993, pp. 88-99.
- [87] V. Vorperian, "*Approximate small-signal analysis of the series and parallel resonant converters,*", IEEE Transaction on Power Electronics, Vol. 4, No. 1, pp. 15-24, 1989.

## Appendix A

### General Solutions for $k^{th}$ Event

The equations representing intervals B ( $\alpha_k$ ) and A ( $\beta_k$ ) are as below:

Interval B ( $t_{0(k)} < t < t_{1(k)}$ )

Let  $t'$  be the running variable.

$$i_L(t') = A_{1B_k} \sin(\omega_0 t') + B_{1B_k} \cos(\omega_0 t') + C_{1B_k} \quad (\text{A.1})$$

$$\begin{aligned} v_{cs}(t') &= A_{2B_k} [1 - \cos(\omega_0 t')] + B_{2B_k} \sin(\omega_0 t') + C_{2B_k}(\omega_0 t') \\ &+ v_{cs}(t_{0(k)}) \end{aligned} \quad (\text{A.2})$$

$$\begin{aligned} v_{ct}(t') &= A_{3B_k} [1 - \cos(\omega_0 t')] + B_{3B_k} \sin(\omega_0 t') + C_{3B_k}(\omega_0 t') \\ &+ v_{ct}(t_{0(k)}) \end{aligned} \quad (\text{A.3})$$

The constants used in the above equations are defined as below:

$$A_{1B_k} = [E(t_{0(k)}) - (v_{cs}(t_{0(k)}) + v_{ct}(t_{0(k)}))] / Z \quad (\text{A.4})$$

$$B_{1B_k} = (i_L(t_{0(k)}) + (C_e/C_t)I(t_{0(k)})); C_{1B_k} = -(C_e/C_t)I(t_{0(k)}) \quad (\text{A.5})$$

$$A_{2B_k} = Z(C_e/C_s)A_{1B_k}; B_{2B_k} = Z(C_e/C_s)B_{1B_k} \quad (\text{A.6})$$

$$C_{2B_k} = Z(C_e/C_s)C_{1B_k}; A_{3B_k} = Z(C_e/C_t)A_{1B_k} \quad (\text{A.7})$$

$$B_{3B_k} = Z(C_e/C_t)B_{1B_k}; C_{3B_k} = -Z(C_e/C_s)C_{1B_k} \quad (\text{A.8})$$

Interval A ( $t_{1(k)} < t < t_{0(k+1)}$ ) .

Let  $t''$  be the running variable for this interval.

$$i_L(t'') = A_{1A_k} \sin(\omega_0 t'') + B_{1A_k} \cos(\omega_0 t'') + C_{1A_k} \quad (\text{A.9})$$

$$\begin{aligned} v_{cs}(t'') &= A_{2A_k} [1 - \cos(\omega_0 t'')] + B_{2A_k} \sin(\omega_0 t'') + C_{2A_k}(\omega_0 t'') \\ &\quad + v_{cs}(t_{1(k)}) \end{aligned} \quad (\text{A.10})$$

$$\begin{aligned} v_{ct}(t'') &= A_{3A_k} [1 - \cos(\omega_0 t'')] + B_{3A_k} \sin(\omega_0 t'') + C_{3A_k}(\omega_0 t'') \\ &\quad + v_{ct}(t_{1(k)}) \end{aligned} \quad (\text{A.11})$$

As before, the constants used in the above equations are defined below:

$$A_{1A_k} = [E(t_{0(k)}) - (v_{cs}(t_{1(k)}) + v_{ct}(t_{1(k)}))] / Z \quad (\text{A.12})$$

$$B_{1A_k} = (i_L(t_{1(k)}) - (C_e/C_t)I(t_{0(k)})); C_{1A_k} = (C_e/C_t)I(t_{0(k)}) \quad (\text{A.13})$$

$$A_{2A_k} = Z(C_e/C_s)A_{1A_k}; B_{2A_k} = Z(C_e/C_s)B_{1A_k} \quad (\text{A.14})$$

$$C_{2A_k} = Z(C_e/C_s)C_{1A_k}; A_{3A_k} = Z(C_e/C_t)A_{1A_k} \quad (\text{A.15})$$

$$B_{3A_k} = Z(C_e/C_t)B_{1A_k}; C_{3A_k} = -Z(C_e/C_s)C_{1A_k} \quad (\text{A.16})$$

It must be pointed out that where ever the above expressions are used to denote the steady state values, the subscript "k" is dropped.

## Appendix B

# Large-Signal State Equations for CCM

The large-signal state equations representing the initial values of the  $(k + 1)^{th}$  event (time instant  $t_s$ ) in terms of the initial values of the  $(k)^{th}$  event (time instant "0"), are given by

$$i_L(t_{0(k+1)}) = A_{1B_k} \cdot \sin(\gamma_k) + B_{1B_k} \cdot \cos(\gamma_k) + C_{1B_k}(2\cos(\beta_k) - 1) \quad (\text{B.1})$$

$$v_{cs}(t_{0(k+1)}) = A_{2B_k}(1 - \cos(\gamma_k)) + B_{2B_k} \sin(\gamma_k) + C_{2B_k}(\alpha_k - \beta_k + 2\sin(\beta_k)) \\ + v_{cs}(t_{0(k)}) \quad (\text{B.2})$$

$$v_{ct}(t_{0(k+1)}) = A_{3B_k}(1 - \cos(\gamma_k)) + B_{3B_k} \sin(\gamma_k) + C_{3B_k}(\alpha_k - \beta_k) \\ + 2 \cdot Z \frac{C_e}{C_t} C_{1B_k} \sin(\beta_k) + v_{ct}(t_{0(k)}) \quad (\text{B.3})$$

## Appendix C

### A, B, C Constants for DCM

The A, B, C coefficients for the equations representing the DCM are defined as follows:

#### Interval A

$$A_{1a_k} = (E(t_{0(k)}) - (v_{cs}(t_{1(k)}) + v_{ct}(t_{1(k)})))/Z \quad (C.1)$$

$$B_{1a_k} = (i_L(t_{1(k)}) - (C_e/C_t)I(t_{0(k)})); C_{1a_k} = (C_e/C_t)I(t_{0(k)}) \quad (C.2)$$

$$A_{2a_k} = Z(C_e/C_s)A_{1a_k}; A_{3a_k} = Z(C_e/C_t)A_{1a_k} \quad (C.3)$$

$$B_{2a_k} = Z(C_e/C_s)B_{1a_k}; B_{3a_k} = Z(C_e/C_t)B_{1a_k} \quad (C.4)$$

$$C_{2a_k} = Z(C_e/C_s)C_{1a_k}; C_{3a_k} = -Z(C_e/C_s)C_{1a_k} \quad (C.5)$$

#### Interval C<sub>1</sub>

$$A_{1c_{1k}} = \sqrt{(C_s/C_t)(E(t_{0(k)}) - v_{cs}(t_{0(k)}))/Z}; B_{1c_{1k}} = (i_L(t_{0(k)})) \quad (C.6)$$

$$A_{2c_{1k}} = (E(t_{0(k)}) - v_{cs}(t_{0(k)})); B_{2c_{1k}} = Z(C_e/C_s)B_{1c_{1k}}; \quad (C.7)$$

$$A_{3c_{1k}} = B_{3c_{1k}} = C_{1c_{1k}} = C_{2c_{1k}} = C_{3c_{1k}} = 0 \quad (C.8)$$

Note that the coefficients for interval  $C_2$  are same as  $C_1$  except that now the values of the initial conditions involved are given by the instantaneous value of the particular variable at the end of interval A. Further  $r_1 = \frac{C_s}{C_t}$  and  $r_2 = \frac{C_e}{C_t}$

## Appendix D

# A, B, C Constants for Fixed Frequency Operation, Predominant Mode

The coefficients for the equations describing the predominant mode fixed frequency pulse width modulated operation are:

$$A_{1T2} = -\frac{1}{Z}(v_{cs(T2i)} + v_{ct(T2i)})$$

$$B_{1T2} = i_{L(T2i)} + \frac{C_e}{C_t}I$$

$$C_{1T2} = -\frac{C_e}{C_t}I$$

$$A_{2T2} = Z\frac{C_e}{C_s}A_{1T2}$$

$$B_{2T2} = Z\frac{C_e}{C_s}B_{1T2}$$

$$C_{2T2} = Z\frac{C_e}{C_s}C_{1T2}$$

$$A_{3T2} = Z\frac{C_e}{C_t}A_{1T2}$$

$$\begin{aligned}
B_{3T2} &= Z \frac{C_e}{C_t} B_{1T2} \\
C_{3T2} &= -Z \frac{C_e}{C_s} C_{1T2} \\
A_{1T1} &= -\frac{1}{Z} (v_{cs(T1i)} + v_{ct(T1i)}) \\
B_{1T1} &= i_{L(T1i)} - \frac{C_e}{C_t} I \\
C_{1T1} &= -\frac{C_e}{C_t} I \\
A_{2T1} &= Z \frac{C_e}{C_s} A_{1T1} \\
B_{2T1} &= Z \frac{C_e}{C_s} B_{1T1} \\
C_{2T1} &= Z \frac{C_e}{C_s} C_{1T1} \\
A_{3T1} &= Z \frac{C_e}{C_T} A_{1T1} \\
B_{3T1} &= Z \frac{C_e}{C_t} B_{1T1} \\
C_{3T1} &= -Z \frac{C_e}{C_s} C_{1T1} \\
A_{1A} &= -\frac{1}{Z} (E - v_{cs(Ai)} + v_{ct(Ai)}) \\
B_{1A} &= i_{L(Ai)} - \frac{C_e}{C_t} I \\
C_{1A} &= -\frac{C_e}{C_t} I \\
A_{2A} &= Z \frac{C_e}{C_s} A_{1A} \\
B_{2A} &= Z \frac{C_e}{C_s} B_{1A} \\
C_{2A} &= Z \frac{C_e}{C_s} C_{1A} \\
A_{3A} &= Z \frac{C_e}{C_T} A_{1A} \\
B_{3A} &= Z \frac{C_e}{C_t} B_{1A}
\end{aligned}$$

$$C_{3A} = -Z \frac{C_e}{C_s} C_{1A}$$

# VITA

Surname: Agarwal

Given Names: Vivek

Place of Birth: Muzaffarnagar, Uttar Pradesh, India

Date of Birth: 13 June, 1964

## Educational Institutions Attended:

University of Victoria, Canada

1990 to 1994

Indian Institute of Science, India

1986 to 1990

University of Delhi, India

1982 to 1985

## Degrees Awarded:

M.E. (Electrical Engineering)

Indian Institute of Science 1990

B.Sc. Physics (Honours)

University of Delhi 1985

## Publications:

1. A.K.S. Bhat and Vivek Agarwal, *Operating Modes and Simulation of the Series-Parallel resonant converter*, International Symposium on Circuits and Systems Conference Records, 1992, pp. 1883 - 1886.
2. Vivek Agarwal and A.K.S. Bhat, *A complete DC analysis of LCC-Type Parallel Resonant Converter*, IEEE IECON 1992, pp. 179 - 184.
3. Vivek Agarwal and A.K.S. Bhat, *Large Signal Analysis of the LCC-Type Parallel Resonant Converter using Discrete Time Domain Modeling*, IEEE IECON 1993, pp. 836-841.
4. Vivek Agarwal, V. Belaguli and A.K.S. Bhat, *Large Signal Analysis using Discrete Time Domain Modeling for LCC-Type Parallel Resonant Converter Operating in Discontinuous Current Mode*, Canadian Conference on Electrical and Computer Engineering 1993, pp. 80-83.

5. Vivek Agarwal and A.K.S. Bhat, *Large Signal Analysis of the LCC-Type Parallel Resonant Converter using Discrete Time Domain Modeling*, Accepted in IEEE Transactions on Power Electronics.
6. Vivek Agarwal and A.K.S. Bhat, *Small Signal Analysis of the LCC-Type Parallel Resonant Converter using Discrete Time Domain Modeling*, IEEE Power Electronics Specialists Conference (PESC), 1994. (Revised paper to be submitted to IEEE Transactions on Industrial Electronics.)
7. Vivek Agarwal and A.K.S. Bhat, *Small signal equivalent circuit modeling of the LCC-Type Parallel Resonant Converter using Discrete Time Domain Modeling* - To be submitted to IEEE Transactions on Aerospace and Electronic Systems.
8. *Steady-state and Dynamic Analysis of the Fixed Frequency Pulse Width Modulated LCC-Type Parallel Resonant Converter* - Paper to be submitted, under preparation.

## PARTIAL COPYRIGHT LICENSE

I hereby grant the right to lend my dissertation to users of the University of Victoria Library, and to make single copies only for such users or in response to a request from the Library of any other university, or similar institution, on its behalf or for one of its users. I further agree that permission for extensive copying of this dissertation for scholarly purposes may be granted by me or a member of the University designated by me. It is understood that copying or publication of this dissertation for financial gain shall not be allowed without my written permission.

Title of Dissertation :

Steady-State and Dynamic Analysis of the LCC-Type Parallel Resonant Converter

Author: \_\_\_\_\_  
Vivek Agarwal

\_\_\_\_\_ 21<sup>st</sup> October, 1994  
Date